

# **Measurement of the inclusive $t\bar{t}$ cross section and search for additional scalars in $t\bar{t}$ final states at the CMS experiment**

## Dissertation

zur Erlangung des Doktorgrades  
an der Fakultät für Mathematik, Informatik und Naturwissenschaften  
Fachbereich Physik  
der Universität Hamburg

vorgelegt von  
**Laurids Jeppe**

Hamburg  
2025

Gutachter der Dissertation:	Prof. Dr. Christian Schwanenberger Dr. Alexander Grohsjean
Zusammensetzung der Prüfungskomission:	Prof. Dr. Christian Schwanenberger Dr. Alexander Grohsjean TBD TBD TBD
Vorsitzender der Prüfungskomission:	TBD
Datum der Disputation:	TBD
Vorsitzender des Fach-Promotionsausschusses PHYSIK:	Prof. Dr. Wolfgang J. Parak
Leiter des Fachbereichs PHYSIK:	Prof. Dr. Markus Drescher
Dekan der Fakultät MIN:	Prof. Dr.-Ing. Norbert Ritter

# Abstract

Several measurements of top quark pair ( $t\bar{t}$ ) production at the CMS experiment are presented. The inclusive  $t\bar{t}$  production cross section  $\sigma_{t\bar{t}}$  is measured for the first time at  $\sqrt{s} = 13.6$  TeV, using  $1.21\text{ fb}^{-1}$  of early LHC Run 3 data. By combining the dilepton and lepton+jets ( $\ell+\text{jets}$ ) decay channels of  $t\bar{t}$  and constraining the lepton and b tagging efficiencies in a likelihood fit, a precision of 3.4% comparable to previous  $\sigma_{t\bar{t}}$  measurements is achieved.

Following this, a study of off-shell  $t\bar{t}$  production and  $t\bar{t}/tW$  interference is performed using the Monte Carlo (MC) generator **bb41**, which is validated for the first time in CMS simulation and compared to other MC generators, finding a significantly improved description of the data.

Finally, a search for spin-0 states decaying to  $t\bar{t}$  in the dilepton channels is presented, using  $138\text{ fb}^{-1}$  of LHC Run 2 data at  $\sqrt{s} = 13$  TeV. The invariant  $t\bar{t}$  mass ( $m_{t\bar{t}}$ ) is combined with spin correlation observables to gain sensitivity to the spin and  $\mathcal{CP}$  structure of possible new states. A statistically significant excess of events over the  $t\bar{t}$  continuum background is observed at low values of  $m_{t\bar{t}}$ , consistent with pseudoscalar spin correlations. It is interpreted in terms of a pseudoscalar  $t\bar{t}$  bound state  $\eta_t$ , and its cross section is measured to be  $\sigma(\eta_t) = 8.7 \pm 1.1\text{ pb}$  using a simplified model inspired by non-relativistic quantum chromodynamics.

The same data is further interpreted in terms of generic additional pseudoscalar or scalar bosons, and exclusion regions on their coupling to the top quark are derived both for the dilepton channels alone as well as in a combination with a separate analysis of the  $\ell+\text{jets}$  channels. As a third interpretation of the data, Axion-Like Particles (ALPs) decaying to  $t\bar{t}$  are considered in the limiting case of vanishing tree-level ALP-gluon couplings, while the more generic case is studied phenomenologically in simulation.



## Zusammenfassung

Es werden mehrere Messungen der Produktion von Top-Quark-Paaren ( $t\bar{t}$ ) am CMS-Experiment vorgestellt. Der inklusive  $t\bar{t}$ -Produktionsquerschnitt  $\sigma_{t\bar{t}}$  wird zum ersten Mal bei  $\sqrt{s} = 13.6$  TeV gemessen, unter Verwendung von frühen LHC Run 3-Daten mit integrierter Luminosität von  $1.21 \text{ fb}^{-1}$ . Durch Kombination der Dilepton- und Lepton+Jets ( $\ell+\text{jets}$ )-Zerfallskanäle von  $t\bar{t}$  und simultane Bestimmung der Lepton- und b-tagging-Effizienzen in einem Likelihood-Fit wird eine mit früheren  $\sigma_{t\bar{t}}$ -Messungen vergleichbare Präzision von 3.4% erreicht.

Anschließend wird Produktion von off-shell  $t\bar{t}$  und  $t\bar{t}/tW$ -Interferenz mit dem Monte Carlo (MC)-Generator `bb41` untersucht, der zum ersten Mal in der CMS-Simulation validiert und mit anderen MC-Generatoren verglichen wird und dabei zu einer deutlich verbesserten Beschreibung der Daten führt.

Schließlich wird eine Suche für nach  $t\bar{t}$  zerfallende Spin-0-Zustände in den Dilepton-Kanälen mit Daten von LHC Run 2, einer integrierten Luminosität von  $138 \text{ fb}^{-1}$  und  $\sqrt{s} = 13$  TeV vorgestellt. Die invariante Masse von  $t\bar{t}$  ( $m_{t\bar{t}}$ ) wird mit Spinkorrelations-Observablen kombiniert, um die Sensitivität gegenüber dem Spin und der  $\mathcal{CP}$ -Struktur möglicher neuer Zustände zu erhöhen. Ein statistisch signifikanter Überschuss von Ereignissen im Vergleich zum  $t\bar{t}$ -Kontinuums-Hintergrund bei geringen Werten von  $m_{t\bar{t}}$ , konsistent mit pseudoskalaren Spinkorrelationen, wird beobachtet. Der Überschuss wird als pseudoskalarer gebundener  $t\bar{t}$ -Zustand  $\eta_t$  interpretiert, und dessen Produktionsquerschnitt wird mithilfe eines vereinfachten, von nichtrelativistischer Quantenchromodynamik inspirierten Modells zu  $\sigma(\eta_t) = 8.7 \pm 1.1 \text{ pb}$  gemessen.

Die selben Daten werden weiterhin als generische zusätzliche pseudoskalare oder skalare Bosonen interpretiert, und Ausschlussregionen hinsichtlich ihrer Kopplungen zum Top-Quark werden sowohl für die Dilepton-Kanäle allein als auch für eine Kombination mit einer separaten Analyse der  $\ell+\text{jets}$ -Kanäle berechnet. Als eine dritte Interpretation der Daten werden zu  $t\bar{t}$  zerfallende Axion-Like Particles (ALPs) im Grenzfall verschwindender ALP-Gluon-Kopplungen betrachtet, während der allgemeinere Fall auf phänomenologische Weise in Simulationsdaten untersucht wird.



# **Eidesstattliche Versicherung**

Hiermit versichere ich an Eides statt, die vorliegende Dissertationsschrift selbst verfasst und keine anderen als die angegebenen Hilfsmittel und Quellen benutzt zu haben.

Sofern im Zuge der Erstellung der vorliegenden Dissertationsschrift auf generativer Künstlicher Intelligenz (gKI) basierende elektronische Hilfsmittel verwendet wurden, versichere ich, dass meine eigene Leistung im Vordergrund stand und dass eine vollständige Dokumentation aller verwendeten Hilfsmittel gemäß der guten wissenschaftlichen Praxis vorliegt. Ich trage die Verantwortung für eventuell durch die gKI generierte fehlerhafte oder verzerrte Inhalte, fehlerhafte Referenzen, Verstöße gegen das Datenschutz- und Urheberrecht oder Plagiate.

---

Datum

---

Unterschrift des Doktoranden

# Contents

<b>1</b>	<b>Introduction</b>	<b>11</b>
<b>2</b>	<b>Theoretical framework</b>	<b>13</b>
2.1	Standard Model . . . . .	13
2.1.1	Top quark . . . . .	14
2.1.2	Higgs mechanism . . . . .	15
2.2	The $p p \rightarrow t\bar{t}$ process . . . . .	16
2.2.1	Spin state of the $t\bar{t}$ system . . . . .	18
2.2.2	Spin density matrix . . . . .	21
2.2.3	Bound state effects in $t\bar{t}$ . . . . .	23
2.3	Beyond the Standard Model . . . . .	26
2.3.1	Heavy scalars in $t\bar{t}$ production . . . . .	27
2.3.2	Two-Higgs Doublet Model . . . . .	30
2.3.3	Axion-Like Particles . . . . .	30
<b>3</b>	<b>Monte Carlo event generation</b>	<b>33</b>
3.1	Matrix Element generators . . . . .	33
3.2	Parton showers and matching . . . . .	35
3.3	Multi-parton interactions . . . . .	37
3.4	Hadronization . . . . .	38
3.5	Pileup . . . . .	39
3.6	Detector and trigger simulation . . . . .	39
<b>4</b>	<b>Experimental methods</b>	<b>40</b>
4.1	The Large Hadron Collider . . . . .	40
4.2	The CMS experiment . . . . .	41
4.3	Object reconstruction . . . . .	43
4.4	Statistical interpretation . . . . .	45
<b>5</b>	<b>Measurement of the inclusive <math>t\bar{t}</math> cross section at <math>\sqrt{s} = 13.6</math> TeV</b>	<b>50</b>
5.1	Introduction . . . . .	50
5.2	Data sets and event selection . . . . .	51
5.2.1	Data sets . . . . .	51
5.2.2	Object definition . . . . .	52
5.2.3	Channel definition . . . . .	53

5.3	Corrections . . . . .	54
5.3.1	Experimental corrections . . . . .	55
5.3.2	Data-driven background estimation . . . . .	59
5.4	Control distributions . . . . .	65
5.5	Systematic uncertainties . . . . .	69
5.6	Fit results . . . . .	75
5.6.1	Statistical checks . . . . .	75
5.6.2	Top quark mass dependence . . . . .	78
5.7	Summary and Outlook . . . . .	79
<b>6</b>	<b>Simulation of on- and off-shell <math>t\bar{t}</math> production with bb4l</b>	<b>81</b>
6.1	Introduction . . . . .	81
6.2	The Monte Carlo generator bb4l . . . . .	81
6.3	Other $t\bar{t}$ Monte Carlo generators . . . . .	82
6.3.1	hvq . . . . .	83
6.3.2	ST_wtch . . . . .	83
6.3.3	ttb_NLO_dec . . . . .	83
6.4	Technical setup . . . . .	84
6.4.1	Parton shower matching . . . . .	84
6.4.2	Same-flavor leptons . . . . .	85
6.5	Results . . . . .	85
6.5.1	Comparison between generators . . . . .	85
6.5.2	Comparison of FSR matching settings . . . . .	91
6.5.3	Recoil in top decay . . . . .	93
6.6	Summary and Outlook . . . . .	94
<b>7</b>	<b>Search for heavy scalar or pseudoscalar bosons in <math>t\bar{t}</math> final states</b>	<b>96</b>
7.1	Introduction . . . . .	96
7.2	Analysis setup . . . . .	97
7.2.1	Data sets . . . . .	97
7.2.2	Object definition . . . . .	100
7.2.3	Event selection . . . . .	101
7.2.4	Experimental corrections . . . . .	101
7.2.5	Reconstruction of the $t\bar{t}$ system . . . . .	104
7.2.6	Sensitive observables . . . . .	108
7.3	Higher-order corrections in $t\bar{t}$ . . . . .	108
7.3.1	NNLO QCD corrections . . . . .	109
7.3.2	NLO EW corrections . . . . .	109
7.4	Matrix element reweighting for A/H signals . . . . .	112
7.4.1	Principle of the method . . . . .	112
7.4.2	Combination of multiple origin samples . . . . .	113
7.4.3	Validation . . . . .	114

7.5	Systematic uncertainties . . . . .	114
7.5.1	Theory uncertainties . . . . .	116
7.5.2	Experimental uncertainties . . . . .	117
7.5.3	Uncertainty smoothing . . . . .	118
7.5.4	Differences between MC generators . . . . .	118
7.6	Pre-fit distributions . . . . .	121
7.7	Interpretation of the excess . . . . .	121
7.7.1	Extraction of $t\bar{t}$ bound state effects . . . . .	121
7.7.2	Parity of the excess . . . . .	128
7.7.3	Checks of the result . . . . .	129
7.7.4	Interpretation in terms of A and H . . . . .	134
7.8	Limits on A/H bosons . . . . .	136
7.9	Combination with the $\ell$ +jets channels . . . . .	138
7.9.1	Analysis strategy in the $\ell$ +jets channel . . . . .	138
7.9.2	A/H limits . . . . .	143
7.9.3	Simultaneous A+H exclusion contours . . . . .	148
7.10	Comparison to other results . . . . .	149
7.10.1	ATLAS $t\bar{t}$ threshold measurement . . . . .	149
7.10.2	ATLAS A/H $\rightarrow t\bar{t}$ search . . . . .	152
7.10.3	Other $t\bar{t}$ measurements . . . . .	153
7.11	Summary and Outlook . . . . .	154
<b>8</b>	<b>Investigation of Axion-Like Particles decaying to <math>t\bar{t}</math></b>	<b>157</b>
8.1	Introduction . . . . .	157
8.2	Translation of experimental limits . . . . .	157
8.3	Phenomenological setup . . . . .	159
8.4	Comparison of ALP and A . . . . .	161
8.5	Projected limits for ALPs . . . . .	163
8.6	Summary and Outlook . . . . .	165
<b>9</b>	<b>Summary and Conclusions</b>	<b>167</b>
<b>A</b>	<b>Bibliography</b>	<b>169</b>
<b>B</b>	<b>Acknowledgements</b>	<b>191</b>
<b>C</b>	<b>Appendices</b>	<b>192</b>
C.1	Sample normalizations in the matrix element reweighting . . . . .	192

# <sup>1</sup> 1 Introduction

<sup>2</sup> It has always been the goal of high-energy physics to decipher the fundamental rules  
<sup>3</sup> of nature. The most recent triumph in this journey was undoubtedly the discovery of  
<sup>4</sup> the Higgs boson at the ATLAS and CMS experiments of the Large Hadron Collider  
<sup>5</sup> (LHC) in 2012 [1–3], thus completing the Standard Model of particle physics (SM).  
<sup>6</sup> Since then, the SM has been measured with ever-growing precision in the hope  
<sup>7</sup> of finding and characterizing possible deviations from its predictions, and searches  
<sup>8</sup> for new physics beyond the Standard Model (BSM) have been performed in many  
<sup>9</sup> possible phase spaces and for many SM extensions. So far, no significant discrepancy  
<sup>10</sup> has been found.

<sup>11</sup> One promising avenue for searches for new physics is the top quark, which is  
<sup>12</sup> the most massive fundamental particle in the SM. It is thus relevant for possible  
<sup>13</sup> new particles with Yukawa couplings, i.e. couplings proportional to the particle  
<sup>14</sup> mass, such as extended Higgs sectors. It is also of interest within the context of  
<sup>15</sup> the SM: as the only colored particle that decays before hadronizing, it allows for  
<sup>16</sup> measurements of spin properties, and poses challenges for its precision modeling in  
<sup>17</sup> quantum chromodynamics (QCD).

<sup>18</sup> In this thesis, different aspects of top quark pair ( $t\bar{t}$ ) production in proton-proton  
<sup>19</sup> collisions at the LHC are studied. It has been performed as part of the Compact  
<sup>20</sup> Muon Solenoid (CMS) experiment [4], which is one of the two large general-purpose  
<sup>21</sup> LHC experiments. The first topic is a measurement of the inclusive  $t\bar{t}$  production  
<sup>22</sup> cross section, performed at a center-of-mass energy of  $\sqrt{s} = 13.6$  TeV [5]. This world-  
<sup>23</sup> record energy was reached by the LHC for the first time in 2022 at the start of LHC  
<sup>24</sup> Run 3, after three years of shutdown and technical upgrades. The measurement  
<sup>25</sup> performed here uses only  $1.21 \text{ fb}^{-1}$  of data, taken directly at the start of Run 3 in  
<sup>26</sup> July and August 2022, to achieve a precision on the  $t\bar{t}$  cross section comparable with  
<sup>27</sup> previous LHC measurements. This was made possible by designing a strategy aimed  
<sup>28</sup> at estimating needed experimental corrections directly as part of the measurement.  
<sup>29</sup> In addition to confirming the SM at a new energy, the result was the first public  
<sup>30</sup> result of LHC Run 3 and showed the high quality of the then-fresh collision data.

<sup>31</sup> Second, the modeling of  $t\bar{t}$  production in off-shell regions of phase space as well  
<sup>32</sup> as the interference between  $t\bar{t}$  and  $tW$  production at CMS is studied [6]. This is  
<sup>33</sup> done using the Monte Carlo (MC) event generator **bb41** [7], which computes the full  
<sup>34</sup>  $pp \rightarrow b\bar{b}\ell^+\ell^-\nu_\ell\bar{\nu}_\ell$  matrix element for the dilepton decay channel of  $t\bar{t}$ , thus naturally  
<sup>35</sup> including off-shell and interference effects. **bb41** is validated for the first time in  
<sup>36</sup> the CMS simulation setup, and compared to other MC generators for  $t\bar{t}$  production,

37 preparing its use in future precision  $t\bar{t}$  measurements at CMS.

38 Finally, a search for new spin-0 states decaying to  $t\bar{t}$  is performed, using the  
39 full CMS Run 2 data set with a luminosity of  $138\text{ fb}^{-1}$  [8, 9]. The dilepton decay  
40 channel of  $t\bar{t}$  is considered, and besides the invariant  $t\bar{t}$  mass ( $m_{t\bar{t}}$ ), spin correlation  
41 observables constructed from the leptons and top quarks are used to distinguish  
42 different spin states of the  $t\bar{t}$  system, giving sensitivity to the  $\mathcal{CP}$  structure of possible  
43 new states. Excitingly, a statistically significant excess is observed in the data  
44 compared to the standard SM predictions, which is located at low  $m_{t\bar{t}}$  values and  
45 prefers pseudoscalar spin states. The excess is interpreted to be consistent with a  
46 pseudoscalar  $t\bar{t}$  (quasi-)bound state, which is expected to exist in the SM according  
47 to non-relativistic QCD calculations, though its modeling remains a challenge. This  
48 constitutes the first time such a  $t\bar{t}$  bound state is experimentally observed.

49 Alternatively, the results are interpreted in terms of generic additional pseu-  
50 doscalar or scalar bosons, as expected e.g. in a Two-Higgs-Doublet Model. The  
51 interference of these new bosons decaying to  $t\bar{t}$  and SM  $t\bar{t}$  production is taken into  
52 account, leading to complex signatures in the  $m_{t\bar{t}}$  spectrum. In addition to an inter-  
53 pretation of the same low- $m_{t\bar{t}}$  excess, exclusion regions are derived for the presence  
54 of either one or two such new bosons in terms of their couplings to the top quark.  
55 For this purpose, the analysis of the dilepton decay channel of  $t\bar{t}$  is further combined  
56 with a separate analysis of the lepton+jets decay channel.

57 As a third interpretation, heavy Axion-Like Particles (ALPs) decaying to  $t\bar{t}$  are  
58 considered for the first time [10]. After explicitly translating the experimental results  
59 for generic pseudoscalars to ALPs in the limiting case of no explicit gluon couplings,  
60 the general case is studied in simulated events. Sensitivity estimates for heavy  
61 ALPs coupling to top quarks, and for the possibility to distinguish them from other  
62 pseudoscalars, are derived for the currently available luminosity as well as future  
63 projections.

64 The thesis is organized as follows. In Chapters 2 to 4, the framework used for  
65 the analyses is outlined. In particular, Chapter 2 describes aspects of the SM and  
66 BSM theories relevant for this work, Chapter 3 briefly discusses the machinery of  
67 Monte Carlo generators as used for all relevant studies, and Chapter 4 describes the  
68 LHC and the CMS detector as well as object reconstruction and statistical inference  
69 techniques. Following that, Chapters 5 to 8 each discuss one of the experimental  
70 or phenomenological results that comprise this work: the inclusive  $t\bar{t}$  cross section  
71 measurement in Chapter 5, the study of off-shell  $t\bar{t}$  production and  $t\bar{t}/tW$  inter-  
72 ference in Chapter 6, the search for spin-0 states in  $t\bar{t}$ , including its interpretation  
73 as a  $t\bar{t}$  bound state, in Chapter 7, and the investigation of ALPs decaying to  $t\bar{t}$   
74 in Chapter 8. Chapters 5 and 6 fully consist of work done as part of this thesis,  
75 while in Chapters 7 and 8 the major contributions from this thesis are summarized  
76 at the beginning of the chapters. Finally, a short summary and outlook is given in  
77 Chapter 9.

## <sup>78</sup> 2 Theoretical framework

<sup>79</sup> This chapter gives an outline of the theoretical concepts and models used in this  
<sup>80</sup> thesis. It is split into two parts: First, the Standard Model of elementary particle  
<sup>81</sup> physics is discussed, with a heavy emphasis on the top quark. Secondly, several  
<sup>82</sup> hypothesized extensions of the Standard Model, relevant for the searches presented  
<sup>83</sup> in Chapters 7 and 8, are briefly introduced and compared.

### <sup>84</sup> 2.1 Standard Model

<sup>85</sup> The Standard Model of elementary particle physics, often simply called the Stan-  
<sup>86</sup> dard Model or SM, is, at the time of writing, the most successful theory describing  
<sup>87</sup> the fundamental particles making up our universe. It is the result of a steady pro-  
<sup>88</sup> gression of increasingly complex models, starting with the introduction of quantum  
<sup>89</sup> mechanics in the early 20th century and ending - for now - with the discovery of the  
<sup>90</sup> Higgs boson at the LHC in 2012. The model has been extensively tested at many  
<sup>91</sup> different experiments, most importantly the large collider experiments like LEP, the  
<sup>92</sup> Tevatron, and the LHC. So far, it has survived all these tests with excellence.

<sup>93</sup> The SM is formulated as a relativistic quantum field theory (QFT). That is, its  
<sup>94</sup> most fundamental objects are fields acting on four-dimensional spacetime which,  
<sup>95</sup> after a quantization procedure, yield physically observable particles as fundamental  
<sup>96</sup> excitations. By the usual counting scheme, there exist seventeen different such fields,  
<sup>97</sup> which can be classified into different groups, as schematically shown in Fig. 2.1.

<sup>98</sup> The first group consists of the twelve fermions, which have spin  $\frac{1}{2}$  and make up  
<sup>99</sup> all visible matter. They are further split into the leptons, consisting of three elec-  
<sup>100</sup> trically charged leptons - electron, muon, and tau lepton - and three corresponding  
<sup>101</sup> electrically neutral neutrinos, as well as the quarks, of which there are six differ-  
<sup>102</sup> ent flavors, called up, down, strange, charm, bottom, and top. The quarks have  
<sup>103</sup> fractional electric charge, and in addition carry color charge as their defining prop-  
<sup>104</sup> erty. Of note is that the fermions are also split into three generations, with each  
<sup>105</sup> generation consisting of a charged lepton, a neutrino, and two quarks. The only fun-  
<sup>106</sup> damental differences between the particles of different generations are their masses,  
<sup>107</sup> though the resulting physically observable properties, such as the lifetime, might be  
<sup>108</sup> dramatically different.

<sup>109</sup> The second group of particles are the bosons, which have integer spin. Here,  
<sup>110</sup> the four gauge bosons with spin 1 act as the force carriers of the four fundamental  
<sup>111</sup> interactions described by the SM: the photon, for the electromagnetic interaction

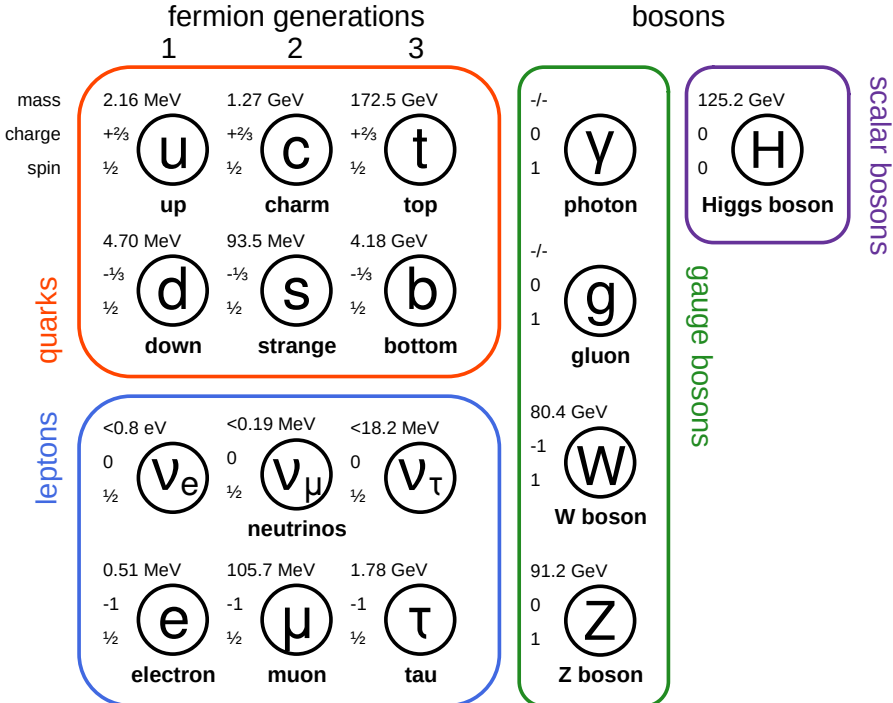


Figure 2.1: **The Standard Model.** A schematic depiction of the particle content of the SM, showing the seventeen fundamental particles, split into six quarks, six leptons, four gauge bosons, and the Higgs boson. The masses, electromagnetic charges, and spin of the particles is given next to the labels. Mass information is taken from Ref. [11].

with coupling strength  $\alpha_{\text{elm}}$ ; the W and Z bosons, for the weak interaction with coupling strength  $\alpha_W$ ; and the gluon, for the strong interaction with coupling strength  $\alpha_S$ . At high enough energies, the electromagnetic and weak interaction unify into the electroweak interaction (coupling strength  $\alpha_{\text{EW}}$ ). The last and final particle is the Higgs boson, which has spin 0. Its most important role in the SM is to give mass to the fermions, as well as the W and Z bosons, through the so-called Higgs mechanism [12, 13], which is briefly outlined in Sec. 2.1.2.

### 2.1.1 Top quark

All results presented as part of this thesis focus on one particular fundamental particle: the top quark. As such, it will be described in further detail in this section.

The top quark was first discovered in 1995 at the Tevatron by the CDF and D0 experiments [14, 15]. With a rest mass of  $m_t \approx 172.5 \text{ GeV}$ , the top quark is the most massive known fundamental particle, and as a result it has unique properties compared to the other quarks: Its extremely short lifetime of  $\sim 5 \times 10^{-25} \text{ s}$  is lower

126 than the typical time needed for a quark to hadronize under the strong interaction,  
 127 making it the only bare quark - that is, the only quark which, via its decay products,  
 128 is observable outside of hadrons. Among others, a consequence of this is that it fully  
 129 preserves spin information during its decay, while such information is typically lost  
 130 for other quarks during hadronization. More details on this are found in Sec. 2.2.2.

131 A second important property of the top quark that follows from its high mass is  
 132 its large Yukawa coupling to the SM Higgs boson, which is of order one. As a result,  
 133 the Higgs boson couples preferentially to the top quark of all SM fermions, and the  
 134 study of both the SM Higgs boson and hypothetical additional Higgs bosons (see  
 135 Sec. 2.3) is tightly connected to the top quark.

136 In the SM, the top quark decays to a bottom quark and a W boson with a branch-  
 137 ing ratio (BR) of almost 100% (to the degree that all other decays are commonly  
 138 neglected). The W boson, in turn, can decay either to a charged lepton ( $e$ ,  $\mu$  or  $\tau$ )  
 139 and the corresponding neutrino with a BR of  $\sim 32.6\%$ , or to a pair of quarks (one  
 140 up- and one down-type) with a BR of  $\sim 67.4\%$ . This results in different final states  
 141 for top production processes, which are discussed more in Sec. 2.2.

### 142 2.1.2 Higgs mechanism

143 The Higgs boson is the most recently discovered particle of the SM. Its existence was  
 144 confirmed in 2012 at the LHC by the ATLAS and CMS collaborations [1–3], firmly  
 145 establishing the SM in its current form as the accepted description of elementary  
 146 particle physics. While this work does not focus on the SM Higgs boson as it  
 147 does on the top quark, a short discussion of its role in the SM - the so-called Higgs  
 148 mechanism - is relevant for possible SM extensions to additional Higgs bosons, which  
 149 are searched for in Chapters 7 and 8.

150 In the SM Lagrangian, the Higgs boson appears as a complex doublet  $\phi$  in the  
 151 form

$$\mathcal{L}_{\text{SM}} \subset (D_\mu \phi)^\dagger D^\mu \phi + V(\phi) \quad (2.1)$$

152 where  $D_\mu$  is the covariant derivative, containing the minimal coupling to the gauge  
 153 fields, and the Higgs potential  $V(\phi)$  is

$$V(\phi) = \mu^2 \phi^\dagger \phi - \lambda (\phi^\dagger \phi)^2. \quad (2.2)$$

154 Here,  $\mu^2$  and  $\lambda$  are free parameters of the model. If both parameters are positive,  
 155 this potential (known as the “Mexican hat potential”) has a minimum at a non-zero  
 156 value of

$$|\phi| = \frac{\mu}{\sqrt{2\lambda}} \equiv \frac{v}{\sqrt{2}} \quad (2.3)$$

157 with the vacuum expectation value  $v = \mu/\sqrt{\lambda}$ . On the other hand, the minimum -

158 corresponding to the vacuum state - is degenerate with respect to the three phases  
159 (i.e. the  $SU(2)$  symmetry) of the complex doublet.

160 In the Higgs mechanism, this symmetry is now spontaneously broken in the transi-  
161 tion from the high-energy state of the early universe (where the minimum is at  
162  $|\phi| = 0$ ) to the low-energy state observed today. The physical particles after sym-  
163 metry breaking are then described by fluctuations around the new vacuum state.  
164 If the Higgs field were to be considered on its own, this would lead to one massive  
165 (corresponding to fluctuations in the  $|\phi|$  direction) and three massless degrees of  
166 freedom (corresponding to the phases).

167 However, the interaction with the electroweak gauge fields encoded within  $D_\mu$   
168 leads to the massless degrees of freedom being absorbed into the gauge fields. This  
169 turns three of the four massless spin-1 gauge fields of the electroweak Lagrangian  
170 (with two degrees of freedom each) into massive fields instead (which have an ad-  
171 ditional longitudinal polarization, and thus three degrees of freedom). These three  
172 massive gauge fields are identified with the W and Z bosons, while the remaining  
173 massless field is identified with the photon. Finally, the leftover massive degree of  
174 freedom from the Higgs doublet  $\phi$  is identified with the spin-0 boson observed at  
175 the LHC.

176 The resulting masses of the Z, W and Higgs bosons can be predicted as a function  
177 of  $\mu^2$ ,  $\lambda$  and the electroweak couplings and thus used to test the Higgs mechanism.  
178 In addition to the electroweak bosons, the Higgs mechanism can also give masses to  
179 fermions (charged leptons and quarks) by including a Yukawa interaction term in the  
180 Lagrangian. This results in couplings between the SM Higgs boson and the different  
181 fermions that are proportional to the respective fermion mass, leading to the largest  
182 coupling to the top quark. In possible extensions of the SM, this proportionality  
183 might be modified, making Yukawa coupling measurements attractive as tests of the  
184 SM.

## 185 2.2 The $p p \rightarrow t \bar{t}$ process

186 In proton-proton collisions at the LHC, the dominant production mode of top quarks  
187 is the production of a top-antitop quark pair ( $t \bar{t}$ ). The different parts of this thesis all  
188 focus on this process in different ways, and so this chapter gives a detailed overview  
189 of relevant effects.

190 At LO in QCD, there are three diagrams (up to permutations of initial and final  
191 states) contributing to  $t \bar{t}$  production, which can be seen in Fig. 2.2. They differ in  
192 their initial states: the first two diagrams are induced by gluon fusion, while the  
193 last one is induced by quark fusion (mostly from  $u\bar{u}$  and  $d\bar{d}$ ). The fraction of these  
194 is determined by the corresponding parton densities; at a center-of-mass energy of  
195  $\sqrt{s} \geq 13$  TeV, gluon fusion dominates with a fraction of roughly 90%.

196 At NLO in QCD, many more diagrams become relevant, including those induced

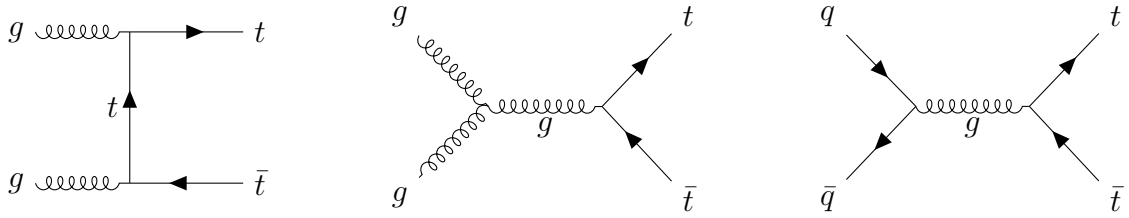


Figure 2.2: **Feynman diagrams for  $pp \rightarrow t\bar{t}$ .** The three diagrams (up to permutations) that contribute to the  $pp \rightarrow t\bar{t}$  process at LO in QCD.

197 by the fusion of one quark and one gluon, while radiating a real quark. Similarly,  
 198 real emissions of gluons can take place in  $gg$  or  $q\bar{q}$  fusion diagrams. These effects change  
 199 the kinematic properties of the produced top quarks, leading to NLO corrections for  
 200 predicted distributions.

201 After production, both the top and antitop quark in the  $t\bar{t}$  pair dominantly decay  
 202 into a W boson and a b (anti)quark each. This leads to three different decay  
 203 channels of the  $t\bar{t}$  pair depending on the decays of the two W bosons, which are  
 204 classified according to their number of leptons: The dilepton channel, with final  
 205 state  $b\bar{b}\ell^+\ell^-\nu\bar{\nu}$ ; the lepton+jets channel, with final state  $b\bar{b}\ell\nu q\bar{q}$ ; and the all-hadronic  
 206 channel, with final state  $b\bar{b}qq\bar{q}\bar{q}$ . Here,  $q$  stands in for any light quark ( $u, d, s$  or  $c$ ).

207 The three channels differ greatly in their experimental challenges: The dilepton  
 208 channel has the lowest branching ratio of  $\sim 10.6\%$ , which is further reduced to  
 209  $\sim 6.5\%$  when excluding  $\tau$  leptons decaying to hadrons due to them being experi-  
 210 mentally hard to reconstruct. It also suffers from the fact that the two produced  
 211 neutrinos escape the detector unobserved and are only measured as missing trans-  
 212 verse momentum, losing both information in the forward direction as well as the  
 213 ability to disentangle the two neutrinos. On the other hand, the final state of two  
 214 opposite-sign charged leptons, two b jets, and missing transverse momentum does  
 215 not have many other contributing processes in the SM, leading to very pure selec-  
 216 tions (particularly when the two leptons are an electron and a muon). All results in  
 217 this thesis make use of this channel prominently.

218 By contrast, the lepton+jets channel has a large BR of  $\sim 43.9\%$  ( $\sim 30.3\%$  when  
 219 excluding  $\tau$  leptons), leading to high data statistics, and allows for easier interpre-  
 220 tation of the missing transverse momentum due to only one neutrino. However, it  
 221 can suffer from contamination by W+jets and multijet QCD background (the latter  
 222 with non-prompt or fake leptons), from issues with combinatorics (i.e. the assign-  
 223 ment of experimentally measured jets to the decay products) and from hadronic jet  
 224 uncertainties, which can be large. This decay channel is employed for the result in  
 225 Chapter 5 as well as in the combination in Chapter 7.

226 Finally, the all-hadronic channel, with a similar BR of  $\sim 45.4\%$ , is typically  
 227 difficult to isolate from the background of QCD multijet production, and in addition  
 228 suffers even more strongly from combinatorics and jet uncertainties than the

Term symbol	Spin multiplicity	$\mathcal{P}$	$\mathcal{C}$
$^1S_0$	singlet	-1	+1
$^3P_0$	triplet	+1	+1
$^3S_1$	triplet	-1	-1
$^1P_1$	singlet	+1	-1
$^3P_1$	triplet	+1	+1
$^3D_1$	triplet	-1	-1

Table 2.1: **Spin states of  $t\bar{t}$ .** Overview of the possible angular momentum states of the  $t\bar{t}$  system with  $J \leq 1$ , including the spin multiplicity, the parity  $\mathcal{P}$  and the charge-parity  $\mathcal{C}$ .

229 lepton+jets channel. As a result, it is in many cases the least precise of the three  
 230 channels, and is not studied further in this work.

### 231 2.2.1 Spin state of the $t\bar{t}$ system

232 As fermions with spin  $\frac{1}{2}$ , top quarks have two possible spin states. As a result, the  
 233 relative spins of the  $t\bar{t}$  system can be either aligned, leading to a total vector state  
 234 with spin  $S = 1$ , or anti-aligned, leading to a scalar state with spin  $S = 0$ . Further-  
 235 more, the  $t\bar{t}$  system as a whole can have orbital angular momentum  $L$ , where  $L$  is a  
 236 non-negative integer. In analogy to atomic orbitals, the total angular momentum is  
 237 then  $\vec{J} = \vec{L} + \vec{S}$ , and for any chosen basis the set of quantum numbers  $\{S, L, J, J_z\}$   
 238 consists of conserved quantities. The angular momentum state is commonly written  
 239 using a term symbol  $^{2S+1}L_J$ , where  $2S+1$  denotes the multiplicity of the spin state,  
 240 and the orbital angular momentum  $L$  is written using spectroscopic notation (S for  
 241  $L = 0$ , P for  $L = 1$ , D for  $L = 2$  etc). An overview of the lowest possible states  
 242 ( $J \leq 1$ ) is given in Tab. 2.1, including also the parities and charge-parities  $\mathcal{P}$  and  
 243  $\mathcal{C}$ , which can be inferred from the intrinsic parities of top and antitop as well as the  
 244 orbital angular momentum. In proton-proton collisions, a mixture of all these states  
 245 is produced, with the ratio depending on the production mode ( $gg$ ,  $q\bar{q}$  or  $gq$ ) as well  
 246 as the energy.

247 In practice, the spins of the top (anti)quarks cannot be observed directly, and  
 248 instead must be inferred from their decay products. The way in which the spin  
 249 information is passed to the decay products is determined by the maximally parity-  
 250 violating nature of the weak interaction together with conservation of angular mo-  
 251 mentum. This is illustrated in Fig. 2.3 for the leptonic decay of the top (anti)quark:  
 252 Since the b quark is almost massless compared to the top quark, so that  $m_b = 0$  can  
 253 be assumed in the following, it will be ultra-relativistic. Like for all fermions, its  
 254 helicity is thus determined by its chirality. As a result, for the decay  $t \rightarrow W^+b$  the b  
 255 quark - left-handed due to the weak interaction - has negative helicity (spin opposite

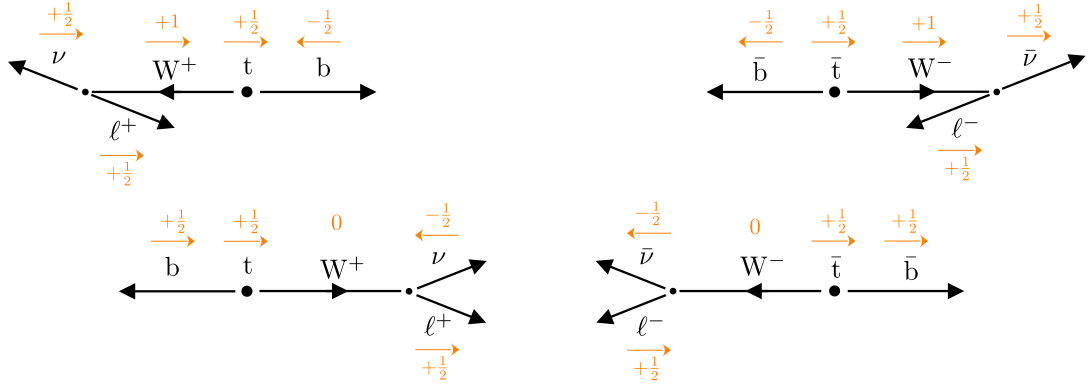


Figure 2.3: **Helicity in top decays.** Sketch of the allowed helicity configurations in a top (left) and antitop quark decay (right) in the rest frame of the quark, involving either a transversely (top,  $S_z = 1$ ) or longitudinally polarized W boson (bottom,  $S_z = 0$ ). The  $z$  axis corresponds to the spin of the top (anti)quark, and the orange arrows and numbers illustrate the spin in the  $z$  direction of the respective particles. It can be seen that, due to conservation of angular momentum and the parity-violating nature of the weak interaction, the  $\ell^+$  is preferred to be emitted in the direction of the  $t$  spin, while the  $\ell^-$  is preferred to be emitted opposite to the direction of the  $\bar{t}$  spin.

256 to its direction of flight), leading to two possibilities for the W boson through  
 257 conservation of angular momentum: transversely polarized (spin 1, top left in Fig. 2.3)  
 258 or longitudinally polarized (spin 0, bottom left in Fig. 2.3).

259 Since the decay of the  $W^+$  into  $\ell^+\nu$  is again mediated by the weak interaction, and  
 260 both decay products are nearly massless, the helicities of  $\ell^+$  and  $\nu$  must be positive  
 261 and negative, respectively. Applying again conservation of angular momentum, one  
 262 then finds from the sketch that in both cases, the charged lepton is emitted preferably  
 263 in the direction of the top quark spin.

264 Repeating the same line of arguments for the decay of the antitop (Fig. 2.3 on  
 265 the right), one finds that the opposite holds there: the charged lepton is emitted  
 266 preferably opposite to the antitop spin. As a result, the direction of flight of the  
 267 charged lepton in the center-of-mass system of its parent (anti)top can be used as a  
 268 proxy for the (anti)top spin (or, equivalently, its polarization). It should be noted  
 269 that this property of the top quark is unique among the quarks of the SM, since all  
 270 other quarks hadronize via the helicity-ignorant strong interaction and thus lose the  
 271 largest part of their spin information<sup>1</sup>.

272 Returning to the full  $t\bar{t}$  system, and applying the above observation to both

<sup>1</sup>See e.g. Ref. [16] for the greatly reduced possibilities of measuring spin correlations in  $b\bar{b}$  or  $c\bar{c}$  systems at the LHC.

273 top and antitop, one can now define observables to probe the  $t\bar{t}$  spin state, or  
 274 equivalently, the spin correlation between  $t$  and  $\bar{t}$ . A simple such variable is the  
 275 azimuthal difference  $\Delta\phi_{\ell\ell}$  between the two leptons in a dileptonic decay. Assuming  
 276 that the top and antitop are emitted back-to-back, a state with the top and antitop  
 277 spins aligned (i.e.  $S = 1$ ) will cause the two leptons to be emitted preferably in  
 278 opposite directions, leading to large  $\Delta\phi_{\ell\ell}$ , while anti-aligned spins ( $S = 0$ ) will  
 279 lead preferably to parallel leptons and thus small  $\Delta\phi_{\ell\ell}$ . While this variable has  
 280 the advantage of being easy to define and experimentally clean to measure, it is  
 281 suboptimal in that it is also strongly affected by the kinematics of the  $t\bar{t}$  production,  
 282 including higher-order corrections in QCD, and is heavily sculpted when selecting  
 283 certain areas of  $t\bar{t}$  phase space. Thus, it is afflicted with large modeling uncertainties.

284 A more powerful variable can be defined by employing suitable reference systems  
 285 as follows: the lepton and antilepton are first Lorentz boosted into the center-of-  
 286 mass frame of the  $t\bar{t}$  system, and then further boosted into the center-of-mass frame  
 287 of their parent (anti)tops. Then, a correlation variable  $c_{\text{hel}}$  is defined as the scalar  
 288 product of their direction unit vectors in these reference frames<sup>2</sup>:

$$c_{\text{hel}} = \hat{\ell}_t^+ \cdot \hat{\ell}_{\bar{t}}^- \quad (2.4)$$

289 It can be shown that, irrespective of the mode of production of the  $t\bar{t}$  system and  
 290 inclusive in the rest of the phase space, the distribution of this observable always  
 291 follows a straight line [18], i.e.

$$\frac{1}{\sigma} \frac{d\sigma}{dc_{\text{hel}}} = \frac{1}{2} (1 - D c_{\text{hel}}) \quad (2.5)$$

292 The slope  $D$  depends on the spin and angular momentum of the produced  $t\bar{t}$   
 293 state. At LO in QCD, it can be shown that  $D = -1$  for pure singlet states (anti-  
 294 aligned spins, e.g.  ${}^1S_0$ ,  ${}^1P_1$ ) and  $D = +\frac{1}{3}$  for pure triplet states (aligned spins, e.g.  
 295  ${}^3S_1$ ,  ${}^3P_0$ ) [19, 20]. Higher-order corrections in QCD can slightly reduce these slopes  
 296 through emissions of real gluons in the decay, which weaken the correlations, but  
 297 these effects are on the order of 0.2% at NLO for leptons [21, 22].

298 In practice, any observed ensemble of  $t\bar{t}$  pairs will be a mixture of the different spin  
 299 states depending on the production mechanism and underlying theory, which can  
 300 be probed by measuring the slope  $D$ . As will be discussed in Sec. 2.3, extensions of  
 301 the SM can change the predicted slope, making measurements of  $D$  attractive tests  
 302 for new physics. The value of  $D$  has been measured e.g. in Refs. [23–25], as well  
 303 as more recently as a proxy variable in the context of measurements of quantum  
 304 entanglement in  $t\bar{t}$  production [26, 27].

---

<sup>2</sup>In this work, the naming convention from Ref. [17] is followed for  $c_{\text{hel}}$ . In e.g. Ref. [18], this variable is instead called  $\cos\varphi$ .

305 **2.2.2 Spin density matrix**

306 A more detailed way to quantify the spin properties of the  $\text{t}\bar{\text{t}}$  system, respective  
307 to an arbitrary spin basis, is the production spin density matrix  $\mathbf{R}$ , which (when  
308 averaged over initial spins and colors, and summed over final colors) can be written  
309 as [19, 20, 28]

$$\mathbf{R} = A \mathbb{1} \otimes \mathbb{1} + B_i^1 \sigma_i \otimes \mathbb{1} + B_i^2 \mathbb{1} \otimes \sigma_i + C_{ij} \sigma_i \otimes \sigma_j. \quad (2.6)$$

310 Here,  $\mathbb{1}$  is the two-dimensional identity matrix,  $\sigma_i$  with  $i = 1, 2, 3$  are the Pauli  
311 matrices, and the first and second components of the tensor product refer to the  
312 spin of the top and antitop quark, respectively. The scalar coefficient  $A$  describes  
313 the overall amplitude (i.e. the differential cross section as a function of the top and  
314 antitop kinematics) of  $\text{t}\bar{\text{t}}$  production, the vectors  $\vec{B}^1$  and  $\vec{B}^2$  describe the polarization  
315 of the top and antitop quark, and the matrix  $\mathbf{C}$  describes the correlation between  
316 their spins. All of them are, in general, functions of the partonic center-of-mass  
317 energy and the scattering angle of the top quark relative to the incoming partons.

318 As explained in Sec. 2.2.1, in a dileptonic decay the spin information is transferred  
319 almost completely to the charged leptons. Defining the lepton directions of flight in  
320 their parent frames  $\hat{\ell}_t^+$  and  $\hat{\ell}_{\bar{t}}^-$  as in Eq. (2.4), the resulting differential cross section  
321 in terms of the lepton angles, collectively denoted as  $\Omega$ , is [28]

$$\frac{1}{\sigma} \frac{d\sigma}{d\Omega} = 1 + \vec{B}^1 \cdot \hat{\ell}_t^+ + \vec{B}^2 \cdot \hat{\ell}_{\bar{t}}^- + (\hat{\ell}_t^+)^T \mathbf{C} \hat{\ell}_{\bar{t}}^-. \quad (2.7)$$

322 By integrating out the remaining angles, it can be shown from this that irrespec-  
323 tive of the chosen basis the slope  $D$  as defined in Eq. (2.5) can be recovered from  
324 the matrix  $\mathbf{C}$  as [18, 29]

$$D = \frac{1}{3} \text{Tr} [\mathbf{C}]. \quad (2.8)$$

325 As discussed in Sec. 2.2.1,  $D$  is maximally negative for pure singlet states (corre-  
326 sponding to a positive slope in  $c_{\text{hel}}$ ), and thus is ideal for separating those in a mixed  
327 ensemble. One can define similar separating observables for other states using the  
328 spin density matrix by choosing a suitable spin basis. In this work, the so-called  
329 helicity basis proposed in Ref. [30] is used. The three axes of this basis, denoted  $\hat{k}$ ,  
330  $\hat{r}$  and  $\hat{n}$ , are defined as follows:  $\hat{k}$  is simply the direction of flight of the top quark in  
331 the center-of-mass frame of the  $\text{t}\bar{\text{t}}$  system, such that the top quark spin with respect  
332 to  $\hat{k}$  is equal to the helicity. The second axis,  $\hat{r}$ , is orthogonal to  $\hat{k}$  in the scattering  
333 plane of the  $\text{pp} \rightarrow \text{t}\bar{\text{t}}$  process. Finally, the third axis  $\hat{n}$  is orthogonal on both  $\hat{k}$  and  
334  $\hat{r}$ , oriented such that the  $\{\hat{k}, \hat{r}, \hat{n}\}$  system is left-handed. If  $\hat{p}$  denotes the beam axis  
335 and  $\theta_t^*$  the top scattering angle, the latter two axes are given by

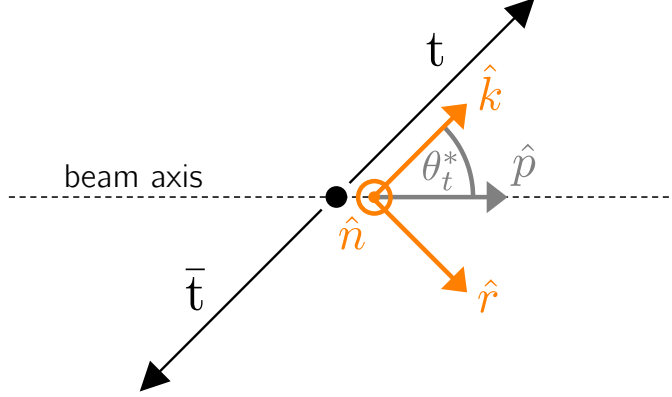


Figure 2.4: **Helicity basis.** Sketch of the helicity basis used to define the top and antitop quark spins. The unit vectors  $\hat{k}$ ,  $\hat{r}$  and  $\hat{n}$  define the right-handed basis, while the beam axis is given by  $\hat{p}$  and the top quark scattering angle by  $\theta_t^*$ .

$$\hat{r} = \frac{\hat{p} - \cos \theta_t^* \hat{k}}{|\hat{p} - \cos \theta_t^* \hat{k}|} \quad \text{and} \quad \hat{n} = \hat{r} \times \hat{k} = \frac{\hat{p} \times \hat{k}}{|\hat{p} \times \hat{k}|}. \quad (2.9)$$

336 This coordinate system is visualized in Fig. 2.4. It is used, among others, in  
 337 Refs. [24, 25] to measure both the polarizations  $\vec{B}^1$  and  $\vec{B}^2$  and spin correlation  
 338 coefficients  $C_{ij}$  ( $i, j = k, r, n$ ). In this work, only the spin correlation is considered.  
 339 Particularly, in addition to  $c_{\text{hel}}$ , the following observable is defined:

$$c_{\text{han}} = -(\hat{\ell}_t^+)_k (\hat{\ell}_{\bar{t}}^-)_k + (\hat{\ell}_t^+)_r (\hat{\ell}_{\bar{t}}^-)_r + (\hat{\ell}_t^+)_n (\hat{\ell}_{\bar{t}}^-)_n \quad (2.10)$$

340 where  $(\hat{\ell}_i)$ ,  $i = k, r, n$  refers to the  $i$ -th component of the respective vector in the  
 341  $\{k, r, n\}$  basis. This observable, like  $c_{\text{hel}}$ , has the advantage of always being linear  
 342 in the absence of phase space cuts, i.e.

$$\frac{1}{\sigma} \frac{d\sigma}{dc_{\text{han}}} = \frac{1}{2} (1 + D^{(k)} c_{\text{han}}) \quad (2.11)$$

343 where [19]

$$D^{(k)} = \frac{1}{3} (C_{kk} - C_{rr} - C_{nn}). \quad (2.12)$$

344 From Eq. (2.12), it can be seen that the slope is maximally negative,  $D^{(k)} = -1$ ,  
 345 when the top and antitop spins are anti-correlated along the top direction of flight  
 346 ( $C_{kk} = -1$ ) and correlated along the orthogonal directions ( $C_{rr} = C_{nn} = +1$ ). The  
 347 (unpolarized) state described by these correlations is a pure triplet state ( $S = 1$ ) [19].

Particularly, the  ${}^3P_0$  state of  $t\bar{t}$  always corresponds to this spin state: It has no total angular momentum, so that its total spin and orbital angular momentum must be anti-aligned. Since the orbital angular momentum is always exactly zero in the direction of flight of the top quarks, the  $t\bar{t}$  system must be in an orbital angular momentum eigenstate with  $L_k = 0$ , and thus also in a total spin eigenstate with  $S_k = 0$ . In other words, the spins in the  $\hat{k}$  direction are anti-aligned, corresponding to  $C_{kk} = -1$ . In order to arrive at  $S = 1$ , i.e. a pure triplet state, it is required that the other entries fulfill  $C_{rr} = C_{nn} = 1$ .

### 2.2.3 Bound state effects in $t\bar{t}$

When predicting distributions of observables for hard scattering processes such as  $t\bar{t}$  production, one usually employs perturbative calculations at a fixed order in the strong coupling constant  $\alpha_S$ , possibly matched to a parton shower (see Chapter 3). However, at low energy scales (or equivalently, long distances) the strong interaction becomes non-perturbative, leading to effects that cannot be captured in the usual perturbative expansion irrespective of the order in  $\alpha_S$  (though they might or might not be captured in expansions or resummations with other parameter choices).

In the  $pp \rightarrow t\bar{t}$  process, such effects might play a role in the vicinity of the  $t\bar{t}$  production threshold, i.e. for  $m_{t\bar{t}} \sim 2m_t$ , where the relative velocities of the produced top quarks become small. In particular, one possible class of effects not included in simple expansions in  $\alpha_S$  are  $t\bar{t}$  bound states (“toponium”). Such states (also called quarkonia) are well-known in  $c\bar{c}$  and  $b\bar{b}$  production, where they lead to composite particles such as  $J/\psi$ ,  $\eta_c$  or  $\Upsilon$ . When translating this knowledge to  $t\bar{t}$ , however, there is a significant difference: due to the large top quark mass, the lifetime of the top quark is expected to be shorter than the (formal) lifetime of any possible  $t\bar{t}$  bound state. As a result, the state would in the majority of cases not decay e.g. to photons, gluons or hadrons like the lighter quarkonia, but instead disassociate by one of the constituent top quarks decaying normally to  $Wb$ . This phenomenon, sometimes called a “quasi-bound state” or a “virtual bound state”, would lead to a possible peak in the  $m_{WWb\bar{b}}$  spectrum slightly below the  $t\bar{t}$  threshold.

Calculations of the  $m_{WWb\bar{b}}$  spectrum at the  $t\bar{t}$  threshold including the effects from a possible bound state have been performed independently in Refs. [31–35]. All of these calculations work in the framework of non-relativistic QCD (NRQCD), which treats the slowly moving ( $v \ll c$ ) top (anti)quarks as non-relativistic particles. This approach can be seen as a low-energy effective field theory (EFT) of the SM where high-energy modes have been integrated out, or alternatively, as an alternate perturbative expansion in the ratio  $\alpha_S/\beta$ , where  $\beta$  is the top quark velocity. The result is a non-relativistic Schrödinger equation for the wavefunction of the  $t\bar{t}$  system, with the interaction between the top quarks described by the low-energy limit of the QCD Coulomb potential, representing the exchange of soft gluons. At LO, it is given by [32]

$$V_{\text{QCD}}^{[1,8]}(q) = -\frac{4\pi\alpha_S C^{[1,8]}}{q^2}, \quad (2.13)$$

where the color factor is  $C^{[1]} = 4/3$  for color-singlet and  $C^{[8]} = -1/6$  for color-octet states. As a result, only  $t\bar{t}$  systems in a color-singlet state feel an attractive force and can possibly form a bound state, while color-octet states are instead repulsed. At the LHC,  $t\bar{t}$  bound states can thus at LO be produced only from gg initial states, since  $q\bar{q}$  systems are always color-octets. From this, the spin state of the produced bound state can be inferred: Since both of the top quarks have low velocity, states with orbital angular momentum  $L \neq 0$  will be strongly suppressed (beyond NLO in NRQCD [32]). Furthermore, the gg initial state in  $t\bar{t}$  production close to the  $t\bar{t}$  threshold always has spin  $S = 0$  (and thus total angular momentum  $J = 0$ ), with  $S = 2$  contributions suppressed by powers of the top velocity [20], so that the resulting  $t\bar{t}$  system must be in the  ${}^1S_0^{[1]}$  state. At NLO in QCD, also  ${}^3S_1^{[1]}$  states can be produced; however, the contribution is very small (less than 0.1% of the total cross section [32]).

Refs. [32–35] agree that the binding energy of the  $t\bar{t}$  bound state, defined as the difference of the peak position in the  $m_{WWb\bar{b}}$  spectrum to  $2m_t$ , is around  $-2$  GeV, resulting in a “mass” of 343 GeV for the  $t\bar{t}$  bound state for a top mass of 172.5 GeV. The exact line shape of the peak is less well known. However, the experimental resolution of  $m_{WWb\bar{b}}$  is expected to be much larger than the bound state width of order  $\sim 2\Gamma_t$  (see Sec. 7.2.5), making the details of the spectrum irrelevant to an experimental search.

The existing NRQCD calculations predict only certain differential distributions and cannot be directly compared to experimental data on a per-event level. Because of this, a simplified model for the  $t\bar{t}$  bound state is introduced following Refs. [19, 36–38]. Instead of a first-principles calculation, the bound state effects are modeled as an additional state spin-0 state  $\eta_t$ , which is added to the conventional perturbative QCD (pQCD) calculation of  $t\bar{t}$ .  $\eta_t$  is defined to couple directly to gluons and top quarks via the Lagrangian

$$\mathcal{L}_{\eta_t} = -\frac{1}{4}g_{gg\eta_t}\eta_t G_{\mu\nu}^a \tilde{G}^{a\mu\nu} - ig_{t\bar{t}\eta_t}\eta_t \bar{t}\gamma_5 t \quad (2.14)$$

where  $G_{\mu\nu}^a$  is the gluon field strength tensor,  $\tilde{G}_{\mu\nu}^a$  its dual, and  $g_{gg\eta_t}$  as well as  $g_{t\bar{t}\eta_t}$  are arbitrary coupling strengths. The resulting model has three free parameters: the binding energy  $E_b = m(\eta_t) - 2m_t$ , the total width  $\Gamma(\eta_t)$  and the production cross section  $\sigma(\eta_t)$  (the latter determining the couplings  $g_{gg\eta_t}$  and  $g_{t\bar{t}\eta_t}$ ). In Ref. [37], they are determined by fitting them to the NRQCD calculation from Ref. [33], yielding

$$E_b = -2 \text{ GeV} \implies m(\eta_t) = 343 \text{ GeV}, \quad \Gamma(\eta_t) = 7 \text{ GeV}, \quad \sigma(\eta_t) = 6.43 \text{ pb} \quad (2.15)$$

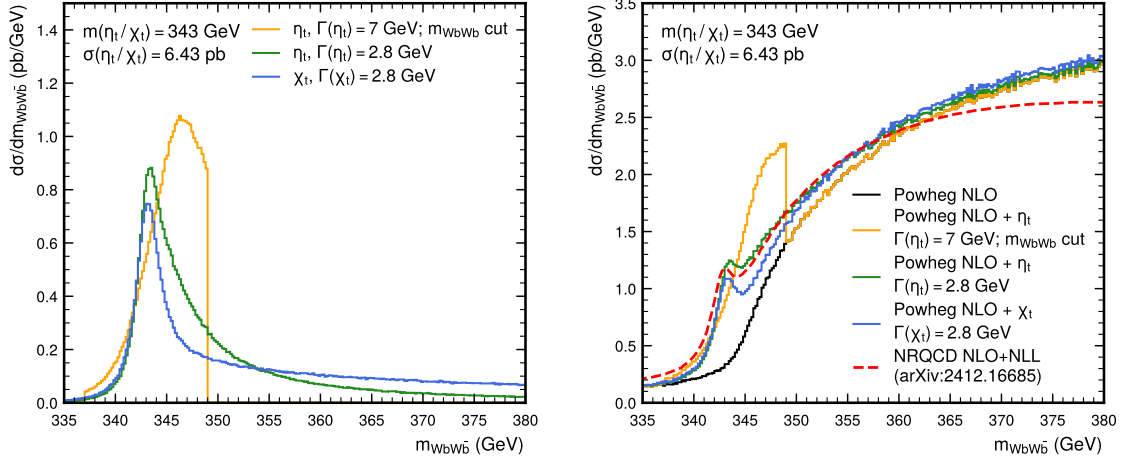


Figure 2.5: **Line shape of  $\eta_t$  and  $\chi_t$ .** The  $m_{WWb\bar{b}}$  distribution close to the  $t\bar{t}$  threshold, as predicted by the  $\eta_t$  and  $\chi_t$  models on their own (left) and stacked on top of a pQCD  $t\bar{t}$  prediction from Powheg hvq (right, see Sec. 3.1). For the orange line, the  $\eta_t$  width is chosen to be 7 GeV, and a cut on  $|m_{WWb\bar{b}} - m(\eta_t)|$  is applied (Eq. (2.15)), while for the green line, the  $\eta_t$  width is chosen as 2.8 GeV, and no further cuts are made (Eq. (2.16)). The blue line shows  $\chi_t$  for a width of 2.8 GeV. In the right plot, all models are compared to an NRQCD prediction from Ref. [35].

In the generation of events, the top quarks are allowed to be fully off-shell by calculating the full amplitude  $pp \rightarrow \eta_t \rightarrow W^+W^-b\bar{b}$ , thus making sure that the phase-space region  $m_{WWb\bar{b}} < 2m_t$  is populated. Furthermore, Ref. [37] recommends that the contribution of  $\eta_t$  should be restricted to the region  $|m_{WWb\bar{b}} - m_{\eta_t}| \leq 6 \text{ GeV}$  so that the bulk of the  $t\bar{t}$  phase space, in which the pQCD calculation is expected to be accurate while the NRQCD calculation misses relativistic corrections, is not affected.

However, Refs. [36, 38] recommend instead

$$E_b = -2 \text{ GeV} \implies m(\eta_t) = 343 \text{ GeV}, \quad \Gamma(\eta_t) = 2\Gamma_t = 2.8 \text{ GeV} \quad (2.16)$$

and no cut on  $|m_{WWb\bar{b}} - m(\eta_t)|$ .

The resulting  $m_{WWb\bar{b}}$  distribution for the combination of pQCD  $t\bar{t}$  and  $\eta_t$  is shown in Fig. 2.5 at the level of hard scattering for both parameterizations, on its own as well as stacked on top of a pQCD prediction of the  $t\bar{t}$  continuum at NLO in QCD. The stacked distributions are compared to an NRQCD prediction from Ref. [35]. At the level of hard scattering, the lower width of  $\Gamma(\eta_t) = 2\Gamma_t$  agrees much better with the predicted NRQCD spectrum and avoids an unphysical discontinuity due to the  $m_{WWb\bar{b}}$  cutoff. Thus, this parameterization will be used in this work wherever

436 possible, i.e. in Secs. 7.7 and 7.8, though the parameterization of Eq. (2.15) is  
437 retained for the sake of consistency with other results in Sec. 7.9. For more details,  
438 see these sections.

439 In the final stages of this work, a more involved model for  $t\bar{t}$  bound states was  
440 published in Ref. [39]. There, instead of simulating an additional pseudoscalar state  
441  $\eta_t$ , the bound state effects are included in leading-order color-singlet  $t\bar{t}$  production  
442 by directly reweighting produced events with the ratio of Green's functions. This  
443 model is in principle fully predictive, i.e. it does not require fitting parameters to  
444 external calculations. However, it could not be validated in time for inclusion in the  
445 results of Chapter 7, it does not explicitly distinguish between  $t\bar{t}$  spin states, and it  
446 is also unclear on how to match it to the  $t\bar{t}$  continuum. Because of this, it is not  
447 further considered here and its investigation left for future work.

448 While NRQCD predicts any possible  $t\bar{t}$  bound state contribution in pp collisions  
449 to be dominated by the  ${}^1S_0^{[1]}$  state, with contributions from excited states strongly  
450 suppressed, experimentally it will still be useful to compare this spin state to other  
451 possibilities. To this end, a second toy model, denoted  $\chi_t$ , is defined in analogy to  
452  $\eta_t$  by the interaction Lagrangian

$$\mathcal{L}_{\chi_t} = -\frac{1}{4}g_{gg\chi_t}\chi_t G_{\mu\nu}^a \tilde{G}^{a\mu\nu} - g_{t\bar{t}\chi_t}\chi_t \bar{t}t \quad (2.17)$$

453 where  $g_{gg\chi_t}$  and  $g_{t\bar{t}\chi_t}$  are again arbitrary couplings. This Lagrangian contains a  $\mathcal{CP}$ -  
454 even coupling to the top quark, compared to the  $\mathcal{CP}$ -odd coupling in Eq. (2.14). It  
455 thus produces  $t\bar{t}$  systems in the  ${}^3P_0^{[1]}$  state, which is the only other possible state  
456 with  $J=0$  (cf. Tab. 2.1). The free parameters of this model are again cross section,  
457 mass, and width; they are set here to the same values as for  $\eta_t$  in all cases<sup>3</sup>. The  
458 resulting  $m_{WWb\bar{b}}$  line shape is also seen in Fig. 2.5. It shows a small peak similar  
459 to  $\eta_t$  at  $\sim 343$  GeV, though it exhibits a more pronounced tail at high  $m_{WWb\bar{b}}$  since  
460 the  ${}^3P_0$  state carries one unit of orbital angular momentum and thus favors higher  
461 top quark velocities. In Sec. 7.7.2, the  $\chi_t$  model will be used in conjunction with  $\eta_t$   
462 to probe the spin state of the observed excess. Other possible states, such as the  
463 vector state  ${}^3S_1^{[1]}$ , are not considered here and instead left for future work.

## 464 2.3 Beyond the Standard Model

465 The Standard Model, greatly successful as it is at describing the results of collider  
466 experiments so far, is nonetheless known to be incomplete. In fact, there exist  
467 several experimental results which cannot be explained by SM predictions, such

---

<sup>3</sup>Based on analogies to  $c\bar{c}$  and  $b\bar{b}$  quarkonia [40], it is likely that a true  ${}^3P_0$  bound state would have a slightly higher mass, though it is unknown whether this would be noticeable even in the hard-scattering level spectrum due to the large smearing from the top width. It is anyway expected to be irrelevant within the experimental resolution.

as the observation of dark matter in many astrophysical contexts [41–43] or the observed masses of the neutrinos [44, 45].

In addition, the SM is plagued by several theoretical challenges that will likely not be overcome without major modifications to the theory. Chief among these is the unification of the forces of the SM - the electroweak and strong interactions - with gravity as described by General Relativity, which is not included in the SM at all. Doing so has proven extremely challenging, and no fully consistent unified theory of all forces is known yet. Further open questions are, for example, the hierarchy or naturalness problem [46–48] or the strong  $\mathcal{CP}$  problem [49, 50].

In order to solve these problems in a satisfactory manner, a more general theory will have to be found, which should include the SM as its low-energy limit. In many cases, this will result in additional as of yet undiscovered particles. There is a multitude of such Beyond the Standard Model (BSM) extensions, each attacking different parts of the problems, and one of the major tasks of particle physics is to explore which parts of the parameter space of these models can be probed with the current experiments.

This work, in particular, aims to probe models predicting new, heavy spin-0 states coupling strongly to the top quark. Such states can be searched for in the  $pp \rightarrow t\bar{t}$  process, as outlined in a generic fashion in Sec. 2.3.1. Following that, two explicit realizations of such models are discussed, namely the Two-Higgs Doublet Model (2HDM) (Sec. 2.3.2) and Axion-Like Particle (ALP) models (Sec. 2.3.3).

### 2.3.1 Heavy scalars in $t\bar{t}$ production

Consider an unspecified BSM extension predicting (possibly among others) a massive spin-0 state  $\Phi$  coupling to top quarks via a Yukawa interaction. In the absence of couplings to other particles, the Lagrangian of such a state can be written as [19]

$$\mathcal{L}_\Phi = \frac{1}{2}(\partial_\mu \Phi)(\partial^\mu \Phi) + \frac{m_\Phi^2}{2}\Phi^2 + g_{\Phi\bar{t}t} \frac{m_t}{v} \bar{t}\Phi (\cos \alpha + i\gamma_5 \sin \alpha) t. \quad (2.18)$$

where  $m_\Phi$  is the mass of the new state and  $g_{\Phi\bar{t}t}$  is a coupling modifier, scaled to the SM Higgs-top Yukawa coupling with the SM Higgs vacuum expectation value  $v$ . The phase  $\alpha$  is a free parameter determining the  $\mathcal{CP}$  structure of the  $\Phi\bar{t}t$  coupling: For  $\alpha = 0$ , the coupling is purely  $\mathcal{CP}$ -even or scalar, while for  $\alpha = \pi/2$ , the coupling is purely  $\mathcal{CP}$ -odd or pseudoscalar. Intermediate values for  $\alpha$  will cause  $\mathcal{CP}$ -mixed couplings, which in general will result in  $\mathcal{CP}$  violation in processes involving top quarks. Possible experimental indicators of such  $\mathcal{CP}$  violation in  $pp \rightarrow t\bar{t}$  are e.g. discussed in Ref. [29].

In the scope of this work, only the  $\mathcal{CP}$ -conserving cases of  $\Phi$  are considered. For convenience, the pure pseudoscalar case will in the following be called A, while the pure scalar case will be called H.

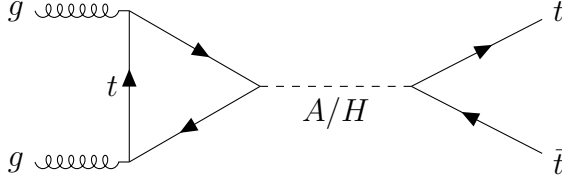


Figure 2.6: **Feynman diagram for  $gg \rightarrow A/H \rightarrow t\bar{t}$ .** Only the leading-order gluon fusion diagram is shown, with a top quark running in the loop.

Similar to the SM Higgs boson, the most important production channel of either state at the LHC will be through loop-induced gluon fusion, followed by associated production with either  $t\bar{t}$  or a single top quark. Only the former is considered here; experimental searches for the latter case can be found e.g. in Ref. [51]. Furthermore, the decay of the new state will depend on its mass: For low masses, the particle will decay either through loop-induced couplings to e.g.  $gg$  or  $\gamma\gamma$  or, if present, through couplings to other SM or BSM particles than the top quark. For masses of  $m_{A/H} > 2m_t$ , however, the decay to  $t\bar{t}$  is kinematically allowed and will in many cases be dominant due to the large Yukawa coupling. In this case, the process  $gg \rightarrow A/H \rightarrow t\bar{t}$  will lead to the same final state as SM  $t\bar{t}$  production, as illustrated in Fig. 2.6. This process will be considered in more detail in the rest of this chapter, and one of the main results of this thesis is an experimental search for such a signature (Chapter 7).

Fig. 2.7 shows the predicted differential cross sections of this model in terms of  $m_{t\bar{t}}$ , the invariant mass of the  $t\bar{t}$  pair, for different  $A/H$  masses. The cross section is shown as the difference to the SM prediction at the level of the hard scattering and at LO in QCD. It can be seen that the total effect of  $A$  and  $H$  is a very distinct peak-dip structure around the  $A/H$  mass. This is because the  $gg \rightarrow A/H \rightarrow t\bar{t}$  production channel interferes with SM  $gg \rightarrow t\bar{t}$  production, which leads to deficits in certain regions of phase space due to destructive interference. For high  $A/H$  masses, there is an additional broad peak at low masses of  $m_{t\bar{t}}$ . This originates from the gluon PDF, which is steeply increasing for small parton momentum fractions, corresponding to low  $m_{t\bar{t}}$ , and thus compensates the suppression by the off-shell  $A/H$  at low  $m_{t\bar{t}}$  for the  $A/H$ -SM interference.

A further consequence of the interference is that the differential cross section scales non-linearly with the coupling modifiers  $g_{At\bar{t}}$  and  $g_{Ht\bar{t}}$ . The dependence (for arbitrary observables) can be parameterized as

$$d\sigma = d\sigma^{\text{SM}} + g_{A/Ht\bar{t}}^2 d\sigma^{\text{int}} + g_{A/Ht\bar{t}}^4 d\sigma^{\text{res}} \quad (2.19)$$

where the superscripts “SM”, “int” and “res” refer to the SM, SM- $A/H$  interference, and resonant  $A/H$  contributions, respectively.

In addition to the  $m_{t\bar{t}}$  spectrum, an  $A/H$  contribution is also expected to modify

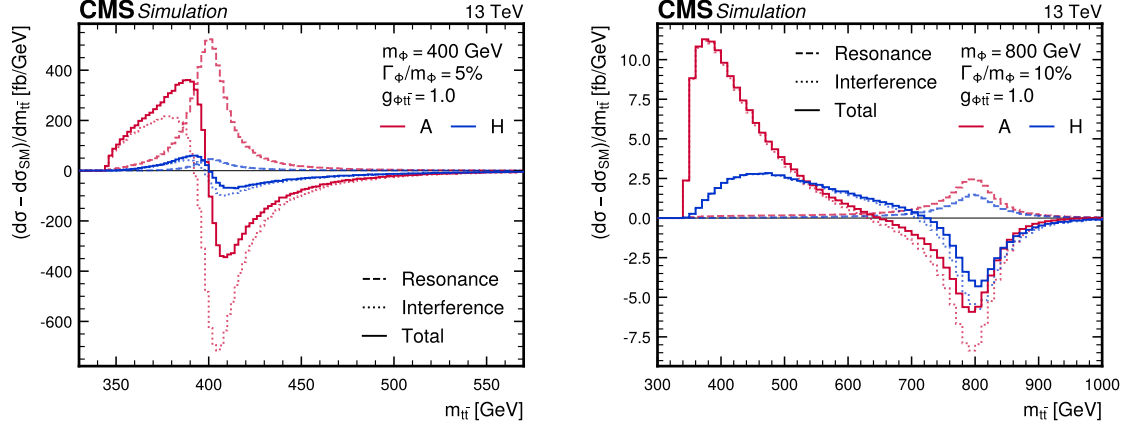


Figure 2.7: **Differential cross sections for  $A/H \rightarrow t\bar{t}$ .** The hadronic differential cross section as a function of the invariant  $t\bar{t}$  mass, with the SM prediction subtracted, for  $m_{A/H} = 400 \text{ GeV}$ ,  $\Gamma_{A/H}/m_{A/H} = 5\%$  (left) and  $m_{A/H} = 800 \text{ GeV}$ ,  $\Gamma_{A/H}/m_{A/H} = 10\%$  (right) as well as for  $A$  (red) and  $H$  (blue), at a coupling modifier of  $g_{A/Ht\bar{t}} = 1$ . The resonance and interference components as well as their sum are shown as dashed, dotted and solid lines, respectively. They are calculated from same the Monte Carlo simulation samples described in Sec. 7.2.1.

the spin state of the  $t\bar{t}$  system. As a single spin-0 particle, an intermediate  $A/H$  resonance has neither spin nor orbital angular momentum. Due to conservation of angular momentum, this implies that the  $t\bar{t}$  system will be produced in a state with  $J = 0$ , which leaves only the  ${}^1S_0$  and  ${}^3P_0$  states (compare Tab. 2.1).

Furthermore, the spin-0 intermediate state has positive intrinsic parity and is charge-neutral. This implies that for  $H$ , whose interaction with the top quark is separately  $\mathcal{C}$ - and  $\mathcal{P}$ -conserving, the  $t\bar{t}$  system will have quantum numbers of  $\mathcal{C} = +1$  and  $\mathcal{P} = +1$ , which is true for the  ${}^3P_0$  state. For  $A$ , on the other hand, the interaction is maximally  $\mathcal{P}$ -violating, leading to quantum numbers of  $\mathcal{C} = +1$  and  $\mathcal{P} = -1$ , which matches the  ${}^1S_0$  state. As a result, the process  $gg \rightarrow A \rightarrow t\bar{t}$  will always produce the  ${}^1S_0$  spin singlet state, while  $gg \rightarrow H \rightarrow t\bar{t}$  will produce the  ${}^3P_0$  spin triplet state.

As explained in Secs. 2.2.1 and 2.2.2, the observable  $c_{\text{hel}}$  has maximal slope  $D$  for spin-singlet states, making it a good discriminator between  $A$  and the SM. For  $H$ , it can be shown that the produced triplet state instead maximizes the slope  $D^{(k)}$  of the observable  $c_{\text{han}}$ , as defined in Eq. (2.10) [19]. Consequently, both  $c_{\text{hel}}$  and  $c_{\text{han}}$  will be used in the experimental search for such states presented in Chapter 7.

### 551 2.3.2 Two-Higgs Doublet Model

552 A common class of models predicting additional scalars as discussed in Sec. 2.3.1  
 553 are Two-Higgs-Doublet Models (2HDMs) [52, 53]. In these models, there are two  
 554 complex  $SU(2)$  Higgs doublets with eight degrees of freedom in total (as opposed  
 555 to a single doublet in the SM), which after electroweak symmetry breaking results  
 556 in five physical states (compare Sec. 2.1.2). Such a structure for the Higgs sector  
 557 arises, for example, in many supersymmetric models [54] or axion models [55].

558 In general, 2HDMs can include  $\mathcal{CP}$ -violating interactions (similar to Sec. 2.3.1)  
 559 as well as flavor-changing neutral currents (FCNCs). Both of these phenomena are  
 560 experimentally well constrained, and so it makes sense to restrict oneself to  $\mathcal{CP}$ -  
 561 and flavor-conserving limits. Doing so leads to definite quantum numbers of the  
 562 five physical scalar states of the 2HDM: two neutral scalar ( $\mathcal{CP}$ -even) states  $h$  and  
 563  $H$ , a neutral pseudoscalar ( $\mathcal{CP}$ -odd) state  $A$ , and two charged states  $H^+$  and  $H^-$ .  
 564 Usually, the state  $h$  is identified with the SM Higgs boson at a mass of 125 GeV.  
 565 Then, the two other neutral states  $H$  and  $A$  - if massive enough - could play the role  
 566 of additional Higgs bosons decaying to  $t\bar{t}$  as discussed in Sec. 2.3.1.

567 Depending on the nature of the discrete symmetry that is used to impose flavor  
 568 conservation, there can be different types of 2HDMs, which differ in the structure of  
 569 the couplings to the SM. No particular 2HDM type is assumed in this work, and the  
 570 results of Chapter 7 are instead presented in terms of the generic model of Sec. 2.3.1.

### 571 2.3.3 Axion-Like Particles

572 Another very generic class of BSM scalars relevant to the  $pp \rightarrow t\bar{t}$  process are ax-  
 573 ions and Axion-Like Particles (ALPs), denoted here as  $a$ . Axions were originally  
 574 conceived as solutions to the strong  $\mathcal{CP}$  problem [49, 50, 56, 57], which is a re-  
 575 sult of the non-trivial vacuum structure of QCD. When deriving the effective QCD  
 576 Lagrangian, the presence of certain classes of topological solutions to the classical  
 577 Yang-Mills equations leads to an additional  $\mathcal{CP}$ -violating term [58]

$$\mathcal{L}^{QCD} \supset \theta \frac{\alpha_S}{8\pi} G_{\mu\nu}^a \tilde{G}^{a\mu\nu}, \quad (2.20)$$

578 where  $G_{\mu\nu}^a$  is again the gluon field strength and  $\tilde{G}_{\mu\nu}^a$  its dual. The coefficient  $\theta$  of this  
 579 term is a free parameter in the range  $[0, 2\pi)$ , with no particular value preferred from  
 580 first principles. However, experimentally, no  $\mathcal{CP}$  violation in pure QCD has been  
 581 observed, and  $\theta$  is strongly bounded at  $|\theta| \leq 10^{-10}$  (the strongest bounds coming  
 582 from measurements of the electromagnetic dipole moment of the neutron [58–60]).  
 583 The strong  $\mathcal{CP}$  problem thus consists of explaining why the  $\mathcal{CP}$ -violating  $G_{\mu\nu}^a \tilde{G}^{a\mu\nu}$   
 584 term vanishes.

585 The most prominent way to solve the strong  $\mathcal{CP}$  problem is by introducing a new  
 586 real scalar field  $a$ , the axion field, with a Lagrangian [58]

$$\mathcal{L}^{\text{ax}} = \frac{1}{2}\partial_\mu a\partial^\mu a + \frac{\alpha_S}{8\pi} \frac{a}{f_a} G_{\mu\nu}^a \tilde{G}^{a\mu\nu} + \text{interaction terms} \quad (2.21)$$

where  $f_a$  is called the axion scale, and all other interaction terms with SM fields are required to be invariant under a shift  $a \rightarrow a + \kappa f_a$  with arbitrary  $\kappa$ . It can be shown that this Lagrangian, when added to the SM QCD Lagrangian including the term in Eq. (2.20), leads to a global minimum at  $a/f_a + \theta = 0$ , so that after a field shift the  $\mathcal{CP}$ -violating term is absorbed in the axion-gluon coupling and no  $\mathcal{CP}$  violation is expected in QCD alone. This is known as the Peccei-Quinn mechanism.

In Eq. (2.21), the axion-gluon interaction term has dimension 5 and is thus non-renormalizable, with the cutoff scale given by  $f_a$ . The axion must thus be necessarily be seen as a low-energy EFT description of different physics at the higher scale  $f_a$ . Many different UV-complete models including axions exist [58, 61–64], which lead to different interaction terms with other SM particles such as photons, electroweak bosons or massive fermions.

In this work, a focus is placed upon models which predict couplings to SM fermions, particularly the top quark. The EFT Lagrangian is parameterized in a model-independent approach as [65]

$$\begin{aligned} \mathcal{L}^{\text{ALP}} = & \frac{1}{2}\partial_\mu a\partial^\mu a + \frac{m_a^2}{2}a^2 - c_G \frac{a}{f_a} G_{\mu\nu}^a \tilde{G}^{a\mu\nu} - c_B \frac{a}{f_a} B_{\mu\nu} \tilde{B}^{\mu\nu} \\ & - c_W \frac{a}{f_a} W_{\mu\nu}^a \tilde{W}^{a\mu\nu} - \sum_f c_f \frac{\partial^\mu a}{f_a} \bar{\Psi}_f \gamma_\mu \Psi_f, \end{aligned} \quad (2.22)$$

where the index  $f$  runs over the SM fermions,  $\Psi_f$  are the fermion fields,  $B_{\mu\nu}$  and  $W_{\mu\nu}^a$  are the EW boson fields before symmetry breaking, and the free parameters are the scale  $f_a$ , the mass  $m_a$ , and the couplings to gluons  $c_G$ , to EW bosons  $c_B$  and  $c_W$  and to fermions  $c_f$  (where no flavor mixing was assumed). This Lagrangian, depending on the choice of the free parameters, might or might not correspond to a UV-complete model and solve the strong  $\mathcal{CP}$  problem. Because of this, the field  $a$  is here called an Axion-Like Particle. Even when it does not correspond to a true axion, it might be a physically well-motivated extension of the SM, e.g. as a dark matter candidate or mediator.

In the ALP-fermion interaction term in Eq. (2.22), the shift symmetry of  $a$  is directly manifest since it only depends on the derivative of  $a$ . However, by employing the equations of motion for  $a$  as well as the Higgs mechanism, one can rewrite Eq. (2.22) with a Yukawa-like interaction instead. Dropping the EW bosons and fermions other than the top quark leads to

$$\mathcal{L}^{\text{ALP}} = \frac{1}{2}\partial_\mu a\partial^\mu a + \frac{m_a}{2}a^2 - c_{\tilde{G}} \frac{a}{f_a} G_{\mu\nu}^a \tilde{G}^{a\mu\nu} + i c_t m_t \frac{a}{f_a} \bar{t} \gamma^5 t. \quad (2.23)$$

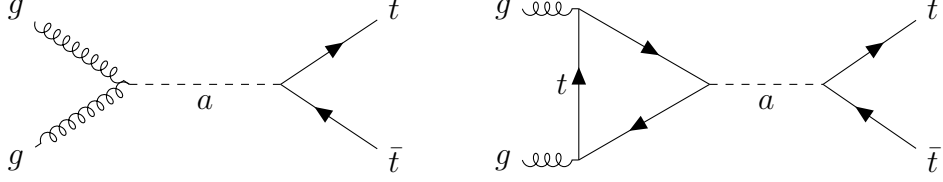


Figure 2.8: **Feynman diagrams for  $gg \rightarrow a \rightarrow t\bar{t}$ .** The left diagram corresponds to the gluon-ALP contact interaction and scales with  $c_{\tilde{G}}c_t$ , while the right diagram shows the top quark loop and scales with  $c_t^2$ .

616 Performing this basis change induces an additional ALP-gluon coupling term (in  
 617 general dependent on the other SM couplings), which was absorbed by redefining  
 618 the Wilson coefficient from  $c_G$  to  $c_{\tilde{G}}$ . This basis will be used in the remainder of  
 619 this work.

620 It can be seen by comparing Eq. (2.23) to Eq. (2.18) that the ALP-top coupling  
 621 has the exact same structure as the generic  $\mathcal{CP}$ -odd boson introduced in Sec. 2.3.1.  
 622 Thus, if the ALP is heavy enough to be produced at the LHC and decay to  $t\bar{t}$ , it  
 623 can be searched for in  $t\bar{t}$  final states similarly to the generic pseudoscalar  $A$ . Such  
 624 heavy ALP masses can be reached naturally and serve as solutions to the strong  $\mathcal{CP}$   
 625 problem e.g. in UV models containing extra non-abelian gauge groups, resulting in  
 626 containing forces with large containment scales [66–69].

627 If, in addition, the ALP couplings also satisfy  $c_{\tilde{G}} = 0$ , the two Lagrangians in  
 628 Eqs. (2.18) and (2.23) are identical, and all conclusions drawn on  $A$  can be directly  
 629 transferred to the ALP. On the other hand, if  $c_{\tilde{G}} \neq 0$ , an additional production  
 630 diagram involving a gluon contact interaction becomes available, as depicted in  
 631 Fig. 2.8. A phenomenological study characterizing both cases in detail forms the  
 632 core of Chapter 8 of this work.

## 633 3 Monte Carlo event generation

634 In order to test the Standard Model or extract any of its parameters at the LHC,  
635 one requires a prediction which can be compared to the experimental data recorded  
636 by the detectors in the form of collision events. This is, in general, a very complex  
637 task consisting of many different subprocesses and physical scales. The generation  
638 starts with the hard parton scattering, then continues with the emission of addi-  
639 tional radiation, effects of interactions with other partons in the colliding protons,  
640 hadronization, interactions between other protons in the same bunch, and ends with  
641 the simulation of the different subdetectors and triggers. Many of these processes  
642 are not only probabilistic, but intractable through direct analytical or numeric inte-  
643 gration due to the large phase space and the complexity of the problems involved.

644 Instead, the Monte Carlo (MC) method is used for this purpose. Here, it amounts  
645 to randomly sampling an event from the phase space of the starting distribution - in  
646 this case, the hard scattering - and then passing it through a chain of simulation tools  
647 for the remaining steps until one arrives at an event that is directly comparable to  
648 events recorded experimentally. This method is advantageous in that the numerical  
649 error in an arbitrary region of phase space always scales with  $1/\sqrt{N}$ , where  $N$  is  
650 the total number of events produced, independently of the dimensionality of the  
651 problem. Thus, getting a numerically accurate prediction is mostly a matter of  
652 producing a sufficient number of MC events.

653 In this chapter, the different tools used in the CMS simulation chain are discussed.  
654 A focus is laid on the hard scattering or matrix element generators (Sec. 3.1) as well  
655 as the parton showering (Sec. 3.2) since these are the focus of the studies presented  
656 in Chapter 6, while interactions with other partons in the colliding protons (“multi-  
657 parton interactions”, Sec. 3.3), hadronization (Sec. 3.4), interactions between other  
658 protons in the same bunch (“pileup”, Sec. 3.5), as well as the detector and trigger  
659 simulation (Sec. 3.6) are only briefly touched upon.

### 660 3.1 Matrix Element generators

661 At the LHC, protons are collided with large center-of-mass energies of multiple  
662 TeV. Because protons are not fundamental particles, but bound states of QCD  
663 which cannot be perturbatively described from first principles, providing accurate  
664 predictions for proton-proton collisions is generally a very challenging task. For the  
665 specific case of hard scattering processes, i.e. processes in which the particles in  
666 the final state  $X$  have large transverse momenta, one can employ the factorization

<sup>667</sup> theorem of QCD [70]:

$$\sigma(pp \rightarrow X) = \int_0^1 dx_1 \int_0^1 dx_2 \sum_{a,b} f_a(x_1, \mu_F) f_b(x_2, \mu_F) \hat{\sigma}(a(x_1 P) + b(x_2 P) \rightarrow X) \quad (3.1)$$

<sup>668</sup> where  $P$  is the incoming momentum of the protons, assumed to be purely longitudinal and thus  $P = \sqrt{s}/2$ , and the sum runs over all possible combinations  $a, b$  of <sup>669</sup> initial state partons (quarks and gluons). This formula factorizes the total hadronic <sup>670</sup> cross section into two parts: The partonic cross section  $\hat{\sigma}(a + b \rightarrow X)$  describes the <sup>671</sup> scattering of two partons at high energies, and can be computed perturbatively in <sup>672</sup>  $\alpha_S$  due to asymptotic freedom of QCD. The functions  $f_a(x, \mu_F)$  on the other hand <sup>673</sup> are the parton distribution functions (PDFs) and describe the probability of finding <sup>674</sup> a parton of type  $a$  with momentum fraction  $p_a/P = x$  in the proton structure. <sup>675</sup> Since they probe low momentum scales where  $\alpha_S$  is large, they cannot be computed <sup>676</sup> perturbatively and instead need to be measured experimentally. In addition to  $x$ , <sup>677</sup> they also depend on the factorization scale  $\mu_F$ , which is the energy scale defining <sup>678</sup> the separation between hard (perturbative) and soft (non-perturbative) QCD. It is <sup>679</sup> typically set to be equal to the characteristic energy of the incoming partons, e.g. <sup>680</sup> half the partonic invariant mass. In contrast to the dependence on  $x$ , the dependence <sup>681</sup> on  $\mu_F$  is a prediction of QCD and follows from the DGLAP equations [71, <sup>682</sup> 72].

<sup>684</sup> The partonic cross section can further be written differentially as [70]

$$d\hat{\sigma}(ab \rightarrow X) = \frac{1}{2\hat{s}} \left( \prod_f \frac{d^3 p_f}{(2\pi)^3} \frac{1}{2E_f} \right) |\mathcal{M}(ab \rightarrow X)|^2 (2\pi)^4 \delta^{(4)} \left( \sum_f p_f \right) \quad (3.2)$$

<sup>685</sup> where  $\hat{s} = x_1 x_2 s$  is the partonic center-of-mass energy squared, the term in the <sup>686</sup> brackets refers to the integral over the final state phase space and depends only <sup>687</sup> on the number and masses of the final state particles  $f$ , the  $\delta$  function encodes <sup>688</sup> momentum conservation, and only the scattering matrix element  $\mathcal{M}$  depends on the <sup>689</sup> details of the process considered.

<sup>690</sup> Events are now generated by drawing randomly from the full kinematically allowed <sup>691</sup> final state phase space, as well as from the PDFs characterizing the initial state, and <sup>692</sup> keeping them with a probability proportional to the corresponding hadronic cross <sup>693</sup> section according to Eq. (3.1). The partonic cross section here might be known analytically for simple processes, or might need to be integrated numerically for complex <sup>694</sup> processes (especially at NLO or higher). The PDFs, based on fits to experimental <sup>695</sup> data, are usually tabulated and interpolated; in this work, the NNPDF 3.1 PDF set <sup>696</sup> is most commonly used for this purpose [73]. In practice, codes usually employ an <sup>697</sup>

698 adaptive sampling algorithm to enhance the fraction of events that pass and thus  
 699 speed up the calculation, see e.g. Ref. [74].

700 ME generators exist at LO, NLO, and (approximate) NNLO in QCD, all of which  
 701 are used at different points in this work. For NLO and NNLO processes, care must  
 702 be taken to cancel ultraviolet (UV) as well as infrared (IR) divergences that often  
 703 appear in the integration of the matrix element. The former is done in the framework  
 704 of renormalization, which usually introduces a dependence on an additional scale,  
 705 the renormalization scale  $\mu_R$ . Similar to  $\mu_F$ , it is typically set to the energy scale  
 706 of the process, and, since the dependence is expected to vanish at infinite order in  
 707 QCD, variations of  $\mu_R$  and  $\mu_F$  are often used to asses the size of uncertainties due  
 708 to missing higher orders [75]<sup>1</sup>.

709 IR divergences, on the other hand, arise when the momenta of massless particles  
 710 in loop diagrams, such as gluons or light quarks, approach zero. They need to  
 711 be canceled with corresponding divergent diagrams containing the emission of a  
 712 real particle, which occur when the emission is soft or collinear with respect to the  
 713 emitter. As a result, NLO calculations for the final state  $X$  will always need to also  
 714 take into account the final state  $X + j$ , where  $j$  can be a gluon or light quark [77].

715 In this work, two different ME generators are used. The first is MG5\_AMC@NLO,  
 716 a general-purpose ME generator that can work both at LO and NLO [78]. It features  
 717 fully automated computation of arbitrary processes in the SM or BSM, where the  
 718 model is specified in the Universal FeynRules Output (UFO) format [79]. It is used  
 719 in this work for both SM and BSM processes.

720 The second ME generator used is POWHEG Box (short for Positive Weighted Hard-  
 721 est Emission Generator), which is a generic framework for NLO and approximate  
 722 NNLO generators [80–82]. In contrast to MG5\_AMC@NLO, it is not automated,  
 723 and requires the manual implementation of each process. Many processes are pub-  
 724 licly available as part of the POWHEG Box collection, and several are used in this  
 725 work. Importantly,  $pp \rightarrow tt$  is generated at NLO with the POWHEG Box process  
 726 `hvq` [83] in Chapters 5, 7 and 8. The two generators also differ in the scheme used  
 727 to match to the parton shower, which is explained in the next section.

## 728 3.2 Parton showers and matching

729 The output of ME generators are events whose final states typically involve quarks  
 730 and gluons with high momenta. Formally, such computations are accurate to some

---

<sup>1</sup>Using  $\mu_R$  and  $\mu_F$  variations as estimates of missing higher order uncertainties, while common, can only give a rough estimate of the magnitude of missing higher order contributions and does not truly give information about shape deficiencies in differential distributions. A recent, more thorough approach are *theory nuisance parameters* quantifying the uncertainty in specific parts of the theory calculation [76]. This method has however not yet been extended to  $tt$  production and is thus not considered here.

fixed order in  $\alpha_S$  at which the calculation was performed, and all further emissions of gluons, as well as splittings of gluons into quark-antiquark-pairs, is suppressed by additional powers of  $\alpha_S$ . However, the matrix elements for such splittings become singular in the limit that the emitted partons are *soft* and/or *collinear* to the emitting particle, leading to IR divergences. The divergences can be regulated by absorbing them in renormalized PDFs, from which the DGLAP equations can be derived [72, 75]. They still lead to large corrections for each additional soft or collinear splitting considered, proportional to  $\alpha_S \log(\hat{s}/\Lambda_{\text{QCD}}^2)$ , where  $\Lambda_{\text{QCD}} \approx 250 \text{ MeV}$  is the scale at which QCD becomes nonperturbative. This term is of order 1 and thus spoils the convergence of the perturbative series if it is cut off at a fixed order in  $\alpha_S$  [70, 72].

A way to approximately incorporate these corrections is by using parton showers. For a parton associated with some scale  $Q_0$ , the probability for no splitting to occur above some scale  $Q$  (with  $Q < Q_0$ ) is called the *Sudakov factor*  $\Delta(Q_0, Q)$ . Because the structure of the IR singularities in QCD is universal, i.e. depending only on the types of particles in the splitting but not the rest of the process, its leading-logarithmic behavior can be computed from the matrix elements of  $q \rightarrow qg$  and  $g \rightarrow q\bar{q}$  splittings (the *splitting kernels*). The parton shower algorithm now iteratively draws random numbers from this distribution, thus generating real emissions and splittings with successively lower scales  $Q$  down to  $\Lambda_{\text{QCD}}$ . In practice, the Sudakov factor usually contains additional terms beyond the leading-logarithmic behavior depending on the details of the algorithm [72].

The scale  $Q$  which determines in which order the splittings are performed is also called the *ordering variable*, and its form can be freely chosen as long as it correctly captures the soft and collinear singularities. Two common choices are the transverse momentum of the emission ( $p_T$ -ordered shower) or the emission angle respective to the emitting particle (angular-ordered shower). The result of either choice is an effective resummation of the logarithms associated to each emission, which is why parton showers are said to be leading-log (LL) accurate for certain observables.

The main parton shower used in this work is a  $p_T$ -ordered dipole shower, included as part of the PYTHIA multi-purpose event generator [84, 85]. It works by collecting quark-antiquark pairs into color dipoles, which radiate gluons together so that the recoil is distributed between the quarks. Here, it is mostly used by matching it to the ME generators described in Sec. 3.1. This is usually trivial at LO: the parton shower simply starts from the final state as given by the ME generator.

At NLO or higher, however, care must be taken that there is no double-counting between the additional real emissions in the final state of the ME generator and the emissions of the shower, as well as between the virtual corrections that are exact in the ME generator and approximated in the shower [72]. Several matching schemes exist to solve this issue. In this work, the MC@NLO and POWHEG schemes are used and briefly explained in the following.

In the MC@NLO scheme [86], as implemented in MG5\_AMC@NLO, the double-

773 counting is corrected for using a subtraction scheme: During the generation of the  
774 real and virtual correction terms in the matrix elements, the approximate corrections  
775 that would be used in the parton shower are subtracted from the squared amplitude.  
776 When the events generated in this way are then showered, the approximate correc-  
777 tion terms are effectively added back, so that formally the exact result is recovered  
778 at NLO accuracy. This strategy is conceptually simple and easy to generalize (and  
779 thus automatize, as done in MG5\_AMC@NLO). However, at phase-space points  
780 where the approximate terms are larger than the exact ones, it inherently results in  
781 events with negative weights, which can greatly increase the MC statistics required.

782 In the POWHEG scheme [80, 81], as used in the POWHEG Box, the fraction  
783 of negative weights is greatly reduced by always generating the first real emission  
784 in the ME generator, so that the real emission term is already exact, and then  
785 only subtracting the approximate virtual correction term. The parton shower then  
786 needs to only generate the second-hardest and higher emissions, which is typically  
787 achieved by starting the shower evolution at the scale of the first, ME-level emission  
788 (sometimes called “wimpy shower”).

789 This approach assumes that the scale definitions in the ME generator and the  
790 parton shower are identical, which in general will not always be the case. In par-  
791 ticular, for the important case of POWHEG matched to PYTHIA, used in this work  
792 for the simulation of  $pp \rightarrow t\bar{t}$ , there is a mismatch in the scales which might lead to  
793 double-counting. A more refined approach here is to use a vetoed shower: the shower  
794 is started at the kinematically allowed limits and evolved downwards as usual, or-  
795 dered by the scale as defined by PYTHIA. For the first emission the scale is then  
796 recomputed according to the POWHEG definition, and it is vetoed and re-showered  
797 if this scale is higher than the one in the ME.

798 A further improvement in the accuracy of the MC prediction can be achieved by  
799 generating any number of additional jets in the matrix element at either LO or NLO,  
800 so that these jets are described exactly by the ME generator instead of approximately  
801 by the shower. This, however, requires complex matching procedures, such as MLM  
802 matching [87] for LO and FxFx matching [88] for NLO matrix elements. In this  
803 work, both schemes are only used tangentially for either background processes in  
804 Chapter 5 or an alternative  $t\bar{t}$  prediction in Chapter 7.

805 More complicated procedures have to be invoked in the case that the ME contains  
806 more than one real emission. This case is studied in detail for the ME generator bb41  
807 in Chapter 6. Furthermore, besides PYTHIA, multi-purpose generator HERWIG [89,  
808 90] is considered in parts of Chapter 7, and briefly described there.

### 809 3.3 Multi-parton interactions

810 In addition to the hard scattering, additional soft QCD interactions might occur  
811 between the other partons in the two colliding protons. This is referred to as multi-

812 parton interactions (MPI) or underlying event (UE). It is handled by PYTHIA based  
813 on heuristic models, interleaved with the parton shower. In general, MPI parameters  
814 need to be tuned to experimental data. This was done by the PYTHIA authors, such  
815 as the different versions of the Monash tune [91], and building on top of this by  
816 the CMS collaboration in the form of the CP tune family, most recently the CP5  
817 tune [92]. Both tunes are based on a large data set of  $e^+e^-$ ,  $ep$ ,  $p\bar{p}$ , and  $pp$  collision  
818 data from many different experiments. The CP5 tune will be used in all parts of  
819 this work.

## 820 3.4 Hadronization

821 The result of the MPI-interleaved parton shower consists of a collection of bare  
822 quarks and gluons at energies of  $\mathcal{O}(\Lambda_{\text{QCD}})$ , at which QCD becomes non-perturbative.  
823 The hadronization of these quarks and gluons into hadrons as well as their subse-  
824 quent decays thus need to be described heuristically.

825 For most of this work, this is done using the Lund string fragmentation model [93,  
826 94], again implemented in PYTHIA. In this model, the strong force between a quark  
827 and an antiquark of opposite color is modeled as a string in space-time, standing in  
828 for e.g. a three-dimensional flux tube. The energy stored in the string is proportional  
829 to its length, consistent with the long-distance behavior of QCD observed e.g. in  
830 lattice QCD. Hard gluons can be accommodated in this model as kinks in the string,  
831 i.e. for a  $q\bar{q}g$  state, the  $q$  and  $\bar{q}$  are connected through the gluon instead of directly.

832 As the quarks move apart, the energy stored in the string increases, until it is  
833 large enough that the string fragments by creating an additional  $q\bar{q}$  pair from the  
834 vacuum. If the energy in the resulting strings is still large enough, the procedure  
835 repeats. Otherwise, the low-mass  $q\bar{q}$  pair is considered a meson, based on the flavors  
836 of its constituents. In its purest form, this model has only two free parameters  
837 which parameterize the distribution of the momentum fraction of the  $q\bar{q}$  pair in  
838 each fragmentation. However, in order to correctly describe e.g. flavor composition  
839 and  $p_T$  spectra of jets, many more parameters are usually needed. For more details  
840 on string fragmentation in PYTHIA, see e.g. Ref. [85]. Similar to MPI, hadronization  
841 parameters need to be tuned to data, and are also included in the Monash and CP5  
842 tunes.

843 One shortcoming of the default MPI and hadronization models is that both work  
844 in the leading color (LC) approximation, i.e. in the limit of a large number of  
845 QCD colors ( $N_c \rightarrow \infty$ ). This simplifies the models greatly because the chance  
846 of two unrelated color lines sharing the same color becomes infinitesimally small.  
847 Corrections to this approximation are typically of order  $1/N_c^2 = 1/9$ , and can be done  
848 via color reconnection (CR), for which different models exist, see e.g. Refs. [95, 96].  
849 The difference between different models is often considered a source of uncertainty  
850 in measurements, such as in Secs. 5.5 and 7.5, and can be a limiting factor for some

851 analyses (e.g. top quark mass measurements).

852 Finally, decays of produced unstable hadrons, including possible decay chains,  
853 are also handled by PYTHIA. Branching ratios are taken from experimental mea-  
854 surements where available, and predicted from heuristic models where not, see e.g.  
855 Ref. [85].

## 856 3.5 Pileup

857 At the currently achieved instantaneous luminosities, the proton bunches colliding at  
858 the LHC contain more than  $10^{11}$  protons on average. Because of this large number, it  
859 is expected that a single collision event contains interactions between more than one  
860 pair of protons from the two colliding bunches. This is known as pileup. It differs  
861 from MPI, in which the different interactions are between multiple partons in the  
862 same proton and are thus correlated from a QFT perspective, while different pileup  
863 interactions are in principle independent from each other. In Run 2, the average  
864 number of pileup interactions per bunch crossing ranged from 23-32 depending on  
865 the era of data taking [97], while it is 40 or higher in Run 3.

866 In simulation, pileup interactions are considered by mixing the generated hard  
867 interaction process with a dedicated sample of purely soft-QCD interactions, also  
868 generated in PYTHIA. The probability distribution of the number of pileup interac-  
869 tions is an input to this procedure, and is typically corrected after the generation  
870 is finished by reweighting in a suitable variable. In Sec. 5.3.1, an experimental ap-  
871 proach to this problem is taken by correcting experimentally accessible pileup-related  
872 parameters directly to data. In Sec. 7.2.4, on the other hand, the distribution of the  
873 true number of interactions is instead reweighted based on a theory prediction, using  
874 the measured total inelastic cross section and integrated luminosity as inputs [98].

## 875 3.6 Detector and trigger simulation

876 After the simulation of the interaction processes, the resulting collection of particles  
877 produced in an event is propagated to a full detector simulation using the program  
878 GEANT4 [99]. The result is a set of detector information from all subdetectors as  
879 well as the outputs of different triggers, similar to true experimental data, and so it  
880 can be passed to the different object reconstruction algorithms (cf. Sec. 4.3) in the  
881 same way as the data. Events are then analyzed by comparing the reconstructed ob-  
882 jects and quantities between data and simulation, ensuring a one-to-one comparison.  
883 Possible residual differences between data and simulation are often corrected for by  
884 applying calibration factors measured using well-known processes. The details of  
885 such calibrations will be explained in Chapters 5 and 7 where relevant.

## 886 4 Experimental methods

### 887 4.1 The Large Hadron Collider

888 At the time of writing, the Large Hadron Collider [100] is the largest and most  
889 powerful particle accelerator in the world. Located underground at the border of  
890 France and Switzerland close to Geneva, it consists of two circular beamlines of  
891 roughly 27 km circumference, in which proton bunches are accelerated and collided.  
892 Superconducting magnets, cooled with liquid helium at around 4 K temperatures,  
893 generate magnetic fields of over 8 T to keep the protons on their circular orbit,  
894 and similarly superconducting electromagnetic radio-frequency cavities accelerate  
895 the protons to beam energies up to 7 TeV. When operating as designed, around  
896 2800 proton bunches per beam containing  $3 \times 10^{14}$  protons total are present in the  
897 beamline simultaneously, revolving with a frequency of about 11.245 kHz. From  
898 this, peak instantaneous luminosities of about  $20 \text{ kHz} \mu\text{b}^{-1}$  can be reliably reached.  
899 Alternatively, the LHC can also collide heavy ions, such as lead or oxygen, instead  
900 of protons.

901 There are four large experiments making use of the colliding beams at the LHC,  
902 located at the four interaction points. The two larger of these are ATLAS [101]  
903 and CMS [4], both of which are general-purpose experiments intended to study  
904 all aspects of the Standard Model in proton-proton collisions. The work of thesis  
905 was performed as part of the CMS collaboration, and so the CMS experiment is  
906 described in Sec. 4.2 in more detail. The two smaller experiments, on the other  
907 hand, are specialized for certain tasks, namely the study of B physics and exotic  
908 hadrons for LHCb [102] and the study of heavy-ion collisions for ALICE [103].

909 The data taken at the LHC so far can be divided into three Runs. Run 1 lasted  
910 from 2010–2012, during which the LHC operated at center-of-mass energies of 7 and  
911 8 TeV, significantly below the original target values, and yielded a total integrated  
912 luminosity of about  $29 \text{ fb}^{-1}$ . It is this data that led to the original discovery of the  
913 Higgs boson. Following this, after two years of pause, Run 2 resumed in 2015 with  
914 a center-of-mass energy of 13 TeV and lasting to 2018. Around  $140 \text{ fb}^{-1}$  of data was  
915 collected during this time. This complete data set, save for the small contribution  
916 from 2015, is analyzed in Chapter 7 of this thesis.

917 Finally, Run 3 of the LHC started in 2022 after another three years of pause, and  
918 is planned to last until 2026 at the time of writing. The center-of-mass energy was  
919 again increased slightly to 13.6 TeV, and in the years 2022–2024 around  $196 \text{ fb}^{-1}$   
920 have been recorded, already surpassing Run 2. In Chapter 5 of this thesis, the very

first data of Run 3, corresponding to  $1.21\text{ fb}^{-1}$  taken in July and August 2022 at CMS, are analyzed in the context of a  $t\bar{t}$  cross section measurement.

In the future, it is planned to upgrade the LHC to be able to run at higher instantaneous luminosities as well as a further increased energy of 14 TeV [104]. The CMS detector will similarly be upgraded to replace aging components and deal with the increased pileup conditions [105, 106], and a total integrated luminosity of around  $3\text{ ab}^{-1}$  is expected to be collected. In Chapter 8, among others, sensitivity projections for this luminosity are made for Axion-Like Particles decaying to  $t\bar{t}$ .

## 4.2 The CMS experiment

The Compact Muon Solenoid experiment [4, 106], located at Interaction Point 5 of the LHC close to Cessy, France, is a general-purpose particle detector targeting a broad range of SM and BSM phenomena. Its main feature is a superconducting solenoid magnet creating a strong magnetic field of 3.8 T. CMS is a hermetic detector, covering almost the full solid angle in space, and is split into a *barrel*, covering pseudorapidities of  $|\eta| \lesssim 1.5$ , and two forward *endcaps*, covering high  $|\eta|$  values. It consists of several subdetectors, which are geared towards different particle types and properties.

**Subdetectors** The innermost part of CMS is the *tracker*, which is a silicon detector comprised of several layers of silicon pixel and strip sensors [108, 109]. These record interactions with particles (“tracker hits”) shooting outwards from the interaction point in the center in three-dimensional space. Through reconstruction of the particle tracks and fits of the curvature due to the magnetic field, the tracker thus allows for the measurement of particle momenta. Furthermore, extrapolating the tracks back to their origin allows for the determination of the point of interaction, and thus for discrimination between particles arising from different proton-proton interactions. Due to the presence of the beam pipe, the tracker covers only pseudorapidities of  $|\eta| < 2.5$ , enabling high precision momentum determination in this range only.

The second-to-innermost subdetector is the *electromagnetic calorimeter* (ECAL), which is intended to measure the energy of electrons and photons [110, 111]. It consists of transparent lead tungstate cells, in which incoming electrons or photons create electromagnetic showers leading to avalanches of electron-positron pairs and photon radiation. These are then recorded by photo diodes, and the energy of the incoming particle can be reconstructed from the amount of measured photons. Pseudorapidities of  $|\eta| < 1.48$  and  $1.65 > |\eta| < 3$  are covered for the barrel and the endcaps, respectively. The majority electrons and photons are fully stopped in the ECAL and do not interact with the further subdetectors.

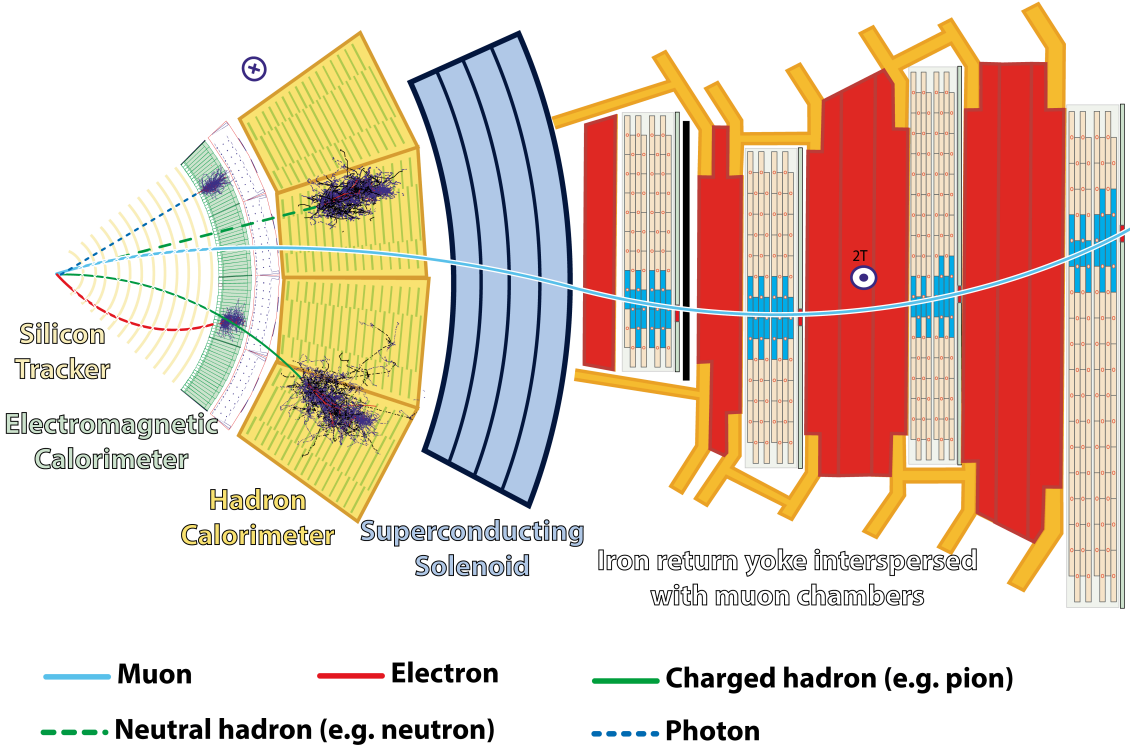


Figure 4.1: **The CMS detector.** A cross section view of the different CMS subdetectors, with the trajectories of example particles and their interactions. *Figure taken from Ref. [107].*

Following the ECAL, and similar in functionality, the *hadronic calorimeter* (HCAL) measures the energy of charged or neutral hadrons [112, 113]. It consists of interleaved absorber plates, which initiate hadronic showers through the strong interaction with the nuclei of the material, and scintillators, which transmute the hadronic showers into photons to be detected by photodetectors. The HCAL covers  $|\eta| < 1.4$  and  $1.4 < |\eta| < 3$  for the barrel and endcaps, respectively, and additionally features a forward section ranging up to  $|\eta| < 5$ , though the latter is not used anywhere in this work.

Surrounding the HCAL lies the superconducting solenoid, followed by the final subdetector: the *muon chambers* [114, 115]. They are interspersed with four layers of the iron return yoke of the magnet, which confines the magnetic field. Since muons interact only sparsely with matter, they escape the calorimeters and the solenoid unhindered, and are detected in four muon subsystems working in accord at different pseudorapidities: the drift tubes ( $|\eta| < 1.2$ ), cathode strip chambers ( $0.9 < |\eta| < 2.4$ ), resistive plate chambers ( $|\eta| < 1.9$ ) and gas electron multipliers ( $1.6 < |\eta| < 2.4$ ). All of them are gas detectors, which are sensitive to the ionization of a gas when a muon passes through it, and record hits of the muon trajectory,

thus allowing for a momentum measurement similar to the tracker.

**Trigger system** Besides the different subdetectors, a crucial part of the CMS experiment is the *trigger system* [116]. It is necessary due to the large number of bunch crossings at the LHC, which, if they were all recorded, would produce data rates far in excess of the computational bandwidth and storage capacities available. To combat this, only events which are of physical interest should be recorded. It is the task of the trigger system to determine what these events should be.

The trigger system is split into two parts. The first is the low-level or level-one trigger (L1T) [117], which is a hardware trigger consisting of custom electronics and whose inputs are directly the output signals of several of the subdetectors. It is designed to trigger on signatures consistent with specific objects, such as electrons, muons or hadronic jets, with significant energy. Since it needs to take a decision for every collision event, it only has a time interval of around  $4\mu\text{s}$  to do so, requiring purpose-build low-latency electronics. Its target is a output event rate of 100 kHz, which can be adjusted by prescaling certain trigger paths so that only a fraction of passing events is recorded.

The second part of the trigger system is the high-level trigger (HLT) [118, 119]. It is a software trigger, running on a GPU-accelerated server farm directly in the CMS service cavern, on which a dedicated, speed-optimized version of the standard CMS object reconstruction algorithm is executed for each event passing the L1T. Specific triggers are then implemented as decisions based on these reconstructed trigger objects, allowing large freedom in selecting events based on the desired physics program. Typical triggers require, for example, the presence of different numbers or combinations of electrons, muons, photons, hadronic jets or missing transverse momentum. The transverse momentum thresholds and further requirements on these objects need to be adjusted so that the total trigger rate is reduced to an average of around 400 Hz. Only these events are then saved to hard drives, and kept for further analysis.

## 4.3 Object reconstruction

In order to interpret the physics behind a collision event, the outputs of the subdetectors have to be translated into physics objects which can be mapped to the underlying physical particles. At CMS, this is done with a single unifying method, the Particle Flow (PF) algorithm [120], which is designed to combine the information from the several subdetectors to build physics objects (called PF candidates) as appropriate. The physics objects relevant to this work are listed in the following.

*Charged particle tracks* are obtained from the tracker by fitting recorded tracker hits using a  $\chi^2$  minimization, and their momentum and charge are estimated from

## 4 Experimental methods

---

their curvature as described above [108]. By extrapolating the tracks back to their origin, the position of vertices in space can also be determined.

From the tracks, the *primary vertices* (PVs) can be determined, which are the locations of the proton-proton interactions that caused the tracks in the first place. By contrast, secondary vertices arise from the decays of particles with long enough lifetime that they move a significant distance from the PV. PVs are determined by a likelihood fit to all tracks of sufficient quality [108]. In each event, the PV whose tracks show the largest  $p_T$  sum is designated the hard-scattering PV, assumed to correspond to the physical process of interest, while further PVs are due to soft-QCD pileup interactions. The number of PVs per event is thus a good measure of the amount of pileup.

The other main ingredient besides tracks and vertices are *calorimeter clusters* from either the ECAL or the HCAL. A clustering algorithm is required here because particles typically deposit their energy in more than one calorimeter crystal.

By matching the positions of calorimeter clusters and charged particle tracks, *electrons* (for the ECAL) and *charged hadrons* (for the HCAL) can be constructed. The combined measurements of the momentum (from the curvature) and the deposited energy (from the calorimeter) allows for the reconstruction of the mass, and thus the identification of the particle. For electrons, the effect of bremsstrahlung originating in the tracker volume has to be considered, usually resulting in multiple calorimeter clusters per electron (called a supercluster) which need to be combined together. Isolation criteria on the clusters are also required to veto electrons that are part of a hadronic jet. By contrast, calorimeter clusters which do not have charged tracks are assigned to *photons* (for the ECAL) or *neutral hadrons* (for the HCAL). CMS furthermore employs algorithms to remove hadrons that are believed to originate from pileup instead of the hard-scattering vertex. In Run 2, the Charged Hadron Subtraction (CHS) method [120] was used for this purpose, while in Run 3, the better performing PUPPI method [97, 121] was used instead.

*Muons* interact only very rarely with the calorimeter, and are instead built by directly combining charged tracks with hits in the muon chambers. In this work, muons are only considered if they match to hits in both subdetectors.

From these definitions, further high-level objects can be build. The first are *hadronic jets*, which are clustered from all other PF candidates using the anti- $k_T$  algorithm with a distance parameter of  $\Delta R = 0.4$  [122] (referred to as AK4 jets). This algorithm is infrared- and collinear-safe, i.e. it is not strongly sensitive to soft nonperturbative QCD effects [72], and has the advantage that the resulting jets are approximately circular in the  $\varphi-\eta$  plane. Since leptons or photons can be created from electroweak decays of hadrons, these also need to be included in the jet clustering; to ensure that they are not double-counted, leptons and photons that are included in jets are removed from further consideration through isolation criteria.

Hadronic jets can further be *b tagged*, that is, identified as originating from a B hadron. Since the strong interaction is flavor-conserving, the decay of B hadrons

1054 to hadrons of other flavors has to be mediated by the flavor-mixing in the weak  
 1055 interaction, leading to comparatively long lifetimes. B hadrons can thus be identified  
 1056 through secondary vertices corresponding to the B hadron decay, which can be  
 1057 displaced from the PV by several millimeters. In practice, machine learning-based  
 1058 classifiers like the DEEPJET algorithm [123] are used, which take more properties  
 1059 of the jet into account besides the displacement of the secondary vertex.

1060 Finally, the *missing transverse momentum*  $\vec{p}_T^{\text{miss}}$  can be calculated as the negative  
 1061 of the vectorial sum of all transverse momenta in the event [124]. Since the initial  
 1062 state of a collision at the LHC has negligible transverse momentum,  $\vec{p}_T^{\text{miss}}$  represents  
 1063 the total transverse momentum of the particles that left the detector unobserved.  
 1064 In the SM, this is the case for neutrinos, but it could also be BSM particles such as  
 1065 e.g. dark matter candidates.

## 1066 4.4 Statistical interpretation

1067 In experimental particle physics, results are typically extracted by comparing detector-  
 1068 level predictions, for example obtained using MC simulation, to the observed data  
 1069 for suitably chosen observables. The measured data here are necessarily afflicted by  
 1070 statistical uncertainties, both due to the inherent randomness of quantum mechanics  
 1071 and the probabilistic behavior of the detector. They should thus be seen as a sample  
 1072 drawn from a random distribution, and in order to extract underlying parameters  
 1073 of any model, statistical methods are required.

1074 In this work, all statistical interpretation is performed in the framework of *binned*  
*1075 profile maximum likelihood fits*. This method follows the Frequentist approach of  
 1076 considering physical properties that should be extracted to be fixed, if unknown,  
 1077 quantities, which enter the random distribution of the observed data as parameters.  
 1078 In order to estimate the desired properties, the observed data points are sorted  
 1079 into orthogonal bins according to one or more sensitive observables, and each bin  
 1080 is treated as an independent counting experiment where the observed number of  
 1081 events is given by a Poisson distribution.

1082 **Likelihood definition** Denoting the set of physical properties to be estimated  
 1083 (the parameters of interest or POIs) collectively as  $\vec{\mu}$ , the likelihood of  $\vec{\mu}$  for bin  $i$ ,  
 1084 given that  $N_i$  events were observed, is [125]

$$L_i(\vec{\mu}, \vec{\theta}) = \text{Pois}\left(N_i | n_i(\vec{\mu}, \vec{\theta})\right). \quad (4.1)$$

1085 Here, Pois refers to the Poisson distribution, and  $n_i(\vec{\mu}, \vec{\theta})$  is the mean expected  
 1086 number of events in bin  $i$  as predicted by the physics model under consideration.  
 1087 The set of parameters  $\vec{\theta}$  are *nuisance parameters* (NPs), which encode the effects

## 4 Experimental methods

---

of different sources of systematic uncertainty affecting the measurement. The full likelihood of the measurement is now given as the product of all bins:

$$L(\vec{\mu}, \vec{\theta}) = \prod_i L_i(\vec{\mu}, \vec{\theta}) \cdot G(\vec{\theta}). \quad (4.2)$$

The function  $G(\vec{\theta})$  represents the *constraint terms* of the NPs, encoding any possible prefit uncertainties on them. For example, an experimental source of uncertainty (e.g. a scale factor)  $f$  might be measured with a mean value of  $\hat{f}$  and standard deviation  $\sigma_f$ . Then, the corresponding NP would be normalized as  $\theta_f = (f - \hat{f})/\sigma_f$ , and the constraint terms  $G(\vec{\theta})$  would include a factor  $\mathcal{N}(\theta_f | 0, 1)$ , i.e. the standard normal distribution for  $\theta_f$ . This way, the range  $\theta_f = \pm 1$  corresponds to one standard deviation of the corresponding systematic uncertainty source.

In practice, the functional form of the expectation  $n_i$  must be given by the physics model studied in the experiment. In this work, the events are modeled as a sum of signal and background processes. An important case is a linear signal, where the only POI is the *signal strength*  $\mu$  and the expectation for bin  $i$  is

$$n_i(\mu, \vec{\theta}) = \mu s_i(\vec{\theta}) + b_i(\vec{\theta}). \quad (4.3)$$

The functions  $s_i$  and  $b_i$  are the signal and background expectations, respectively, which both can be influenced by NPs.

To extract a best-fit value of the POI (or multiple POIs), one now maximizes the full likelihood simultaneously over both the POIs  $\vec{\mu}$  and the NPs  $\vec{\theta}$ , giving the *maximum likelihood estimator* for  $\vec{\mu}$ . In practice, usually the function  $-2 \ln L$  is minimized instead to have numerically tractable quantities.

**Confidence intervals** In the Frequentist approach to statistics, an uncertainty can be assigned to the estimate in the form of *confidence intervals*. To do so, a *test statistic* has to be defined, which usually takes the form of a *profile likelihood ratio*, e.g. [125]

$$\lambda(\vec{\mu}) = -2 \ln \frac{\hat{L}(\vec{\mu})}{\max_{\vec{\mu}'} \hat{L}(\vec{\mu}')} \quad \text{with} \quad \hat{L}(\vec{\mu}) = \max_{\vec{\theta}} L(\vec{\mu}, \vec{\theta}). \quad (4.4)$$

$\hat{L}(\vec{\mu})$  is the profile likelihood, i.e. the likelihood maximized over the NPs, and the ratio is taken between the probed POI values  $\vec{\mu}$  and the best-fit values  $\vec{\mu}'$ . Small values of  $\lambda(\vec{\mu})$  now signalize good agreement with the data for the POI values  $\vec{\mu}$ . The value of the test statistic  $\lambda$  depends on the observed data  $N_i$ , and can thus be seen as a random variable with a probability density  $f(\lambda|\vec{\mu})$ , which again depends on the POIs as parameters. Then, given an observed value of the test statistic  $\lambda^{\text{obs}}$ , a set of POIs  $\vec{\mu}$  is excluded at confidence level (CL)  $\alpha$  if

$$P(\lambda(\vec{\mu}) < \lambda^{\text{obs}}) = \int_0^{\lambda^{\text{obs}}} f(\lambda|\vec{\mu}) d\lambda > \alpha. \quad (4.5)$$

1118 The probability density  $f(\lambda|\vec{\mu})$  can be evaluated numerically using toy data sets.  
 1119 Alternatively, for simple signal models like the linear signal given in Eq. (4.3), it  
 1120 can be analytically shown that  $\lambda$  is approximately  $\chi^2$ -distributed, with the degrees  
 1121 of freedom equaling the number of POIs [126, 127].

1122 In particular, for the case of one POI  $\mu$  with best-fit value  $\hat{\mu}$ , a two-sided confi-  
 1123 dence interval at  $\sim 68\%$  CL (corresponding to one standard deviation of the normal  
 1124 distribution) is then simply given as [125]

$$\lambda(\hat{\mu} \pm \Delta\mu) = -2(\ln \hat{L}(\hat{\mu} \pm \Delta\mu) - \ln \hat{L}(\hat{\mu})) = 1. \quad (4.6)$$

1125 That is, the uncertainty corresponds to a change in negative profile log-likelihood  
 1126  $-2 \ln \hat{L}$  by 1 with respect to the best-fit point.

1127 **Significance** The framework of confidence intervals can also be used to define the  
 1128 *significance* of an observed signal. To do so, a hypothesis test is performed, with the  
 1129 background-only case as the null hypothesis to be rejected. For an observed value  
 1130 of the test statistic  $\lambda^{\text{obs}}$  (defined again by Eq. (4.4)), the probability to make this  
 1131 observation under the background-only hypothesis (the *p-value*) is

$$p_0 = \int_0^{\lambda^{\text{obs}}} f(\lambda|\vec{\mu} = 0) d\lambda. \quad (4.7)$$

1132 To translate this into a significance, the *p*-value is compared to the area under  
 1133 the curve of a standard normal distribution: a significance of 2 standard deviations,  
 1134 giving  $\approx 95\%$  probability under the normal distribution, corresponds to a *p*-value  
 1135 of 0.05. Similar to the case described above, the *p*-value can be obtained from  
 1136 analytical approximate distributions in the case of a simple linear signal.

1137 **Exclusion limits** A different application of confidence intervals are *exclusion limits*,  
 1138 used in experiments where no or little signal was observed. Here, for a POI that  
 1139 is bounded from below (usually by zero, e.g. a signal strength), an upper limit  $\mu^{\text{up}}$   
 1140 is sought such that all values  $\mu > \mu^{\text{up}}$  are excluded at a certain CL. At the LHC,  
 1141 the CL<sub>s</sub> method [128, 129] is commonly used for this purpose. The test statistic is  
 1142 modified from Eq. (4.4) to be

$$q(\mu) = \begin{cases} \lambda(\mu), & \hat{\mu} \leq \mu \\ 0, & \hat{\mu} > \mu \end{cases} \quad (4.8)$$

1143 where  $\hat{\mu}$  again refers to the best-fit value of  $\mu$ . The point of this modification is that  
 1144 a certain value of  $\mu$  should not be seen as excluded if the data is more compatible

## 4 Experimental methods

---

1145 with a higher  $\mu$  value; thus, the test statistic is set to zero in this case.

1146 Following that, for an observed test statistic  $q^{\text{obs}}$ , the  $\text{CL}_s$  value is defined as

$$\text{CL}_s(\mu) = \frac{p_{s+b}(\mu)}{1 - p_b} \quad (4.9)$$

1147 with

$$p_{s+b}(\mu) = \int_0^{q^{\text{obs}}} f(q|\mu) dq \quad \text{and} \quad p_b = \int_0^{q^{\text{obs}}} f(q|\mu = 0) dq. \quad (4.10)$$

1148  $p_{s+b}$  and  $p_b$  are the probabilities to observe a test statistic of  $q^{\text{obs}}$  under the  
1149 signal+background and background-only hypotheses, respectively, defined similarly  
1150 as in Eq. (4.7). The ratio of the two probabilities is used instead of  $p_{s+b}$  directly to  
1151 prevent exclusion of small signals in the case that the data is not well compatible  
1152 with neither the background-only or the signal+background hypothesis (particularly  
1153 if the experiment is not very sensitive to a certain kind of signal and  $p_{s+b}$  and  $p_b$  are  
1154 thus similar). The exclusion limit at CL  $\alpha$  is then simply given by  $\text{CL}_s(\mu^{\text{up}}) = 1 - \alpha$ .  
1155 A common choice, used in this work, is  $\alpha = 95\%$  (corresponding to a  $p$ -value of 0.05).

1156 **Nuisance parameter diagnostics** Real maximum likelihood fits used in anal-  
1157 yses at the LHC are often very complex, with more NPs than there are bins. In  
1158 such under-constrained fits, the behavior of the different NPs - encoding the dif-  
1159 ferent sources of uncertainty - is often not intuitively clear a priori, and it is thus  
1160 important to investigate their postfit behavior to check whether the fit is healthy  
1161 and numerically stable.

1162 To do so, first, the *pulls and constraints* of the NPs are defined as their best-  
1163 fit values and profiled postfit uncertainties, similar as for the POIs above, relative  
1164 to their prefit uncertainties. To have a NP pulled means that its best-fit value is  
1165 different from the prefit expectation. Similarly, to have it constrained means that its  
1166 estimated postfit uncertainty is smaller than the assumed prefit value. Both of these  
1167 effects are not necessarily a sign of an unhealthy fit: If the observables considered in  
1168 the fit are sensitive to a particular physical or experimental parameter as encoded  
1169 by the NP in question, a constraint, and possibly a pull, are expected, and simply  
1170 show the power of the fit to measure that particular parameter.

1171 If, on the other hand, a strong constraint or pull (beyond what is expected from  
1172 statistical fluctuations) is seen in a NP to which no sensitivity is expected, it might  
1173 be a sign of problems with the fit, such as spurious constraints from noisy inputs,  
1174 missing degrees of freedom to describe the data, or too small prefit uncertainties.  
1175 Whether this casts doubt on the result or not needs to be gauged on a case-by-case  
1176 basis, and depends on the relevance of the NP in question.

1177 The relevance of individual NPs to the result can be quantified using *impacts*.  
1178 The impact of a NP  $\theta$  with best-fit value  $\hat{\theta}$  and postfit uncertainty  $\Delta\theta$  is defined by

repeating the maximum likelihood fit at values of  $\hat{\theta} \pm \Delta\theta$ , with  $\theta$  then held fixed in the maximization of Eq. (4.4). The shift in the resulting POI values with respect to the best-fit POI is the impact on that particular POI. In a fit with a single POI, the impacts can be used to rank the NPs and the systematic uncertainties they encode in order of importance to the fit result. In particular, NPs with very small impact can be considered irrelevant for the fit result. However, it should be kept in mind that this procedure does not fully account for possible correlations between the NPs.

**Uncertainty breakdown** Related but not identical to the concept of impacts is an *uncertainty breakdown*, which can be used to quantify the contribution from different sources of uncertainty to the total postfit uncertainty on the POI. To do so, either a single NP or a group of NPs originating from the same source (e.g. all NPs corresponding to a certain correction) are frozen at their postfit values, and the fit is repeated with the POI and remaining parameters left untouched. The result will yield the same best-fit value for the POI, but with a possibly reduced uncertainty (as estimated from the likelihood). The uncertainty due to the frozen NP or NP group is then defined as the quadratic difference to the nominal uncertainty. This method does not account for correlations between different uncertainty sources (though it does consider correlations between the NPs in a certain group). As a result, the uncertainties obtained in this way will in general not sum up in quadrature to the original uncertainty.

A further use of this method is to define the statistical component of the uncertainty on a POI: it is simply the remaining uncertainty when all considered NPs are frozen to their postfit values simultaneously. Conversely, the quadratic difference between the total and the statistical uncertainty can be considered the systematic uncertainty.

**Technical implementation** In this work, two different tools are used to implement the methods described above. In Chapters 5 and 7, where experimental data is analyzed, the CMS general-purpose statistics tool `combine` is used [130]. In Chapter 8, on the other hand, the Python-based tool `pyhf` [131] is employed for the purpose of calculating expected significances and limits.

1209 **5 Measurement of the inclusive  $t\bar{t}$  cross**  
1210 **section at  $\sqrt{s} = 13.6$  TeV**

1211 **5.1 Introduction**

1212 In July 2022, the LHC officially resumed collecting data after over three years of  
1213 shutdown, thereby starting LHC Run 3. It did so at a new, unprecedented center-  
1214 of-mass energy of  $\sqrt{s} = 13.6$  TeV, inviting the experiments to measure physical  
1215 observables at the new energy frontier.

1216 One important such observable is the inclusive  $t\bar{t}$  production cross section. It is, in  
1217 essence, the total rate of top quark pair production at the LHC, integrated over the  
1218 kinematic distributions of the particles produced. As mentioned in Chapter 2, the  
1219 top quark has a special place in the standard model as the heaviest known elementary  
1220 particle, as well as the only colored particle that decays before hadronizing. It is  
1221 thus important for many potential BSM scenarios, such as models with additional  
1222 Higgs bosons, which might couple strongly to the top quark. As such, measurements  
1223 of top quark-related observables at the highest possible energies are attractive tests  
1224 of the SM. The inclusive  $t\bar{t}$  production cross section, as one of the simplest top quark  
1225 observables, is well suited for a first measurement at the new center-of-mass energy.

1226 Simultaneously, restarting such a large experiment as CMS after a three-year  
1227 shutdown poses many experimental challenges. Due to the change in energy, as  
1228 well as physical changes in the accelerator and detector, new calibrations as well as  
1229 validations of some previous calibrations are required to ensure that the detector  
1230 performance is understood. An early measurement of the inclusive  $t\bar{t}$  cross section  
1231 is well suited to serve as such a cross-check: Because of the decay chain of the top  
1232 quark, a top quark measurement involves many of the different objects reconstructed  
1233 at CMS, which allows for a check of a wide landscape of calibrations.

1234 The measurement described in this chapter was designed specifically with these  
1235 motivations in mind, and as such exhibits several novel features. Firstly, it com-  
1236 bines events from both the dilepton and  $\ell$ +jets decay channels of  $t\bar{t}$ , categorized  
1237 by lepton flavor content, combining the higher statistics of the  $\ell$ +jets channel with  
1238 the high purity of the epi channel and allowing to constrain uncertainties on the  
1239 lepton identification efficiency directly from the data. This is done using a sim-  
1240 taneous maximum likelihood fit to the event yields in the different categories, with  
1241 experimental and theoretical uncertainties treated as nuisance parameters.

1242 Secondly, the events are additionally categorized by their number of b-tagged jets,

which similarly allows for an in-situ measurement of the b-tagging efficiencies. This averts needing to wait for external b-tagging calibrations, allowing for a measurement as early as possible.

The results of this work were first presented as a Physics Analysis Summary in September 2022 [132], only two months after the start of data taking, as the first public physics result of LHC Run 3. It was later published in *JHEP* as Ref. [5], again representing the first published Run 3 result. A similar result by ATLAS was later published in Ref. [133].

This chapter is structured as follows: In Sec. 5.2, the used data sets, object definitions, and event selection criteria are described, followed by the derivation and application of needed corrections in Sec. 5.3, and the resulting data-MC agreement is shown in Sec. 5.4. The considered systematic uncertainties are listed in Sec. 5.5, and the fit results are presented in Sec. 5.6. The chapter is concluded by a short summary and outlook in Sec. 5.7.

## 5.2 Data sets and event selection

In this section, the choice of data sets for experimental data and for simulation, as well as the choice of triggers, is described. Following that, the object and event selection procedure is outlined and several event categories to be used in the likelihood fit are defined.

### 5.2.1 Data sets

**Experimental data** The measurement is performed on data recorded during the period between July 27<sup>th</sup> and August 02<sup>nd</sup> 2022, corresponding to an integrated luminosity of  $1.21 \text{ fb}^{-1}$ . This amount of data is chosen as a balance between sensitivity and speed for the early measurement: It roughly corresponds to the point where the measurement precision is no longer primarily limited by the quantity of the data, while at the same time restricting to a data set where beam and detector conditions were stable and comparable to the data-taking in Run 2.

Both single-lepton and dilepton triggers were used to select events used in this measurement during detector operation, identifying leptons in the range of  $|\eta| < 2.5$ . The  $p_T$  requirements of the triggers are summarized in Tab. 5.1.

**Simulation** To compare the data with predictions, Monte Carlo (MC) simulation is used to simulate both the  $t\bar{t}$  signal as well as most important background processes, specifically single-top quark production in the  $t$ -channel, associated  $tW$  production,  $Z+jets$  production,  $W+jets$  production, and diboson ( $WW$ ,  $WZ$  and  $ZZ$ ) production. The MC generator POWHEG v2 [80–82] is used to generate  $t\bar{t}$ ,  $t$ -channel single-top, and  $tW$  events at next-to-leading order (NLO) in perturbative QCD, while the

Trigger	Lepton requirement
e+jets	$e(p_T > 32 \text{ GeV})$
$\mu + \text{jets}$	$\mu(p_T > 27 \text{ GeV})$
ee	$e(p_T > 23 \text{ GeV}) \text{ and } e(p_T > 12 \text{ GeV})$
$\mu\mu$	$\mu(p_T > 17 \text{ GeV}) \text{ and } \mu(p_T > 8 \text{ GeV})$
$e\mu$	$e(p_T > 23 \text{ GeV}) \text{ and } \mu(p_T > 8 \text{ GeV}) \text{ or }$ $e(p_T > 12 \text{ GeV}) \text{ and } \mu(p_T > 23 \text{ GeV})$

Table 5.1: **Trigger definitions** as used for the  $t\bar{t}$  cross section measurement. The leptons are required to be isolated and in the pseudorapidity range  $|\eta| < 2.5$ .

generators MADGRAPH5\_AMC@NLO [78] and PYTHIA 8 [84] are used to generate Z+jets/W+jets and diboson events, respectively, at leading order (LO). For Z+jets and W+jets, up to four additional jets are included in the matrix element using the MLM matching scheme [87]. For  $t$ -channel single-top, MADSPIN is used to simulate the top decay.

All of the generated events are interfaced to PYTHIA 8 for parton showering and hadronization, and further processed in a full simulation of the CMS detector as described in Chapter 3. The proton structure in the matrix element calculation is described by the NNPDF3.1 parton distribution function (PDF) set at NNLO. Note that another background contribution, from QCD-produced multijet events with fake or non-prompt leptons, is not simulated, but estimated from data (see Sec. 5.3.2).

Theoretical predictions, as well as the measured integrated luminosity, are used to normalize the cross sections of the signal and background samples as follows: The  $t\bar{t}$  signal, is normalized to a cross section of  $921^{+29}_{-37}\text{pb}$  computed at NNLO+NNLL in QCD [134], which is also used as a prediction for comparison with the SM. For the other backgrounds, the following orders in QCD and methods or programs are used: MCFM [135] (NNLO) for single-top, DYTURBO [136] (NNLO) for W+jets and Z+jets, MATRIX [137] (NLO) for diboson, and an NNLO calculation from Ref. [138] for tW.

## 5.2.2 Object definition

**Leptons** Electrons or muons are considered for the analysis if they have  $p_T > 10$  GeV and  $|\eta| < 2.4$ . For electrons, the range  $1.44 < |\eta_{\text{SC}}| < 1.57$  is removed, where  $\eta_{\text{SC}}$  is the pseudorapidity of the ECAL supercluster from which the electron was reconstructed and the interval corresponds to the transition region between barrel and endcaps in the ECAL. Furthermore, additional identification criteria (ID) are applied to remove non-prompt or fake (i.e. wrongly reconstructed) leptons and

enrich the selection with  $t\bar{t}$  events.

For electrons, the “tight” working point of the cut-based ID described in Ref. [111] is applied, which includes information from both the details of the electromagnetic shower in the ECAL and the track, as well as the matching between the two. It also includes a requirement for the electron to be isolated from other particles such as hadrons, which is implemented in the form of the relative isolation variable  $I_{\text{rel}}$ . It is defined as the scalar  $p_T$  sum of all particles in a cone around the lepton in question, divided by the lepton  $p_T$ . Here,  $\Delta R = \sqrt{(\Delta\eta)^2 + (\Delta\varphi)^2} < 0.3$  is used for the radius of the cone. Additional corrections accounting for pileup particles are applied.

For muons, a similar cut-based ID is used as described in Ref. [139], also at the tight working point. Here, criteria on the compatibility of tracks in the inner tracker, the muon detectors and the reconstructed primary vertex are employed. Again, a cut on  $I_{\text{rel}}$  is used, defined equivalently but with a cone size of  $\Delta R < 0.4$ .

**Jets** The anti- $k_T$  algorithm [122] is used to cluster reconstructed particles into jets with a distance parameter of 0.4. In order for a jet to be considered, it is required to have  $p_T > 30$  GeV and  $|\eta| < 2.4$ , and jets overlapping with any considered leptons (i.e. fulfilling the above criteria) are removed.

**Tagging of b jets** A special role is played by jets originating from the showering and hadronization of b quarks. Naively, two such jets are expected per  $t\bar{t}$  event from the two top decays, although in practice one or both jets may fall out of acceptance of the detector or otherwise not be identified. Furthermore, additional b quarks may be produced by radiation at higher orders in QCD. Correctly tagging these jets as such can greatly improve signal purity by cutting away backgrounds such as Z+jets, W+jets and QCD multijet events.

Here, the DEEPJET algorithm [123, 140], which is based on a deep neural network (DNN) classifier, is used to identify (“tag”) b jets. A working point with an identification efficiency of more than 75% is used, with misidentification rates of around 17% for charm jets and around 1% for other jets from light quarks or gluons.

### 5.2.3 Channel definition

Events are selected with either one or two leptons, corresponding respectively to the  $\ell$ +jets and dilepton decay channels of  $t\bar{t}$ . They are categorized into separate channels by their lepton flavor content, and additional requirements are applied for the different channels.

**Dilepton channels** Events with exactly two leptons, required to have opposite electric charge, are sorted into three dilepton channels ( $e\mu$ ,  $ee$ , and  $\mu\mu$ ). The presence of at least one jet is required, and in the same-flavor channels ( $ee$  and  $\mu\mu$ ), at least

1342 one jet is required to be b tagged in order to reject Z+jets and QCD multijet  
1343 background. In the much purer epi channel, on the other hand, events without b  
1344 tags are retained to later help constrain the b tagging efficiency in the fit to data.

1345 In order to reject even more Z+jets background, events in the same-flavor channels  
1346 with an invariant dilepton mass of  $|m_{\ell\ell} - m_Z| < 15$  GeV, where  $m_Z$  is the Z boson  
1347 mass, are removed.

1348  **$\ell$ +jets channels** Events with exactly one lepton are sorted into the e+jets or  
1349  $\mu$ +jets channels based on their flavor. At least three jets are required, of which  
1350 at least one needs to be b tagged. Note that regardless of these selections, there  
1351 is still non-negligible background from QCD multijet events where the lepton is  
1352 non-prompt or fake, which is estimated from data (see Sec. 5.3.2).

1353  **$p_T$  requirement** In all channels, the considered leptons are required to have  $p_T >$   
1354 35 GeV. This requirement is needed in the  $\ell$ +jets channels in order to stay above the  
1355 single-lepton trigger  $p_T$  thresholds (compare Tab. 5.1). In this measurement, the  
1356 choice is made to apply the same  $p_T$  requirement also both leptons in the dilepton  
1357 channels to ensure consistency between the lepton definitions. This is done to help  
1358 constrain the lepton ID scale factors using the combination of lepton flavor channels,  
1359 which otherwise might not be accurate since the scale factors for different lepton  
1360 definitions might differ. In particular it opens up the possibility to extract a result  
1361 on the cross section without any prior knowledge on the lepton ID efficiencies, which  
1362 was done in the first published version of this analysis [132].

1363 **b tag and jet categorization** In practice, the efficiency of the b tagging algo-  
1364 rithm used might be different between simulation and data, necessitating a correc-  
1365 tion to prevent bias. In this analysis, this efficiency is measured simultaneously with  
1366 the cross section directly in the data. To do so, the lepton flavor channels are ad-  
1367 ditionally split into categories based on the number (exactly 0, 1, or 2) of b tagged  
1368 jets. Since only the ep channel allows events with 0 b tags, this results in 11 cate-  
1369 gories total. To gain further sensitivity to the b tagging efficiency and to increase  
1370 possible separation between  $t\bar{t}$  signal and background, the selected events are finally  
1371 coarsely binned into the number of accepted jets for the eventual fit, giving a total  
1372 number of 40 bins.

### 1373 5.3 Corrections

1374 While the simulation used in CMS tries to describe as many physics and detector  
1375 effects as possible, in practice it should always be expected that not all observables  
1376 agree with the experimental data perfectly. This is especially true for an early  
1377 analysis such as this, as the detector conditions might have changed significantly

1378 during the long shutdown between LHC Runs 2 and 3, and the simulation had not  
1379 been recalibrated at the time of the measurement.

1380 Because of this, the analysis setup is designed to either directly measure or cross-  
1381 check as many required experimental calibration and correction factors as possible.  
1382 This includes pileup corrections, efficiency scale factors for triggers, electrons, muons  
1383 and b tags, as well as jet energy corrections, all of which are briefly described in this  
1384 section.

1385 In addition to these experimental corrections, background processes might also  
1386 be imperfectly described by the simulation because of theoretical shortcomings. In  
1387 this case, ways have to be found to correct them directly from the experimental  
1388 data. Here, two such cases are relevant and will be presented in the latter half of  
1389 this section: The Z+jets background in the dilepton channels and in the presence  
1390 of b tagged jets, for which the normalization is taken from data; and the QCD  
1391 background in the  $\ell$ +jets channels, which uses a fully data-driven estimation and  
1392 foregoes simulation entirely.

### 1393 5.3.1 Experimental corrections

1394 **Pileup reweighting** The simulation samples used in this analysis were generated  
1395 before the start of Run 3 data taking using a projected estimate of the average  
1396 pileup. As a result, the pileup distribution in the simulation does not match the  
1397 one observed in data, which could influence mostly jet-related variables such as the  
1398 number of jets and the jet  $p_T$ .

1399 Since at the time of the measurement, no theory-based calculation for the cor-  
1400 rect pileup distribution were available, an experimental approach was taken. Three  
1401 experimental observables that are strongly correlated with pileup were identified:

- 1402 • The number of well-reconstructed primary vertices per event  $n_{\text{PV}}$ ;
- 1403 • The median  $p_T$  density in the calorimeter, calculated from calorimeter-only  
1404 jets as  $\rho^{\text{calo}} = \text{med}(p_T/A)$ , where  $A$  is the jet area defined in the  $\varphi$ - $\eta$  plane  
1405 and the median is taken over all jets in the event;
- 1406 • The median  $p_T$  density in the tracker  $\rho^{\text{trk}}$ , defined equivalently as  $\rho^{\text{calo}}$ , but  
1407 for jets calculated only from tracker information.

1408 A binned reweighting from simulation to data is derived for each observable based  
1409 on the full data sample, and the average of the three weights is applied to the  
1410 simulation, so that approximate agreement is achieved in all three variables. The  
1411 distributions before and after reweighting can be seen in Fig. 5.1.

## 5 Measurement of the inclusive $t\bar{t}$ cross section at $\sqrt{s} = 13.6$ TeV

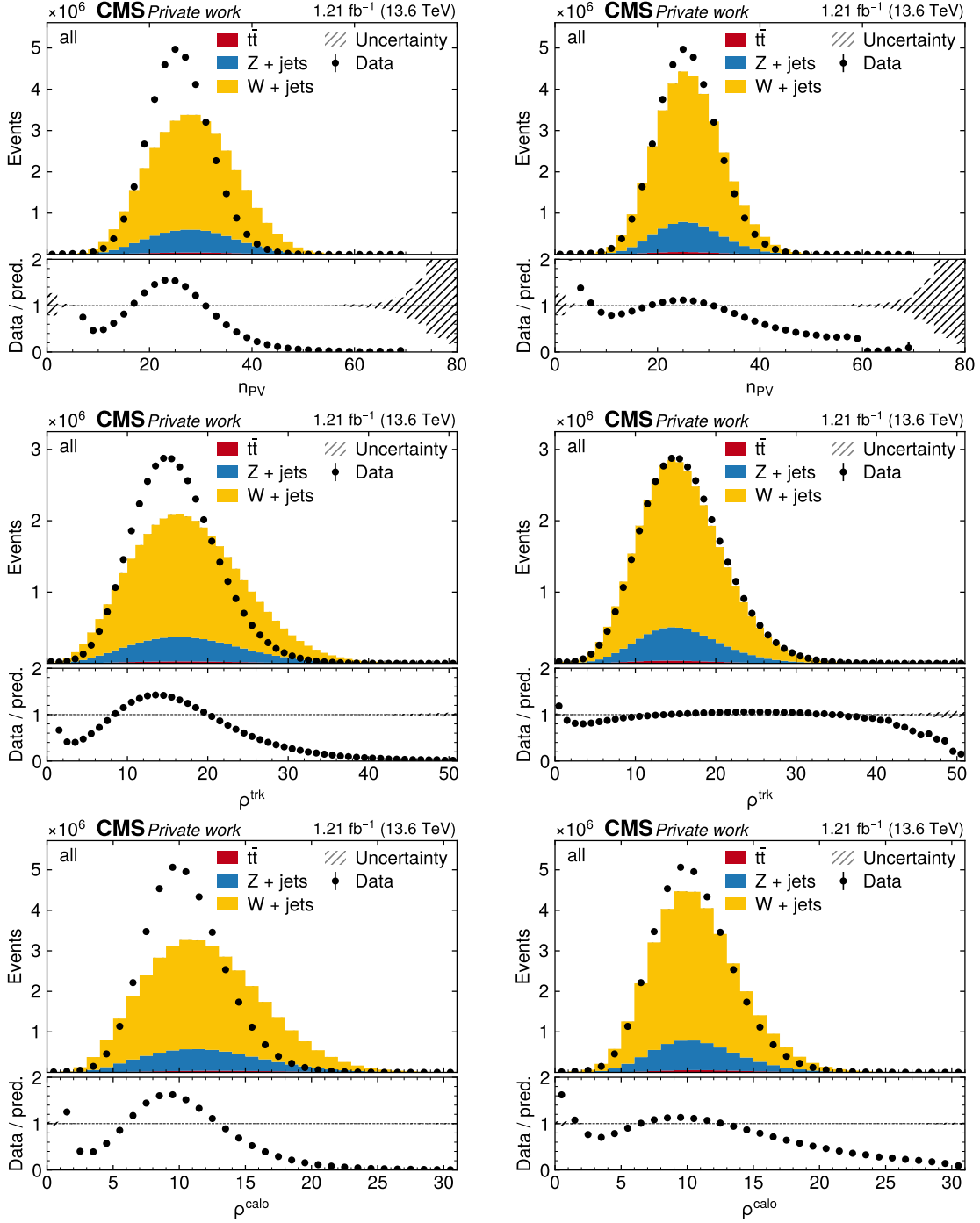


**Figure 5.1: Pileup reweighting.** Pileup-related distributions in MC and data in before (left) and after reweighting (right). From top to bottom: number of primary vertices as well as the mean energy densities  $\rho^{trk}$  (calculated using tracker input) and  $\rho^{calo}$  (calculated using calorimeter input).

1412 **Trigger scale factors** The trigger efficiency, i.e. the probability for an event  
 1413 falling into the selection phase space to be triggered by the low- and high-level  
 1414 triggers, can differ between simulation and data. In principle, both dilepton and  
 1415 single-lepton triggers are used for this measurement and should be considered for  
 1416 the efficiency calculation. However, due to the high offline  $p_T$  requirements for the  
 1417 two leptons applied in all channels, the fraction of events that are triggered only  
 1418 by the dilepton triggers is negligibly small, and can be neglected for the purpose of  
 1419 determining the scale factor. Thus, only the single-lepton triggers are considered in  
 1420 this section for simplicity.

1421 The efficiency measurement is performed by the so-called tag-and-probe (T&P)  
 1422 method, using  $Z \rightarrow e^+e^-$  and  $Z \rightarrow \mu^+\mu^-$  events. They are selected using the same  
 1423 definitions presented above, including the lepton identification, except for requiring  
 1424 their invariant mass to fulfill  $|m_{\ell\ell} - m_Z| < 20$  GeV. At least one of the leptons  
 1425 is required to pass the relevant single-lepton trigger and is then designated the  
 1426 tag, while the other lepton might or might not pass the trigger and is designated  
 1427 the probe. Assuming the probability for the two leptons to pass the trigger to be  
 1428 independent of each other, the trigger efficiency, given by probability of the probe  
 1429 to pass, can be written as

$$\epsilon_{\text{tr}} = \frac{N(\text{Probe passes})}{N(\text{Probe passes}) + \frac{1}{2}N(\text{Probe fails})} \quad (5.1)$$

1430 where  $N$  corresponds to the number of events in which the second lepton either  
 1431 passes or fails the trigger, and the combinatoric factor  $\frac{1}{2}$  comes from the fact that  
 1432 either one or the other lepton can fail.

1433 The efficiency is measured in this way in coarse bins of lepton  $p_T$  and  $|\eta|$ , separately  
 1434 for muons and electrons, in both simulation and experimental data. It is then applied  
 1435 to simulation in the following way: For  $\ell+\text{jets}$  events, a simple ratio  $\epsilon_{\text{tr,data}}/\epsilon_{\text{tr,sim}}$   
 1436 is applied to each simulation event as a scale factor, which is displayed in Fig. 5.2.  
 1437 For dilepton events, on the other hand, the fact that only one lepton needs to pass  
 1438 the single-lepton trigger needs to be taken into account. This leads to a per-event  
 1439 efficiency given by

$$\epsilon_{\text{tr},\ell\ell} = \epsilon_{\text{tr},\ell 1} + \epsilon_{\text{tr},\ell 2} - \epsilon_{\text{tr},\ell 1}\epsilon_{\text{tr},\ell 2} \quad (5.2)$$

1440 where  $\epsilon_{\text{tr},\ell 1}$  and  $\epsilon_{\text{tr},\ell 2}$  are the efficiencies evaluated at the  $p_T$  and  $|\eta|$  of the two  
 1441 leptons, respectively. Again, the ratio of this event efficiency in data and simulation  
 1442 is applied to the simulation.

1443 **Lepton scale factors** Similarly to the triggers, the reconstruction and identifi-  
 1444 cation of leptons can exhibit different efficiencies between simulation and data, and  
 1445 thus require scale factors. The efficiencies are measured with a similar tag-and-  
 1446 probe method as for the triggers, and the simulation is corrected to the data. This

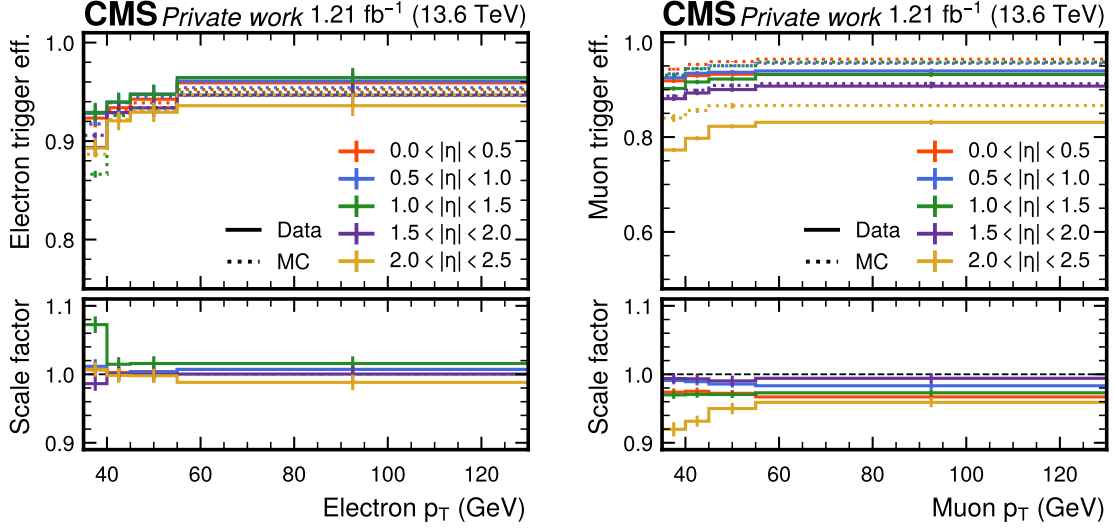


Figure 5.2: **Trigger scale factors.** Single-lepton trigger efficiencies in data and MC (top) and scale factors (bottom) for electrons (left) and muons (right) as a function of lepton  $p_T$  and  $| \eta |$ , calculated using a tag-and-probe-method. The error bars designate both statistical and systematic uncertainties.

<sup>1447</sup> is the standard approach commonly taken in CMS, detailed in Refs. [111, 139] for  
<sup>1448</sup> electrons and muons, respectively. The efficiency measurement was not performed as  
<sup>1449</sup> part of this thesis, but is still shown in Figs. 5.3 and 5.4 for reference. The muon  
<sup>1450</sup> scale factors are split into a reconstruction and an identification part, while these  
<sup>1451</sup> are combined for the electron scale factors.

<sup>1452</sup> **b tagging scale factors** The performance of b tagging algorithms, such as the  
<sup>1453</sup> DEEPJET algorithm used in this analysis, is known to differ between simulation and  
<sup>1454</sup> data, necessitating corrections. This is particularly relevant here, as the multivariate  
<sup>1455</sup> classifier behind DEEPJET had not been re-trained on Run 3 data at the time of the  
<sup>1456</sup> measurement; instead, the Run 2 calibration was used.

<sup>1457</sup> Since no external calibration of b tagging efficiencies for Run 3 was available within  
<sup>1458</sup> the timeframe of this study, the b tagging efficiency in data is extracted directly from  
<sup>1459</sup> the data itself. This is achieved by performing a simultaneous likelihood fit with the  
<sup>1460</sup> ttbar cross section, as described in Sec. 5.5. As a result, no b tagging scale factors  
<sup>1461</sup> are applied beforehand.

<sup>1462</sup> **Jet energy corrections** Another observable that often differs significantly be-  
<sup>1463</sup> tween observed data and simulation is the measured energy response of the jets.  
<sup>1464</sup> Both its mean value, the jet energy scale (JES), and the jet energy resolution (JER)  
<sup>1465</sup> require corrections, which are together referred as jet energy corrections (JECs).

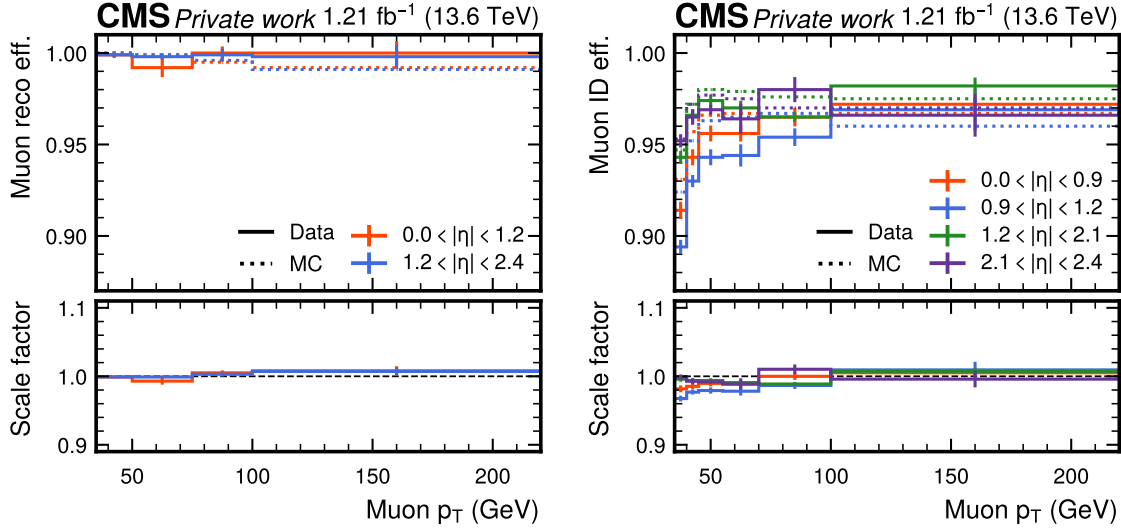


Figure 5.3: **Muon scale factors.** Muon efficiencies in data and MC (top) and scale factors (bottom), split into reconstruction (left) and identification (right) and shown as a function of lepton  $p_T$  and  $|\eta|$ , calculated using a tag-and-probe-method. The error bars designate both statistical and systematic uncertainties.

<sup>1466</sup> Both are centrally provided by CMS following the methods of Ref. [141].

<sup>1467</sup> The derivation of the JES is performed in multiple steps: first, the expected  
<sup>1468</sup> fraction of jet energy due to pileup, determined from MC simulation, is removed  
<sup>1469</sup> from all jets in data and MC. Second, the difference in jet energy between detector-  
<sup>1470</sup> and particle-level jets in simulation is determined as a function of jet kinematics,  
<sup>1471</sup> and detector-level jets are corrected accordingly in both data and simulation.  
<sup>1472</sup> Third, residual disagreements of the simulation with the data are corrected using  
<sup>1473</sup> experimental jet measurements in dijet,  $\gamma$ +jets, Z+jets, and multijet events, again  
<sup>1474</sup> parametrized as a function of jet kinematics [141].

<sup>1475</sup> Similarly, JER scale factors are determined by correcting the resolution in simu-  
<sup>1476</sup> lation to the one seen in data, based on dijet,  $\gamma$ +jets and Z+jets events [142]. They  
<sup>1477</sup> are then applied to jets in simulation by scaling the difference between detector- and  
<sup>1478</sup> particle-level jet energy for jets where a matched particle-level jet is found, while a  
<sup>1479</sup> stochastic smearing is used otherwise.

### <sup>1480</sup> 5.3.2 Data-driven background estimation

<sup>1481</sup> **QCD background** A significant background contribution in the  $\ell$ +jets channels,  
<sup>1482</sup> especially in the categories with only one b tag, is given by QCD multijet events  
<sup>1483</sup> with one reconstructed lepton. The lepton in question might be non-prompt, e.g.

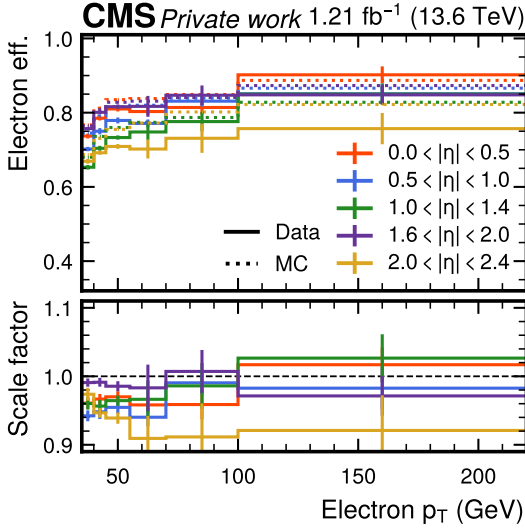


Figure 5.4: **Electron scale factors.** Combined electron efficiencies in data and MC (top) and scale factors (bottom) as a function of lepton  $p_T$  and  $|\eta|$ , calculated using a tag-and-probe-method. The error bars designate both statistical and systematic uncertainties.

from radiated photons splitting into leptons or decays of heavy flavor hadrons, or it might be fake, i.e. a different particle (such as a photon or pion in the case of electrons) misidentified as a lepton.

It is often not practical to estimate this background using MC simulation as is done for the other backgrounds in this analysis. The reason is that, due to the large cross section of QCD multijet events at the LHC but low ratio of events with a fake or non-prompt lepton, very large MC data sets are needed to achieve significant statistics in the selected phase space, requiring excessive computing power. In addition to that, fake leptons are known not to be well-described by the simulation.

Instead, a fully data-driven approach is taken to estimate the QCD background in the  $\ell+jets$  channels. For this, multiple control regions (CRs) orthogonal to the signal region (SR) are defined. In the first CR, denoted “QCD CR”, the same cuts as in the SR are applied, except that the requirement for the single lepton to be isolated from other particles ( $I_{rel}$ , see Sec. 5.2.2) is inverted. It is expected that QCD events that fall in either the QCD CR or the SR show similar shapes in observable distributions, as long as said observables are uncorrelated with the lepton isolation. Thus, the shape of the QCD background can be extracted from the CR and applied in the SR. Figs. 5.5 and 5.6 show the distributions of several key distributions for the QCD background in the  $\mu+jets$  and  $e+jets$  channels, respectively, which is estimated by subtracting all simulated (MC) processes from the data.

The normalization of the QCD background is fixed through the so-called *ABCD*

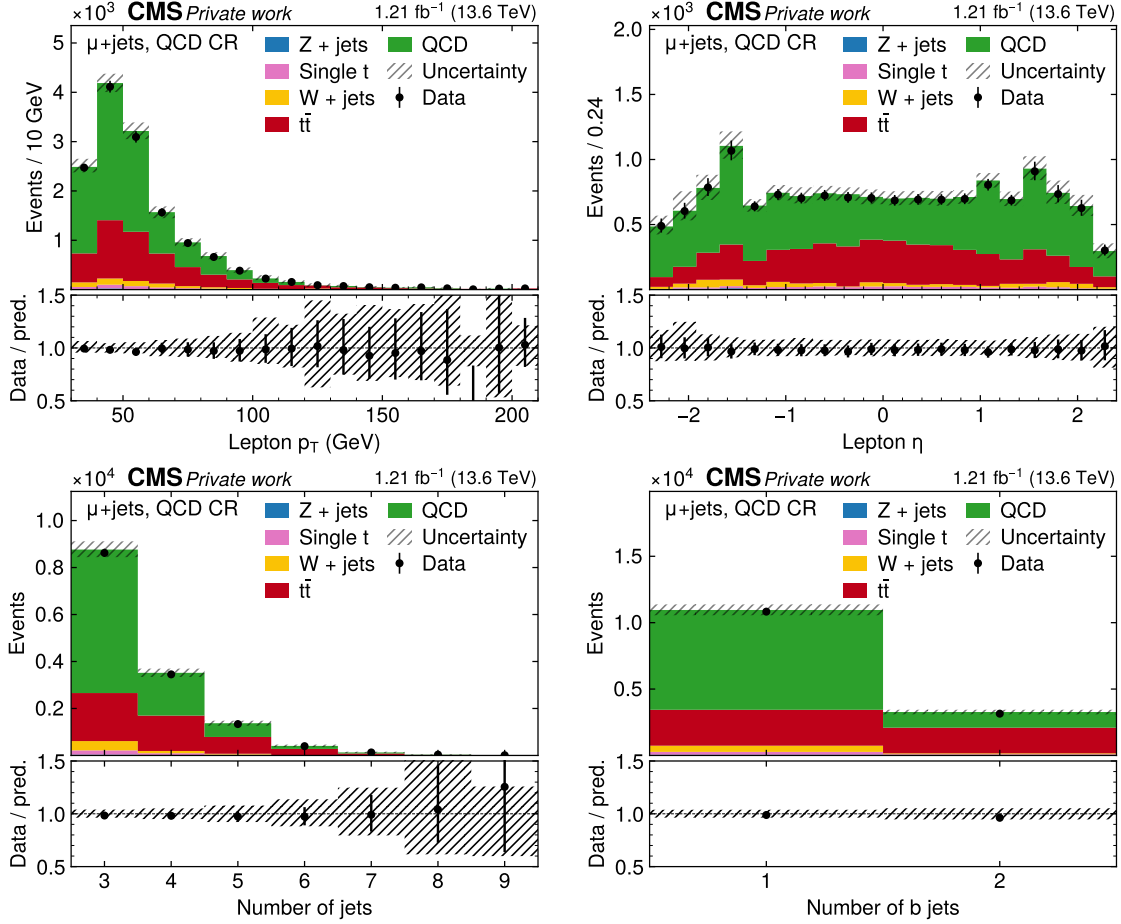


Figure 5.5: **QCD control region for  $\mu$ +jets.** Distributions in the QCD CR for the  $\mu$ +jets channel. From top left to bottom right:  $p_T$  of the lepton,  $\eta$  of the lepton, the number of jets, and the number of b-tagged jets. The uncertainty bands include MC statistical and systematic uncertainties. The difference between data and MC prediction is considered QCD background and shown in green.

1505 method [143, 144], for which an additional CR (the “1-jet CR”) is defined. It again  
 1506 contains events that pass the main selection, except for requiring exactly one jet (as  
 1507 opposed to at least three jets in the SR or QCD CR). These events are enriched with  
 1508 QCD events and contain negligible amounts of  $t\bar{t}$  signal. They are used to measure  
 1509 the ratio  $f_{\text{fake}}$  of QCD events that pass or fail the lepton isolation requirement, given  
 1510 by

$$f_{\text{fake}} = \frac{N_{1\text{ jet, pass}}^{\text{data}} - N_{1\text{ jet, pass}}^{\text{MC}}}{N_{1\text{ jet, fail}}^{\text{data}} - N_{1\text{ jet, fail}}^{\text{MC}}} \quad (5.3)$$

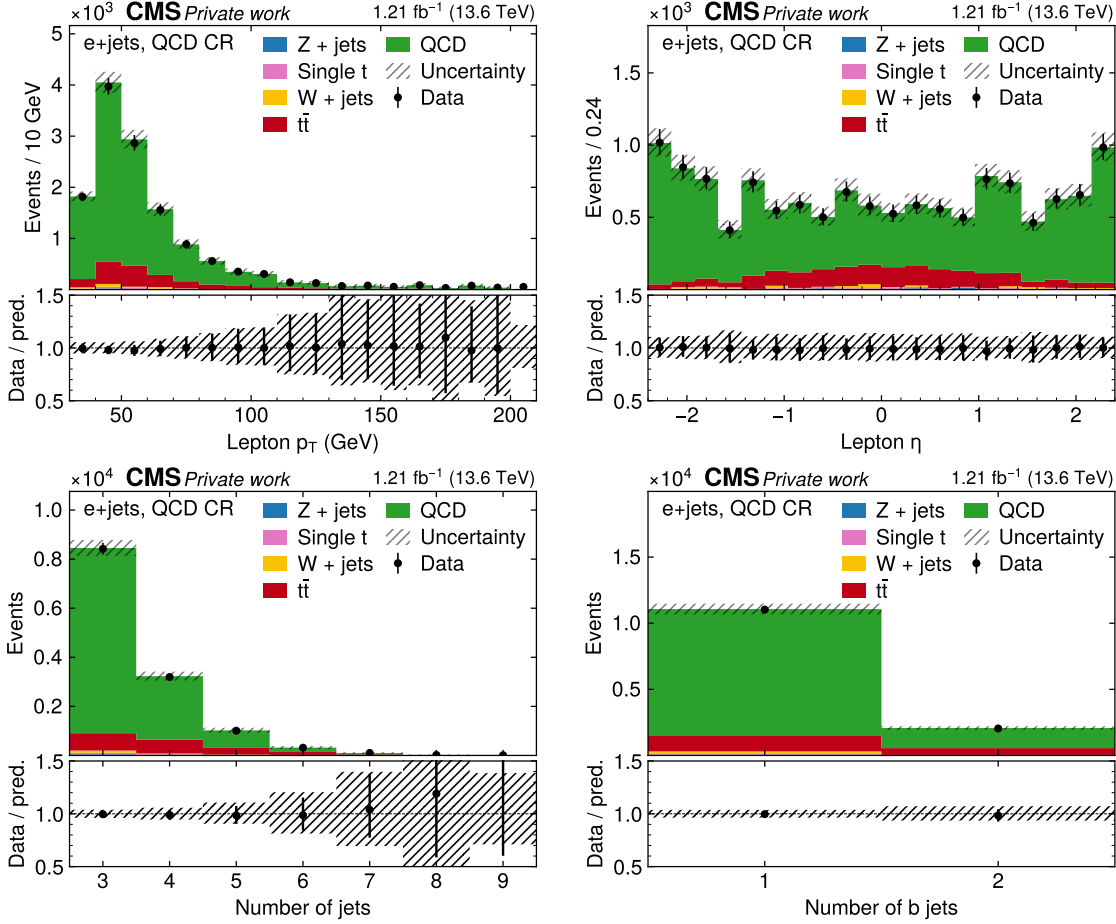


Figure 5.6: **QCD control region for e+jets.** Distributions in the QCD CR for the e+jets channel, same as in Fig. 5.5. The difference between data and MC prediction is considered QCD background and shown in green.

where  $N_{1 \text{ jet, pass}}$  and  $N_{1 \text{ jet, fail}}$  denote 1-jet-events that pass and fail the lepton isolation requirement, respectively; “data” refers to the experimental data, and “MC” refers to the sum of all non-QCD processes, which are estimated by MC simulation. Here, this ratio is measured in four coarse bins of lepton  $p_T$  and  $|\eta|$  to accurately model lepton-related distributions; it can be seen in Fig. 5.7.

Naively, the full distribution of the QCD background in the SR for any observable can then be written as

$$N_{\text{SR}}^{\text{QCD}} = (N_{\text{CR}}^{\text{data}} - N_{\text{CR}}^{\text{MC}}) \times f_{\text{fake}} \quad (5.4)$$

where  $N_{\text{CR}}^{\text{data}}$  and  $N_{\text{CR}}^{\text{MC}}$  refer to the total data and non-QCD MC yields in the QCD CR.

In practice, this is complicated by the fact that a non-negligible amount of  $t\bar{t}$

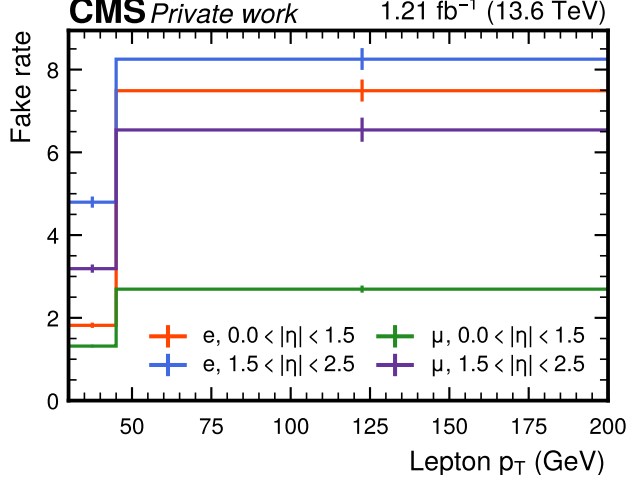


Figure 5.7: **QCD fake rate.** The fake rate for the QCD background estimated in the 1 jet bin, separately for electrons and muons as, a function of lepton  $p_T$  and  $|\eta|$ . The error bars designate statistical uncertainties only.

1521 signal is present in the QCD CR, whose cross section, as the parameter of interest  
 1522 in the measurement, is not known *a priori*. To circumvent this problem, a modified  
 1523 method is introduced, which is agnostic about the prediction for the  $t\bar{t}$  cross section.  
 1524 One sets for the SR

$$N_{\text{SR}}^{\text{data}} = N_{\text{SR}}^{t\bar{t}} + N_{\text{SR}}^{\text{MC,BG}} + N_{\text{SR}}^{\text{QCD}} \quad (5.5)$$

1525 and similarly for the QCD CR

$$N_{\text{CR}}^{\text{data}} = N_{\text{CR}}^{t\bar{t}} + N_{\text{CR}}^{\text{MC,BG}} + N_{\text{CR}}^{\text{QCD}}, \quad (5.6)$$

1526 where  $N^{\text{data}}$  is the total data yield,  $N^{t\bar{t}}$  is the  $t\bar{t}$  signal contribution,  $N^{\text{MC,BG}}$  is the  
 1527 contribution of non-QCD backgrounds as predicted by MC, and  $N^{\text{QCD}}$  is the QCD  
 1528 contribution. It is assumed that the ratio  $f_{\text{sig}}$  of signal events in the SR and QCD  
 1529 CR (but not necessarily the normalization) is correctly predicted by MC:

$$f_{\text{sig}} := \frac{N_{\text{CR}}^{t\bar{t}}}{N_{\text{SR}}^{t\bar{t}}} = \frac{N_{\text{CR}}^{t\bar{t},\text{MC}}}{N_{\text{SR}}^{t\bar{t},\text{MC}}} \quad (5.7)$$

1530 Furthermore, one sets similar to Eq. (5.4)

$$N_{\text{SR}}^{\text{QCD}} = N_{\text{CR}}^{\text{QCD}} \times f_{\text{fake}} \quad (5.8)$$

1531 where  $f_{\text{fake}}$  is still given by Eq. (5.3), which is unaffected since the  $t\bar{t}$  signal contam-  
 1532 ination in the 1-jet CR is negligible.

1533 Combining all these equations, one can first replace  $N_{\text{CR}}^{t\bar{t}}$  in Eq. (5.6) by  $f_{\text{sig}} N_{\text{SR}}^{t\bar{t}}$

1534 according to Eq. (5.7), then eliminate  $N_{\text{SR}}^{\text{tf}}$  in favor of  $N_{\text{SR}}^{\text{data}}$ , i.e. the total data yield  
1535 in the SR, and get

$$N_{\text{SR}}^{\text{QCD}} = f_{\text{fake}} \left( N_{\text{CR}}^{\text{data}} - N_{\text{CR}}^{\text{MC,BG}} - f_{\text{sig}} \left( N_{\text{SR}}^{\text{data}} - N_{\text{SR}}^{\text{MC,BG}} - N_{\text{SR}}^{\text{QCD}} \right) \right). \quad (5.9)$$

1536 Solving this equation for  $N_{\text{SR}}^{\text{QCD}}$  finally yields the corrected QCD contribution in  
1537 the SR:

$$N_{\text{SR}}^{\text{QCD}} = \left( N_{\text{CR}}^{\text{data}} - N_{\text{CR}}^{\text{MC,BG}} - f_{\text{sig}}(N_{\text{SR}}^{\text{data}} - N_{\text{SR}}^{\text{MC,BG}}) \right) \times \frac{f_{\text{fake}}}{1 - f_{\text{sig}}f_{\text{fake}}} \quad (5.10)$$

1538 The resulting QCD distributions from this method are further treated in the same  
1539 way as the MC backgrounds, and can be seen together with them in Figs. 5.8 to 5.10.

1540 **Z+jets background** In contrast to the QCD background, the Z+jets background  
1541 is generally well-described by MC simulation. However, in the considered phase  
1542 space, the requirement of at least one reconstructed b jet can introduce modeling  
1543 challenges, as b quarks are treated as massless at the matrix-element level. This  
1544 approximation may lead to inaccuracies in the predicted kinematic properties of b  
1545 quarks compared to those observed in data.

1546 Here, a data-driven normalization is derived for Z+jets events with one or two b  
1547 tags in the dilepton channels, following the method of Ref. [51]. This is important  
1548 especially in the same-flavor channels, where Z+jets is a dominant background.

1549 The normalization is derived using a CR in which the cut on  $m_{\ell\ell}$  is inverted, i.e.  
1550 in events with  $|m_{\ell\ell} - m_Z| < 15$  GeV (“inside the Z window”), which are strongly  
1551 enriched in Z+jets contributions. It is assumed that the Z+jets contribution in the  
1552 e $\mu$  channel (which stems mostly from  $Z \rightarrow \tau\tau$  events) is negligible compared to the  
1553 ee and  $\mu\mu$  channels, and that all other backgrounds (including  $t\bar{t}$ ) are approximately  
1554 equal in the three dilepton channels up to combinatorics, in the sense that their  
1555 differences are small compared to the Z+jets event yield. Then, said Z+jets yield  
1556 in the Z window in the same-flavor channels can be estimated directly from data by  
1557 subtracting the e $\mu$  channel – and with it, the other backgrounds – from the ee and  
1558  $\mu\mu$  channels. This results in

$$N_{\text{ee}/\mu\mu}^{\text{Z+jets}} = N_{\text{ee}/\mu\mu, \text{in}}^{\text{data}} - \frac{1}{2} N_{\text{e}\mu, \text{in}}^{\text{data}} k_{\text{ee}/\mu\mu, \text{in}} \quad (5.11)$$

1559 where  $N_{\ell\ell, \text{in}}^{\text{data}}$  refers to the number of observed events inside the Z window for the  
1560 respective channel, and  $k_{\text{ee}} = k_{\mu\mu}^{-1} = \sqrt{N_{\text{ee}, \text{in}}^{\text{data}}/N_{\mu\mu, \text{in}}^{\text{data}}}$  is a efficiency factor to correct  
1561 for the different acceptance of electrons and muons.

ee	ep	$\mu\mu$
$1.36 \pm 0.04$	$1.32 \pm 0.03$	$1.28 \pm 0.03$

Table 5.2: **Z+jets scale factors.** Ratio of the Z+jets event yields estimated in data using the method described in Sec. 5.3.2 to the prediction by the MC simulation. Uncertainties are statistical only.

To estimate the Z+jets background in the SR, the ratio  $R_{\text{in/out}} = N_{\text{in}}^{\text{Z+jets}}/N_{\text{out}}^{\text{Z+jets}}$ , defined as the number of Z+jets events inside and outside the Z mass window, needs to be determined. While this ratio could be taken directly from simulation (as done in Refs. [17, 145]), it may be inaccurately modeled in MC. To reduce potential bias, a more conservative strategy is adopted. A second CR with zero b-tagged jets, which is not used in the main measurement for the same-flavor channels, is introduced to estimate the ratio under looser assumptions:

$$\frac{R_{\text{in/out}}^{\text{data}}(\geq 1 \text{ b tag})}{R_{\text{in/out}}^{\text{MC}}(\geq 1 \text{ b tag})} = \frac{R_{\text{in/out}}^{\text{data}}(0 \text{ b tags})}{R_{\text{in/out}}^{\text{MC}}(0 \text{ b tags})} \quad (5.12)$$

This equation means that the *ratio of ratios*  $R_{\text{in/out}}(\geq 1 \text{ b tag})/R_{\text{in/out}}(0 \text{ b tags})$  is assumed to be well described by MC. It can be solved for the Z+jets yield outside of the Z window in the same-flavor channels, yielding

$$\begin{aligned} N_{\text{out}}^{\text{Z+jets}} &= \frac{N_{\text{in}}^{\text{Z+jets}}}{R_{\text{in/out}}^{\text{data}}(\geq 1 \text{ b tag})} \\ &= \frac{R_{\text{in/out}}^{\text{MC}}(0 \text{ b tags})}{R_{\text{in/out}}^{\text{data}}(0 \text{ b tags})} \frac{N_{\text{in}}^{\text{Z+jets}}}{R_{\text{in/out}}^{\text{MC}}(\geq 1 \text{ b tag})} \end{aligned} \quad (5.13)$$

where  $N_{\text{in}}^{\text{Z+jets}}$  is given by Eq. (5.11). In practice, this yield is quoted as a scale factor compared to the nominal MC prediction. For the ep channel (in which Z+jets is much less important), the scale factor is simply assumed to be the geometric mean of the ee and  $\mu\mu$  scale factors.

The final scale factors can be seen in Tab. 5.2.

## 5.4 Control distributions

The agreement between simulation and data in several control distributions is presented in Figs. 5.8 to 5.10. All corrections described in the previous section are applied in these figures. In addition, they are scaled by the b tagging efficiency scale factors obtained in the final likelihood fit (Sec. 5.6) to better reflect the estimates for essential calibrations.

## 5 Measurement of the inclusive $t\bar{t}$ cross section at $\sqrt{s} = 13.6$ TeV

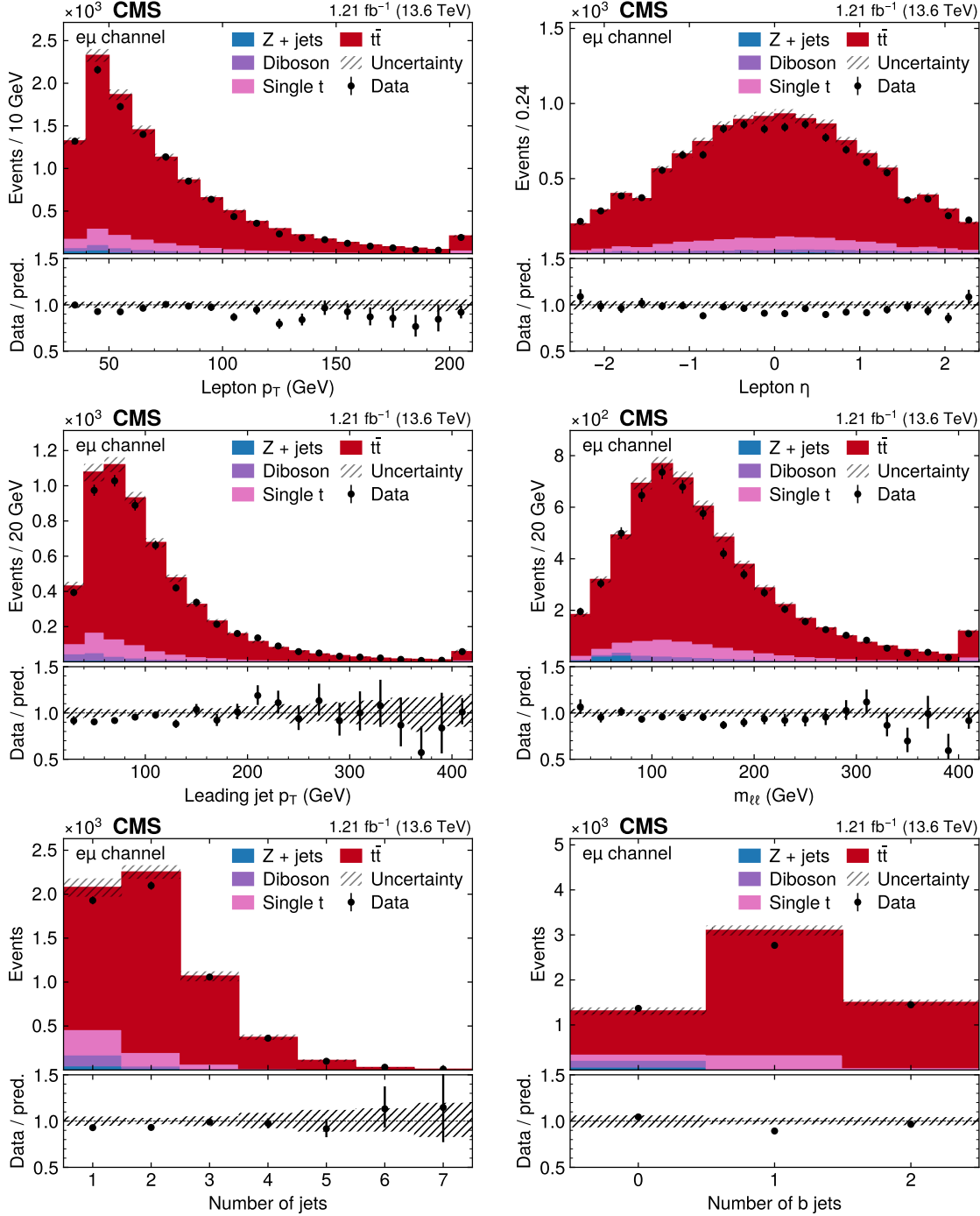


**Figure 5.8: Control distributions in the  $e\mu$  channel.** Shown are (from top left to bottom right) the distributions of  $p_T$  of both leptons,  $|\eta|$  of both leptons,  $p_T$  of the leading jet, the invariant lepton mass  $m_{\ell\ell}$ , the number of jets and the number of b jets. All figures show both data (black dots) and different simulated background processes (colored bars). For the latter, all corrections described in Sec. 5.3 as well as post-fit b tagging scale factors (Sec. 5.6) are applied, and the shaded area covers both statistical and systematic uncertainties. *Figure taken from Ref. [5].*

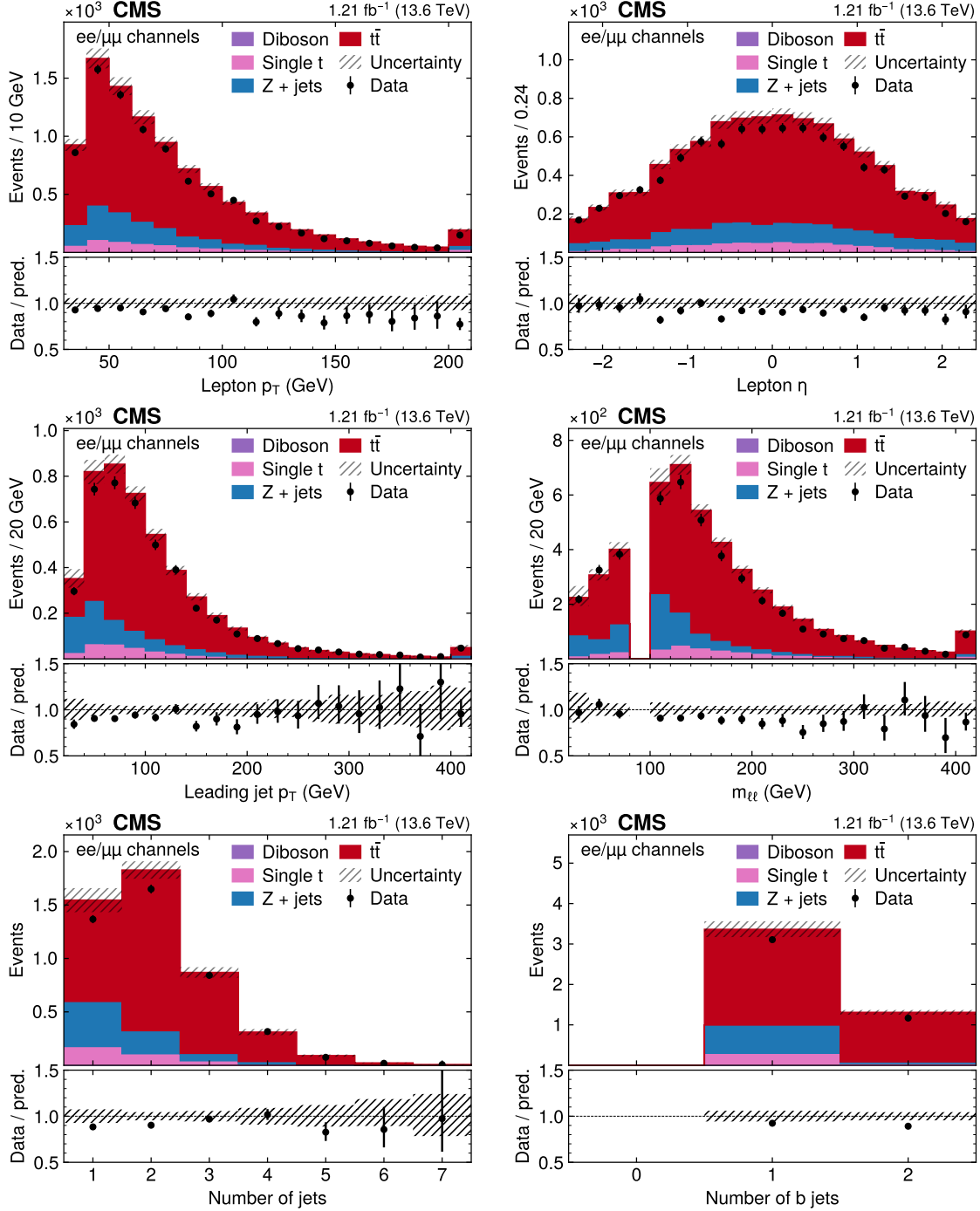


Figure 5.9: **Control distributions in the ee and  $\mu\mu$  channels.** The distributions are shown in the same manner as in Fig. 5.8. *Figure taken from Ref. [5].*

## 5 Measurement of the inclusive $t\bar{t}$ cross section at $\sqrt{s} = 13.6$ TeV

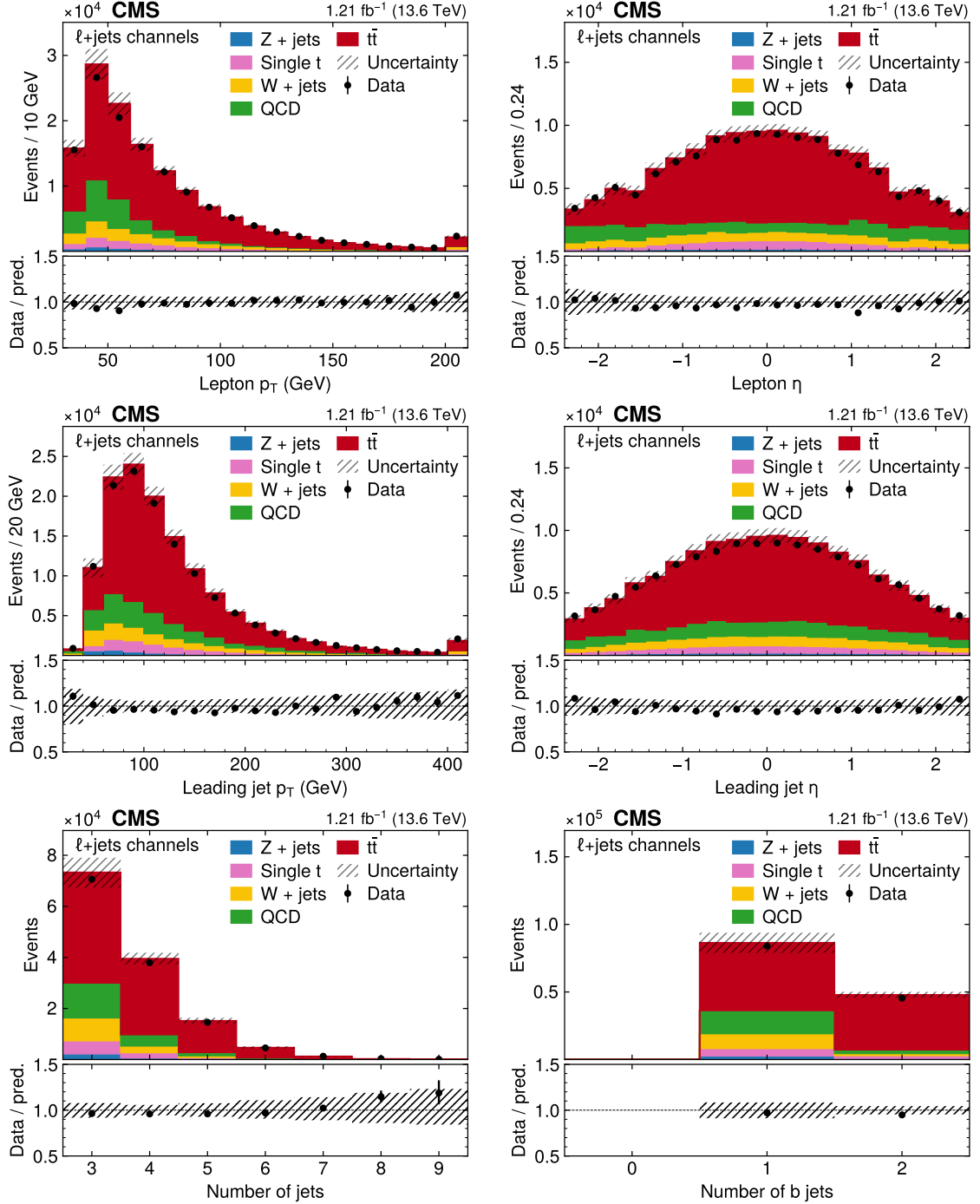


Figure 5.10: **Control distributions in the  $\ell + \text{jets}$  channels.** The distributions are shown in the same manner as in Fig. 5.8, except for the center-right figure, which here shows  $|\eta|$  of the leading jet. *Figure taken from Ref. [5].*

1583 Good agreement between data and simulation within the full uncertainties is seen  
1584 in all distributions.

## 1585 5.5 Systematic uncertainties

1586 In order to translate the distribution of observed and expected events into a result  
1587 for the inclusive  $t\bar{t}$  cross section while taking into account all relevant sources of  
1588 systematic uncertainties, a binned profile maximum likelihood fit as described in  
1589 Sec. 4.4 is performed using the tool `combine` [130]. The parameter of interest (POI)  
1590 used for this fit is the signal strength  $r = \sigma_{t\bar{t}}/\sigma_{t\bar{t}}^{\text{pred}}$ , i.e. the inclusive  $t\bar{t}$  cross section  
1591 normalized to its theoretical prediction. A linear signal model is used as defined in  
1592 Eq. (4.3), and the  $t\bar{t}$  cross section is extracted using its maximum likelihood estimate  
1593 and uncertainty.

1594 This section describes the considered systematic uncertainties, which can be di-  
1595 vided into experimental uncertainties, arising from incomplete knowledge of the  
1596 details of the detector and resulting differences between data and simulation, and  
1597 theoretical uncertainties, which concern imperfect modeling of the underlying phys-  
1598 ical processes in the different event generators.

1599 All systematic uncertainties are included in the fit as nuisance parameters (NPs) as  
1600 discussed in Sec. 4.4. In practice, NPs which encode shape effects on the considered  
1601 observables are implemented using *template morphing*, i.e. a smooth polynomial  
1602 interpolation between the nominal shape and the shapes encoding the variations  
1603 by  $\pm 1$  standard deviations. NPs that encode only normalization effects are instead  
1604 implemented as simple log-normal uncertainties. Both definitions can be found in  
1605 detail in Ref. [130].

1606 Special attention is given in this section to some experimental uncertainties which  
1607 are important to this measurement. This includes the luminosity, which is the  
1608 dominating uncertainty, as well as the b tagging uncertainties due to the special  
1609 way they are treated in the fit.

1610 **Luminosity uncertainty** In order to translate event yields into a result on any  
1611 cross section, the total integrated luminosity is required as a calibration constant.  
1612 Any experimental error on the luminosity will be directly transferred to the total  
1613 error on the measurement, and thus minimizing the luminosity uncertainty is crucial  
1614 for any cross section measurement.

1615 For the data set used in this analysis, the total integrated luminosity was mea-  
1616 sured by the CMS Collaboration with an estimated uncertainty of 2.3%. Of this  
1617 number, 2.1% is due to the calibration of the integrated luminosity, using the meth-  
1618 ods presented in Ref. [98].

1619 The agreement in the absolute scale is checked by comparing different indepen-  
1620 dently calibrated luminosity measurements. The integrated luminosity measured

with the hadronic forward calorimeter and the silicon pixel detector is found to agree at a level of better than 0.8%. Accounting for residual differences in time stability and linearity between the luminosity detectors results in a total uncertainty of 2.3%. This preliminary estimate of the integrated luminosity at the time of publication was further validated using the yield of reconstructed Z bosons decaying into muon pairs [146]. After correcting for efficiencies and normalizing to the fiducial cross section predicted at NNLO with next-to-NNLL corrections, good agreement was observed.<sup>1</sup>

In contrast to all other uncertainties described below, the uncertainty in the integrated luminosity is not directly included in the likelihood fit, but rather treated as an external uncertainty and added in quadrature afterwards, since it is expected to factorize completely from all other uncertainties. The impact of varying the normalization of the backgrounds estimated from simulation by the integrated luminosity uncertainty was found to be negligible.

**b tagging uncertainty** As mentioned in Sec. 5.3.1, the efficiency for correctly identifying a jet originating from a b quark (b tagging) is expected to be different in data and simulation. At the time of this measurement, directly after the start of Run 3, no general-purpose b tagging studies had been available. Thus, the approach adopted here is to consider the b tagging efficiency in data to be completely unknown and measure it concurrently with the cross section in the likelihood fit.

For this purpose, the probability for an event with  $n_{\text{jet}}$  selected jets to have  $n_{\text{btag}}$  correctly identified b jets, depending on the assumed b tagging efficiency  $\epsilon_b$ , is assumed to be a multinomial of the form

$$P(n_{\text{btag}}|n_{\text{jet}}) \propto \epsilon_b^{n_{\text{btag}}} (1 - \epsilon_b)^{n_{\text{no tag}}} \quad (5.14)$$

Here,  $n_{\text{no tag}}$  is the number of true b jets in the event which fall into the acceptance of the selection, but fail to be tagged by DEEPJET. It is estimated from MC simulation.

By taking the ratio of eq. 5.14 in data and simulation, one can derive a per-event weight which corrects the number of b tags in MC:

$$w_b = \frac{(\epsilon_b^{\text{data}})^{n_{\text{btag}}} (1 - \epsilon_b^{\text{data}})^{n_{\text{no tag}}}}{(\epsilon_b^{\text{MC}})^{n_{\text{btag}}} (1 - \epsilon_b^{\text{MC}})^{n_{\text{no tag}}}} = (f_b)^{n_{\text{btag}}} \left( \frac{1 - f_b \epsilon_b^{\text{MC}}}{1 - \epsilon_b^{\text{MC}}} \right)^{n_{\text{no tag}}} \quad (5.15)$$

Here,  $f_b = \epsilon_b^{\text{data}} / \epsilon_b^{\text{MC}}$  is the unknown b tagging scale factor. It is left freely floating in the likelihood fit. This is technically implemented by producing shape templates from MC with  $f_b$  varied up and down by a fixed value and interpolating in between. This shape template can be seen in Fig. 5.11, where it is evident that

---

<sup>1</sup>Since publication of this result, a more precise luminosity measurement for 2022 data has become available in Ref. [147].

1653 the categorization in the number of b tags gives significant constraining power for  
 1654  $f_b$ . In the 1b categories, the shape with respect to the number of jets deviates  
 1655 significantly from a flat variation proportional to  $f_b$  as naively expected. This is  
 1656 because of out-of-acceptance jets, corresponding to the second factor in Eq. (5.15).

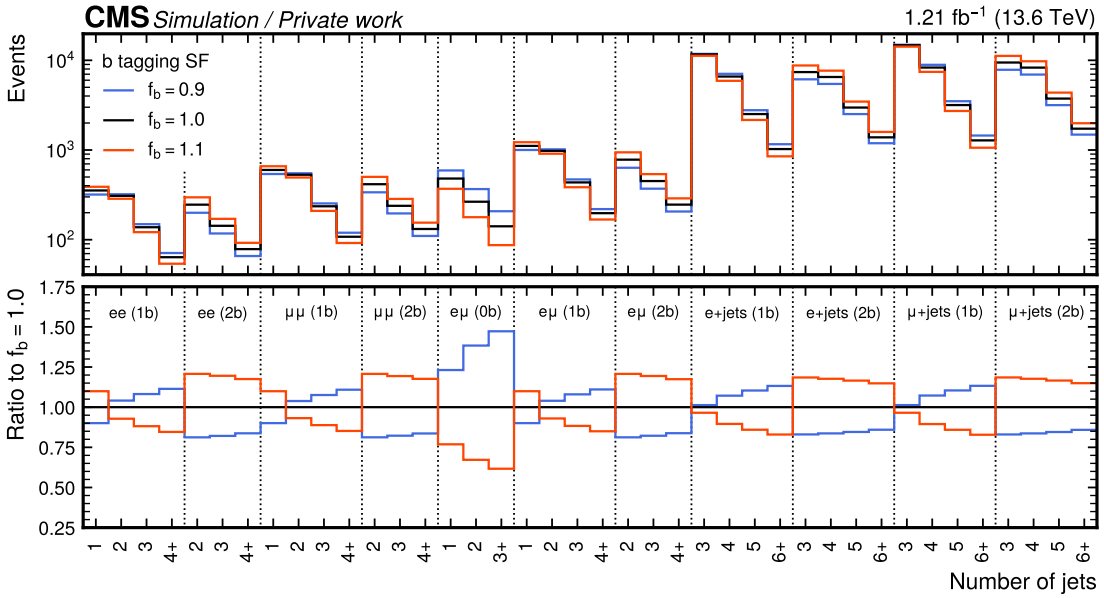


Figure 5.11: **b tagging scale factor variation.** The effect of varying the b tagging scale factor  $f_b$  in  $t\bar{t}$  MC by an arbitrary value of  $\pm 0.1$ , shown for the number of jets in the 11 fit categories.

1657 Note that, since  $f_b$  is taken to be a single number, this method only corrects the  
 1658 overall b jet efficiency and does not consider any dependence of  $\epsilon_b$  on jet kinematics.  
 1659 Because this measurement uses the same jet quality requirements (particularly the  
 1660 same  $p_T$  cuts) in all channels, and assuming that the b jet  $p_T$  and  $\eta$  spectra in  
 1661 the different channels are roughly similar, any kinematic dependence is effectively  
 1662 integrated out in the overall efficiency scale factor  $f_b$ . The lack of corrections to the  
 1663 spectrum is not considered problematic in this context, as the likelihood fit does not  
 1664 rely directly on kinematic information.

1665 **Lepton identification uncertainty** The uncertainty assumed on the lepton iden-  
 1666 tification scale factors comes from two different sources: First, an inherent uncer-  
 1667 tainty originating in the tag-and-probe method (as described in Sec. 5.3.1) is con-  
 1668 sidered. It consists of statistical uncertainties from both data and simulation, a  
 1669 systematic uncertainty derived from a comparison with a different Z+jets simula-  
 1670 tion sample produced at NLO in QCD, and another systematic uncertainty due  
 1671 to the choice of fitting function. Together, they make up for an uncertainty of

1672  $\sim 0.8\%$  ( $0.5\%$ ) on the electron (muon) scale factors in the bulk of the phase space,  
1673 and can rise up towards  $\sim 5\%$  for high lepton  $p_T$ .

1674 Secondly, it is taken into account that the scale factor between data and simulation  
1675 might be slightly different in the Z+jets selection used for the T&P method and  
1676 the  $t\bar{t}$  selection used for the measurement of the cross section. The most important  
1677 reason for this is the requirement of (b tagged) jets in almost all considered cate-  
1678 gories, as well as the requirement for at least three jets in the lepton+jets channels.  
1679 This effect has been studied at CMS in the past and the difference found to be less  
1680 then  $0.5\%$  for muons and  $1.0\%$  for electrons. Taking a conservative approach, these  
1681 values are used as an additional component in the respective uncertainties.

1682 In the first, preliminary version of this measurement [132], the dedicated lepton  
1683 efficiency scale factors as measured with the T&P method were not yet available,  
1684 and a different approach was taken. Similar to the b tagging efficiency, the lepton  
1685 efficiency scale factors were kept freely floating the likelihood fit. Due to the different  
1686 dependency on the lepton efficiencies in the different lepton flavor channels, the fit  
1687 was able to constrain the efficiencies to a precision of  $2\%$  [5]. The resulting scale  
1688 factors were later found to be in good agreement with those obtained from the T&P  
1689 method, serving as a valuable cross-check. However, this method ultimately led to  
1690 less precision and was thus not used in the final result. **TODO decide on removing**  
1691 **as Alexander suggested**

1692 **Pileup uncertainty** As described in Sec. 5.3.1, three different pileup-related vari-  
1693 ables are employed to reweight the simulation to the observed data, and the average  
1694 of the three weights is used as the nominal value. This method is repeated using  
1695 only one of the variables - the number of good reconstructed vertices  $n_{PV}$  - and the  
1696 difference in expected yields treated as an uncertainty. This procedure was com-  
1697 pared to the usual estimation of pileup-related uncertainties in CMS. There, the  
1698 theoretical expectation for the number of interactions is taken as the product of the  
1699 instantaneous luminosity and the total inelastic cross proton-proton cross section of  
1700  $69.2(32)$  mb at  $\sqrt{s} = 13$  TeV [98]. It was found that the heuristic method used here  
1701 leads to larger uncertainties than the one from the inelastic cross section, and can  
1702 thus be considered more conservative.

1703 **Jet energy uncertainties** Uncertainties in the jet energy calibration are split  
1704 into 26 different sources concerning different experimental and theoretical effects,  
1705 following the standard CMS procedure outlined in Ref. [141]. 17 of these sources  
1706 are found to be non-negligible and included in the fit, while the others are indis-  
1707 tinguishable from fluctuations due to limited MC statistics. These sources include,  
1708 among others, uncertainties due to jet  $p_T$  resolution and jet flavor composition,  
1709 statistical uncertainties in the derivations of the energy corrections, and residual  
1710 differences between data and simulation.

1711 **Trigger uncertainties** Since the trigger scale factors are derived using the tag-  
1712 and-probe method in the same way as the lepton scale factors, similar uncertainties  
1713 are applied, including the uncertainties of 0.5% for muons and 1.0% for electrons due  
1714 to extrapolation between Z+jets and tt topologies. The only difference is that in the  
1715 dilepton channels the uncertainties need to be propagated according to Eq. (5.2).  
1716 This has the effect of greatly reducing the impact of the trigger uncertainties in  
1717 those channels compared to the lepton ID uncertainties, since the nominal per-event  
1718 trigger efficiency is already very close to one.

1719 **Matrix element scale uncertainties** The theoretical predictions of both sig-  
1720 nal and background are calculated using matrix elements at either LO or NLO in  
1721 perturbative QCD, matched to a parton shower. Since this effectively means trun-  
1722 cating the perturbative expansion of the scattering amplitude at a given power in  
1723 the strong coupling constant, the effect of higher-order terms is neglected in the  
1724 calculation.

1725 At the same time, the necessity of renormalization of divergent diagrams and  
1726 factorization of non-perturbative contributions introduces non-physical parameters  
1727 into the prediction in the form of the renormalization and factorization scales  $\mu_R$   
1728 and  $\mu_F$  (cf. Sec. 3.1). These parameters are usually set to typical energy scales of  
1729 the considered process, and might also depend on the event kinematics (dynamic  
1730 scales).

1731 To estimate possible uncertainties due to these missing terms as well as due to the  
1732 choice of scales, the scales  $\mu_R$  and  $\mu_F$  are varied separately by a factor of 2 up and  
1733 down, and the resulting change in simulation is taken as an uncertainty in the form  
1734 of shape templates [148]. To avoid double-counting uncertainties in the background  
1735 cross section predictions (see below) while still accounting for possible rate variations  
1736 due to acceptance effects, the templates are normalized to the nominal cross section  
1737 values before applying any selection cuts.

1738 **PDF uncertainties** The PDFs used to evaluate the non-perturbative contribu-  
1739 tion of the proton-proton collision have systematic uncertainties attached. They are  
1740 estimated by independently reweighting the simulation to 100 different replicas of  
1741 the used NNPDF 3.1 PDF set and taking the envelope of the resulting changes,  
1742 following the recommendations of the PDF4LHC working group [149]. Additionally,  
1743 the effect of the choice of the strong coupling constant in the PDF is assessed using  
1744 a similar reweighting, and attached as a separate nuisance parameter. Analogously  
1745 to the matrix element uncertainties, the resulting variations are normalized before  
1746 any selection cuts to keep acceptance and shape effects while not double-counting  
1747 cross section changes.

**1748 Parton shower uncertainties** The parton shower model used for the predictions  
**1749** is only accurate (at most) at LL and LC in QCD (cf. Sec. 3.2) and thus requires  
**1750** appropriate uncertainties. For this purpose, the scales at which the strong coupling  
**1751** constant is evaluated are varied up and down by a factor 2 separately for initial  
**1752** and final state radiation and for different processes, and the resulting changes are  
**1753** propagated to the fit as shape templates.

**1754 ME/PS matching uncertainty** For the simulation of the  $t\bar{t}$  signal, an additional  
**1755** uncertainty concerning the matching between matrix element simulation in POWHEG  
**1756** and parton showering in PYTHIA is considered. This is done by varying the  $h_{\text{damp}}$   
**1757** parameter in POWHEG controlling the amount of radiation generated at matrix  
**1758** element level, following Ref. [150].

**1759 Top quark  $p_T$  uncertainty** It has been shown in previous measurements of  $t\bar{t}$   
**1760** differential cross sections that the  $p_T$  spectrum of the top quark is significantly  
**1761** softer in data than in the standard POWHEG MC simulation [151–153]. This effect  
**1762** is propagated to the  $p_T$  spectra of the top decay products and can thus lead to  
**1763** misestimation of the acceptance due to lepton and b jet  $p_T$  requirements. Fixed-  
**1764** order predictions at NNLO in QCD and NLO in EW are known to largely alleviate  
**1765** the discrepancy [154]. Thus, a common strategy is to reweight the top quark  $p_T$   
**1766** spectrum in MC simulation to the one extracted from such fixed-order predictions.

**1767** At the time of the measurement, fixed-order predictions at NNLO in QCD and  
**1768** NLO EW were available only for  $\sqrt{s} = 13$  TeV and could not be directly applied to  
**1769** the MC simulation at  $\sqrt{s} = 13.6$  TeV. Instead, the simulation is left uncorrected  
**1770** for the nominal prediction, and a variation is constructed by calculating the ratio  
**1771** of the fixed-order prediction from Ref. [154] and the POWHEG MC simulation at  
**1772**  $\sqrt{s} = 13$  TeV, and applying it to the POWHEG MC simulation at  $\sqrt{s} = 13.6$  TeV.  
**1773** The difference between uncorrected prediction and the variation is assigned as an  
**1774** additional uncertainty, which is one-sided by construction.

**1775 Background cross section uncertainties** For the cross sections of the different  
**1776** processes, log-normal rate uncertainties are assigned based on the process and order  
**1777** at which it was calculated. Separate 15% uncertainties are used for the  $t$ -channel  
**1778** single-top and tW backgrounds since they are generated at NLO with a NNLO  
**1779** prediction for the cross section, while for W+jets and Diboson, 30% is used since  
**1780** these samples are only generated at LO. For Z+jets, this is reduced to 20% due  
**1781** to the data-driven estimation of the normalization. Additionally, for the fully data-  
**1782** driven QCD background, two separate nuisance parameters for the e+jets and  $\mu$ +jets  
**1783** channels are defined, covering a conservative uncertainty of 30% each.

1784 **Background statistical uncertainties** Finally, since the background in this  
1785 measurement is estimated either using MC simulation or data-driven methods, an  
1786 independent statistical uncertainty needs to be attached to each bin, reflecting the  
1787 finite number of events it contains. This is done using the so-called *Barlow–Beeston*  
1788 *light* method [155]. For MC backgrounds, these uncertainties are minuscule. How-  
1789 ever, for the data-driven QCD background, they also contain the propagated statis-  
1790 tical uncertainty due to the limited number of data events in the CRs, which is in  
1791 general non-negligible.

## 1792 5.6 Fit results

1793 Performing the fit yields a  $t\bar{t}$  signal strength of  $r = 0.959 \pm 0.025$ , where the un-  
1794 certainty includes statistical and all systematic contributions, except for the 2.1%  
1795 uncertainty on the luminosity. This corresponds to an inclusive  $t\bar{t}$  cross section of

$$\sigma_{t\bar{t}} = 881 \pm 23 \text{ (stat+syst)} \pm 20 \text{ (lumi) pb.}$$

1796 The result is in good agreement with the standard model prediction of  $\sigma_{t\bar{t}}^{\text{pred}} =$   
1797  $924^{+32}_{-40} \text{ pb.}$

1798 Fig. 5.12 shows the agreement between data and simulation before and after the  
1799 fit. It can be immediately seen that the fit greatly reduces the uncertainty on the  
1800 prediction by constraining systematic uncertainties and simultaneously improves the  
1801 agreement compared to the data.

1802 Of particular note here is the free-floating b tagging efficiency (compare sec. 5.5),  
1803 whose effect can be directly read off from the categorization in the number of b jets:  
1804 Before the fit (Fig. 5.12 top), the event yield for two or more b jets is overestimated in  
1805 the simulation, while the yield for zero b jets is underestimated. This suggests that  
1806 the b tagging efficiency is slightly lower in the data than assumed in the simulation.  
1807 Indeed, the fit confirms this: the b tagging scale factor between data and simulation  
1808 in the phase space of this measurement is measured to be  $f_b = 0.980 \pm 0.009$ . As a  
1809 result, after the fit (Fig. 5.12 bottom), the event yields agree in all b jet categories.

### 1810 5.6.1 Statistical checks

1811 To better understand the sources of systematic uncertainty, as well as the contribu-  
1812 tions of the different measurement channels, the fit is repeated twice, restricted to  
1813 either the dilepton or the  $\ell+\text{jets}$  channels. For both cases as well as the combination,  
1814 the contribution of different groups of nuisance parameters is calculated by freezing  
1815 the groups to their postfit values and repeating the fit, as explained in Sec. 4.4.  
1816 It should be noted that this procedure does not take into account correlations be-  
1817 tween the groups, and thus the sum in quadrature of the separate components will  
1818 in general not add up to the total uncertainty.

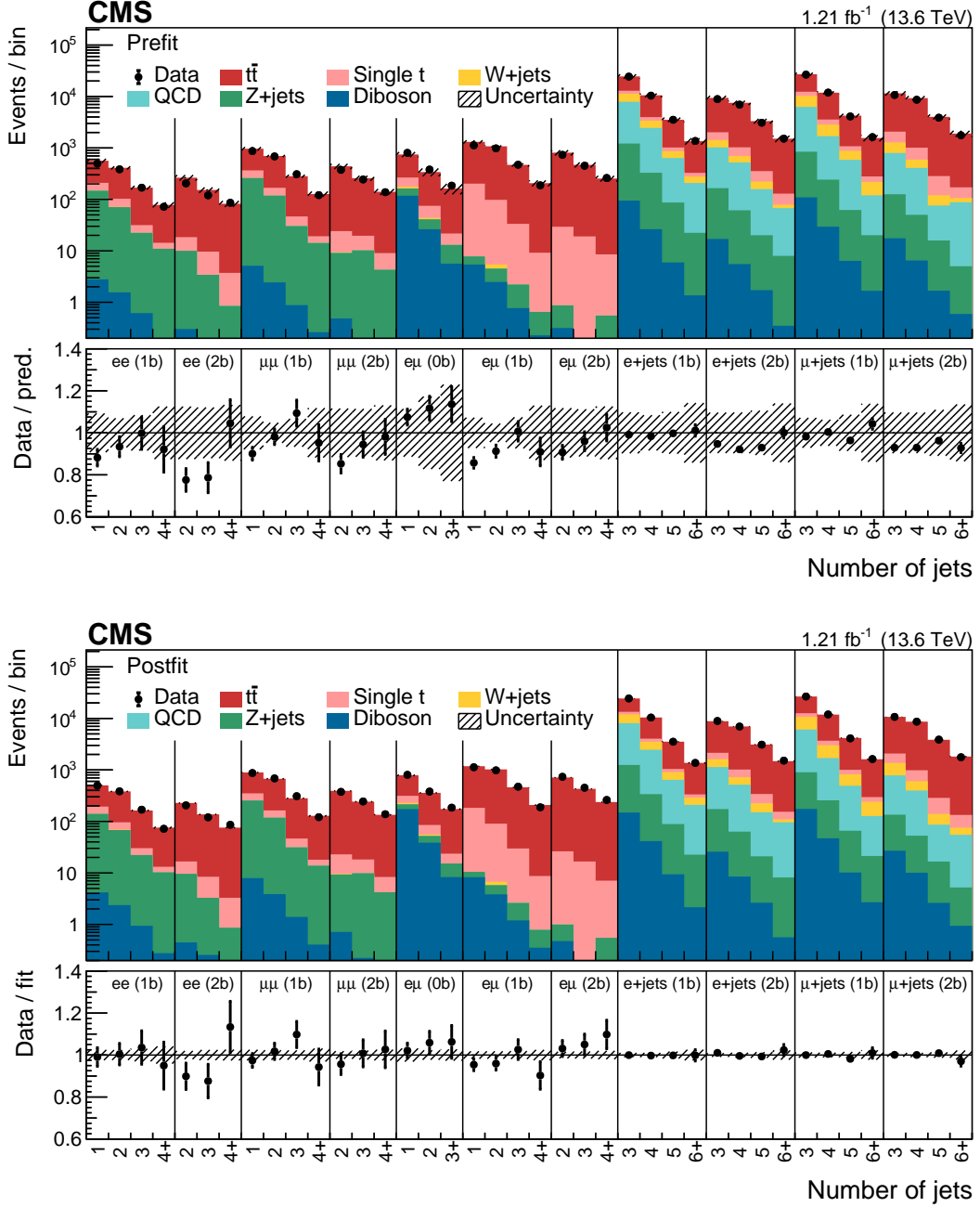


Figure 5.12: **Comparison of data and simulation before and after the fit.**

The distribution of the number of jets in the different fit categories is shown for data and simulation before (top) and after the likelihood fit (bottom). The fit greatly improves the agreement and strongly constrains the background uncertainties. *Figure taken from Ref. [5].*

---

Source	Full measurement	dilepton only	$\ell+$ jets only
Lepton ID efficiencies	1.6	2.2	1.0
Trigger efficiency	0.3	<0.1	0.5
JES	0.6	0.7	1.1
b tagging efficiency	1.1	0.8	2.1
Pileup reweighting	0.5	0.2	1.1
ME scale, $t\bar{t}$	0.5	0.4	0.5
ME scale, backgrounds	0.2	0.1	0.3
ME/PS matching	0.1	0.4	0.7
PS scales	0.3	0.5	0.4
PDF and $\alpha_S$	0.3	0.4	0.4
Top quark $p_T$	0.5	0.3	0.5
tW background	0.7	1.0	0.4
$t$ -channel single-t background	0.4	<0.1	0.5
Z+jets background	0.3	0.2	<0.1
W+jets background	<0.1	<0.1	0.2
Diboson background	0.6	0.6	<0.1
QCD multijet background	0.3	—	0.5
Statistical uncertainty	0.5	1.2	0.5
Combined uncertainty	2.6	3.4	3.3
Integrated luminosity	2.3	2.3	2.3

Table 5.3: **Sources of systematic uncertainty.** The relative per-cent contribution of different groups of sources of systematic uncertainty for the full measurement as well as for restrictions to the dilepton and  $\ell+$ jets channels only. They are calculated according to Sec. 4.4 and do not take correlations between the different groups into account.

1819 The results can be found in Tab. 5.3, where it can be seen how the combination  
 1820 of channels helps to reduce the total uncertainty: in the dilepton channels, the dom-  
 1821 inating uncertainties are the lepton identification uncertainty, which enters twice  
 1822 compared to the  $\ell+$ jets channels, as well as the statistical uncertainty of the data  
 1823 due to the relatively low branching ratio. In the  $\ell+$ jets channels, b tagging, JES,  
 1824 and pileup uncertainties dominate, reflecting the less clean selection and increased  
 1825 importance of jets. When the channels are combined, the uncertainty contribution  
 1826 of these groups lies inbetween the two separate numbers, showing how the chan-  
 1827 nel combination represents a tradeoff between the advantages and disadvantages of  
 1828 either channel.

1829 Furthermore, the nuisance parameter pulls, constraints and impacts, as defined in

Sec. 4.4, are shown in Fig. 5.13 for the channel combination. One can see how the electron identification scale factors, which are the leading impact, are constrained by the combination of channels, while the same is not true of the muon identification scale factors due to their lower prefit uncertainty.

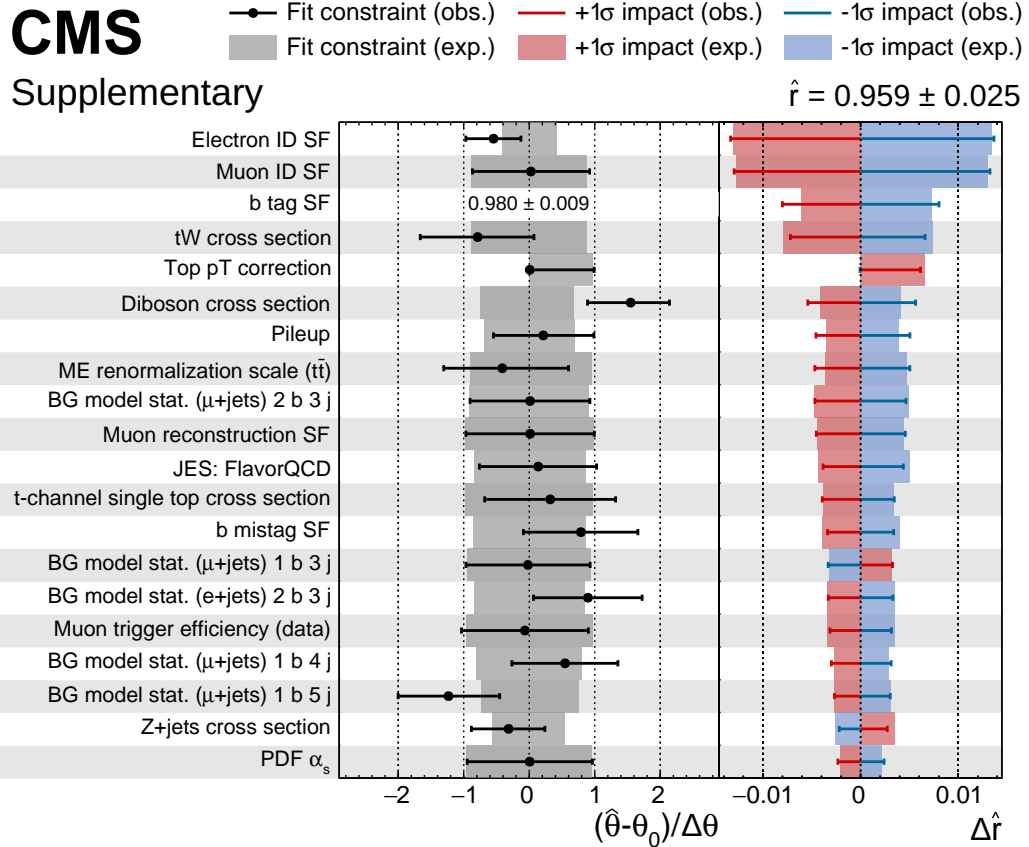


Figure 5.13: **Nuisance parameter pulls, constraints and impacts.** The expected and observed values are shown as shaded bands and error bars, respectively. Nuisance parameters are sorted by their observed impact on the signal strength  $r$ . For the b tagging scale factor, for which no prefit uncertainty is defined, the post-fit uncertainty is shown instead of the pull. *Figure taken from the supplementary material of Ref. [5].*

## 5.6.2 Top quark mass dependence

An additional source of uncertainty that has not been considered so far is the choice of top quark mass in the  $t\bar{t}$  MC simulation. It affects the selection efficiency indirectly via the  $p_T$  cuts on leptons and jets, with higher top quark mass values leading to harder spectra and thus to larger efficiencies.

Contrary to other uncertainty sources, the top quark mass is not profiled in the likelihood fit. Instead, the dependence of the extracted  $t\bar{t}$  cross section is explicitly quantified as a function of the top quark mass by shifting its value in simulation by  $\pm 3$  GeV from its default of  $m_t = 172.5$  GeV. The extraction of  $\sigma_{t\bar{t}}$  is then repeated and the dependence on  $m_t$  extracted through a simple linear fit. This strategy has been taken in previous CMS and ATLAS  $t\bar{t}$  cross section measurements [156, 157], and thus facilitates comparison with previous results.

For an upwards shift of  $\Delta m_t = 1$  GeV, the  $t\bar{t}$  cross section is found to shift downwards by 8.5 pb, and vice versa. If one takes the current experimental uncertainty of 0.3 GeV [11] as an allowed range for  $m_t$ , this would lead to an additional uncertainty on  $\sigma_{t\bar{t}}$  of 0.3%.

## 5.7 Summary and Outlook

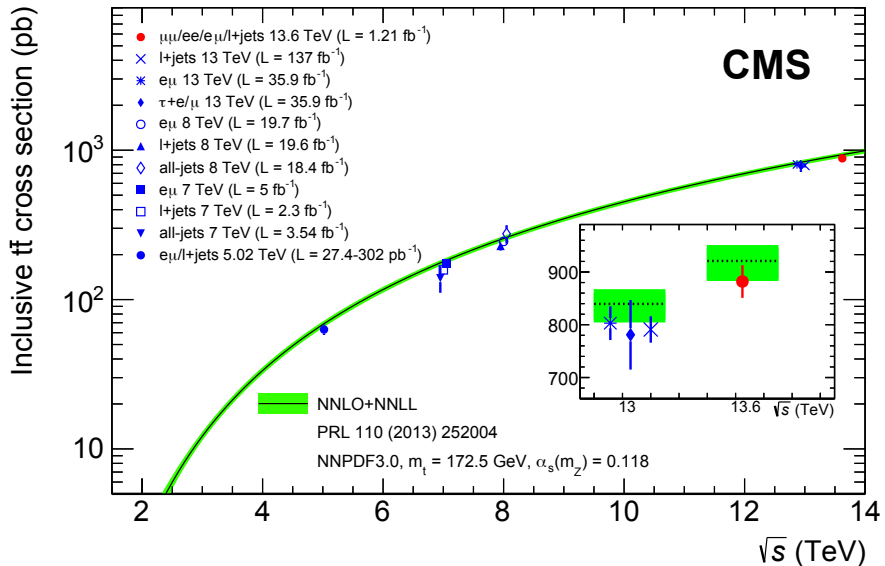


**Figure 5.14: Summary of  $\sigma_{t\bar{t}}$  measurements.** An overview of inclusive  $t\bar{t}$  cross section measurements at CMS at different center-of-mass energies [156, 158–164] as well as comparison to the SM prediction [165]. This measurement is displayed as the red dot. *Figure taken from Ref. [5].*

In this chapter, the inclusive  $t\bar{t}$  cross section is measured for the first time at a center-of-mass energy of  $\sqrt{s} = 13.6$  TeV. Data corresponding to an integrated luminosity of  $1.21 \text{ fb}^{-1}$  from the beginning of LHC Run 3 are analyzed. Despite this comparatively small amount of data, a total precision of ca. 3% with respect to the inclusive cross section is achieved.

1856 Fig. 5.14 compares the result of this chapter to other inclusive  $t\bar{t}$  cross section  
1857 measurements performed by CMS at other center-of-mass energies [156, 158–164],  
1858 as well as to the SM prediction [165]. The precision is comparable to other measure-  
1859 ments at  $\sqrt{s} = 7, 8$ , and  $13$  TeV, some of them with significantly higher integrated  
1860 luminosities. All results are in agreement with the SM.

1861 This measurement was designed specifically for the earliest data of Run 3, in  
1862 order to achieve high precision without relying on a full suite of calibrations being  
1863 available. In particular, b tagging and lepton efficiencies can be constrained *in situ*  
1864 using the combination of dilepton and  $\ell + \text{jets}$  channels as well as the categorization  
1865 by number of b-tagged jets. No large inconsistencies for any of the considered physics  
1866 objects were found. The measurement was made public in September of 2022 just  
1867 two months after the start of Run 3 and constituted the first public physics result  
1868 of LHC Run 3. At the time, it provided a valuable first proof that CMS data taken  
1869 in Run 3 were of high quality and ready for physics.

1870 The next step for this result would be to transfer the technique developed in this  
1871 work to well-understood data and high integrated luminosities in order to achieve  
1872 the highest precision possible for  $\sigma_{t\bar{t}}$ . Such a measurement will certainly be domi-  
1873 nated by systematic uncertainties, most importantly the luminosity and the lepton  
1874 identification efficiencies (as already partly the case here). The channel combination  
1875 method developed here could potentially help reduce the latter uncertainty through  
1876 an *in situ* constraint, while the former is independent of the analysis strategy and  
1877 requires more precise luminosity measurements for improvement. In addition, a  
1878 more detailed study of the individual sources of uncertainty will likely be necessary  
1879 to assess whether some can be reduced through improved calibrations.

1880 Additionally, one could try to use such a high-precision  $t\bar{t}$  cross section measure-  
1881 ment to indirectly measure the top quark mass, one of the fundamental parameters  
1882 of the Standard Model, by comparing the measured value of  $\sigma_{t\bar{t}}$  to SM predictions  
1883 for different top quark masses. For this purpose, it would be important to reduce  
1884 the dependence on the top quark mass in simulation (c.f. Sec. 5.6.2), for example by  
1885 reducing the  $p_T$  requirements on leptons and jets as much as experimentally feasible.  
1886 All of this leaves multiple parts for future studies to tread, which will be exciting  
1887 to follow in the coming years as larger parts of the Run 3 data set are analyzed at  
1888 CMS.

1889 **6 Simulation of on- and off-shell  $t\bar{t}$**   
1890 **production with bb41**

1891 **6.1 Introduction**

1892 The accurate modeling of top quark production processes at the LHC is of crucial  
1893 importance for precision measurements of top quark properties. In particular, the  
1894 fact the top quark is an unstable colored resonance with a short lifetime presents  
1895 challenges for correctly modeling its mass line shape as used for top mass and width  
1896 measurements [166–168]. Typically, the modeling is done with full NLO MC sim-  
1897 ulations matched to a parton shower (NLO+PS), and multiple such generators are  
1898 available with different features and degrees of accuracy.

1899 In this chapter, the predictions of some of these generators from the POWHEG  
1900 framework [80, 81] are compared to each other, as well as to unfolded data mea-  
1901 sured in Ref. [169], for different variables relevant to top mass and/or width mea-  
1902 surements. A particular focus is the generator **bb41** [7], which specifically improves  
1903 the treatment of the unstable top resonance and of the interference between  $t\bar{t}$  and  
1904  $tW$ , and is described in detail in Sec. 6.2. In this work, **bb41** is implemented and  
1905 validated for the first time in the CMS simulation setup. The comparison is done  
1906 at the generator level, i.e. including parton showering and hadronization but not  
1907 detector simulation and experimental reconstruction.

1908 The results of this work have been published in a CMS public note as Ref. [6].  
1909 Since the publication of this note, a new version of **bb41** has been made avail-  
1910 able [170]. In this thesis, updated results including both versions will be shown.

1911 **6.2 The Monte Carlo generator bb41**

1912 **bb41** [7, 170] is a full NLO+PS MC generator for the process  $pp \rightarrow b\bar{b}\ell^+\ell^-\nu_\ell\bar{\nu}_\ell$ ,  
1913 including all off-shell contributions. This includes the dilepton decay channel of  
1914 both  $t\bar{t}$  and  $tW$  production, as well as non-resonant contributions involving Z or  
1915 Higgs bosons, as shown in Fig. 6.1. Since these processes all lead to the same  
1916 final state at NLO in QCD, they interfere with each other and cannot be easily  
1917 separated. **bb41** includes this interference by construction since it computes the full  
1918 amplitude including all diagrams at once.

1919 In addition, by considering the full amplitude instead of splitting it into pro-  
1920 duction and decay, **bb41** treats the top quark as an unstable resonance without

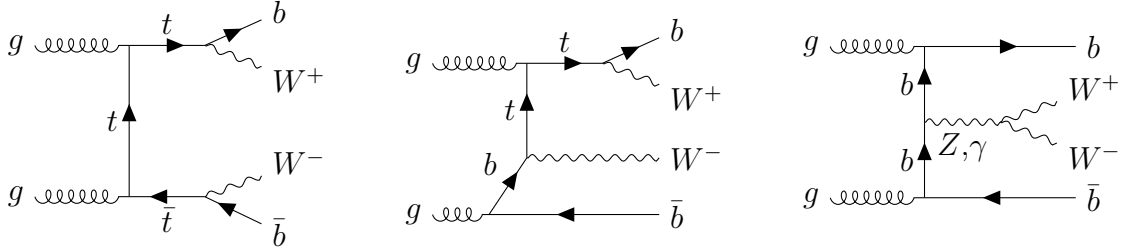


Figure 6.1: **Feynman diagrams for bb41.** Examples of Feynman diagrams for the  $pp \rightarrow b\bar{b}W^+W^-$  process as described by bb41, including double-resonant (left), single-resonant (center) and non-resonant contributions (right). The decay of the W bosons into leptons is not shown for brevity.

1921 approximations. It is implemented in the “resonance-aware” version of POWHEG,  
 1922 called POWHEG vRES [171], which includes the hardest QCD radiation also for  
 1923 unstable resonances - such as top quarks - in addition to the hardest initial state  
 1924 radiation always provided by POWHEG. As a result, an event generated by bb41 can  
 1925 have up to three hard emissions at matrix element level. The correct description of  
 1926 these FSR emissions is relevant e.g. for observables related to the mass of the top  
 1927 quark, and can be challenging for parton showers, leading to large uncertainties.

1928 This work investigates two different versions of bb41. The first version is the one  
 1929 originally published in Ref. [7] and publicly available on the POWHEG website [172].  
 1930 In the following, it will be referred to as bb41 v1.

1931 The second version of bb41 was recently published in Ref. [170]. Its most promi-  
 1932 nent feature compared to the previous version is the addition of the lepton+jets  
 1933 decay channel of  $t\bar{t}$ , i.e. the  $b\bar{b}\ell\nu_\ell q\bar{q}'$  final state. Moreover, it includes several im-  
 1934 provements to the dilepton final state, such as avoidance of spurious finite width  
 1935 effects and improved resonance history projectors (see Ref. [170] for details). At the  
 1936 time of writing this thesis, the new code is not publicly available. A preview version  
 1937 was made available to the CMS collaboration by the authors, and the dilepton final  
 1938 state of this version - referred to as bb41 v2 - is shown in this work. The lepton+jets  
 1939 final state, on the other hand, was not ready for validation in the preview version,  
 1940 and so could not be included.

### 1941 6.3 Other $t\bar{t}$ Monte Carlo generators

1942 The distributions predicted by bb41 are compared to three other MC generators  
 1943 for the  $t\bar{t}/tW$  final state, which are briefly presented in this section. All of these  
 1944 are implemented in POWHEG v2, and as such do not contain explicit treatment of  
 1945 radiation in unstable resonances.

**1946 6.3.1 hvq**

1947 `hvq` [83], standing for *heavy quark*, is the standard code used, at the time of writing,  
1948 by both the ATLAS and CMS collaborations for producing  $t\bar{t}$  MC events. It applies  
1949 the narrow-width approximation (NWA) to generate stable  $t\bar{t}$  pairs at NLO in QCD,  
1950 with up to one additional ISR emission. The top quarks are then randomly smeared  
1951 according to the top quark width, giving an approximate treatment of finite-width  
1952 effects. Following this, the top quarks are decayed - in this case, in the dilepton  
1953 channel for all lepton flavors - using internal POWHEG routines [173]. These rou-  
1954 tines work at tree level at LO in QCD and preserve spin correlations. Further ISR  
1955 emissions as well as all FSR emissions are provided by the parton shower.

**1956 6.3.2 ST\_wtch**

1957 Since `hvq` generates only the double-resonant  $t\bar{t}$  amplitude, a second generator has to  
1958 be used alongside it for the single-resonant  $tW$  and  $t\bar{t}/tW$  interference contributions.  
1959 Here, `ST_wtch` [174] is used for this purpose. It works very similar to `hvq`, also  
1960 generating a stable  $tW$  pair in the NWA, smearing with the top width and decaying  
1961 the particles using the same routines.

1962 However, in order to at least approximately recover the full  $b\bar{b}W^+W^-$  amplitude,  
1963 it is necessary to select a scheme for the treatment of the  $t\bar{t}/tW$  interference to  
1964 prevent double-counting. Since the separation between  $t\bar{t}$  and  $tW$  is not well defined  
1965 at NLO, such schemes will to some degree always be ad-hoc and ambiguous. Two  
1966 such schemes are implemented for `ST_wtch`, and both are compared in this work:  
1967 in the first, called diagram removal (DR), all terms involving the square of double-  
1968 resonant diagrams are simply removed from the squared amplitude. This is the  
1969 most intuitive choice, but has the disadvantage of not being gauge invariant [175].  
1970 The second method, diagram subtraction (DS), keeps double-resonant diagrams in  
1971 the squared amplitude, and subtracts a gauge invariant counter-term to remove the  
1972 double counting [174–176]. For both schemes, the prediction of `ST_wtch` is added  
1973 to the one of `hvq` (together called  $t\bar{t} + tW$ ) to produce distributions that can be  
1974 compared to `bb41`.

**1975 6.3.3 ttb\_NLO\_dec**

1976 The generator `ttb_NLO_dec` [177], similar to `hvq`, works in the NWA and thus  
1977 generates stable  $t\bar{t}$  pairs with ad-hoc smearing. However, unlike `hvq`, it is fully  
1978 NLO-accurate not only in the production, but also in the decay of the top quarks.  
1979 This means that, like `bb41`, it generates up to one hard FSR emission per decaying  
1980 top quark, leading to up to three hard emissions in the final state.

1981 It also provides an LO-accurate treatment of the  $t\bar{t}/tW$  interference by reweighting  
1982 the generated  $t\bar{t}$  events to the full off-shell LO amplitude. Thus, like `bb41`, it can

Parameter	Value
POWHEG settings	
Top quark mass	172.5 GeV
Top quark width	1.33 GeV
$h_{\text{damp}}$	$1.38 m_t$ [150]
PDF set	NNPDF 3.1 [73]
PYTHIA settings	
PYTHIA version	8.307
PYTHIA tune	CP5 [92]
PowhegHooks settings [85]	
POWHEG:veto	on
POWHEG:pThard	0
POWHEG:pTdef	1

Table 6.1: **Generator settings.** An overview of the settings for POWHEG and PYTHIA, as well as the matching between them, for all considered generators.

1983 be used on its own and does not need to be added together with e.g. `ST_wtch`, but  
1984 is expected to work at a lower accuracy since it includes more approximations.

## 1985 6.4 Technical setup

1986 For all generators, LHE events were generated and then showered and hadronized  
1987 with the multi-purpose generator PYTHIA. Wherever possible, the same settings  
1988 were used for the different generators, an overview of which can be found in Tab. 6.1.  
1989 They are mostly identical to the default settings used by CMS for MC generation,  
1990 as discussed in Ref. [92].

### 1991 6.4.1 Parton shower matching

1992 Special care has to be taken regarding the matching of the POWHEG ME gener-  
1993 ators to the parton shower as provided by PYTHIA. For `hvq` and `ST_wtch`, this  
1994 is accomplished here using a shower veto as described in Sec. 3.2, and technically  
1995 implemented using the `PowhegHooks` module of PYTHIA. By default, this module  
1996 can only handle one ISR emission at matrix element level, and thus needs to be  
1997 extended for `bb41` and `ttb_NLO_dec`, which also contain FSR emissions in the top  
1998 decay. This was implemented by the `bb41` authors in the `PowhegHooksBB4L` module  
1999 as described in detail in Ref. [178]. An updated form of this module compatible  
2000 with `bb41` v2 is used here. Similarly to the ISR case, it is possible to directly start  
2001 the shower at the energy scale of the POWHEG emission, or alternatively employ a

2002 veto for emissions above this scale. The latter is used as the default option, and  
 2003 compared to the former in Sec. 6.5.2.

### 2004 6.4.2 Same-flavor leptons

2005 By default, both versions of `bb41` generate only dilepton final states with opposite-  
 2006 flavor leptons (electrons, muons or  $\tau$  leptons). This is because, in principle, there  
 2007 are additional diagrams contributing to the  $b\bar{b}\ell^+\ell^-\nu_\ell\bar{\nu}_\ell$  amplitude for same-flavor  
 2008 leptons, such as  $b\bar{b}ZZ$  with  $ZZ \rightarrow \ell^+\ell^-\nu_\ell\bar{\nu}_\ell$ , that are not included in `bb41`.

2009 In practice, the effect of these diagrams will be small, especially in experimental  
 2010 analyses where a cut is applied to reject resonant same-flavor lepton pairs close to  
 2011 the Z boson mass (compare Sec. 5.2.3). To make sure that `bb41` can be used in CMS  
 2012 for experimental analyses involving all lepton flavors, a relabeling procedure already  
 2013 included in `bb41` is extended to also produce same-flavor lepton final states, neglect-  
 2014 ing the aforementioned diagrams. This procedure is used for all `bb41` distributions  
 2015 shown in this chapter.

## 2016 6.5 Results

### 2017 6.5.1 Comparison between generators

2018 In this section, the two `bb41` versions are compared against each other, as well as  
 2019 to the alternative generators introduced in Sec. 6.3, for different observables. All of  
 2020 these comparisons are done after parton showering and hadronization, but without  
 2021 any detector simulation.

2022 The package RIVET [179] was used to analyze the events. For some observables,  
 2023 publicly available analysis packages were employed, which is stated in the captions  
 2024 of the figures where applicable. Furthermore, some observables include distributions  
 2025 at the jet level, which are obtained by running an anti- $k_T$  algorithm with distance  
 2026 parameter  $\Delta R = 0.4$  (AK4) [122].

2027 **Lepton observables** To begin the comparison, events with at least two leptons of  
 2028 opposite sign satisfying  $p_T > 20 \text{ GeV}$  and  $|\eta| < 2.4$  are selected. Photons surround-  
 2029 ing the leptons in a small cone of  $\Delta R < 0.1$ , originating from photon radiation,  
 2030 are clustered together with the leptons (“dressed leptons”). The  $p_T$  distributions of  
 2031 the leading and subleading of these two leptons are shown in Fig. 6.2. They show  
 2032 good agreement between the generators within the renormalization and factorization  
 2033 scale uncertainties.  $t\bar{t} + tW$  using the DR scheme predicts a slightly harder lepton  
 2034 spectrum than the others, while the DS scheme agrees with `bb41` and `ttb_NLO_dec`.

2035 The same trend can be seen in Fig. 6.3 for the invariant lepton mass  $m_{\ell\ell}$ , both  
 2036 inclusively and split by lepton flavor channels. The per-channel distributions are all

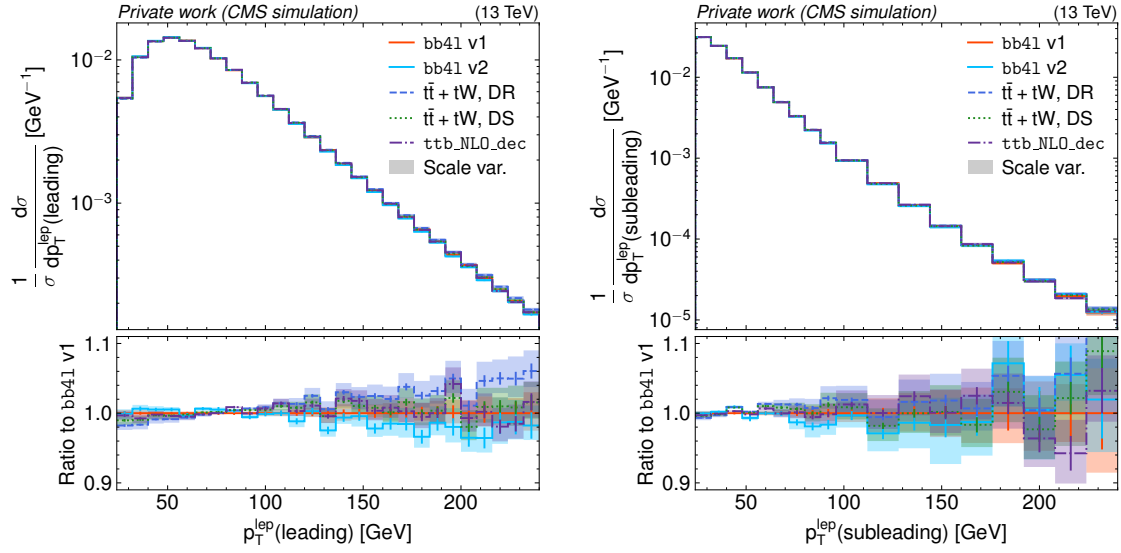


Figure 6.2: **Distributions of lepton  $p_T$**  of the leading (left) and subleading (right) lepton for **bb41** v1 (red), v2 (aqua),  $t\bar{t} + tW$  with the DR (blue) and DS scheme (green), as well as **ttb\_NLO\_dec** (magenta). The shaded bands show the uncertainty due to scale variations, while the error bars show the statistical uncertainty. *Figure adapted from Ref. [6].*

comparable within statistical uncertainties, which validates the extension to same-flavor leptons for **bb41** presented in Sec. 6.4.2.

**Jet observables** Next, some selected AK4 jet observables are compared. Jets containing a B hadron are identified as b jets using a ghost association technique [180, 181].

Fig. 6.4 shows the inclusive jet multiplicity and the transverse momentum of the leading b jet for the different generator setups. Several differences can be observed, both between the two versions of **bb41** and between **bb41** and the other generators. For the jet multiplicity, the variations are largely covered by the scale uncertainties. However, for the leading b jet transverse momentum, a discrepancy remains at very low  $p_T$  that is not accounted for by these uncertainties. It is interesting to note that the number of jets agrees well between  $t\bar{t} + tW$  and **bb41** v2, while **bb41** v1 and **ttb\_NLO\_dec** disagree and predict a larger number of jets. The origin of these discrepancies, especially between the **bb41** versions, is not yet understood and subject of discussion with the authors of the program.

Next, Fig. 6.5 shows the b quark fragmentation, defined as the fraction of energy of the central B hadron in a jet compared to the total jet energy, as well as the average differential b jet shape  $\langle \rho(R) \rangle$ , which is the transverse momentum density of the particles making up the b jet as a function of its radius  $R$ . Both of these variables

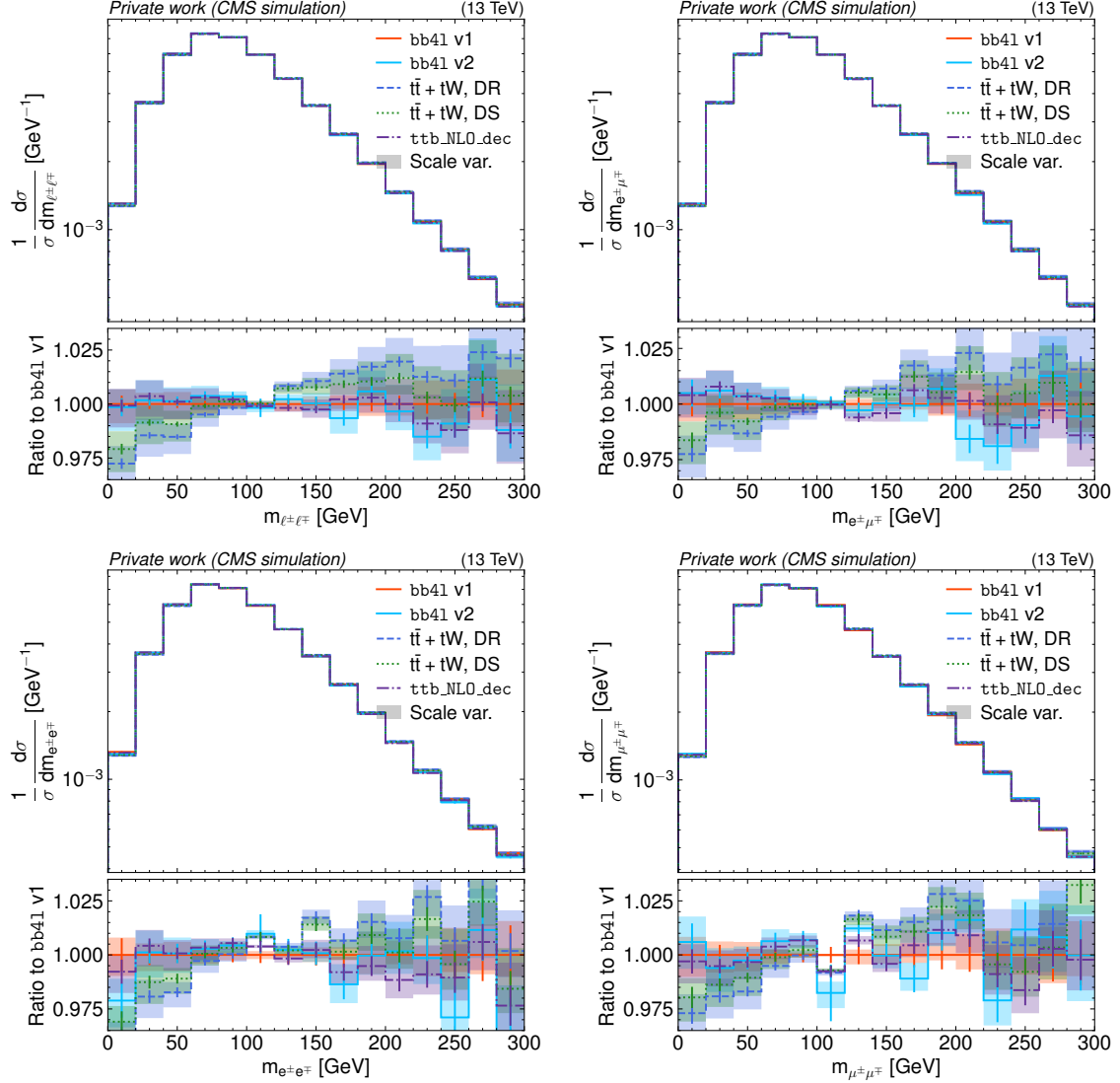


Figure 6.3: **Distributions of  $m_{\ell\ell}$**  for all lepton flavors combined (upper left) as well as in the  $e\mu$  (upper right),  $ee$  (lower left) and  $\mu\mu$  channels (lower right), shown in the same manner as in Fig. 6.2. *Figure adapted from Ref. [6].*

## 6 Simulation of on- and off-shell $t\bar{t}$ production with bb41

---

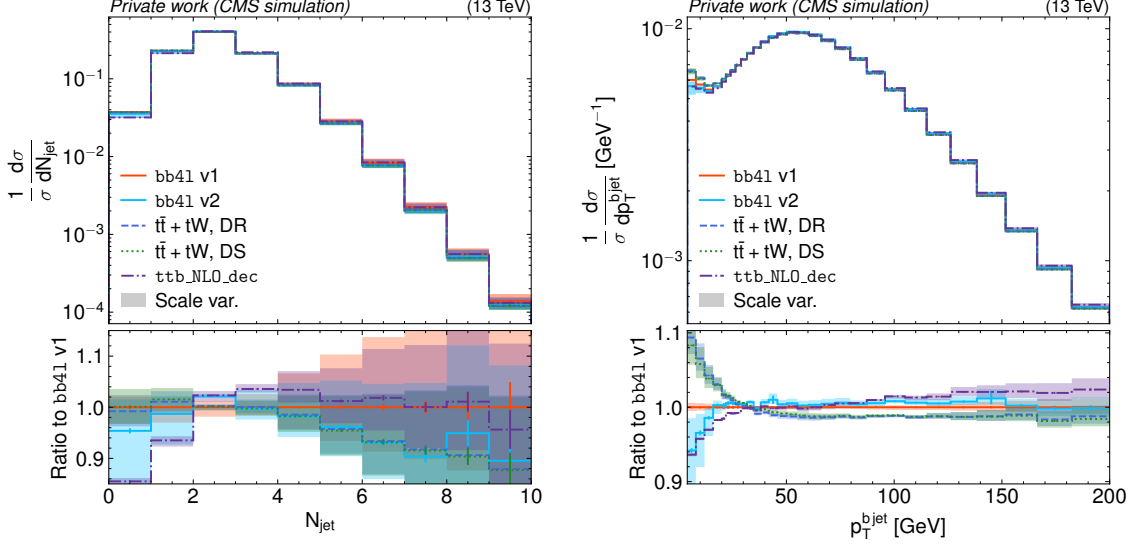


Figure 6.4: **Number of jets and b jet  $p_T$ .** Distributions of the inclusive number of AK4 jets (left) and the  $p_T$  of the leading b jet (right, RIVET analysis MC\_HFJETS), shown in the same manner as in Fig. 6.2. *Figure adapted from Ref. [6].*

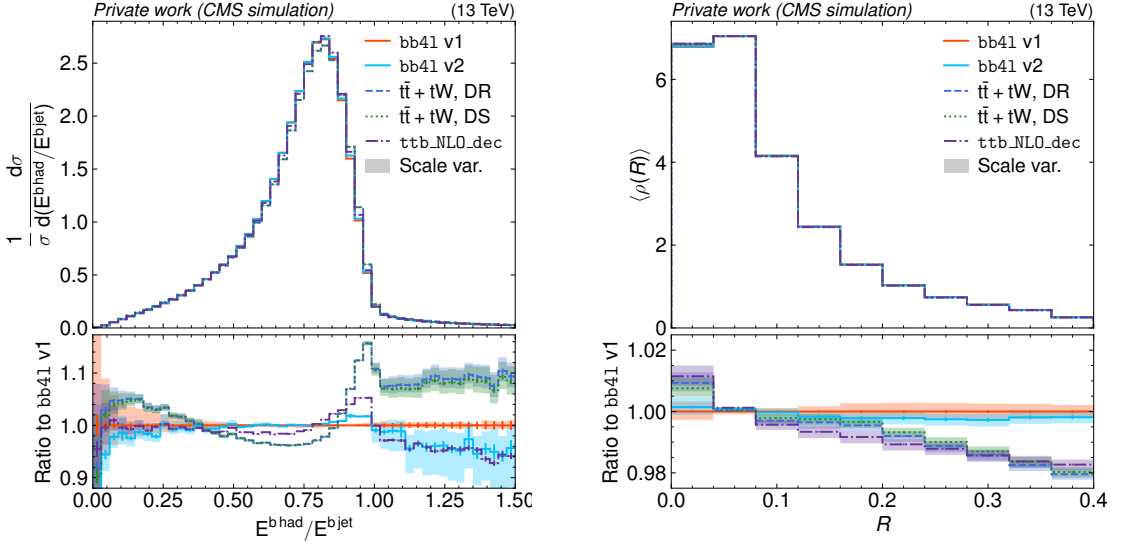


Figure 6.5: **b fragmentation and jet shape.** Distributions of the b quark fragmentation (left, RIVET analysis MC\_HFJETS) and the average differential b jet shape (right, RIVET analysis MC\_HFDECAYS), shown in the same manner as in Fig. 6.2. *Figure adapted from Ref. [6].*

are sensitive to final-state radiation from the top decay, and are thus expected to be affected by the full NLO calculation performed by `bb41`. It can be seen that both versions of `bb41` predict softer b jet spectra and wider jets than both  $t\bar{t} + tW$  and `ttb_NLO_dec`, which can be interpreted as more FSR emissions being generated. Notably, this effect cannot be solely due to the inclusion of hard FSR emissions in `bb41` since these are also present in `ttb_NLO_dec`.

In general, all of these trends for `bb41` (softer lepton and b jet spectra as well as wider jets) agree with what was observed in Refs. [178, 182], but differ from the results initially reported in Ref. [7].

**Invariant  $b\ell$  mass** A common proxy observable to use for measurements of the top quark mass in dilepton events is the invariant mass of a b jet and a lepton,  $m_{b\ell}$ . To do so, a procedure is needed to unambiguously assign the leptons and b jets (of which there might be varying numbers per event depending on the event selection) to each other. Here, exactly two b jets per event are required, and the so-called minimax mass is used, defined as

$$m_{b\ell}^{\text{minimax}} = \min [\max(m_{b_1\ell_1}, m_{b_2\ell_2}), \max(m_{b_1\ell_2}, m_{b_2\ell_1})]. \quad (6.1)$$

This prescription amounts to maximizing the invariant mass over the two  $b\ell$  pairs in the event, and then minimizing it over the two possible assignments of b jets and leptons. It is notable in that, for double-resonant  $t\bar{t}$  events, it shows a kinematic cutoff at a value of  $\sqrt{m_t^2 - m_W^2} \approx 150$  GeV. As a result, the tail above this cutoff is sensitive to single-resonant  $tW$  events as well as  $t\bar{t}/tW$  interference and thus to the top quark width.

Fig. 6.6 shows the distribution of  $m_{b\ell}^{\text{minimax}}$ , again for all considered cases. It can be seen that both versions of `bb41` are in good agreement with each other, and are also in agreement with `ttb_NLO_dec` except for the lowest bin. Unfolded ATLAS data taken from Ref. [169] is overlaid on top of the predictions, and shows good agreement for both `bb41` and `ttb_NLO_dec`. In the tail, the two interference handling schemes for  $t\bar{t} + tW$  show significant differences as expected, with `bb41` and `ttb_NLO_dec` lying between them. Since `bb41` is expected to provide a more accurate prediction of the interference than either scheme, this validates that using the difference of the schemes as an uncertainty covers the true values, as is done in many CMS and ATLAS measurements. Going forward, such uncertainties could be dropped from future measurements by using `bb41` predictions directly.

**Top quark reconstruction** Finally, in order to directly study the effects on top quark observables, a simple generator-level top quark reconstruction is performed. To do so, two dressed leptons and two b jets are selected as before, while the two neutrinos in the dileptonic top decay are taken from truth-level information. The W bosons are reconstructed from the neutrinos and charged leptons according to the

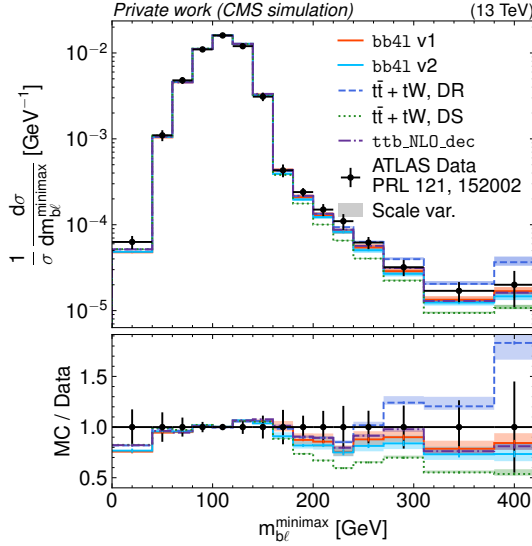


Figure 6.6: **Distribution of  $m_{b\ell}^{\text{minimax}}$** , shown in the same manner as in Fig. 6.2. ATLAS data from Ref. [169] is overlaid as black dots, and the RIVET routine from said reference was used to obtain the distributions. *Figure adapted from Ref. [6].*

lepton charge, and then combined with the b jets by choosing the pairs for which the difference  $\Delta m_t$  between the invariant masses is minimal.

This reconstruction procedure is not equivalent to a full experimental reconstruction, in which neutrinos are measured only as missing transverse momentum and thus cannot be directly assigned to the leptons. It also does not include any detector resolution effects. However, it does take into account the effects of FSR in the top decay by considering the full b jets instead of parton-level b quarks, which is why it was chosen for the comparison.

Fig. 6.7 shows the resulting distributions for the top quark mass and  $p_T$ . It can be seen that the different generators show different line shapes for the top quark mass: **bb41** predicts a small shift towards lower values compared to  $t\bar{t} + tW$  for both interference handling schemes as well as **ttb\_NLO\_dec**, and also predicts significantly lower amounts of off-shell tops with masses below the pole mass compared to  $t\bar{t} + tW$ . Both of these facts are important for precision top mass measurements, in which such shifts can influence the final fit results. The presence of these differences is expected: due to the use of the NWA for both  $t\bar{t} + tW$  and **ttb\_NLO\_dec**, the top line shape can only be modeled approximately in these generators, while **bb41** provides a true NLO-accurate description. It can furthermore be seen that the two **bb41** versions are not in perfect agreement with each other, though the difference is within the scale uncertainties.

For the top quark  $p_T$ , on the other hand, any trend in the comparison between the

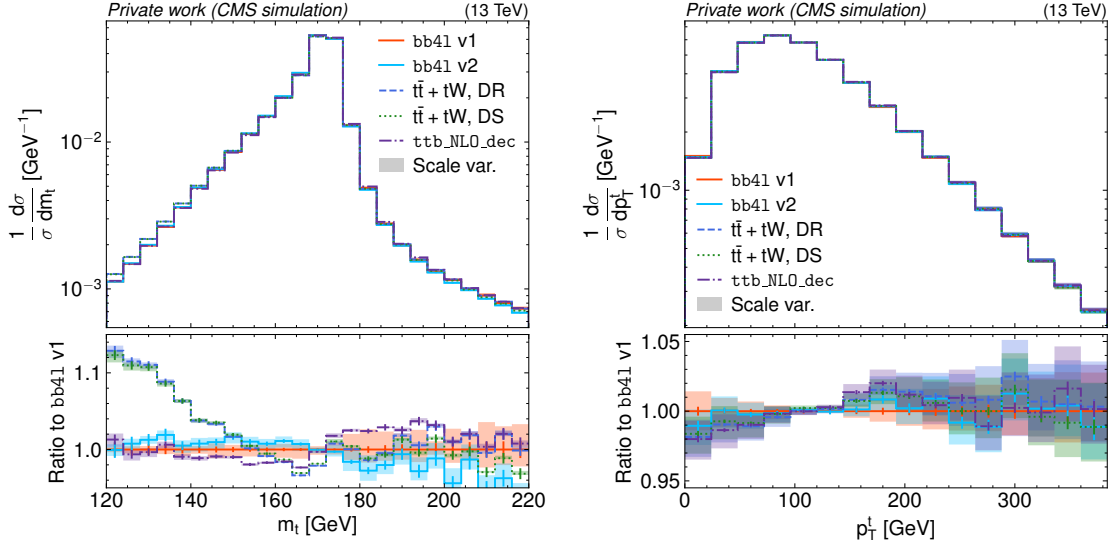


Figure 6.7: **Top quark line shape and  $p_T$ .** Distributions of the reconstructed top quark mass (left) and  $p_T$  (right), summed for both top and antitop quark, shown in the same manner as in Fig. 6.2. *Figure adapted from Ref. [6].*

generators is covered by the scale uncertainties, though **bb41** does seem to again predict softer  $p_T$  spectra than the other generators, consistent with the trends observed for the lepton  $p_T$  and  $m_{\ell\ell}$ .

Lastly, the invariant mass and  $p_T$  distributions of the  $t\bar{t}$  system as a whole are shown in Fig. 6.8. For  $m_{t\bar{t}}$ , no clear trend can be seen for any of the considered generators. The  $p_T$  of the  $t\bar{t}$  system, on the other hand, shows significant differences both between the two **bb41** versions and between **bb41** and the other generators (which agree with each other). It should be noted that, since the initial state of the  $pp \rightarrow t\bar{t}$  process has no  $p_T$ <sup>1</sup>, this variable is exactly zero at LO in QCD, and consequently determined only by emissions at NLO and beyond. As a result, it is expected to be sensitive to the NLO calculation and matching between matrix element and parton shower.

### 6.5.2 Comparison of FSR matching settings

Complementary to the previous generator comparisons, this section investigates the effect of the matching between matrix element and parton shower for FSR in **bb41**. As explained in Sec. 6.4.1, two principal options are available to match **bb41** to PYTHIA in the used module PowhegHooksBB4L: In the first and nominal approach

<sup>1</sup>Non-zero  $p_T$  of the incoming partons can be modeled with transverse momentum distributions [183], but this is not considered here.

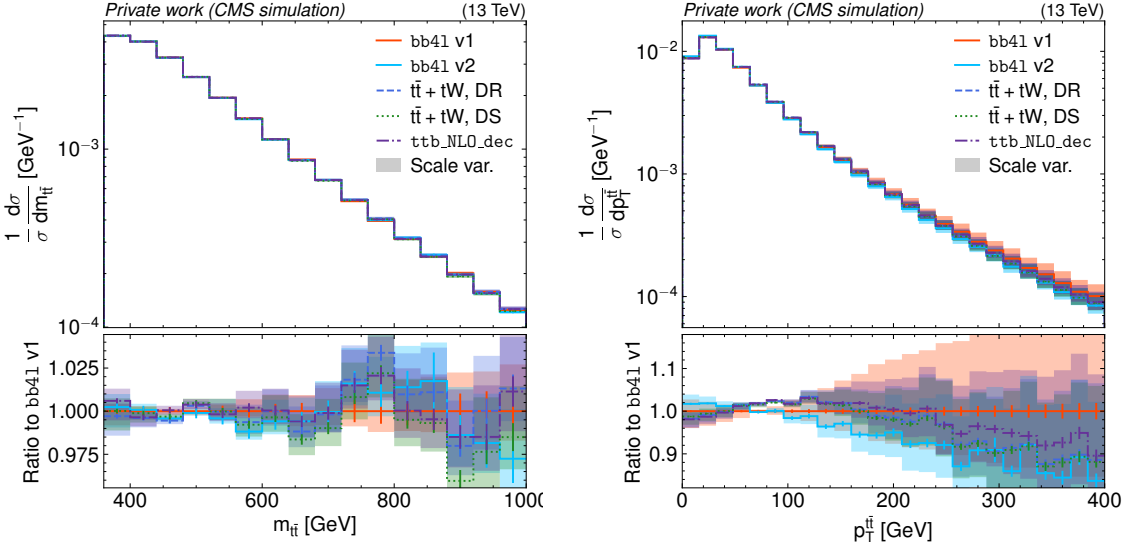


Figure 6.8: **Kinematics of the  $t\bar{t}$  system.** Distributions of the reconstructed invariant mass (left) and  $p_T$  (right) of the  $t\bar{t}$  system, shown in the same manner as in Fig. 6.2. *Figure adapted from Ref. [6].*

(denoted “FSR veto”), the parton shower is started at the kinematic limit, and FSR emissions that lie above the POWHEG energy scale of the relevant emission from the top decay as generated by POWHEG are vetoed.

In the second approach (“Res. scale”), the shower is directly started at the energy scale of the POWHEG FSR emission. This neglects the fact that the hardness scale definitions used in POWHEG and PYTHIA as ordering variables are similar but do not match exactly. When the PYTHIA emission is only slightly softer (by the PYTHIA definition) than the POWHEG emission, it is thus possible that it is in fact harder than the POWHEG emission by the POWHEG definition, leading to double-counting. Similarly, an emission that is only slightly harder by the PYTHIA definition and is thus not generated might in fact be softer by the POWHEG definition, leading to under-counting.

In order to demonstrate the importance of correct parton shower matching, a third case (“Kin. limit”) is considered, in which the parton shower for FSR emissions is started naively at the kinematic limit without any veto procedure specifically directed at **bb41**. This approach is thus expected to double-count FSR emissions.

The comparison in this section has been performed with **bb41 v1**. The matching for ISR emissions, done by **PowhegHooks**, is left identical between the three cases, as given in Tab. 6.1.

Fig. 6.9 shows the distributions of the top quark mass, reconstructed the same as before, and the b fragmentation for the different matching choices. Both of these observables were chosen for their sensitivity to FSR effects. It can be seen that

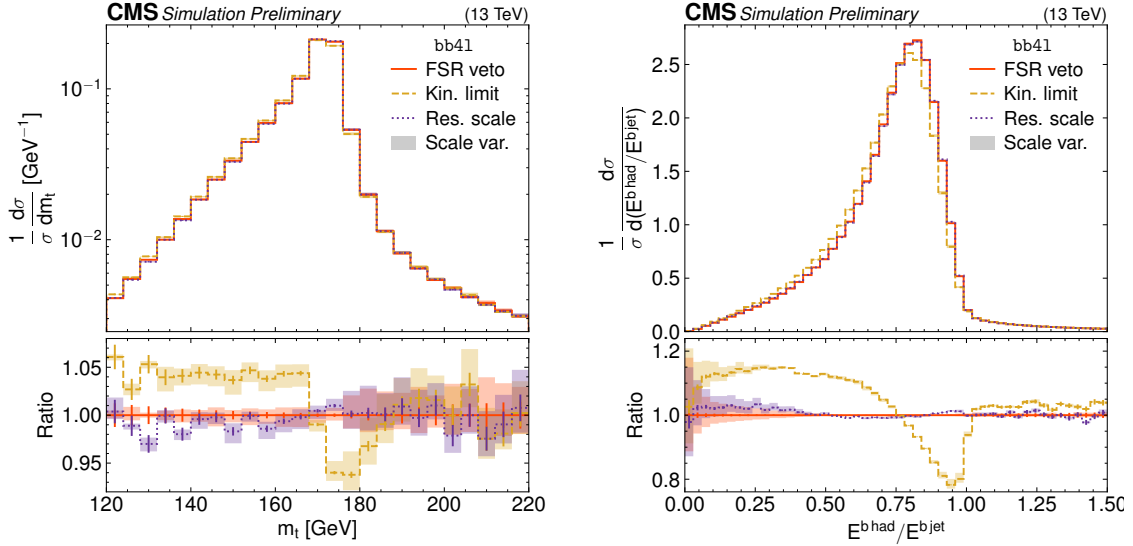


Figure 6.9: **Comparison of FSR matching settings.** Distributions of the reconstructed top quark mass (left, same as in Fig. 6.7) and the b quark fragmentation (right, same as in Fig. 6.5), for bb41 with different FSR matching settings as explained in the text (Sec. 6.5.2). The shaded bands show scale uncertainties. *Figure taken from Ref. [6].*

the options “FSR veto” and “Res. scale” agree reasonably well with each other, with the top mass line shape showing a small shift between them within the scale uncertainties. This implies that the mismatch between the POWHEG and PYTHIA energy scale definitions has a subleading effect in practice. On the other hand, the naive “Kin. limit” approach shows a large discrepancy due to its double-counting of FSR emissions, highlighting the importance of correct FSR matching procedures for NLO generators.

### 6.5.3 Recoil in top decay

In the simple parton shower in PYTHIA, there is a well-known problem affecting the virtualities of heavy unstable colored resonances, such as the top quark, in the treatment of FSR emissions in the resonance decay [184]. In particular, when performing a gluon emission off the decaying top quark and thus changing a  $t \rightarrow Wb$  configuration to  $t \rightarrow Wbg$ , there is an ambiguity on how to distribute the recoil imposed by the gluon between the top decay products (W and b quark) such that the four-momentum of the  $Wbg$  system is conserved.

PYTHIA 8.307, which is the version used for the previous studies in this chapter, offers two different treatments for this problem, which amount to assigning the recoil to only the W (“recoil to W”) or only to the b quark (“recoil to b”). Both of these

2171 are approximations, since a true treatment would distribute the recoil between the  
 2172 W and b quark in some form. CMS, and thus the studies previously shown in this  
 2173 chapter, use the “recoil to b” option.

2174 Since PYTHIA 8.310, a third option (“recoil to top”) has been made available  
 2175 via the setting `TimeShower:recoilStrategyRF`. For this option, the W is chosen  
 2176 as the recoiler at first, but the emissions are then reweighted in such a way as to  
 2177 approximate the radiation pattern expected in a true resonance-aware shower [184].  
 2178 It has been found in Ref. [185] that the difference between this improved method  
 2179 and the old ones can have a substantial impact on top mass proxy observables and  
 2180 consequently measured top mass values, and there have been discussions on whether  
 2181 such a difference should be included as a systematic uncertainty.

2182 This problem, in its core, is an issue of the parton shower and not the ME gen-  
 2183 erator. Nonetheless, **bb41** is expected to alleviate some of the ambiguities since it  
 2184 always includes the hardest gluon emission in each top decay at the ME level, where  
 2185 no question of assigning the recoil is raised. For subsequent and thus subleading  
 2186 emissions, the issue in principle still persists.

2187 To estimate the effect of the top recoil in **bb41** and compare it to  $t\bar{t} + tW$ , events  
 2188 from both generators are re-showered in PYTHIA 8.310 with the two choices of setting

```
TimeShower:recoilStrategyRF = 1 ("recoil to b") and
TimeShower:recoilStrategyRF = 2 ("recoil to top").
```

2189 **bb41** v2 is used for this comparison, and all other settings are kept at the nominal.  
 2190 For  $t\bar{t} + tW$ , only the DR scheme is considered for the interference handling.

2191 The results are shown in Fig. 6.10 for the reconstructed top mass and the b  
 2192 quark fragmentation. Large differences are visible between the two recoil strategies  
 2193 for  $t\bar{t} + tW$ , as expected from Refs. [184, 185]. For **bb41**, on the other hand, the  
 2194 differences are very small, and lie within the scale uncertainties for the top quark  
 2195 mass. This implies that the effect of the recoil in subleading emissions is negligible  
 2196 in **bb41** for the shown observables. As a result, **bb41** circumvents the problem of  
 2197 top recoil that can otherwise be significant for  $t\bar{t}$  analyses. **TODO** After discussion  
 2198 with Afiq I am not really convinced whether these results are actually correct... In  
 2199 particular, are we sure that the recoil strategy option in pythia works correctly when  
 2200 matched to bb4l? Simone is unfortunately no longer around to ask. Should I remove  
 2201 it?

## 2202 6.6 Summary and Outlook

2203 In this chapter, several generator-level studies of the MC generator **bb41**, which  
 2204 generates the full  $b\bar{b}\ell^+\ell^-\nu_\ell\bar{\nu}_\ell$  final state including  $t\bar{t}/tW$  interference and off-shell  
 2205 top effects at NLO in QCD, have been presented. **bb41** has been compared to

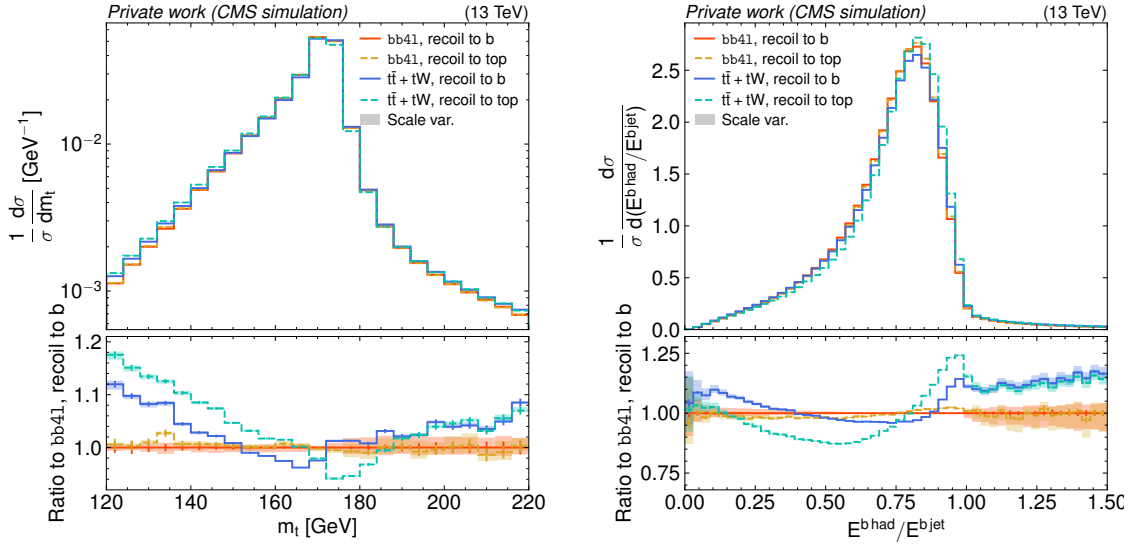


Figure 6.10: **Comparison of top recoil strategies.** Distributions of the reconstructed top quark mass (left, same as in Fig. 6.7) and the b quark fragmentation (right, same as in Fig. 6.5), for bb41 and  $t\bar{t} + tW$  with two different recoil treatments, as defined in the text (Sec. 6.5.3). The shaded bands show scale uncertainties.

other common  $t\bar{t}$  generators, namely `hvq`, `ST_wtch` (with two interference handling schemes) and `ttb_NLO_dec`, for different lepton, (b) jet and reconstructed top quark observables. For  $m_{bl}^{\text{minimax}}$ , `bb41` agrees well with ATLAS data from Ref. [169], improving greatly upon the two interference handling schemes DR and DS for  $t\bar{t} + tW$ . For the reconstructed top quark mass, `bb41` shows a significant shift compared to  $t\bar{t} + tW$ . In addition, two different `bb41` versions have been compared, finding slight differences within scale uncertainties, and the matching of ME and parton shower as well as the treatment of the top recoil in `bb41` have been studied further.

These studies represent valuable information for the choice of  $t\bar{t}$  MC generator in upcoming CMS measurements. For analyses in which  $t\bar{t}$  and  $tW$  are major backgrounds, `bb41` can help reduce uncertainties originating in the  $t\bar{t}/tW$  interference treatment, and provide a more accurate description when off-shell regions of phase space are probed. This is briefly explored in Sec. 7.5.4 in the context of a search for  $t\bar{t}$  bound state effects, which are naturally located in an off-shell-region. Furthermore, `bb41` will be crucial for a simultaneous top mass and width measurement using MC templates, as originally proposed in Ref. [178], in CMS. Alternatively, one might perform an differential  $t\bar{t} + tW$  cross section measurement, where `bb41` could be used to unfold the data to generator level.

2224 **7 Search for heavy scalar or pseudoscalar  
2225      bosons in  $t\bar{t}$  final states**

2226 **7.1 Introduction**

2227 Additional spin-0 particles are predicted in many attractive extensions of the Stan-  
2228 dard Model, and can be searched for in  $t\bar{t}$  final states at the LHC if the new states are  
2229 heavy (i.e. have a mass larger than  $2m_t$ ), electrically neutral, and exhibit Yukawa-  
2230 like couplings to fermions (see Sec. 2.3.1). A generic model for such states with either  
2231 pseudoscalar (A) or scalar (H) couplings to top quarks was given in Eq. (2.18).

2232 In addition,  $t\bar{t}$  bound state effects are expected in the SM in several calculations,  
2233 with a pseudoscalar component dominating at the LHC as discussed in Sec. 2.2.3.  
2234 Since additional BSM particles and bound state effects are expected to lead to  
2235 similar experimental signatures, it makes sense to search for them for using the  
2236 same methods.

2237 This chapter presents such a search for new spin-0 states with either scalar or  
2238 pseudoscalar interactions with the top quark, using the full Run 2 data set with an  
2239 integrated luminosity of  $138 \text{ fb}^{-1}$  at the CMS experiment. It follows up on a similar  
2240 search done using only  $35.9 \text{ fb}^{-1}$  of data taken in 2016 [17]. Similar searches have  
2241 also been published by ATLAS, one with  $20.3 \text{ fb}^{-1}$  of data taken at  $\sqrt{s} = 8 \text{ TeV}$  [186]  
2242 and one with  $140 \text{ fb}^{-1}$  of data taken at  $\sqrt{s} = 13 \text{ TeV}$  [187].

2243 The work done as part of this thesis focused on the dilepton decay channel of  $t\bar{t}$ ,  
2244 which is thus described in detail in Secs. 7.2 to 7.6. A significant excess of events  
2245 is observed at invariant masses close to the  $t\bar{t}$  threshold, which is interpreted either  
2246 as a pseudoscalar  $t\bar{t}$  bound state (Secs. 7.7.1 to 7.7.3) or as an additional scalar or  
2247 pseudoscalar boson (Sec. 7.7.4). For the latter interpretation, exclusion limits for a  
2248 large mass range are also presented in Sec. 7.8. Following this, the dilepton channel  
2249 is combined with a similar analysis of the  $\ell+\text{jets}$  decay channel, which is discussed  
2250 in Sec. 7.9, and exclusion regions are provided for the presence of either one or  
2251 two additional bosons. The results of this work are briefly compared in Sec. 7.10  
2252 to preliminary ATLAS results in Ref. [188] which confirmed this measurement, to  
2253 earlier ATLAS results in Ref. [187] in which no excess was observed, and to other  
2254  $t\bar{t}$  measurements. Finally, a summary and outlook are given in Sec. 7.11.

2255 The results presented here were first made public as a Physics Analysis Sum-  
2256 mary [189], and later submitted to *Reports on Progress in Physics* in an updated  
2257 form in two parts: first in Ref. [8] focusing solely on the interpretation of a  $t\bar{t}$  bound

state, and second in Ref. [9] focusing on the interpretation in terms of additional bosons. They build upon the framework developed in Ref. [190], with this work consisting of the implementation of matrix element reweighting for the signal simulation (Sec. 7.4), the simulation and scrutinization of the  $t\bar{t}$  bound state signal (Sec. 2.2.3), the comparison with other MC generators for the  $t\bar{t}$  continuum (Sec. 7.5.4), the interpretation of the observed excess in terms of  $t\bar{t}$  bound states or additional bosons including all corresponding cross-checks (Sec. 7.7), the combination with the  $\ell+\text{jets}$  channel (Sec. 7.9), the comparison to other results (Sec. 7.10), and the preparation of the results for publication in Refs. [9] and [8].

## 2267 7.2 Analysis setup

2268 This section describes the analysis strategy in the dilepton channels, consisting of  
2269 the considered data sets, object definitions, event selection criteria, corrections and  
2270 reconstruction algorithms.

### 2271 7.2.1 Data sets

2272 **Experimental data** The analysis is performed using the full CMS Run 2 ultra-  
2273 legacy (UL) data set, which is the final, re-reconstructed and recalibrated data set  
2274 recommended by CMS for physics analyses. It is split into the three data taking  
2275 years of Run 2: 2016, 2017 and 2018, where 2016 is further split into two parts,  
2276 denoted “2016pre” and “2016post”, because of a modification of the APV readout  
2277 chip settings that affects the efficiency of the track hit reconstruction during the  
2278 2016 data-taking period [191].

2279 A similar combination of dilepton and single-lepton triggers as in Sec. 5.2.1 is  
2280 used for all years, with the  $p_T$  thresholds varying slightly between data taking eras,  
2281 as shown in Tab. 7.1.

2282 **Background simulation** Since the final state of the signals considered in this  
2283 analysis are the same as in the SM  $t\bar{t}$  background, it is clear that a large irreducible  
2284 background is expected. As a result, it is essential that the SM Monte Carlo sim-  
2285 ulation is as both theoretically precise and has sufficient statistics, and that any  
2286 remaining imprecisions are covered by the systematic uncertainty model.

2287 The SM  $t\bar{t}$  background is again simulated at NLO in QCD with the  $h\nu q$  process  
2288 from the MC generator package POWHEG v2 and interfaced to PYTHIA 8 for show-  
2289 ering. Equivalent settings as in Sec. 5.2.1 and Sec. 6.4, corresponding to the CMS  
2290 defaults, have been used. To achieve the necessary precision, the NLO simulation is  
2291 reweighted to higher orders in both QCD and electroweak (EW) processes, which is  
2292 described in Sec. 7.3.

Trigger	Year	Lepton $p_T$ requirement
single-e	2016	e ( $p_T > 27 \text{ GeV}$ )
	2017	e ( $p_T > 35 \text{ GeV}$ )
	2018	e ( $p_T > 32 \text{ GeV}$ )
single- $\mu$	2016	$\mu$ ( $p_T > 24 \text{ GeV}$ )
	2017	$\mu$ ( $p_T > 27 \text{ GeV}$ )
	2018	$\mu$ ( $p_T > 24 \text{ GeV}$ )
ee	all	e ( $p_T > 12 \text{ GeV}$ ) and $\mu$ ( $p_T > 23 \text{ GeV}$ ) or e ( $p_T > 23 \text{ GeV}$ ) and $\mu$ ( $p_T > 8 \text{ GeV}$ )
ee	all	e ( $p_T > 23 \text{ GeV}$ ) and e ( $p_T > 12 \text{ GeV}$ )
$\mu\mu$	all	$\mu_1$ ( $p_T > 17 \text{ GeV}$ ) and $\mu_2$ ( $p_T > 8 \text{ GeV}$ )

Table 7.1: **Trigger  $p_T$  thresholds.** Overview of the used triggers in the three data taking years, as well as their lepton  $p_T$  thresholds.

2293 In addition, several minor backgrounds are included, a summary of which can be  
 2294 found in Tab. 7.2. Of note here is the Z+jets background, which is simulated at  
 2295 NNLO in QCD using the MiNNLO method in POWHEG v2 [192, 193]. It was found  
 2296 here that the higher-order corrections are relevant to the analysis especially for low  
 2297 values of the invariant dilepton mass  $m_{\ell\ell}$ . Most processes are normalized to cross  
 2298 sections predicted at higher orders of QCD where available, which can be found in  
 2299 Tab. 7.3.

2300 **Signal simulation** The signal for the general A/H model described in Sec. 7.1  
 2301 is generated at LO in QCD using MG5\_AMC@NLO with a custom Universal  
 2302 FeynRules Output (UFO) model. The  $pp \rightarrow A/H \rightarrow t\bar{t}$  resonance and the A/H-SM  
 2303 interference are simulated separately, and both are again showered with PYTHIA 8.  
 2304 In order to cover the phase space of the A/H model, the signals are generated for  
 2305 all combinations of the following values of the A/H masses and widths:

$$\begin{aligned}
 m_{A/H} &\in \{365, 400, 500, 600, 800, 1000\} \text{ GeV} \\
 \Gamma_{A/H}/m_{A/H} &\in \{2.5, (5), 10, 25\} \%
 \end{aligned} \tag{7.1}$$

2306 Samples with a width of 5%, indicated by the bracket, were generated only for a  
 2307 mass of 400 GeV, which leads to 38 signal points total. In addition, samples for the  
 2308 pseudoscalar case only were generated with

$$m_A \in \{450, 550, 700, 900\} \text{ GeV}, \quad \Gamma_A/m_A = 9\%. \tag{7.2}$$

2309 All of these samples were combined and reweighted at matrix element level to  
 2310 obtain phase space points between these mass and width values, as described further

Process	QCD order	ME Generator
$t\bar{t}$	NLO	POWHEG v2 (hvq)
$tW$	NLO	POWHEG v2 (ST_wtch)
$Z/\gamma^* + \text{jets}$	NNLO	POWHEG v2 (Zj MiNNLO)
$t$ -channel single top	NLO	POWHEG v2 (ST_tch) + MADSPIN
$s$ -channel single top	NLO	MG5_AMC@NLO
$t\bar{t}W$	NLO	MG5_AMC@NLO
$t\bar{t}Z$	NLO	MG5_AMC@NLO
WW, WZ & ZZ	LO	PYTHIA 8.2
A/H signal	LO	MG5_AMC@NLO
$\eta_t$ signal	LO	MG5_AMC@NLO

Table 7.2: **Simulated background and signal samples.** An overview of the different background and signal processes considered, as well as the theoretical order in QCD and the ME generator used to simulate them. For all samples, PYTHIA 8.2 is used for showering and hadronization.

Process	Cross section (pb)	Order	Program / reference
$t\bar{t}$	833.9	NNLO+NNLL	Top++ [134]
$tW$	71.7	NNLO (approx.)	[138]
$t$ -channel single top	217.0	NLO	Hathor [194, 195]
$s$ -channel single top	10.3	NLO	Hathor [194, 195]
$t\bar{t}W$	0.64	NLO	MG5_AMC@NLO
$t\bar{t}Z$	0.75	NLO	MG5_AMC@NLO
$Z/\gamma^* + \text{jets} \rightarrow \ell\ell, m_{\ell\ell} > 10 \text{ GeV}$	$24.7 \times 10^3$	NNLO	FEWZ [196, 197]
WW	118.7	NNLO	[198]
WZ	471.3	NLO	MCFM [199]
ZZ	165.2	NLO	MCFM [199]

Table 7.3: **Cross sections for background processes.** The cross sections used for the normalization of background processes, as well as the orders in QCD at which they were computed. Where applicable, cross sections are given as the sum of the process and its charge conjugate.

2311 in Sec. 7.4.

2312 Furthermore, signal samples for possible  $t\bar{t}$  bound state effects are generated us-  
2313 ing the color-singlet  $\eta_t$  and  $\chi_t$  models as defined in Sec. 2.2.3, using custom UFO  
2314 models implemented in MG5\_AMC@NLO and again showered with PYTHIA. The  
2315 branching ratio of  $W \rightarrow \ell\nu$  is taken to be 11.1%, corresponding to the default value  
2316 used by MG5\_AMC@NLO.

2317 For all signal and background samples, the detector response is simulated with  
2318 GEANT 4 and the full CMS simulation and reconstruction chain as described in  
2319 Sec. 3.6 is performed.

## 2320 7.2.2 Object definition

2321 **Leptons** All electrons and muons are required to have  $p_T > 20\text{ GeV}$  and  $|\eta| < 2.4$ .  
2322 Similar to Sec. 5.2.2, electrons in the transition region between barrel and endcaps  
2323 in the ECAL, corresponding to  $1.44 < |\eta_{\text{SC}}| < 1.57$ , are removed, and additional ID  
2324 criteria are applied for both types of leptons.

2325 For electrons, the multivariate classifier (MVA)-based ID described in Ref. [111] is  
2326 used at a working point giving 90 % background rejection. This ID already includes  
2327 an isolation requirement as part of the MVA training, and no further requirement  
2328 is applied.

2329 For muons, the same cut-based ID from Ref. [139] as in Sec. 5.2.2, also at the tight  
2330 working point, is used, and the same  $I_{\text{rel}}$  requirement using a cone size of  $\Delta R < 0.4$   
2331 is applied in addition.

2332 **Jets** Jets are again reconstructed using the anti- $k_T$  algorithm [122] with a distance  
2333 parameter of 0.4. They are required to fulfill  $p_T > 20\text{ GeV}$ ,  $|\eta| < 2.4$ , and have a  
2334 minimum distance of  $\Delta R > 0.4$  from all leptons passing the above criteria in the  
2335 event. The Charged Hadron Subtraction (CHS) method [120] is used to remove  
2336 hadrons that originate from pileup from the jet clustering.

2337 Additional ID criteria are applied to reject jets originating in detector noise and  
2338 reconstruction failures [97]. They consist of requirements on the multiplicities of  
2339 the different jet constituents (charged hadrons, neutral hadrons, and electrons or  
2340 photons) as well as their energy fractions relative to the total jet energy. The  
2341 required values are centrally provided depend on the jet  $|\eta|$  as well as on the analysis  
2342 era. In total, a genuine jet efficiency of about 99 % is achieved, while about 99.9 %  
2343 of noise jets are rejected in the relevant  $|\eta|$  range [97].

2344 The DEEPJET algorithm [123], same as in Sec. 5.2.2, is used to identify jets  
2345 originating from the showering and hadronization of b quarks. The medium working  
2346 point of DEEPJET in CMS is chosen, which has a b jet identification efficiency of  
2347 77 %, as well as a misidentification rate of 15 % for c quark jets and of 2 % for light  
2348 quark and gluon jets [140].

**Missing transverse momentum** In the dileptonic decay of  $t\bar{t}$ , the two neutrinos cannot be measured experimentally, and escape the detector unseen. However, their presence can be inferred from momentum conservation: In a proton-proton collision, the longitudinal component of the incoming partons in the hard scattering process is unknown, while the transverse component can be assumed to be close to zero. Thus, the missing transverse momentum  $\vec{p}_T^{\text{miss}}$  can be inferred as the negative vectorial sum of all reconstructed objects (jets, leptons and photons) [124]. As with the jets, hadrons likely to originate from pileup are removed from the calculation of  $\vec{p}_T^{\text{miss}}$  using the CHS method [120]. Along with the leptons and jets,  $\vec{p}_T^{\text{miss}}$  will be used to reconstruct the  $t\bar{t}$  system.

### 7.2.3 Event selection

Events are selected with exactly two leptons of opposite electric charge and sorted into three channels ( $ee$ ,  $e\mu$  and  $\mu\mu$ ) by lepton flavor, similar to Sec. 5.2.3. The two leptons need to fulfill  $p_T > 25 \text{ GeV}$  and  $p_T > 20 \text{ GeV}$  for the leading and subleading lepton, respectively, and their invariant mass is required to be  $m_{\ell\ell} > 20 \text{ GeV}$  in order to reject background from  $\gamma^* + \text{jets}$  production and low-mass resonances.

In all channels, at least two jets with  $p_T > 30 \text{ GeV}$  are required, of which at least one needs to be b-tagged. Furthermore, in the same-flavor lepton channels ( $ee$  and  $\mu\mu$ ), additional cuts are applied to reject  $Z + \text{jets}$  background: Events with  $|m_{\ell\ell} - m_Z| < 15 \text{ GeV}$ , i.e. close to the  $Z$  boson mass peak, are discarded (again just as in Sec. 5.2.3), and the magnitude of the missing transverse momentum is required to be  $p_T^{\text{miss}} > 40 \text{ GeV}$ .

The effect of all selection cuts is summarized in Tab. 7.4.

### 7.2.4 Experimental corrections

Similar as in Sec. 5.3, several corrections are applied to the MC simulation in order to achieve good agreement with the data. In contrast to the  $t\bar{t}$  cross section measurement, where most of these corrections were derived as part of this work, many of the experimental corrections used in this chapter were provided centrally by the CMS collaboration. These will only be described very briefly; more details can be found in the associated references.

**Trigger scale factors** The selection efficiency of the triggers from Tab. 7.1 needs to be corrected in simulation to the one measured in data. This is done via scale factors, which were centrally derived by CMS as a function of the  $p_T$  of the two leptons using the so-called cross-trigger method: Events are selected using a different set of triggers - here, a combination of jet and  $p_T^{\text{miss}}$  triggers - which is assumed to be fully orthogonal to the lepton triggers used for the main selection. Thus, the event sample is unbiased with respect to the lepton triggers, and the lepton trigger

Cut	Data yield/ $10^3$			$t\bar{t} \rightarrow \ell\ell$ MC	
	ee	e $\mu$	$\mu\mu$	efficiency (%)	purity (%)
Triggers	3504932			64.4	0.4
Two OC leptons	65589	2240	108363	20.6	1.4
Lepton $p_T$	65189	2169	106112	20.3	1.4
$m_{\ell\ell} > 20$ GeV	64746	2081	103276	19.8	1.4
Z window (ee/ $\mu\mu$ )	5795	2081	9367	17.6	12.7
At least 2 jets	1235	1287	1947	15.4	43.2
Jet $p_T$	644	999	985	12.9	59.2
At least one b tag	319	853	489	11.7	84.6
$p_T^{\text{miss}}$ (ee/ $\mu\mu$ )	234	853	354	10.7	88.9

Table 7.4: **Selection cuts and event yields.** The data yield in all analysis eras after successively applying all selection cuts, separately for the three lepton flavor channels. The second-to-last column shows the selection efficiency of  $t\bar{t} \rightarrow \ell\ell$  events ( $\ell = e, \mu, \tau$ ), and the last column shows the purity, defined as the fraction of  $t\bar{t} \rightarrow \ell\ell$  events and total event yield. Both efficiency and purity are evaluated using simulation.

efficiency can be measured as the fraction of the events who pass the lepton triggers in addition to the jet/ $p_T^{\text{miss}}$  triggers. This is done independently for all data taking years. The resulting scale factor can differ from unity by up to 5 % for leptons with  $p_T \approx 20$  GeV and less then 1 % for higher  $p_T$  values.

**Lepton scale factors** Differences in the efficiency for a lepton to pass the identification and isolation criteria as defined in Sec. 7.2.2 are measured using the tag-and-probe method, as in Sec. 5.3, and applied to simulation using scale factors binned in  $p_T$  and  $|\eta|$  of the lepton. The scale factor typically differs from unity by about 1-5 %, with the magnitude increasing for high  $|\eta|$ . For more details on this method see Refs. [111, 139].

**Pileup reweighting** In contrast to the data-driven reweighting method used for the inclusive  $t\bar{t}$  cross section measurement (Sec. 5.3), the mean number of pileup interactions per bunch crossing in simulation is reweighted to year-dependent distributions provided centrally by CMS. These have been derived from measurements of the instantaneous luminosity combined with a total inelastic proton-proton cross section of 69.2(32) mb at  $\sqrt{s} = 13$  TeV [98].

**Jet energy and  $p_T^{\text{miss}}$  corrections** The difference in the jet energy response of the detector (JES) as well as the jet energy resolution (JER) in data and simulation was corrected in the same way as described in Sec. 5.3, using centrally derived jet

energy corrections (JECs) as described in Ref. [141]. These corrections are further propagated to the calculation of  $\vec{p}_T^{\text{miss}}$  [124]. Possible additional corrections to the  $x$  and  $y$  components of  $\vec{p}_T^{\text{miss}}$  were investigated, but found to not be required for good description of the observables considered in this analysis.

**b-tagging scale factors** The identification efficiency of the DEEPJET b-tagging algorithm was calibrated using events with jets containing a muon, likely originating from the semileptonic decay of a B hadron, following the methodology described in Ref. [140]. Note that the calibration done on dileptonic  $t\bar{t}$  events presented in the same reference is not used as an input here, since it was derived in part on the same data set and would thus lead to double-counting. However, similar to the discussion in Sec. 5.6, it is expected that the b-tagging efficiency will be constrained from the data during the likelihood fit.

**ECAL L1 pre-firing** In the 2016 and 2017 data-taking years, the L1 trigger of the electromagnetic calorimeter was affected by a gradual shift in the timing of the inputs in the forward region ( $|\eta| > 2.0$ ) [117]. This effect, called L1 pre-firing, is corrected for using simulation scale factors computed from data.

**Z+jets background normalization** In the same-flavor lepton channels (ee and  $\mu\mu$ ), Z+jets events constitute a minor but important background. Since this analysis is sensitive to small shape effects, it is necessary to precisely model this background both in shape and normalization. An NNLO Monte Carlo simulation (see Tab. 7.2) is used for this purpose, which generates up to two additional partons (including b quarks) in the final state, as required by the event selection of at least two jets and at least one b tag. Still, in order to be certain of the Z+jets rate, the same data-driven estimation as presented in Sec. 5.3.2, using a control region with  $|m_{\ell\ell} - m_Z| < 15 \text{ GeV}$  and a sideband with zero b-tagged jets, is performed. The resulting ratios of Z+jets yields compared to the prediction of the original simulation can be found in Tab. 7.5.

	2016pre	2016post	2017	2018
ee	$0.96 \pm 0.010$	$0.97 \pm 0.008$	$0.87 \pm 0.006$	$0.88 \pm 0.005$
$e\mu$	$0.96 \pm 0.007$	$0.97 \pm 0.005$	$0.88 \pm 0.004$	$0.89 \pm 0.003$
$\mu\mu$	$0.96 \pm 0.009$	$0.97 \pm 0.006$	$0.90 \pm 0.005$	$0.90 \pm 0.004$

**Table 7.5: Z+jets scale factors.** Ratio of the Z+jets event yields estimated in data using the method described in Sec. 5.3.2 to the prediction by the MC simulation for the four data-taking periods. The results in the  $e\mu$  channel are the geometric means of those in the ee and  $\mu\mu$  channels. Uncertainties are statistical only.

### 2431 7.2.5 Reconstruction of the $t\bar{t}$ system

2432 Having identified the relevant objects - leptons, jets and  $\vec{p}_T^{\text{miss}}$ - in an event, the next  
 2433 step consists of reconstructing the  $t\bar{t}$  system, i.e. the four-momenta of the top and  
 2434 antitop quark. The presence of two neutrinos in dileptonic  $t\bar{t}$  decays, which escape  
 2435 detection except through missing transverse momentum, leads to a significant loss  
 2436 of information. As a result, reconstructing the full event kinematics is non-trivial  
 2437 and requires several assumptions. In this work, a variation of the algorithm first  
 2438 presented in Ref. [200] is used, which is briefly outlined in this section.

2439 The algorithm works in two steps, starting with the assignment of jets to the b  
 2440 and  $\bar{b}$  quarks originating from the  $t\bar{t}$  decay. To do so, pairs of jets are selected from  
 2441 all jets in the event (passing the requirements outlined in Sec. 7.2.2) depending on  
 2442 the number  $n_b$  of b-tagged jets: For events with  $n_b \geq 2$ , all permutations of two  
 2443 b-tagged jets each are considered as candidate pairs, while for events with  $n_b = 1$ ,  
 2444 the candidate pairs are formed by pairing the single b-tagged jet with all other jets  
 2445 in the event.

2446 From these candidates, the best pair is now chosen based on the invariant masses  
 2447  $m_{\ell+b}$  and  $m_{\ell-\bar{b}}$  of the b/ $\bar{b}$  candidate and the corresponding (anti)lepton. First, the  
 2448 expected truth-level distribution of  $m_{\ell b}$  is determined from MC simulation, which  
 2449 can be seen in Fig. 7.1. Then, in each event, the likelihoods to observe the respective  
 2450 values of  $m_{\ell+b}$  and  $m_{\ell-\bar{b}}$  for each candidate pair are computed from the expected  
 2451 distribution. The candidate pair that maximizes the product of the two likelihoods  
 2452 for  $m_{\ell+b}$  and  $m_{\ell-\bar{b}}$  is chosen for the remainder of the reconstruction.

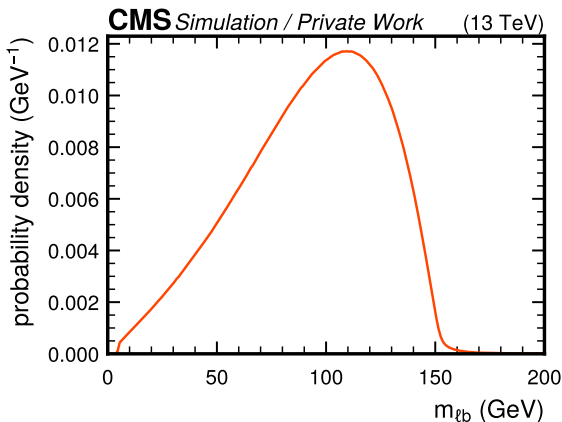


Figure 7.1: **Probability distribution of  $m_{\ell b}$ .** The truth-level probability distribution of  $m_{\ell b}$ , as calculated from  $t\bar{t}$  MC simulation and used for assigning the b/ $\bar{b}$  candidates as well as for the weighted average over the smeared solutions. *Figure reproduced from Ref. [190].*

2453 Next, the four-momenta of the top and antitop quark are reconstructed using the

2454 momentum conservation equations. That is, one demands

$$\begin{aligned} p_t &= p_{W^+} + p_b = p_{\ell^+} + p_{\nu_\ell} + p_b \\ p_{\bar{t}} &= p_{W^-} + p_{\bar{b}} = p_{\ell^-} + p_{\bar{\nu}_\ell} + p_{\bar{b}} \end{aligned} \quad (7.3)$$

2455 where all variables are understood as four-momenta. The lepton and b-quark  
 2456 momenta are experimentally measured, while the neutrino momenta are unknowns.  
 2457 Demanding them to be massless, i.e.  $p_{\nu_\ell}^2 = p_{\bar{\nu}_\ell}^2 = 0$ , yields the six components of the  
 2458 two neutrino three-momenta as free parameters.

2459 To resolve the ambiguities, several assumptions need to be made. First, it is  
 2460 assumed that all of the missing transverse momentum in the event stems from the  
 2461 neutrinos, i.e.

$$p_{\nu_\ell,x} + p_{\bar{\nu}_\ell,x} = p_x^{\text{miss}}, \quad p_{\nu_\ell,y} + p_{\bar{\nu}_\ell,y} = p_y^{\text{miss}} \quad (7.4)$$

2462 Additionally, it is assumed that both the top quarks and W bosons are exactly  
 2463 on-shell, that is

$$p_{W^+}^2 = m_W^2, \quad p_{W^-}^2 = m_W^2 \quad (7.5)$$

2464 and

$$p_t^2 = m_t^2, \quad p_{\bar{t}}^2 = m_t^2 \quad (7.6)$$

2465 where  $m_t$  and  $m_W$  are the pole masses of the top quark and W boson, respectively.  
 2466 Applying these six constraints leads to a system of quartic equations for the neutrino  
 2467 three-momenta  $\vec{p}_{\nu_\ell}$  and  $\vec{p}_{\bar{\nu}_\ell}$ , which was solved in Ref. [201]. From these, the top and  
 2468 antitop quark four-momenta can then be calculated. Since the quartic equation  
 2469 can in general have up to four solutions, the solution with the lowest value of the  
 2470 invariant  $t\bar{t}$  mass  $m_{t\bar{t}}$  is chosen. This was found in Ref. [202] to minimize the bias  
 2471 in  $m_{t\bar{t}}$  especially for low- $m_{t\bar{t}}$  events.

2472 In practice, however, this method will often not give a solution even for those b  
 2473 jets which are correctly assigned to the truth-level b quarks. This is because the  
 2474 experimental inputs to the method - the jet and lepton four-momenta as well as  
 2475  $\vec{p}_T^{\text{miss}}$  - will deviate from their truth-level values within the experimental resolution  
 2476 of the detectors and object reconstruction. In addition, the constraints will not  
 2477 be fulfilled exactly: There might be additional  $p_T^{\text{miss}}$  in the event because of e.g.  
 2478 neutrinos produced in  $\tau$  lepton or B hadron decays, and the W bosons and top  
 2479 quarks might be off-shell with respect to their pole masses within their respective  
 2480 widths.

2481 To alleviate this, several of the input variables are randomly smeared to model  
 2482 the experimental resolution. For both the b jets and leptons, the energies are varied  
 2483 while keeping their masses constant, and the directions of their three-momenta are

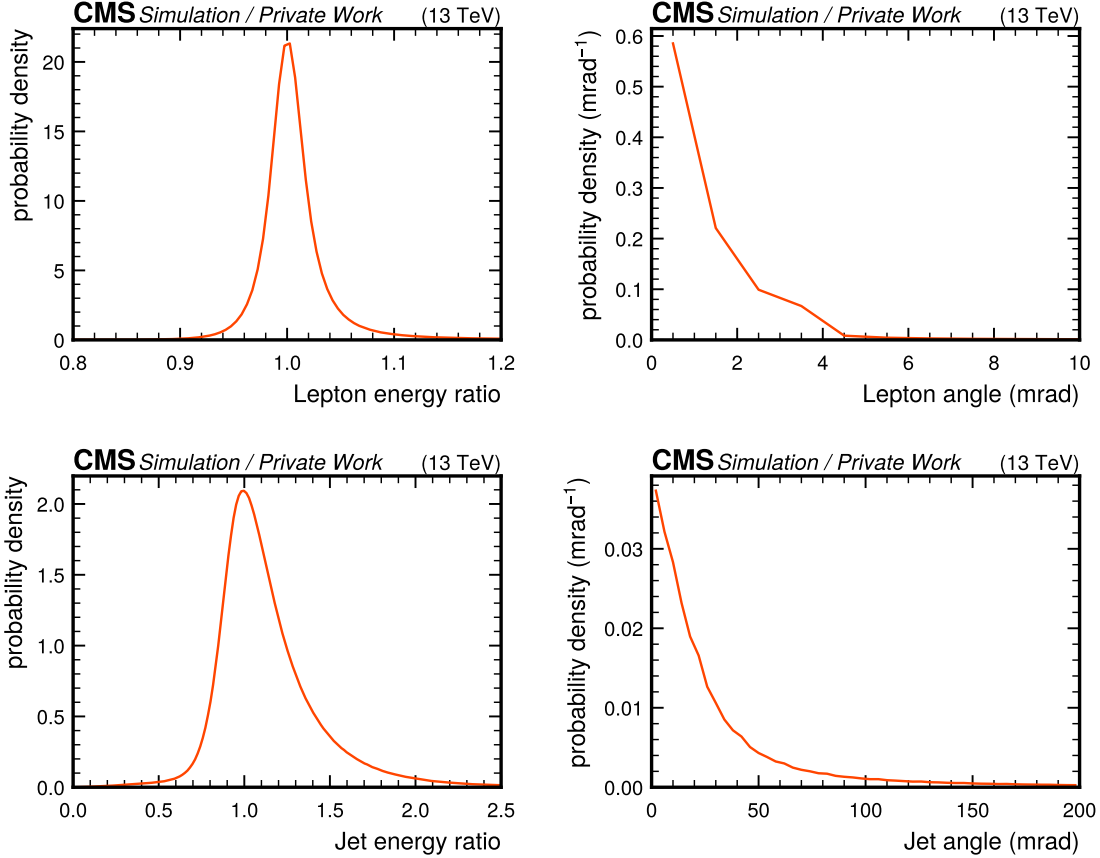


Figure 7.2: **Probability distributions used in the smearing of jets and leptons.** The probability distributions for the ratio of measured and truth-level energies (left) as well as the angular difference between measured and truth-level three-momenta (right) for leptons (top) and jets (bottom). All distributions were calculated using  $t\bar{t}$  MC simulation. *Figure reproduced from Ref. [190].*

varied in a uniformly random direction. For both of these cases, the variations are randomly sampled from distributions obtained by comparing the measured and truth-level four-momentum in the nominal  $t\bar{t}$  MC simulation, as shown in Fig. 7.2. The smearing of the jets is also propagated to the calculation of  $\vec{p}_{T\text{miss}}^{\text{miss}}$ . Additionally, the values of  $m_W$  used for the constraints on  $p_{W+}$  and  $p_{W-}$  are randomly sampled from a relativistic Breit-Wigner distribution corresponding to the W boson width  $\Gamma_W$ . This smearing procedure is repeated 100 times per event with different random values, resulting in up to 100 reconstructed  $t\bar{t}$  systems per event, depending on the number of cases where there is no real solution.

Finally, one unambiguous solution per event is constructed by again using the

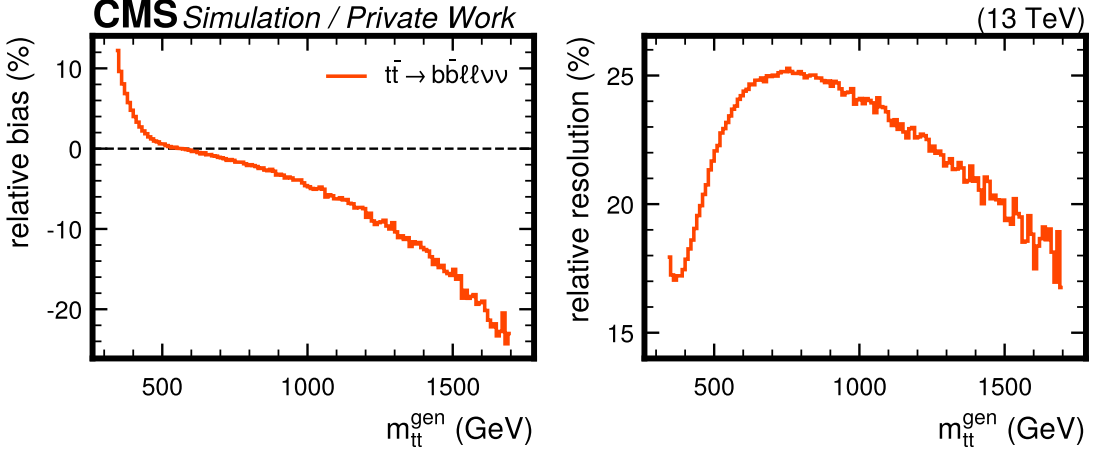


Figure 7.3: **Bias and resolution of  $m_{t\bar{t}}$ .** Relative bias and resolution of the  $t\bar{t}$  reconstruction algorithm, defined in Eq. (7.8), as a function of truth-level  $m_{t\bar{t}}$  and evaluated in MC simulation of dileptonic  $t\bar{t}$ .

invariant lepton-b quark masses and their truth-level likelihoods. For each iteration of the smearing procedure that yielded a real solution, a weight is defined as the product of the likelihoods for obtaining the smeared values of  $m_{\ell+b}$  and  $m_{\ell-\bar{b}}$ , i.e.

$$w = \mathcal{P}(m_{\ell+b}) \cdot \mathcal{P}(m_{\ell-\bar{b}}) \quad (7.7)$$

The final solution for the reconstructed top and antitop four-momenta is defined as the weighted average over all real solutions, using the weight as given in Eq. (7.7).

For  $t\bar{t} \rightarrow b\bar{b}\ell\ell\nu\nu$  events passing all previous selection steps, the efficiency of the full reconstruction algorithm is ca. 90%, as evaluated in MC simulation. To assess the accuracy of the reconstruction relative to the truth-level top quarks, defined after parton showering, a per-event relative deviation is defined as

$$\Delta m_{t\bar{t}} = \frac{m_{t\bar{t}}^{\text{reco}} - m_{t\bar{t}}^{\text{gen}}}{m_{t\bar{t}}^{\text{gen}}}, \quad (7.8)$$

where  $m_{t\bar{t}}^{\text{reco}}$  and  $m_{t\bar{t}}^{\text{gen}}$  stand for the reconstructed and truth-level  $m_{t\bar{t}}$ , respectively. The mean and standard deviation of  $\Delta m_{t\bar{t}}$  are then the relative bias and resolution of the reconstruction algorithm. They are evaluated in simulation of dileptonic  $t\bar{t}$  and shown in Fig. 7.3 as a function of truth-level  $m_{t\bar{t}}$ . The method shows a bias towards high  $m_{t\bar{t}}$  for events with  $m_{t\bar{t}}^{\text{gen}} \lesssim 500$  GeV and towards low  $m_{t\bar{t}}$  for  $m_{t\bar{t}}^{\text{gen}} \gtrsim 600$  GeV, with resolutions in the range of 17 – 25%. It should be noted here that this bias relative to the truth level is by itself not problematic, since it is expected to be the same in both simulation and data and e.g. no unfolding of the reconstructed distributions to the truth level is attempted.

### 2512 7.2.6 Sensitive observables

2513 To extract the A/H and  $\eta_t$  signals from the background, three sensitive observables  
2514 are considered. The first is simply the invariant  $t\bar{t}$  mass  $m_{t\bar{t}}$ , defined with the  
2515 reconstruction procedure as explained in the last section. As shown in Fig. 2.7,  
2516 an A/H signal is expected to result in a peak-dip structure in  $m_{t\bar{t}}$  around the SM  
2517 background, where the zero crossing between peak and dip should be in the vicinity  
2518 of the A/H mass, and the magnitude as well as ratio of the peak and the dip  
2519 depends non-linearly on the coupling modifier. The  $\eta_t$  signal, on the other hand, is  
2520 expected to peak slightly below the  $t\bar{t}$  production threshold at  $m_{t\bar{t}} \simeq 2m_t - 2$  GeV  
2521 as discussed in Sec. 2.2.3 and shown in Fig. 2.5. In practice, due to the limited  
2522 detector resolution, the exact position of this peak will not be observable, and the  
2523 signal will result in a generic enhancement of the yield for very low values of  $m_{t\bar{t}}$ .

2524 In addition, the two spin correlation observables  $c_{\text{hel}}$  and  $c_{\text{han}}$ , as defined in  
2525 Eq. (2.4) and Eq. (2.10), are used to gain further sensitivity. Both variables are  
2526 again defined using the  $t\bar{t}$  system reconstruction as described in the previous sec-  
2527 tion. As discussed in Sec. 2.2.2, they are ideal for separating spin-singlet and spin-  
2528 triplet states, respectively. Thus, A and  $\eta_t$  signals, producing singlet states, will  
2529 have enhanced contributions at high values of  $c_{\text{hel}}$ , while H signals, producing  ${}^3P_0$   
2530 triplet states, will be enhanced at low values of  $c_{\text{han}}$ . This allows not only for better  
2531 discrimination between signal and background, but also to probe the  $\mathcal{CP}$  structure  
2532 of a possible observed signal.

2533 To combine all three variables, three-dimensional templates are created with  $20 \times$   
2534  $3 \times 3$  bins in the three observables  $m_{t\bar{t}}$ ,  $c_{\text{hel}}$  and  $c_{\text{han}}$ . For  $m_{t\bar{t}}$ , an irregular binning  
2535 is chosen to account for the decrease in production cross section at high values. An  
2536 example can be seen in Fig. 7.4 for SM  $t\bar{t}$  and three different signals (A, H and  $\eta_t$ ).

## 2537 7.3 Higher-order corrections in $t\bar{t}$

2538 In this analysis, the SM  $t\bar{t}$  background is irreducible - after all, it leads to the exact  
2539 same final state as the signal. As a result, it is crucial to model it as precisely as  
2540 possible: a mismodeling of the  $t\bar{t}$  kinematic distribution, especially in  $m_{t\bar{t}}$ , might  
2541 otherwise be confused for a signal and lead to bias.

2542 The MC simulation used for the SM  $t\bar{t}$  background is performed at NLO in QCD  
2543 using the POWHEG v2 subprocess `hvq`, as studied also in Chapter 6. On top of  
2544 this, two different sets of corrections are applied to include missing higher orders,  
2545 namely NNLO QCD and NLO electroweak (EW) corrections. Both of these are  
2546 estimated by comparing the MC simulation, which is matched to a parton shower,  
2547 to fixed-order predictions. The simulation is then reweighted using scale factors  
2548 binned two-dimensionally in  $m_{t\bar{t}}$  and  $\cos\theta_t^*$ , where the latter is the cosine of the  
2549 scattering angle of the top quark to the beam axis in the  $t\bar{t}$  rest frame. These two

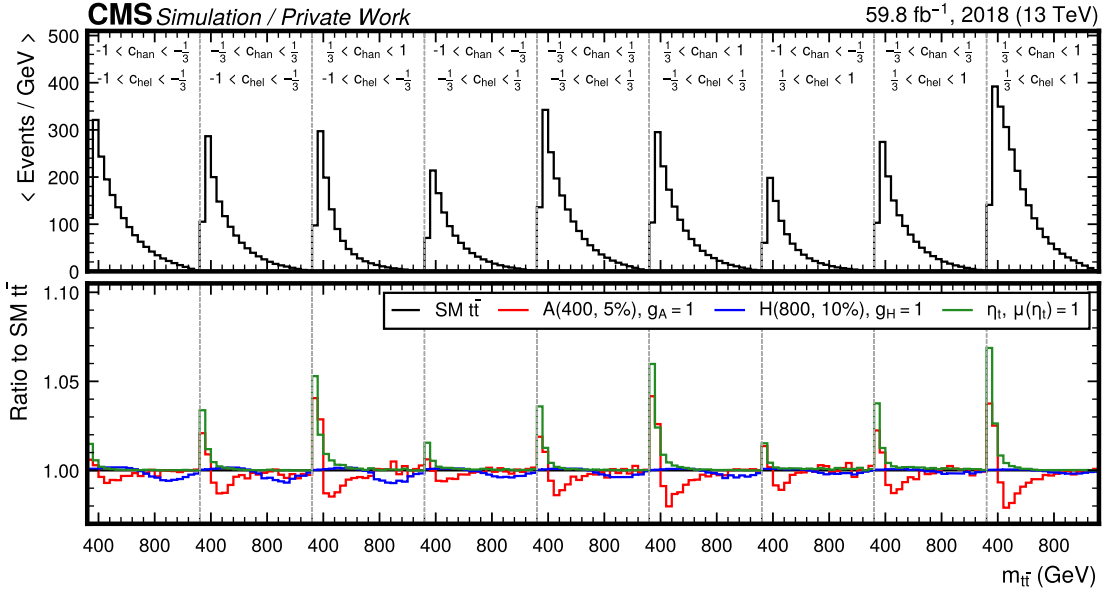


Figure 7.4: **3D template for  $m_{t\bar{t}} \times c_{\text{hel}} \times c_{\text{han}}$**  for SM  $t\bar{t}$  (top) as well as three different example signals (bottom, shown as the ratio to SM  $t\bar{t}$ ), corresponding to the luminosity taken in 2018 only.

variables fully define the kinematics of the top quarks in the  $t\bar{t}$  rest frame, save for FSR emissions.

### 7.3.1 NNLO QCD corrections

The NNLO QCD predictions are obtained with the program MATRIX [137]. They are computed at the level of stable top quarks with a dynamic scale choice of  $\sqrt{m_t^2 + p_{T,t}^2}$ , where  $p_{T,t}$  is the top quark transverse momentum. Fig. 7.5 shows the resulting effect on the 3D  $m_{t\bar{t}} \times c_{\text{hel}} \times c_{\text{han}}$  distribution at the detector level as the black line. They are on the order of 1 – 2%.

### 7.3.2 NLO EW corrections

The NLO corrections in the electroweak coupling  $\alpha_{\text{EW}}$  are computed with the HATHOR code [194, 203–205] using the same nominal scale choices. Of particular interest here is a class of diagrams which contain an exchange of a virtual SM Higgs boson, an example of which is seen in Fig. 7.6. The matrix element for this diagram is proportional to the square of the SM Higgs-top Yukawa coupling  $y_t$ , giving a  $y_t^2$ -dependent correction to  $t\bar{t}$  distributions from the interference with LO diagrams. This correction is sizable mostly for low  $m_{t\bar{t}}$  values, and is important for this analysis because the SM Higgs exchange might change the  $t\bar{t}$  spin state and thus

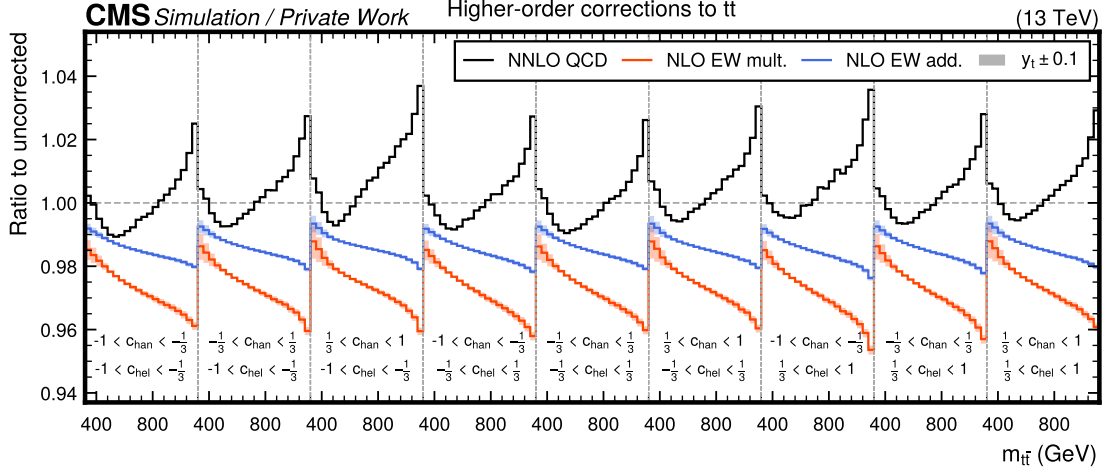


Figure 7.5: **Effect of NNLO QCD and NLO EW corrections** on the 3D  $m_{t\bar{t}} \times c_{\text{hel}} \times c_{\text{han}}$  distribution after reconstruction in the form of ratios to the uncorrected distributions. The NNLO QCD corrections are shown as the solid black line, while the NLO EW corrections are shown in orange for the multiplicative scheme and in blue for the additive scheme. The effect of varying  $y_t$  by  $\pm 0.1$  in the NLO EW corrections is shown as the shaded bands.

2567  $c_{\text{hel}}$  and  $c_{\text{han}}$ . To accurately account for this, the correction is derived separately for  
2568 the different initial states ( $gg$ ,  $q\bar{q}$  and  $gq$ ) of  $t\bar{t}$  production.

2569 The results obtained with HATHOR are accurate only to LO in  $\alpha_S$ , i.e.  $\mathcal{O}(\alpha_S^2)$ ,  
2570 and as of the time of writing no full calculation including both NLO QCD and EW  
2571 effects exists. Thus, there is an ambiguity on how the NLO-accurate (in QCD) MC  
2572 simulation and the NNLO-accurate corrections presented in the previous section  
2573 should be combined with the EW corrections.

2574 Formally, the differential cross section as predicted by Powheg can be decomposed  
2575 as

$$d\sigma_{\text{POWHEG}} = \alpha_S^2 d\sigma_{\text{LO}} + \alpha_S^3 d\sigma_{\text{NLO}} \quad (7.9)$$

2576 where additional terms beyond  $\mathcal{O}(\alpha_S^3)$  due to additional radiation in Powheg and  
2577 Pythia are not written for simplicity. On the other hand, HATHOR predicts

$$d\sigma_{\text{HATHOR}} = \alpha_S^2 d\sigma_{\text{LO}} + \alpha_S^2 \alpha_{\text{EW}} d\sigma_{\text{EW}}. \quad (7.10)$$

2578 One possible way to combine the calculations is the additive scheme, given by

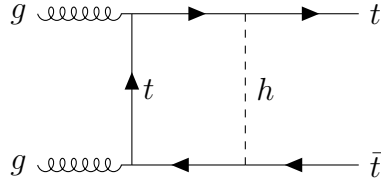


Figure 7.6: **EW correction involving a SM Higgs boson.** An example Feynman diagram for NLO EW corrections to  $t\bar{t}$  production involving the exchange of a virtual SM Higgs boson  $h$ .

$$\begin{aligned} d\sigma_{\text{add.}} &= d\sigma_{\text{POWHEG}} + d\sigma_{\text{HATHOR}} - \alpha_S^2 d\sigma_{\text{LO}} \\ &= \alpha_S^2 d\sigma_{\text{LO}} + \alpha_S^3 d\sigma_{\text{NLO}} + \alpha_S^2 \alpha_{\text{EW}} d\sigma_{\text{EW}} \end{aligned} \quad (7.11)$$

which is formally accurate to  $\mathcal{O}(\alpha_S^3)$  and  $\mathcal{O}(\alpha_S^2 \alpha_{\text{EW}})$ . This approach does not include any cross terms of order  $\mathcal{O}(\alpha_S^3 \alpha_{\text{EW}})$ , which are not fully calculated by either Powheg or HATHOR. However, it is reasonable to assume that these cross terms factorize approximately, leading to the alternative multiplicative scheme [205]

$$\begin{aligned} d\sigma_{\text{mult.}} &= d\sigma_{\text{POWHEG}} \times \frac{d\sigma_{\text{HATHOR}}}{\alpha_S^2 d\sigma_{\text{LO}}} \\ &= \alpha_S^2 d\sigma_{\text{LO}} + \alpha_S^3 d\sigma_{\text{NLO}} + \alpha_S^2 \alpha_{\text{EW}} d\sigma_{\text{EW}} + \alpha_S^3 \alpha_{\text{EW}} \frac{d\sigma_{\text{NLO}} d\sigma_{\text{EW}}}{d\sigma_{\text{LO}}} \end{aligned} \quad (7.12)$$

The difference between the two schemes is in the last term of order  $\mathcal{O}(\alpha_S^3 \alpha_{\text{EW}})$ , which is an approximation to the QCD-EW cross terms. In this work, the multiplicative approach is used for all nominal results, while the difference to the additive approach is included as a systematic uncertainty. In both cases, the needed term  $\alpha_S^2 d\sigma_{\text{LO}}$  is computed with MG5\_AMC@NLO.

The effect of both approaches on the 3D  $m_{t\bar{t}} \times c_{\text{hel}} \times c_{\text{han}}$  distribution at the detector level after parton showering can be seen in Fig. 7.5 for different values of  $y_t$ . The multiplicative scheme leads to a larger correction of roughly 2 – 4%, while the additive scheme only gives 1 – 2%. Notably, the effect of varying  $y_t$  modifies not only the  $m_{t\bar{t}}$  distribution close to the  $t\bar{t}$  threshold, but also the distribution of  $c_{\text{hel}}$ . As a result, such a variation in data could potentially be confused for a pseudoscalar signal. It is thus important to include it as a systematic uncertainty, as described in Sec. 7.5.

## 2596 7.4 Matrix element reweighting for A/H signals

2597 In order to probe the full phase space of the generic A/H model as described in  
 2598 Sec. 7.1, predictions at different A/H masses and widths with a sufficiently small  
 2599 spacing are required so that interpolation between the points is possible. However,  
 2600 generating a separate MC sample for each mass and width point is computationally  
 2601 very expensive.

### 2602 7.4.1 Principle of the method

2603 As an alternative, it is possible to re-use existing samples for different mass and  
 2604 width points via matrix element reweighting. This method works by noting that a  
 2605 given MC sample can be seen as a random sample, drawn from a PDF of the form

$$\mathcal{P}(x_i^{\text{ME}}, x_j^{\text{reco}}) = \mathcal{P}^{\text{ME}}(x_i^{\text{ME}}) \cdot \mathcal{P}^{\text{rem}}(x_j^{\text{reco}} | x_i^{\text{ME}}) \quad (7.13)$$

2606 Here,  $x_i^{\text{ME}}$  are all variables defining the event at the matrix element (ME) level,  
 2607 i.e. at the level of the hard interaction, and  $x_j^{\text{reco}}$  are all variables after detector  
 2608 simulation and object reconstruction. For the case of the A/H signals, which are  
 2609 generated at LO in QCD,  $x_i^{\text{ME}}$  is given fully by the four-momenta and helicities of  
 2610 the final-state particles (leptons, neutrinos and b quarks) in the hard process. The  
 2611  $x_j^{\text{reco}}$  consist of all possible reconstruction-level variables that are relevant to the  
 2612 analysis, such as e.g. jet and lepton four-momenta, lepton identification criteria or  
 2613  $\vec{p}_T^{\text{miss}}$ .

2614  $\mathcal{P}^{\text{ME}}(x_i^{\text{ME}})$  refers to the probability density of the ME-level variables as predicted  
 2615 by the ME generator, which will be proportional to the absolute square of the matrix  
 2616 element. This function will depend on the chosen scenario of the A/H model, i.e.  
 2617  $m_{\text{A}/\text{H}}$  and  $\Gamma_{\text{A}/\text{H}}$ . Meanwhile, the conditional probability density  $\mathcal{P}^{\text{rem}}(x_j^{\text{reco}} | x_i^{\text{ME}})$   
 2618 encodes the effects of all other components of the simulation chain, such as the  
 2619 parton shower, hadronization, detector simulation and reconstruction. It gives the  
 2620 probability to observe reconstruction-level variables  $x_j^{\text{reco}}$  for an event with ME-level  
 2621 variables  $x_i^{\text{ME}}$ .

2622 The principal assumption of the method is now that  $\mathcal{P}^{\text{rem}}$ , and thus the whole  
 2623 simulation chain except for the matrix element, is independent of the underlying  
 2624 A/H signal scenario ( $m_{\text{A}/\text{H}}$  and  $\Gamma_{\text{A}/\text{H}}$ ). This assumption is certainly true for the  
 2625 detector simulation and reconstruction, while care must be taken for the parton  
 2626 shower, which in general needs to be matched to the matrix element and can this  
 2627 way have a residual dependence. The validity of the assumption will be discussed  
 2628 in more detail below.

2629 If the assumption is fulfilled, a given A/H MC sample generated with parameters  
 2630  $m_{\text{A}/\text{H}}^0$  and  $\Gamma_{\text{A}/\text{H}}^0$  can now be reweighted to a different A/H scenario with parameters  
 2631  $\hat{m}_{\text{A}/\text{H}}$  and  $\hat{\Gamma}_{\text{A}/\text{H}}$  by applying to each event  $i$  a weight

$$w_i = \frac{\mathcal{P}^{\text{ME}}(x_i^{\text{ME}} | \hat{m}_{\text{A}/\text{H}}, \hat{\Gamma}_{\text{A}/\text{H}})}{\mathcal{P}^{\text{ME}}(x_i^{\text{ME}} | m_{\text{A}/\text{H}}^0, \Gamma_{\text{A}/\text{H}}^0)} \quad (7.14)$$

2632 The quantities in the denominator and nominator are the ME-level probability  
 2633 densities for each event, evaluated at the original and target A/H parameters, respec-  
 2634 tively. When this weight is inserted into Eq. (7.13), the original probability cancels,  
 2635 giving the correct probability density for the target scenario  $\hat{m}_{\text{A}/\text{H}}$  and  $\hat{\Gamma}_{\text{A}/\text{H}}$ .

2636 In practice, this method will only work if the MC sample used for the reweighting  
 2637 has sufficient phase space overlap with the target A/H scenario, i.e. if the two  
 2638 probabilities in Eq. (7.14) are not too different from each other for the majority of  
 2639 the events. Otherwise, the weights will become very small in some regions of the  
 2640 phase space and very large in others, resulting in poor statistics for the reweighted  
 2641 sample.

2642 The method was implemented by directly evaluating the squared matrix elements  
 2643 for the different A/H hypotheses, using the standalone reweighting interface pro-  
 2644 vided by MG5\_AMC@NLO and the same UFO model as for the signal generation.

#### 2645 7.4.2 Combination of multiple origin samples

2646 For the purpose of this analysis, a set of signal samples for different A/H scenarios  
 2647 (as given in Sec. 7.2.1) was already available at the time of starting these studies.  
 2648 These samples were used as origin samples for the reweighting. In order to maximize  
 2649 the statistics achieved after reweighting for each target A/H scenario, and mitigate  
 2650 problems from poor phase space overlap, a subset of the available samples were  
 2651 combined after reweighting for each target scenario.

2652 This procedure works as follows: First, a set of several origin samples  $j$  with  
 2653 different parameters  $m_{\text{A}/\text{H}}$  and  $\Gamma_{\text{A}/\text{H}}$  are all reweighted separately to the same target  
 2654 parameters  $\hat{m}_{\text{A}/\text{H}}$  and  $\hat{\Gamma}_{\text{A}/\text{H}}$  with per-event weights  $w_{i,j}$  as given in Eq. (7.14). These  
 2655 need to be multiplied with a possible generator weight of the origin sample  $u_{i,j}$ , giving  
 2656 the total per-event weight  $\hat{w}_{i,j} = w_{i,j} u_{i,j}$ . For fully unweighted origin samples,  
 2657  $u_{i,j} = 1$ .

2658 Then, the different samples are again weighted with a per-sample weight  $v_j$  pro-  
 2659 portional to

$$v_j \propto \langle \hat{w}_{i,j} \rangle^{-1} = \frac{\sum_i \hat{w}_{i,j}}{\sum_i \hat{w}_{i,j}^2} \quad (7.15)$$

2660 where the sums run over all events  $i$  in the considered sample  $j$ . This expression is the  
 2661 inverse of the average ME weight for sample  $j$ . It is chosen such that samples with  
 2662 large phase space overlap with the target A/H scenario - and thus small ME weights  
 2663  $w_{i,j}$  - are assigned a large weight  $v_j$  in the combination of samples. Similarly, samples  
 2664 with poor phase space overlap, and thus large average ME weights, get assigned

2665 small weights and contribute less strongly to the combined sample. Finally, the total  
2666 combined sample is normalized to the expected cross section for the target scenario,  
2667 which is calculated independently. It is shown in App. C.1 that this procedure  
2668 minimizes the total statistical error of the combined sample.

2669 In practice, all available masses and parities (A and H) are combined for each tar-  
2670 get A/H mass. Resonance and interference contributions are treated separately from  
2671 each other. Furthermore, it was found that, for the resonance contribution only,  
2672 it is necessary to split the combination of different A/H widths into two halves:  
2673 those with  $\Gamma_{A/H}/m_{A/H}$  less or greater than 10%. This is due to an interplay of  
2674 MG5\_AMC@NLO and the PYTHIA shower leading to a dependency on the A/H  
2675 width in the matrix element, which is not taken into account in the reweighting. For  
2676  $\Gamma_{A/H}/m_{A/H} < 10\%$  (narrow resonance), MG5\_AMC@NLO includes the interme-  
2677 diate A/H particle in the event record, which is then treated by PYTHIA as a unstable  
2678 resonance and its virtuality as predicted by the matrix element is preserved. For  
2679  $\Gamma_{A/H}/m_{A/H} \geq 10\%$  (broad resonance), the A/H particle is not included in the event  
2680 record, and its virtuality is thus not preserved. This leads to slight differences in  
2681 distributions affected by the parton showering. The choice of 10% for the transition  
2682 between the two modes is an arbitrary parameter, and thus not necessarily physical.  
2683 Nonetheless, it was decided in this analysis to not mix the two width ranges in the  
2684 reweighting in order to obtain full closure with a standalone generation.

### 2685 7.4.3 Validation

2686 The combined reweighting is validated for three masses of  $m_{A/H} = 400, 600$  and  $800$   
2687 GeV as well as widths of 2.5 and 10%. For each of these points, the reweighting is  
2688 performed as stated above, but leaving out A/H scenarios with the same mass from  
2689 the combination of origin samples since otherwise the weights would be trivially  
2690 one. The reweighted  $m_{t\bar{t}}$  distributions at generator level are then compared to the  
2691 standalone samples at the same  $m_{A/H}$  and  $\Gamma_{A/H}$ .

2692 The resulting comparisons and residuals can be seen in Fig. 7.7 for A and H,  
2693 separated into the resonance and interference contributions. It can be seen that  
2694 the closure between reweighting and standalone generation is excellent within the  
2695 statistical uncertainties.

## 2696 7.5 Systematic uncertainties

2697 Similar to Sec. 5.5, systematic uncertainties affect the distributions of both SM  
2698 background and signal processes. They are listed in this section, split into theory  
2699 (Sec. 7.5.1) and experimental uncertainties (Sec. 7.5.2).

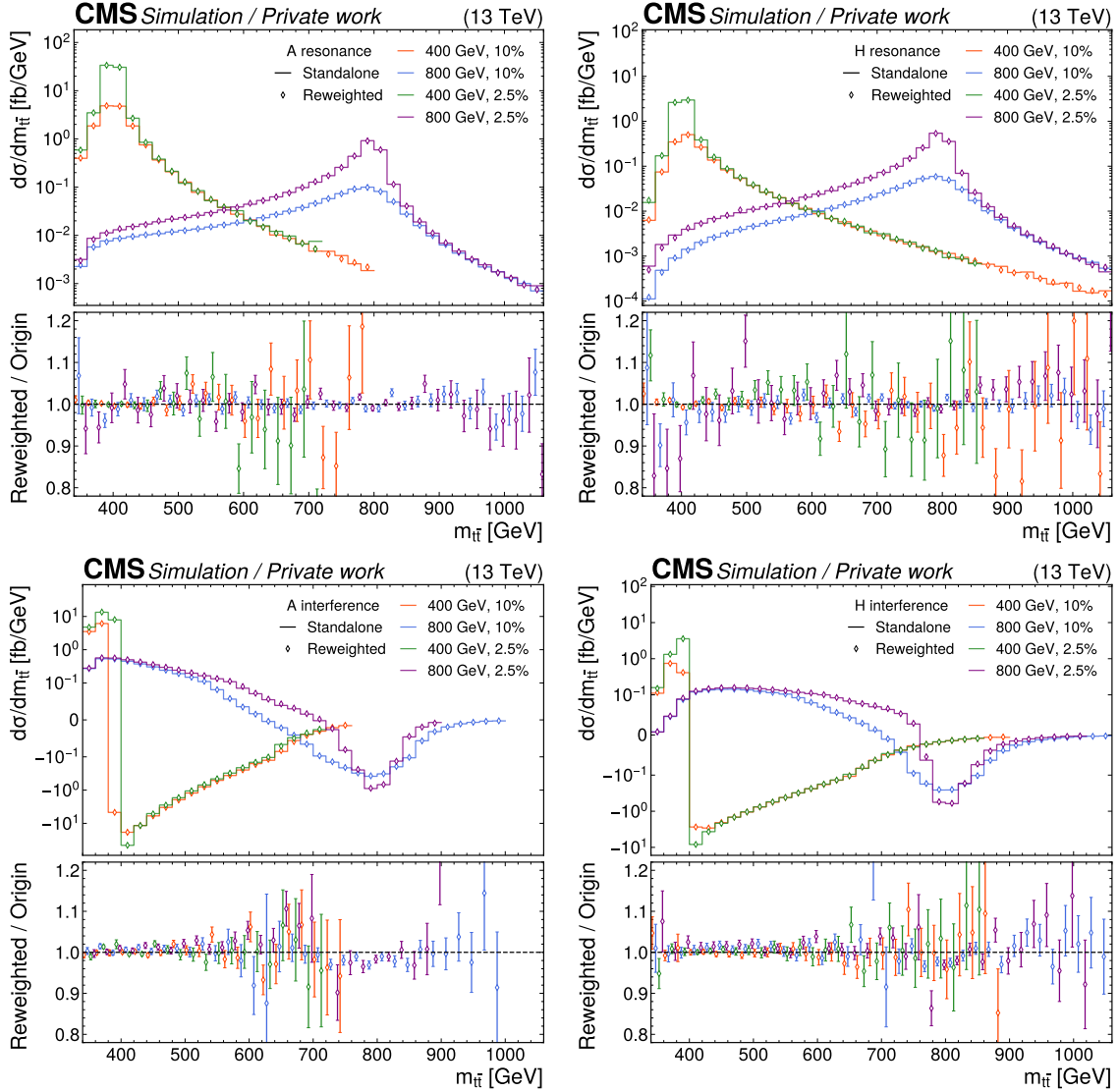


**Figure 7.7: Validation of the ME reweighting.** Comparison of standalone generated (lines) and reweighted (diamond markers)  $m_{t\bar{t}}$  distributions for different values of  $m_{A/H}$  and  $\Gamma_{A/H}$ . From top left to bottom right: A resonance, H resonance, A interference, H interference. The lower panel shows the ratio of reweighted and standalone distributions. The error bars give the combined statistical uncertainty of the reweighted and standalone sample.

### 2700 7.5.1 Theory uncertainties

2701 **Scale uncertainties** Uncertainties due to missing higher orders in the matrix el-  
2702 ement as well as the parton shower are included separately for the SM  $t\bar{t}$ ,  $tW$ , and  
2703  $Z/\gamma^* + \text{jets}$  backgrounds as well as all considered signals by varying the associated  
2704 scales by a factor 2 up and down independently, same as in Sec. 5.5. For  $A$  and  
2705  $H$ , the uncertainties are considered uncorrelated between the resonance and inter-  
2706 ference components, which is found to be conservative. For  $\eta_t$ , the renormalization  
2707 scale uncertainty is not included since the considered model does not encode any  
2708 dependence on either  $\mu_R$  or  $\alpha_S$ .

2709 **PDF uncertainties** For the SM  $t\bar{t}$  background, the uncertainty due to the PDF is  
2710 again included based on the 100 provided eigenvalues of the used NNPDF 3.1 PDF  
2711 set. However, it is not considered sufficient to simply take the envelope of these  
2712 variations since this would distort possible shape variations. Instead, a principal  
2713 component analysis (PCA) is performed on the final 3D  $m_{t\bar{t}} \times c_{\text{hel}} \times c_{\text{han}}$  templates  
2714 obtained from the different eigenvalues, thus finding those linear combinations that  
2715 have a noticeable shape effect. It is found that only the first eigenvector (correspond-  
2716 ing to the largest eigenvalue) is non-negligible, and this variation is considered as  
2717 the PDF uncertainty. For more details on this procedure, see Ref. [190]. Independ-  
2718 ently of this, another uncertainty based on the value of  $\alpha_S$  in the PDF is considered  
2719 similarly to Sec. 5.5.

2720 **EW correction uncertainties** As described in Sec. 7.3.2, two independent un-  
2721 certainties are attached to the NLO electroweak correction of SM  $t\bar{t}$ : First, the  
2722 value of the SM top-Higgs Yukawa coupling is allowed to vary in the range  $y_t =$   
2723  $1.00^{+0.11}_{-0.11}$ , with the range given by the uncertainty of the experimental measurement  
2724 in Ref. [206]. Second, the difference between the additive and multiplicative appli-  
2725 cation scheme (Eqs. (7.11) and (7.12)) is considered as a separate uncertainty, as  
2726 recommended in Ref. [205], and symmetrized around the nominal.

2727 **Top quark mass uncertainty** The top quark mass uncertainty in SM  $t\bar{t}$  is es-  
2728 timated by varying it from its nominal value of  $m_t = 172.5 \text{ GeV}$  by  $\pm 3 \text{ GeV}$  in  
2729 the POWHEG simulation, and then scaling down the resulting relative deviation by  
2730 a factor  $1/3$ , leading to a  $\pm 1 \text{ GeV}$  uncertainty. This is done since the variation,  
2731 obtained from an independent MC sample, is otherwise plagued by large statisti-  
2732 cal uncertainties. Furthermore, the top mass is also varied in all considered signal  
2733 samples directly by  $\pm 1 \text{ GeV}$  through an ME reweighting method similar to Sec. 7.4.  
2734 The top mass uncertainties between background and signals are considered as fully  
2735 correlated.

2736 **Further uncertainties in SM  $t\bar{t}$**  Additionally, separate SM  $t\bar{t}$  samples are used  
2737 to evaluate uncertainties due to ME/PS matching (same as in Sec. 5.5), the under-  
2738 lying event tune [92], and the color reconnection model in PYTHIA [96, 207]. All of  
2739 these effects are found to be small in the channels considered here.

2740 **Background cross section uncertainties** For the SM  $t\bar{t}$  background, instead of  
2741 including an explicit cross section uncertainty, the shift in the predicted NNLO+NNLL  
2742  $t\bar{t}$  cross section due to the ME scales and the top quark mass is correlated with the  
2743 respective uncertainties. For minor backgrounds, explicit uncertainties of 15% for  
2744  $tW$  and t-channel single top [208–210], 30% for diboson and  $t\bar{t} + X$  [211, 212], and  
2745 5% for the data-driven  $Z/\gamma^* + \text{jets}$  normalization [213] are considered, which are all  
2746 based on the precision of relevant cross section measurements.

2747 **Background statistical uncertainties** Again similar to Sec. 5.5, per-bin back-  
2748 ground statistical uncertainties for all simulated processes are included following  
2749 Ref. [155].

## 2750 7.5.2 Experimental uncertainties

2751 **Jet and  $p_T^{\text{miss}}$  uncertainties** The uncertainty on the calibration of the jet  $p_T$   
2752 detector response is split into five subsources, of which three are considered uncor-  
2753 related between years and two (related to the response to jets of different flavor)  
2754 are correlated. Further subsources as provided by CMS are found to be negligible  
2755 for this analysis [141]. Furthermore, the uncertainty in the jet  $p_T$  resolution is con-  
2756 sidered separately, again uncorrelated between years. All jet uncertainties are fully  
2757 propagated to the calculation of  $p_T^{\text{miss}}$ , and an additional  $p_T^{\text{miss}}$  uncertainty based on  
2758 soft, unclustered hadronic activity is also considered.

2759 **b tagging uncertainties** Similarly, the uncertainty on the b tagging efficiency  
2760 is split into 17 subsources, corresponding e.g. to different parton shower modeling,  
2761 the treatment of leptons in the jet, or the propagation of the jet  $p_T$  scale uncer-  
2762 tainties [140]. One component represents the statistical uncertainty and is thus  
2763 considered uncorrelated, while all others are correlated among years. Moreover, an  
2764 uncertainty on mistagging of light-flavor jets is included, also split into a statistical  
2765 and a systematic component.

2766 **Lepton and trigger uncertainties** Uncertainties on the lepton reconstruction,  
2767 identification, and isolation efficiencies, as measured centrally in CMS using the tag-  
2768 and-probe method, are considered separately for muons and electrons [111, 139].  
2769 For the muons, the uncertainty is split into a statistical component (uncorrelated  
2770 between the analysis years) and a systematic component (correlated). Similarly, the

2771 dilepton trigger efficiency uncertainties are considered uncorrelated between years  
2772 and lepton flavor channels. Finally, in data taken in 2016 or 2017, an additional  
2773 uncertainty is assigned due to an inefficiency in the ECAL L1 trigger [117], as  
2774 described in Sec. 7.2.4.

2775 **Luminosity uncertainty** The uncertainty on the total integrated luminosity is  
2776 included following Refs. [98, 214, 215], leading to a total luminosity uncertainty of  
2777 1.6%, split into a total of seven components with different correlations between the  
2778 years.

2779 **Pileup uncertainty** To estimate the uncertainty on the amount of pileup per pp  
2780 bunch crossing, the effective inelastic proton-proton cross section used for pileup  
2781 reweighting in the simulation is varied by 4.6% from its nominal value [216].

### 2782 7.5.3 Uncertainty smoothing

2783 Several of the considered uncertainty sources, e.g. the top quark mass in SM  $t\bar{t}$ , are  
2784 estimated by either comparing to separate MC samples, which causes the relative  
2785 deviation due to the source to be affected by large statistical noise. A similar problem  
2786 appears for uncertainties which effectively vary the cuts applied on MC events, such  
2787 as e.g. the jet  $p_T$  scale uncertainties by way of jet acceptances. If left untreated,  
2788 fitting these noisy shape templates to the data could lead to erroneous constraints  
2789 in the likelihood fit. To prevent this, the smoothing algorithm LOWESS [217, 218]  
2790 is applied to the relative deviations for these sources, with the bandwidth used for  
2791 the smoothing determined separately through cross-validation for each source. For  
2792 more details on the procedure, see Ref. [28].

### 2793 7.5.4 Differences between MC generators

2794 It has been observed in previous analyses that the theoretical uncertainties collected  
2795 in Sec. 7.5.1 do not necessarily cover the differences in the predictions of different MC  
2796 generators for  $t\bar{t}$  [26, 27, 169, 219]. To assess the size of these effects, the standard  
2797  $t\bar{t}$  prediction as computed using POWHEG hvq matched to PYTHIA is compared to  
2798 alternate generator setups.

2799 The first of these is the same POWHEG hvq matrix element matched to the  
2800 multi-purpose event generator HERWIG instead of PYTHIA. The angular-ordered  
2801 parton shower in HERWIG is used (as opposed to the  $p_T$ -ordered dipole shower in  
2802 PYTHIA) together with the CMS CH3 tune [220]. Furthermore, HERWIG uses a clus-  
2803 ter hadronization model [221] instead of the string hadronization model of PYTHIA  
2804 as described in Sec. 3.4.

2805 Figure 7.8 shows the ratios of the predictions from HERWIG and PYTHIA for the  
2806 reconstructed  $m_{t\bar{t}}$  distribution, as well as for the  $c_{\text{hel}}$  distribution close to the  $t\bar{t}$

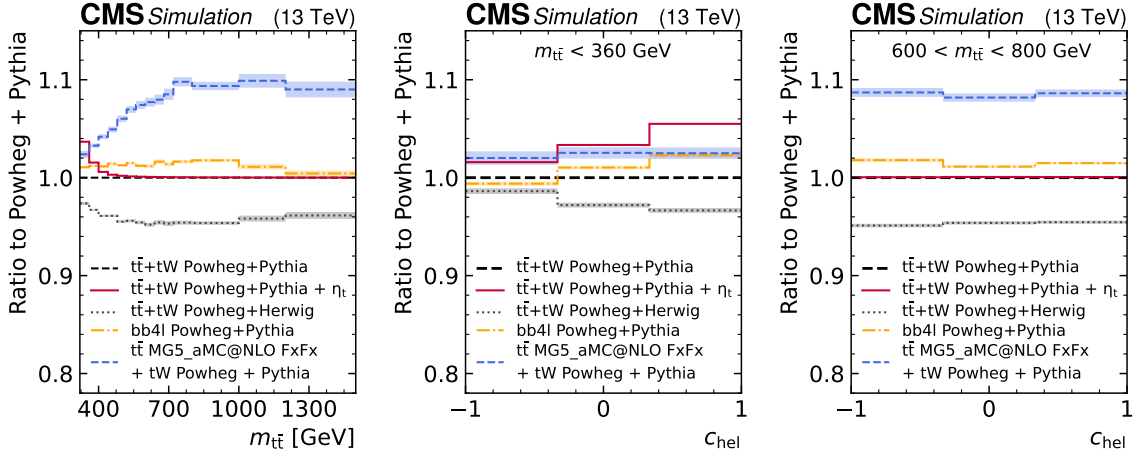


Figure 7.8: **Comparison between MC generators for  $t\bar{t} + tW$ .** The predictions of different MC setups, namely POWHEG  $t\bar{t} + tW$  matched to HERWIG (grey), bb4l matched to PYTHIA (orange), and MG5\_AMC@NLO matched to PYTHIA (blue), all shown as the ratio to the prediction of POWHEG  $t\bar{t} + tW$  matched to PYTHIA, for the inclusive reconstructed  $m_{t\bar{t}}$  distribution (left) as well as the reconstructed  $c_{\text{hel}}$  distribution, restricted to  $m_{t\bar{t}} < 360 \text{ GeV}$  (center) and to  $600 < m_{t\bar{t}} < 800 \text{ GeV}$  (right). The effect of the  $\eta_t$  signal is also shown in red for comparison. *Figure taken from Ref. [8].*

threshold (i.e. where the  $\eta_t$  signal is located) and in the  $t\bar{t}$  continuum. Besides a significantly lower  $t\bar{t}$  acceptance, HERWIG predicts an increase of events at the  $t\bar{t}$  threshold similar to  $\eta_t$ . This appears concerning at first glance since, should the data follow the prediction from HERWIG instead of PYTHIA, this enhancement could be confused with an  $\eta_t$  signal if PYTHIA is used as the baseline prediction. However, as seen in Fig. 7.8 in the center, HERWIG at the same predicts a flatter slope in  $c_{\text{hel}}$  than PYTHIA at the  $t\bar{t}$  threshold, equivalent to a dilution of  $t\bar{t}$  spin correlations<sup>1</sup>. This is in contrast to the  $\eta_t$  signal, in which the  $t\bar{t}$  spins are maximally anti-correlated. The inclusion of the spin correlation variable  $c_{\text{hel}}$  in the analysis thus makes it possible to separate the differences between POWHEG and HERWIG with respect to  $\eta_t$ .

The second alternative generator is bb4l matched to PYTHIA, as studied extensively in Chapter 6. Here, particularly the off-shell effects included in bb4l might be of interest for the extraction of  $\eta_t$  since the latter is located below the  $t\bar{t}$  threshold. The setup denoted as “bb4l v2” in Sec. 6.2, corresponding to Ref. [170], is used, and compared to the sum of the POWHEG hvq  $t\bar{t}$  and tW predictions for consistency.

A caveat here is presented by the corrections to NNLO QCD and NLO EW as described in Sec. 7.3. These are derived from fixed-order corrections assuming stable

<sup>1</sup>This effect was also seen in the context of Ref. [27].

2824 top quarks, and are not available for the full  $b\bar{b}\ell\ell\nu\nu$  final state. To still be able to  
2825 apply them to **bb41** predictions, the **bb41** sample is split into a  $t\bar{t}$  and a  $tW$  part  
2826 in an ad-hoc way by using the matrix element history projectors implemented in  
2827 **bb41** v2 [170]. The corrections are then applied to the  $t\bar{t}$  part only, in the same  
2828 manner as to **POWHEG hvq**.

2829 The ratios of the predictions are also shown in Fig. 7.8. It can be seen that **bb41**  
2830 does not predict major differences in the reconstructed  $m_{t\bar{t}}$  spectrum even at its  
2831 lower edge. However, it results in a significantly steeper slope in reconstructed  $c_{hel}$   
2832 close to the threshold. This increase in slope is of similar magnitude as the effect  
2833 expected due to  $\eta_t$ .

2834 The source of this difference is not yet fully understood. **bb41** contains NLO  
2835 QCD corrections to the top decay which are not present in **hvq** (though they are  
2836 approximated through the matrix element corrections in **PYTHIA**). However, NLO  
2837 corrections to spin correlations are expected to not only be small, but reduce the  
2838 spin correlation instead of enhancing it [18].

2839 It is possible that the effect instead originates in the  $t\bar{t}/tW$  interference: For the  
2840  $tW$  contribution, where one of the leptons is not actually the decay product of a top  
2841 quark,  $t\bar{t}$  spin correlation is not truly definable. The slope of the reconstructed  $c_{hel}$   
2842 distribution, obtained under the assumption that the events contain a  $t\bar{t}$  system,  
2843 will thus be arbitrary with no clear *a priori* expectation, and in general different  
2844 to the slope in SM  $t\bar{t}$ . The same holds for the  $t\bar{t}/tW$  interference. Since **bb41** now  
2845 gives a true (though effectively LO) prediction of the  $t\bar{t}/tW$  interference instead of  
2846 the ad-hoc treatment of the DR and DS schemes (cf. Sec. 6.3), it is expected that  
2847 the magnitude of the interference contribution in **bb41** will be different. Thus, it is  
2848 possible that the total  $c_{hel}$  slope, arising from the combination of  $t\bar{t}$ ,  $tW$ , and  $t\bar{t}/tW$   
2849 interference, will be different as well. However, since  $t\bar{t}$  and  $tW$  are not cleanly  
2850 separable in **bb41**, however, this hypothesis is difficult to confirm, and such studies  
2851 are beyond the scope of this analysis.

2852 A third alternative prediction is provided by  $t\bar{t}$  + jets production simulated with  
2853 **MG5\_AMC@NLO**, matched to **PYTHIA** with the FxFx scheme [88]. While this  
2854 prediction is formally also NLO-accurate in QCD in the NWA, and thus comparable  
2855 to **POWHEG hvq**, it has been observed in past measurements that **MG5\_AMC@NLO**  
2856 does not agree as well with data as **POWHEG** for  $t\bar{t}$  production. Indeed it shows a  
2857 large slope in the  $m_{t\bar{t}}$  distribution, as also seen in Fig. 7.8. As a result, **MG5\_AMC@NLO**  
2858 is given less focus compared to the other two predictions in this work.

2859 In this work, **POWHEG hvq + PYTHIA** is considered for the nominal background  
2860 prediction in all cases. A comparison to **POWHEG hvq + HERWIG**, **MG5\_AMC@NLO**  
2861 + **PYTHIA**, and **bb41 + PYTHIA** is shown in Sec. 7.7.3 in the context of measuring  
2862 the  $\eta_t$  cross section. Furthermore, the effect of including the differences to **POWHEG**  
2863 **hvq + HERWIG** and **bb41 + PYTHIA** as two additional shape-based nuisance param-  
2864 eters in the fit is similarly given in Sec. 7.7.3. Note that in Ref. [8], these nuisance  
2865 parameters were considered as part of the main result in order to be conservative

2866 with respect to the total uncertainty.

## 2867 7.6 Pre-fit distributions

2868 The agreement between the total MC prediction, including all corrections described  
2869 in Secs. 7.2.4 and 7.3, and the observed data are presented in this section. Shown  
2870 observables are lepton  $p_T$ ,  $\eta$ , and  $\Delta\phi_{\ell\ell}$  (Fig. 7.9); jet  $p_T$ ,  $\eta$ , and number of jets  
2871 (Fig. 7.10); as well as  $p_T^{\text{miss}}$ , the invariant mass of the two leptons  $m_{\ell\ell}$ , and the  
2872 invariant mass of the two leptons and two b-tagged jets  $m_{b\bar{b}\ell\ell}$  (Fig. 7.11). All of  
2873 them are shown after all lepton, jet, b tag and  $p_T^{\text{miss}}$  requirements, but before the  
2874  $t\bar{t}$  reconstruction, summed over all analysis years, and separately for the same-  
2875 flavor (ee and  $\mu\mu$ ) and opposite-flavor ( $e\mu$ ) channels, since the latter have different  
2876 backgrounds and cuts.

2877 Furthermore, different distributions resulting from the  $t\bar{t}$  reconstruction are shown  
2878 in Fig. 7.12, this time summed also over lepton flavor. They consist of top quark  
2879  $p_T$ ,  $\eta$ , and scattering angle  $\cos\theta^*$ , as well as the three observables used for the fit  
2880  $m_{t\bar{t}}$ ,  $c_{\text{hel}}$ , and  $c_{\text{han}}$ .

2881 It can be seen that there is a slight but consistent over-prediction of the back-  
2882 ground normalization compared to the data in almost all distributions. Furthermore,  
2883 there is a slight slope in the ratio of data and simulation yields in the  $p_T$  of leptons,  
2884 jets or the reconstructed top quarks. This is likely a result of the well-known top  
2885 quark  $p_T$  mismodeling at the LHC, which is not fully removed by NNLO QCD cor-  
2886 rections as used here [151, 153]. Further discrepancies are found for high values of  $|\eta|$   
2887 and for large number of jets, both of which are covered by systematic uncertainties.

2888 Finally, the three-dimensional  $m_{t\bar{t}} \times c_{\text{hel}} \times c_{\text{han}}$  distribution used for the statistical  
2889 analysis is shown before the fit, including all systematic uncertainties, in Fig. 7.13.  
2890 A notable excess of the data compared to the prediction is observed for low val-  
2891 ues of  $m_{t\bar{t}}$ , consistent with the excess seen in the one-dimensional  $m_{t\bar{t}}$  distribution  
2892 (Fig. 7.12) and in the related observables  $m_{\ell\ell}$  and  $m_{b\bar{b}\ell\ell}$  (Fig. 7.11). The excess is  
2893 stronger for large values of  $c_{\text{hel}}$  as seen from the multi-dimensional binning, while  
2894 no trend can be seen by eye regarding  $c_{\text{han}}$ .

## 2895 7.7 Interpretation of the excess

### 2896 7.7.1 Extraction of $t\bar{t}$ bound state effects

2897 The prefit excess visible in Fig. 7.13 is interpreted in terms of a pseudoscalar  $t\bar{t}$   
2898 bound state by performing a signal+background fit with  $\eta_t$  as the signal, as defined  
2899 in Sec. 2.2.3. The POI in the fit is  $\sigma(\eta_t)$ , the cross section of the  $\eta_t$  model, which can  
2900 be understood as the difference between the data and the fixed-order perturbative  
2901 QCD (FO pQCD) background prediction. It is measured to be

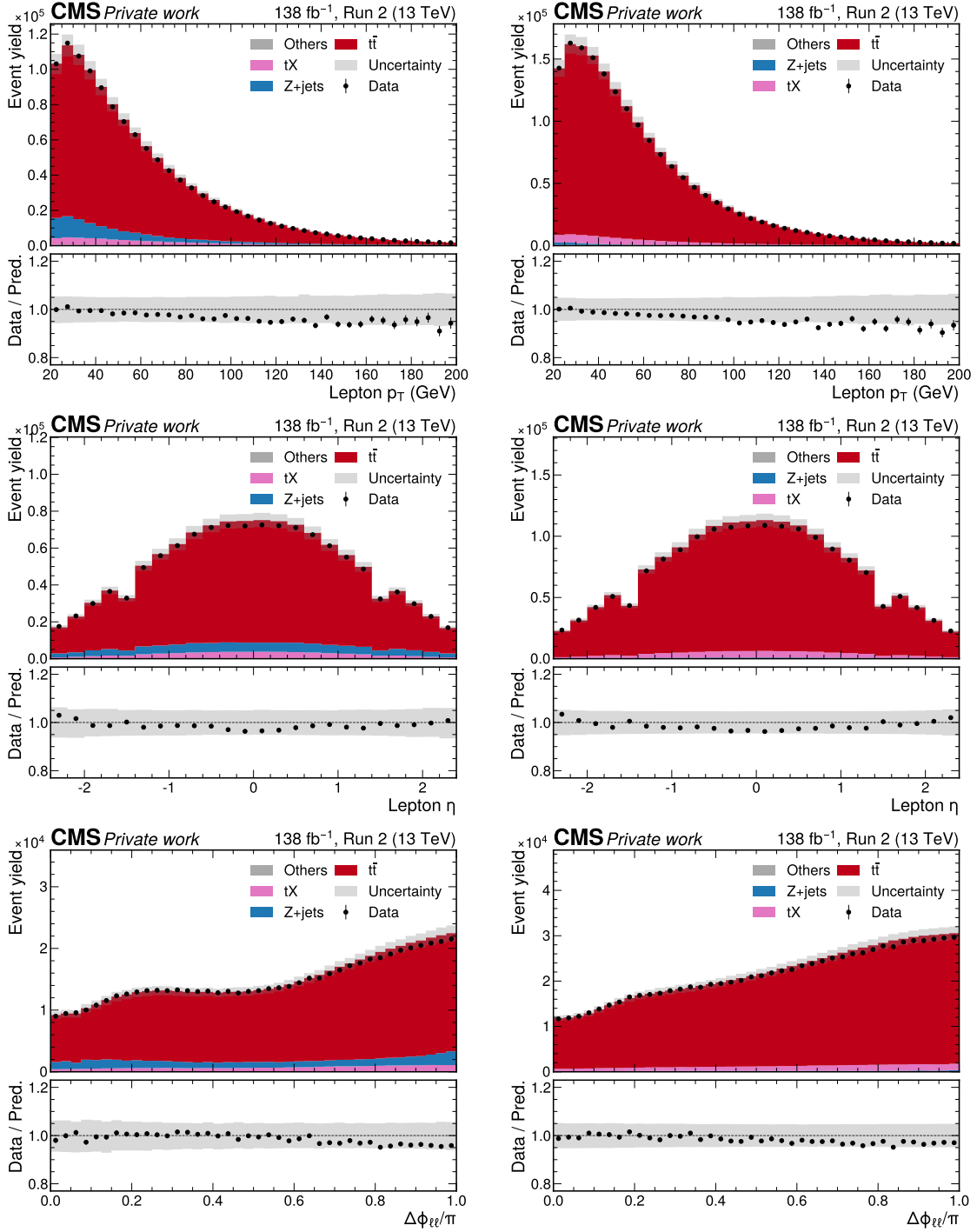


**Figure 7.9: Control distributions.** Shown are the distributions of  $p_T$  of both leptons (top),  $\eta$  of both leptons (center), and the azimuthal angle  $\Delta\phi_{\ell\ell}$  between the leptons (bottom) in the ee/ $\mu\mu$  (left) and e $\mu$  channels (right). All figures show both data (black dots) and different simulated background processes (colored bars), as well as the total systematic uncertainty (gray band).

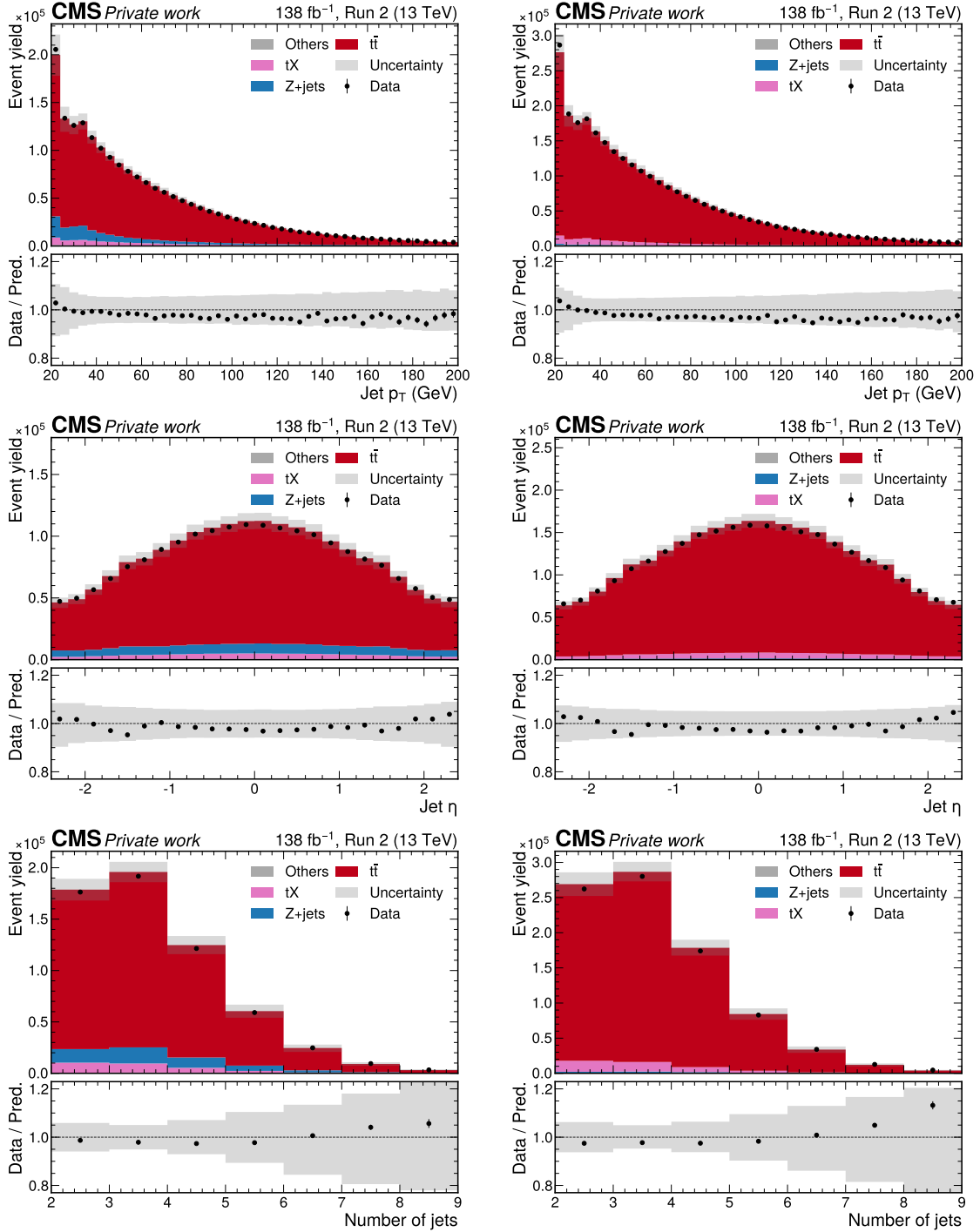
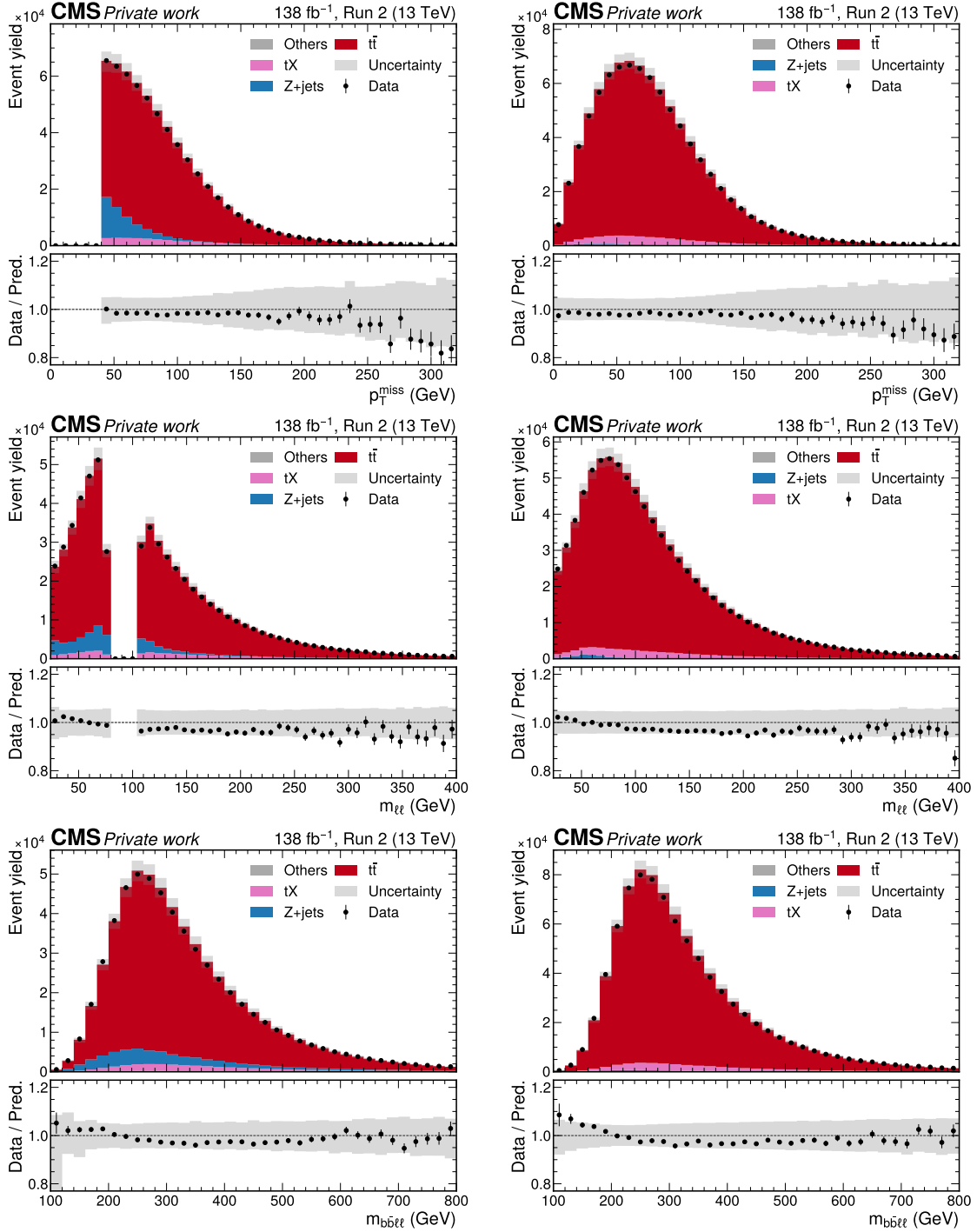
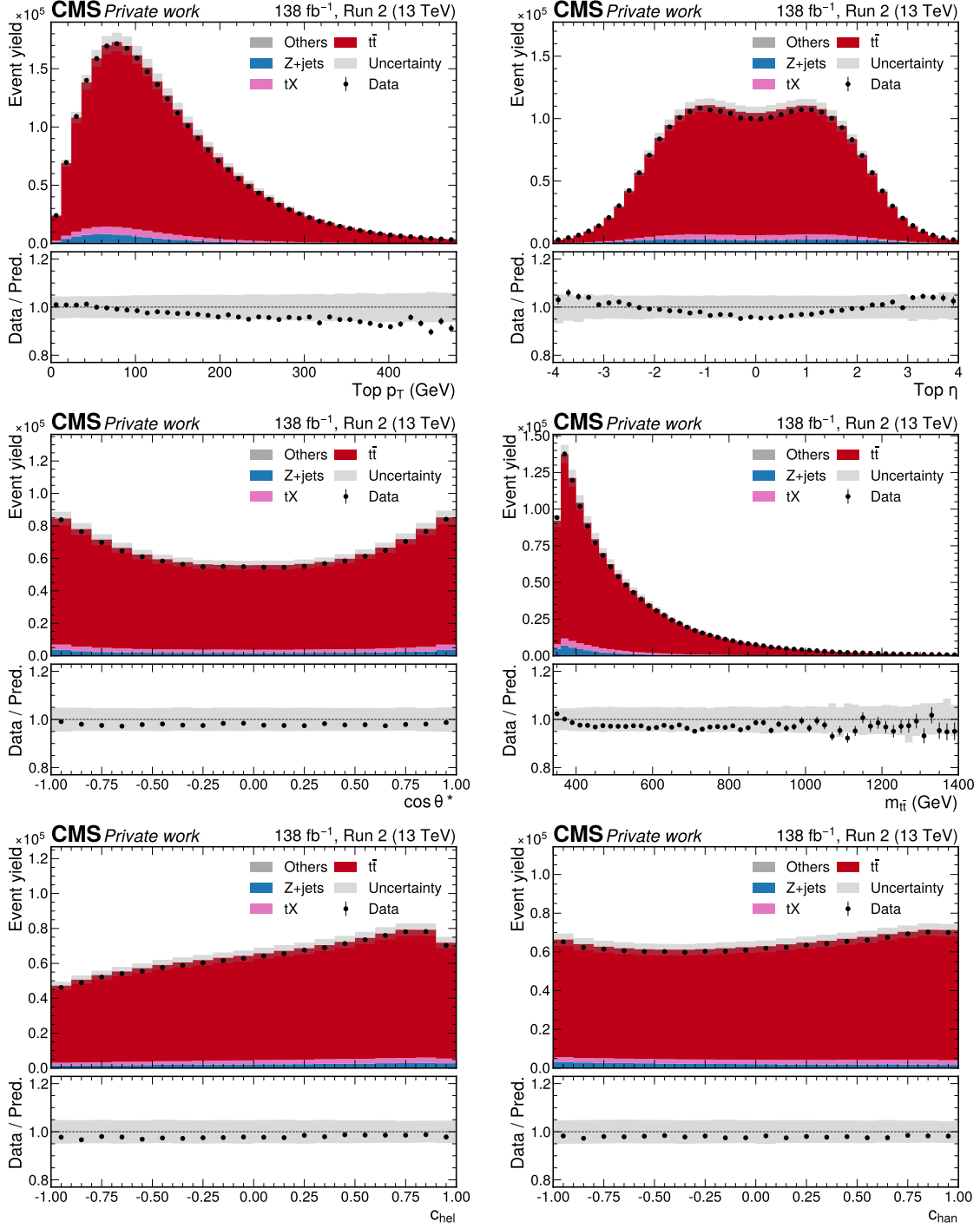


Figure 7.10: **Control distributions.** Shown are the distributions of  $p_T$  of all jets (top),  $\eta$  of all jets (center), and the number of jets (bottom) in the ee/ $\mu\mu$  (left) and e $\mu$  channels (right). All figures show both data (black dots) and different simulated background processes (colored bars), as well as the total systematic uncertainty (gray band).



**Figure 7.11: Control distributions.** Shown are the distributions of  $p_T^{\text{miss}}$  (top),  $m_{\ell\ell}$  (center), and the invariant mass  $m_{bb\ell\ell}$  of both b candidates and both leptons (bottom) in the ee/ $\mu\mu$  (left) and e $\mu$  channels (right). All figures show both data (black dots) and different simulated background processes (colored bars), as well as the total systematic uncertainty (gray band).



**Figure 7.12: Control distributions after  $t\bar{t}$  reconstruction.** Shown are (from top left to bottom right) the distributions of the top quark  $p_T$ , top quark  $\eta$ ,  $m_{t\bar{t}}$ ,  $\cos \theta^*$ ,  $c_{\text{hel}}$  and  $c_{\text{han}}$  for the sum of all dilepton channels. All figures show both data (black dots) and different simulated background processes (colored bars), as well as the total systematic uncertainty (gray band).

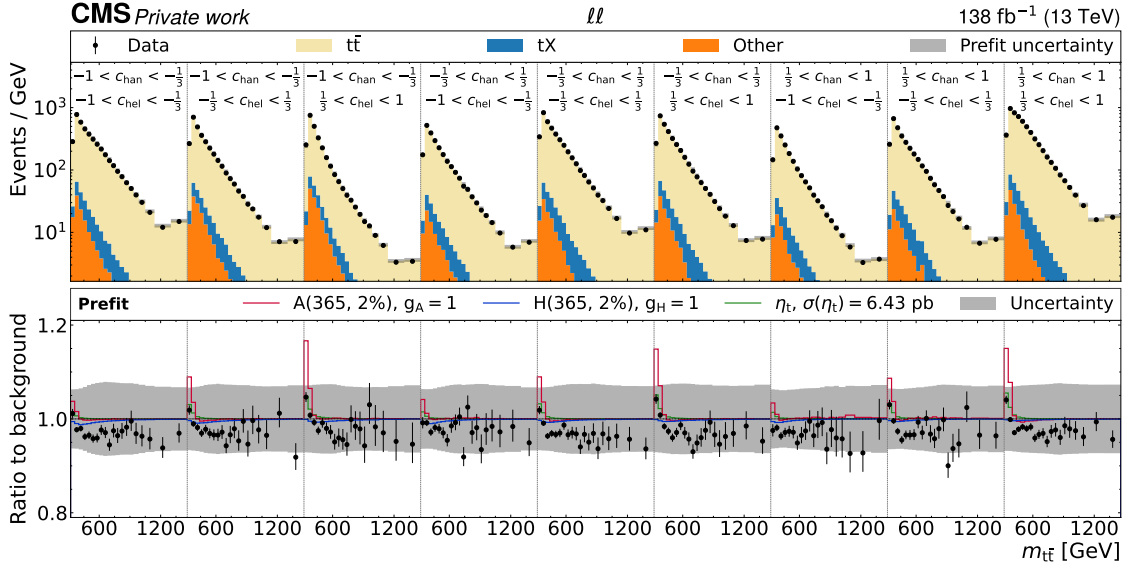


Figure 7.13: **Prefit distributions of  $m_{t\bar{t}} \times c_{\text{hel}} \times c_{\text{han}}$ .** The unrolled three-dimensional distribution in  $m_{t\bar{t}}$ ,  $c_{\text{hel}}$  and  $c_{\text{han}}$  as used for statistical analysis before the fit to the data, summed over all years and lepton flavors. The upper panel shows the sum of the background simulation (colored bars) and the observed data (black dots), while the lower panel shows the ratio of the data to the prediction, with different signals overlaid: A (red) and H (blue), both for  $m_{A/H} = 365$  GeV and  $\Gamma_{A/H}/m_{A/H} = 2\%$ , and  $\eta_t$  (green). *Figure adapted from Ref. [9].*

$$\sigma(\eta_t) = 8.7 \pm 0.5(\text{stat}) \pm 1.0(\text{syst}) \text{ pb} = 8.7 \pm 1.1 \text{ pb}. \quad (7.16)$$

2902     The statistical and systematic component of the uncertainty are estimated as  
 2903     described in Sec. 4.4. The significance of the result compared to a background-only  
 2904     hypothesis, i.e. without a bound state, is more than five standard deviations.

2905     The result is of a similar order of magnitude as the prediction of 6.43 pb given in  
 2906     Ref. [37], obtained by fitting the results of an NRQCD calculation from Ref. [33],  
 2907     though this result is not one-to-one comparable since it considers only the range of  
 2908      $m_{t\bar{t}} \in [338, 350]$  GeV. It should be noted that the results of Ref. [33] (as well as the  
 2909     newer ones in Ref. [35]) were obtained by using NLO hard functions for the NRQCD  
 2910     calculations, and moving to NNLO might give a significant increase in cross section,  
 2911     by analogy to the difference in NNLO and NLO cross sections for the  $t\bar{t}$  continuum.  
 2912     Furthermore, the NRQCD approach employed in these calculations considers only  
 2913     the ground state wavefunction of the bound  $t\bar{t}$  system, and independent calculations  
 2914     have shown that including contributions from excited states could increase the cross  
 2915     section by orders of 15–20% [222, 223].

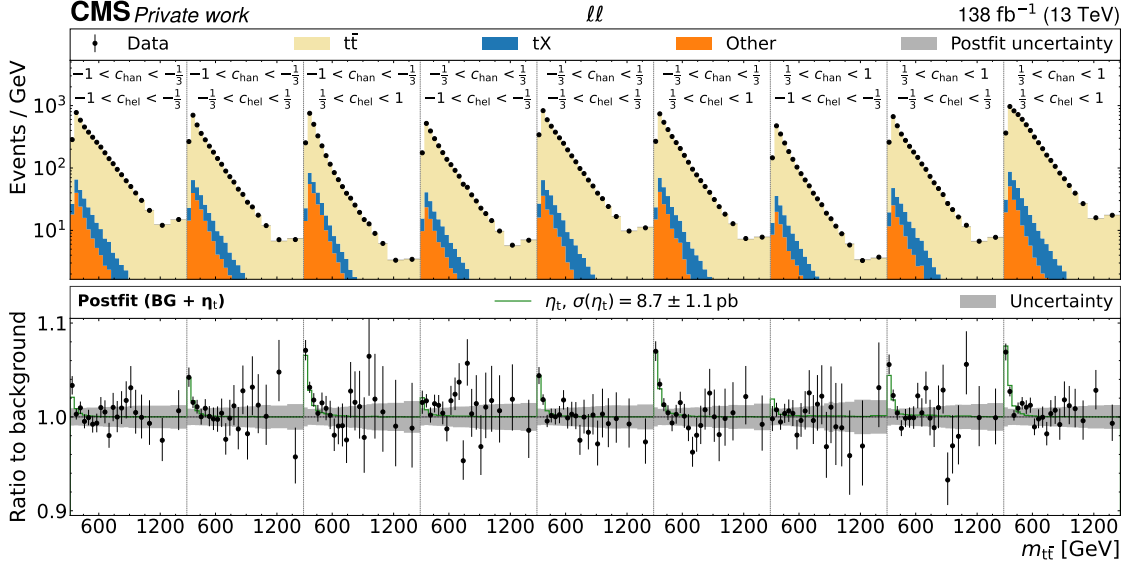


Figure 7.14: **Postfit distributions of  $m_{t\bar{t}} \times c_{\text{hel}} \times c_{\text{han}}$  for the  $\eta_t$  fit.** The unrolled three-dimensional distribution in  $m_{t\bar{t}}$ ,  $c_{\text{hel}}$  and  $c_{\text{han}}$  as after the fit to data with  $\eta_t$  as the signal, summed over all years and lepton flavors. The upper panel shows the sum of the background simulation (colored bars) and the observed data (black dots), while the lower panel shows the ratio of the data to the prediction with the postfit  $\eta_t$  signal overlaid. *Figure adapted from Ref. [8].*

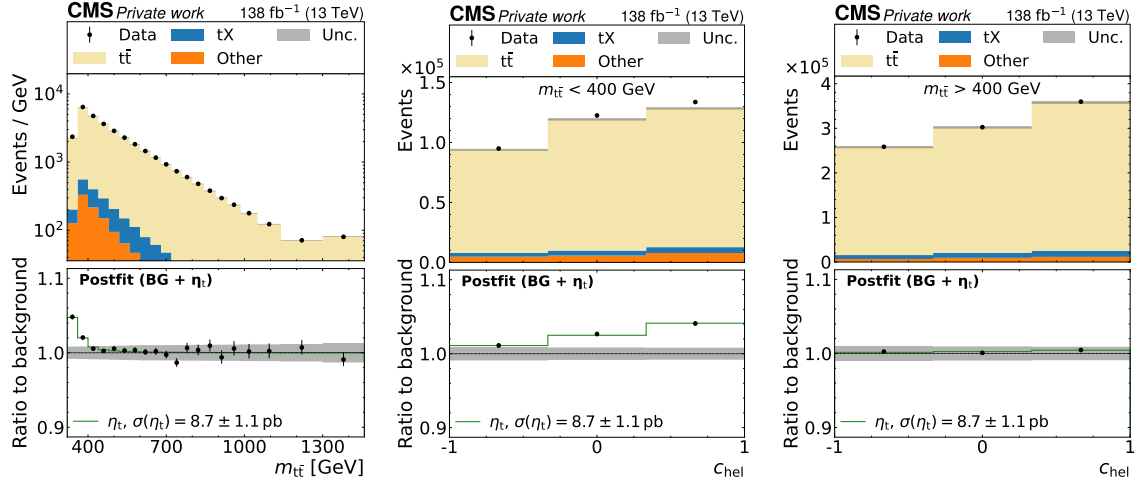


Figure 7.15: **Postfit distributions of  $m_{t\bar{t}}$  and  $c_{\text{hel}}$  for the  $\eta_t$  fit.** One-dimensional distributions of inclusive  $m_{t\bar{t}}$  (left),  $c_{\text{hel}}$  for  $m_{t\bar{t}} < 400$  GeV (center), and  $c_{\text{hel}}$  for  $m_{t\bar{t}} > 400$  GeV (right), projected from the  $m_{t\bar{t}} \times c_{\text{hel}} \times c_{\text{han}}$  template in Fig. 7.14 with the same notations. *Figure adapted from Ref. [8].*

2916 The postfit  $m_{t\bar{t}} \times c_{\text{hel}} \times c_{\text{han}}$  distribution can be seen in Fig. 7.14. The data,  
 2917 including the excess at low  $m_{t\bar{t}}$ , is described well by the  $\eta_t$  model combined with the  
 2918 FO pQCD background. To illustrate this further, one-dimensional projections of the  
 2919  $m_{t\bar{t}} \times c_{\text{hel}} \times c_{\text{han}}$  template into inclusive  $m_{t\bar{t}}$ , as well as into  $c_{\text{hel}}$  for both low and high  
 2920  $m_{t\bar{t}}$ , are shown in Fig. 7.15. One can clearly see that the data at the  $t\bar{t}$  threshold  
 2921 shows a stronger slope in data than in the FO pQCD prediction, consistent with the  
 2922  $\eta_t$  signal, while no such slope is seen at high  $m_{t\bar{t}}$ , i.e. in the  $t\bar{t}$  continuum.

### 2923 7.7.2 Parity of the excess

2924 To investigate whether the observed excess is  $\mathcal{CP}$ -odd (pseudoscalar) or  $\mathcal{CP}$ -even  
 2925 (scalar) in nature, a simultaneous fit is performed with both  $\eta_t$  and  $\chi_t$ , as defined in  
 2926 Sec. 2.2.3, as freely floating signals. These correspond to pure  $^1S_0$  and  $^3P_0$   $t\bar{t}$  states,  
 2927 respectively, both localized at the  $t\bar{t}$  threshold.

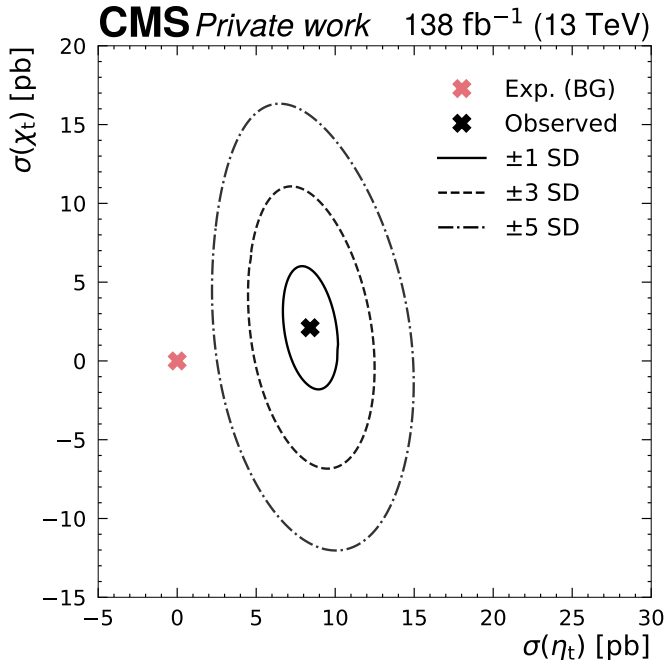


Figure 7.16: **Parity of the excess.** Observed compatibility contours in a simultaneous fit of  $\eta_t$  (corresponding to  $^1S_0$ ) and  $\chi_t$  (corresponding to  $^3P_0$ ). The best-fit point is shown as the black cross, while the BG-only expectation (i.e.  $\sigma(\eta_t) = \sigma(\chi_t) = 0$ ) is marked in pink. *Figure adapted from Ref. [8].*

2928 The result is shown in Fig. 7.16 in the form of compatibility contours. Consistent  
 2929 with the result of the  $\eta_t$ -only fit, a non-zero  $\eta_t$  contribution is preferred by the fit by  
 2930 more than 5 standard deviations. By contrast, the measured  $\chi_t$  cross section, which

can be seen as the  ${}^3P_0$  component of the excess, is compatible with zero within one standard deviation. Based on this, it can be said that the observed excess is dominated by a pseudoscalar or  ${}^1S_0$  spin state.

### 7.7.3 Checks of the result

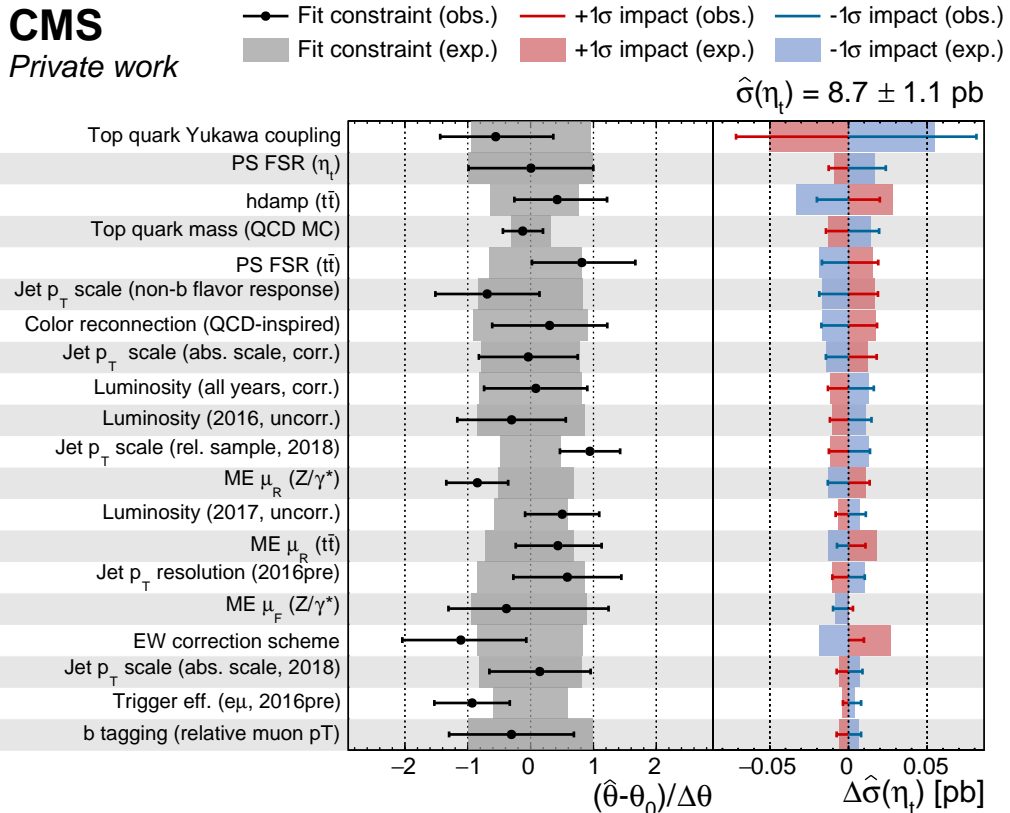


Figure 7.17: **Nuisance parameter pulls and impacts.** Expected and observed pulls, constraints, and impacts on the  $\eta_t$  cross section for the most impactful nuisance parameters in the  $\eta_t$ -only fit. *Figure adapted from Ref. [8].*

**Nuisance parameter pulls and impacts** In Fig. 7.17, nuisance parameter pulls, constraints and impacts for the  $\eta_t$  extraction fit are presented, following the definitions in Sec. 4.4. The most impactful nuisances are all related to the modeling of the  $t\bar{t}$  background. In particular, the value of the top Yukawa coupling  $y_t$  in the EW corrections is the leading uncertainty. This is notably one of the few uncertainties which can lead to a steeper  $c_{\text{hel}}$  slope in the  $t\bar{t}$  prediction and could thus to some degree be confused for  $\eta_t$ , as discussed in Sec. 7.3.2.

2942 Further important modeling uncertainties are the FSR scales in the  $t\bar{t}$  parton  
2943 shower as well as the top quark mass. The latter is constrained to a postfit uncer-  
2944 tainty of  $\pm 0.4$  GeV, and fully compatible with the nominal value of 172.5 GeV. This  
2945 strong constraint is similar in size to the current most precise direct top quark mass  
2946 measurements [224, 225]. While it is expected that the  $m_{t\bar{t}}$  distribution is strongly  
2947 sensitive to the top quark mass, it is still surprising that the constraint competes  
2948 with dedicated top quark mass measurements.

2949 To verify that the constraint does not lead to an underestimation of the un-  
2950 certainty on  $\sigma(\eta_t)$ , the top quark mass nuisance parameter is decorrelated in two  
2951 different ways: either by splitting it into three regions defined by  $m_{t\bar{t}} < 400$  GeV,  
2952  $400 < m_{t\bar{t}} < 600$  GeV, and  $m_{t\bar{t}} > 600$  GeV, or by decorrelating it between the nine  
2953  $c_{\text{hel}}$  and  $c_{\text{han}}$  bins used for the measurements. In both cases, similar constraints are  
2954 found on at least some of the resulting nuisance parameters, and the extracted  $\eta_t$   
2955 cross section is compatible with the nominal result.

2956 A strong pull of around  $-1$  is further observed in the EW correction scheme un-  
2957 certainty. This uncertainty effectively encodes missing knowledge from NLO QCD-  
2958 NLO EW cross terms in the higher-order corrections to  $t\bar{t}$  as discussed in Sec. 7.3.2,  
2959 with a nuisance parameter value of  $+1$  corresponding to no cross terms (the additive  
2960 scheme) and  $0$  corresponding to approximated cross terms (the multiplicative  
2961 scheme). A pull of  $-1$  could thus imply that the cross terms are underestimated by  
2962 this approximation, though this is speculation as no full computation of the cross  
2963 terms has been performed at the time of writing.

2964 Experimental nuisances like the jet energy scales, on the other hand, influence  
2965 mostly  $m_{t\bar{t}}$  and thus do not have a large impact on the POI. Of note here are  
2966 the pulls and constraints in nuisance parameters which influence only one of the  
2967 four analysis eras, namely a subsource of the jet  $p_T$  scale in 2018, the uncorrelated  
2968 component of the integrated luminosity in 2017, and the  $e\mu$  trigger efficiency in  
2969 2016pre. The pulls imply that there are small inconsistencies (within one standard  
2970 deviation) between the eras that are not accounted for in the MC simulation. Since  
2971 this measurement is performed in a high-statistics region of phase space and with a  
2972 large luminosity, it is expected to constrain ratios between normalization effects in  
2973 different years, while of course the overall normalization (i.e. the total integrated  
2974 luminosity) should be not pulled or significantly constrained. The exact source of  
2975 the per-year differences is not clear; however, due to the small impact on the POI,  
2976 this is not considered a problem.

2977 In total, no pulls much larger than one prefit standard deviation are observed,  
2978 indicating that the uncertainty model accommodates the data well.

2979 **Fit using  $m_{b\bar{b}\ell\ell}$  instead of  $m_{t\bar{t}}$**  The three observables  $m_{t\bar{t}}$ ,  $c_{\text{hel}}$  and  $c_{\text{han}}$  are  
2980 all obtained from the kinematic reconstruction as described in Sec. 7.2.5. This  
2981 procedure assumes, among others, that the top quarks are exactly on-shell with

2982 a fixed mass of 172.5 GeV. For  $\eta_t$ , which is located below the  $t\bar{t}$  threshold, this  
 2983 assumption is clearly violated. Since the same kinematic reconstruction procedure  
 2984 is applied to simulation and data, this is in principle not a problem as long as  
 2985 the virtuality of the top quarks is well described by simulation. However, since the  
 2986 modeling of  $\eta_t$  in particular is rather uncertain, it is still important to check whether  
 2987 this assumption in the kinematic reconstruction introduces any bias.

2988 This is done by repeating the fit with the observable  $m_{t\bar{t}}$  replaced by  $m_{b\bar{b}\ell\ell}$  (as  
 2989 shown also in Fig. 7.11), thus removing kinematic information obtained via the  
 2990 reconstruction from the fit. The kinematic reconstruction is still performed, however,  
 2991 to obtain  $c_{\text{hel}}$  and  $c_{\text{han}}$ <sup>2</sup>.

2992 The resulting  $m_{b\bar{b}\ell\ell} \times c_{\text{hel}} \times c_{\text{han}}$  postfit distribution can be found in Figs. 7.18  
 2993 and 7.19. It can be seen that the excess is still clearly present, though with a wider  
 2994 spread due to the coarser resolution of  $m_{b\bar{b}\ell\ell}$  compared to  $m_{t\bar{t}}$ . An  $\eta_t$  cross section  
 2995 of  $\sigma(\eta_t) = 7.5 \pm 1.8 \text{ pb}$  is extracted, which is in agreement with the nominal result  
 2996 within one standard deviation.

2997 **Alternate generator setups** The influence of the choice of generator setup for  
 2998 the  $t\bar{t}$  prediction is further quantified by repeating the  $\eta_t$  extraction fit with alternate  
 2999 setups. Besides the nominal setup from POWHEG hvq matched to PYTHIA, the three  
 3000 setups introduced in Sec. 7.5.4 are considered: POWHEG hvq matched to HERWIG,  
 3001 MG5\_AMC@NLO matched to PYTHIA with the FxFx scheme, and bb4l matched  
 3002 to PYTHIA.

Generator setup	$\sigma(\eta_t) [\text{pb}]$
POWHEG hvq + PYTHIA (nominal)	$8.7 \pm 1.1$
POWHEG hvq + HERWIG	$8.6 \pm 1.1$
MG5_AMC@NLO FxFx + PYTHIA	$9.8 \pm 1.3$
POWHEG bb4l + PYTHIA	$6.6 \pm 1.4$

Table 7.6: **Results for alternate generators.** Results for  $\sigma(\eta_t)$  obtained with different simulated event samples for the FO pQCD  $t\bar{t}+tW$  prediction.

3003 The results can be found in Tab. 7.6. The results from PYTHIA and HERWIG are  
 3004 fully in agreement with each other, while MG5\_AMC@NLO results in a higher  $\eta_t$   
 3005 cross section by about one standard deviation, and bb4l results in a lower  $\eta_t$  cross  
 3006 section by about  $\sim 1.5$  standard deviations.

3007 As an additional check, the differences between the predictions from POWHEG hvq  
 3008 + HERWIG and POWHEG hvq + PYTHIA as well as between bb4l and  $t\bar{t}+tW$  are  
 3009 included in the fit as additional nuisance parameters. In both cases, the POWHEG

<sup>2</sup>It has separately been checked that the requirement for events to pass the kinematic reconstruction does not bias the result, either.

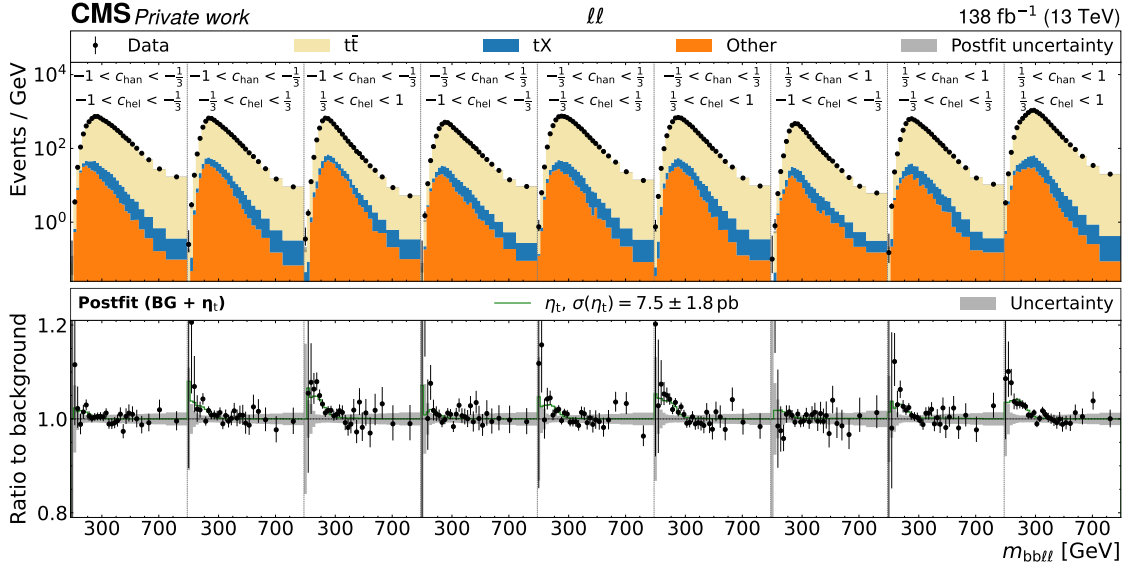


Figure 7.18: **Postfit distributions of  $m_{bb\ell\ell} \times c_{hel} \times c_{han}$  for the  $\eta_t$  fit.** The unrolled three-dimensional distribution in  $m_{bb\ell\ell}$ ,  $c_{hel}$  and  $c_{han}$  after the fit to data with  $\eta_t$  as the signal using  $m_{bb\ell\ell}$  instead of  $m_{t\bar{t}}$ , summed over all years and lepton flavors. The first  $m_{bb\ell\ell}$  bin in each  $c_{hel} \times c_{han}$  slice is an underflow bin containing events with  $m_{bb\ell\ell} < 180$  GeV. Otherwise, notations are as in Fig. 7.14.

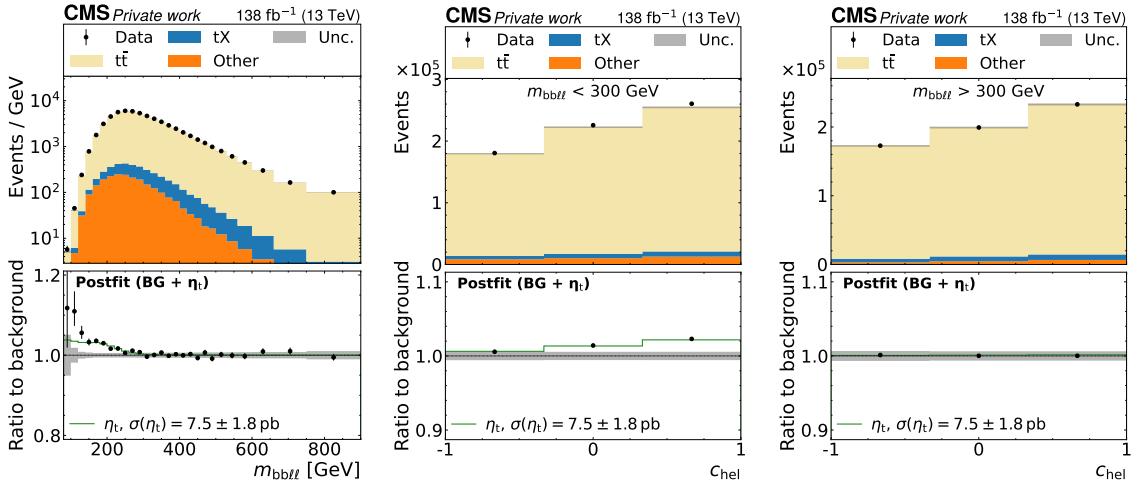


Figure 7.19: **Postfit distributions of  $m_{bb\ell\ell}$  and  $c_{hel}$  for the  $\eta_t$  fit.** One-dimensional distributions of inclusive  $m_{bb\ell\ell}$  (left),  $c_{hel}$  for  $m_{bb\ell\ell} < 300$  GeV (center), and  $c_{hel}$  for  $m_{bb\ell\ell} > 300$  GeV (right), projected from a 3D template of  $m_{bb\ell\ell} \times c_{hel} \times c_{han}$ . The first  $m_{bb\ell\ell}$  bin in the left figure is an underflow bin containing events with  $m_{bb\ell\ell} < 180$  GeV. Otherwise, notations are as in Fig. 7.14. *Figure adapted from Ref. [8].*

3010 hvq + PYTHIA prediction is considered the nominal, and the alternate prediction  
 3011 is considered the  $+1\sigma$  template. The  $-1\sigma$  template is constructed by symmetrizing  
 3012 the relative difference around the nominal, and intermediate values are obtained by  
 3013 interpolation as usual.

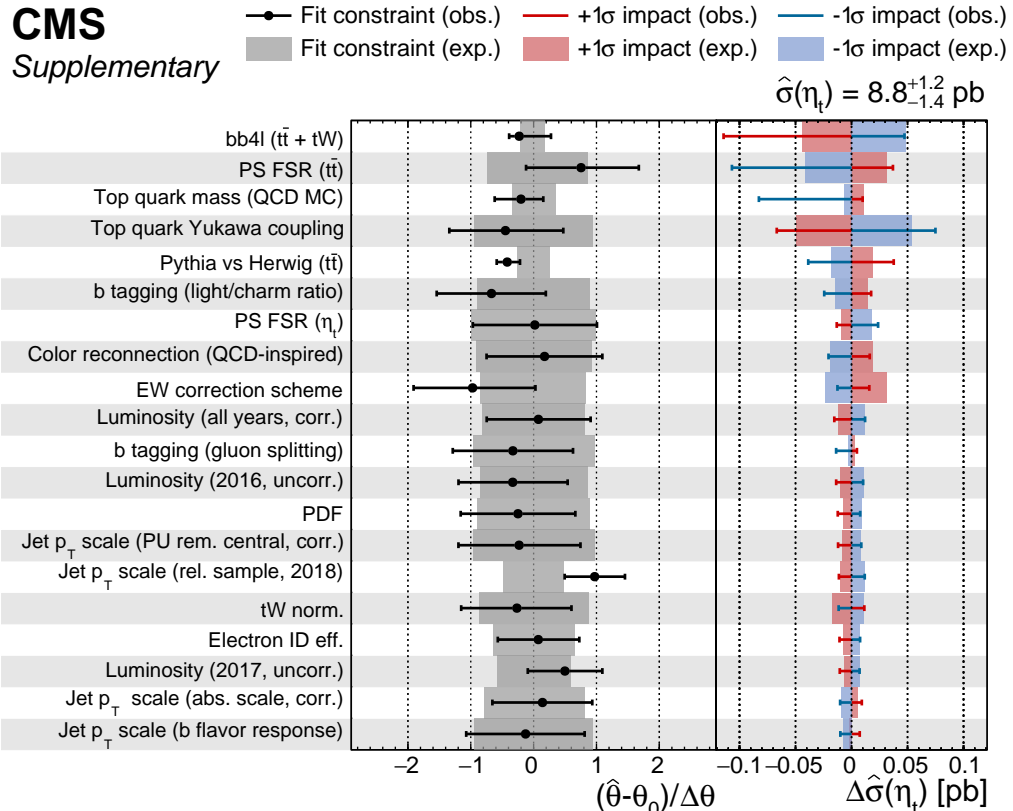


Figure 7.20: **Nuisance parameter pulls and impacts including alternate generators.** Expected and observed pulls, constraints, and impacts on the  $\eta_t$  cross section for the most impactful nuisance parameters in the  $\eta_t$ -only fit where the differences between the predictions from POWHEG hvq + HERWIG and bb4l + PYTHIA compared to POWHEG hvq + PYTHIA are included as additional nuisance parameters. *Figure adapted from Ref. [8].*

3014 The resulting  $\eta_t$  cross section with these nuisance parameters included is  $\sigma(\eta_t) =$   
 3015  $8.8^{+1.2}_{-1.4} \text{ pb}$ <sup>3</sup>. This figure is fully compatible with the nominal result with an asymmet-  
 3016 rically increased uncertainty. The reason for the increase can be seen in Fig. 7.20,  
 3017 showing the nuisance parameter pulls and impacts: The nuisance parameter encod-  
 3018 ing the difference between bb4l and  $t\bar{t} + tW$  represents the leading impact on the

<sup>3</sup>This figure is considered the nominal result in Ref. [8]

3019  $\eta_t$  cross section and is asymmetric. This is understandable from the steeper slope  
 3020 in  $c_{\text{hel}}$  for **bb41** as seen in Fig. 7.8, which is similar to the  $\eta_t$  signal, and is also in  
 3021 agreement with the reduced  $\eta_t$  cross section for a **bb41** background prediction shown  
 3022 in Tab. 7.6. It is furthermore significantly constrained towards zero, i.e. towards the  
 3023 default  $t\bar{t} + tW$  prediction, implying that the data prefers the NWA approach over  
 3024 the *a priori* superior **bb41** prediction. The reason for this is not readily apparent.  
 3025 One possible cause could be the fact that the NLO EW and NNLO QCD correc-  
 3026 tions are applied to **bb41** in a necessarily ad-hoc manner, and might thus spoil the  
 3027 agreement with the data (cf. Sec. 7.5.4). However, in the scope of this work, this  
 3028 remains speculation.

3029 On the other hand, the nuisance parameter encoding the difference of PYTHIA  
 3030 and HERWIG is less impactful, consistent with the results for HERWIG in Tab. 7.6,  
 3031 and similarly strongly constrained. This is likely because the difference between  
 3032 PYTHIA and HERWIG can be distinguished from  $\eta_t$  based on the combination of  $m_{t\bar{t}}$   
 3033 and  $c_{\text{hel}}$  information, as expanded upon in Sec. 7.5.4.

### 3034 7.7.4 Interpretation in terms of A and H

3035 While a  $t\bar{t}$  bound state is the conceptually simplest explanation of the enhancement  
 3036 at the  $t\bar{t}$  threshold in the sense that it is predicted in the SM and does not invoke any  
 3037 further (BSM) degrees of freedom, it is also possible to perform an interpretation  
 3038 in terms of the generic spin-0 bosons A and H as introduced in Sec. 2.3.1. For this  
 3039 purpose, fits allowing the presence of both A and H at the same time are performed.  
 3040 The two independent POIs are the A/H-top coupling modifiers  $g_{A\bar{t}\bar{t}}$  and  $g_{H\bar{t}\bar{t}}$ , and the  
 3041 interference with the SM is fully taken into account through a parameterization in  
 3042 terms of  $g_{A/H\bar{t}\bar{t}}^2$  and  $g_{A/H\bar{t}\bar{t}}^4$  (cf. Eq. (2.19)), thus allowing negative A/H contributions  
 3043 with respect to the SM.

3044 A scan is performed over all pairs of considered A/H masses and widths (see  
 3045 Sec. 7.2.1), and the pair with the largest difference in logarithmic likelihood  $\Delta \ln L$   
 3046 is identified as the best-fit point. This results in  $m_A = 365 \text{ GeV}$ ,  $\Gamma_A/m_A = 2\%$  for  
 3047 A and  $m_H = 925 \text{ GeV}$ ,  $\Gamma_H/m_H = 3\%$  for H. It should be noted here that 365 GeV is  
 3048 the lowest mass point considered in the available signals for A and H, while  $\eta_t$  and  
 3049  $\chi_t$  are located at a lower value of 343 GeV. It is possible that considering a lower  
 3050 value of  $m_A$  would lead to an even better fit; however, close to the  $t\bar{t}$  threshold,  
 3051 modeling the interference with the SM might be difficult due to large corrections at  
 3052 higher orders in QCD [226, 227].

3053 Figure 7.21 shows the postfit  $m_{t\bar{t}} \times c_{\text{hel}} \times c_{\text{han}}$  distribution, and Fig. 7.22 shows  
 3054 the allowed region for the two couplings  $g_{A\bar{t}\bar{t}}$  and  $g_{H\bar{t}\bar{t}}$  as obtained from a likelihood  
 3055 scan. From the latter, the best-fit values and total ranges for the coupling modifiers  
 3056 are found to be

$$g_{A\bar{t}\bar{t}} = 0.79^{+0.04}_{-0.05} \quad \text{and} \quad g_{H\bar{t}\bar{t}} = 1.47^{+0.17}_{-0.30}. \quad (7.17)$$

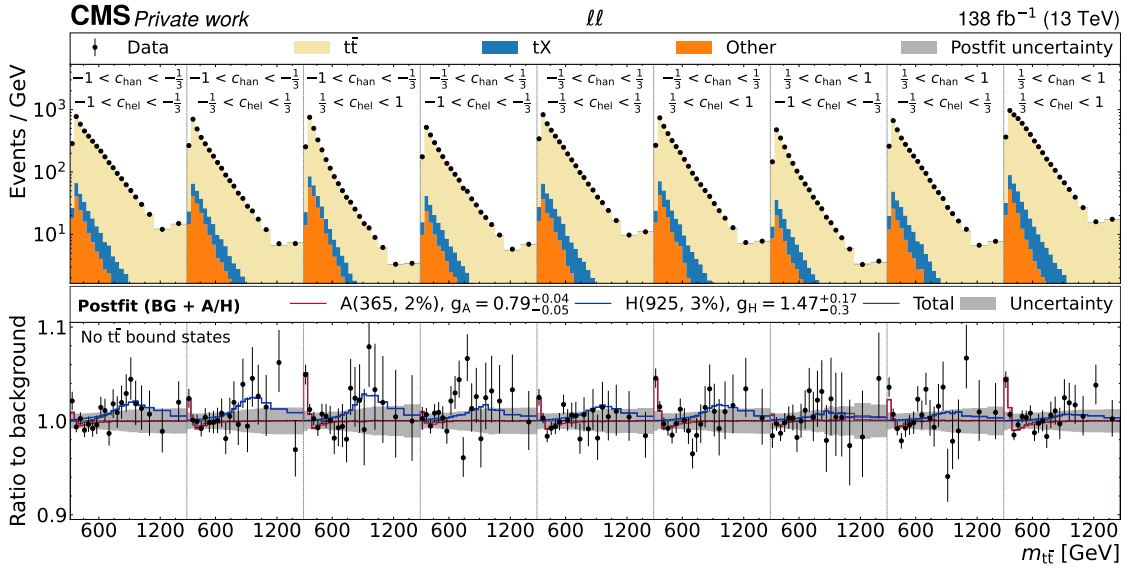


Figure 7.21: **Postfit distributions of  $m_{t\bar{t}} \times c_{\text{hel}} \times c_{\text{han}}$  for the A+H fit.** The unrolled three-dimensional distribution in  $m_{t\bar{t}}$ ,  $c_{\text{hel}}$  and  $c_{\text{han}}$  as after the fit to data with A and H as signals, summed over all years and lepton flavors. The A/H signals correspond to the best-fit masses and widths of  $m_A = 365 \text{ GeV}$ ,  $\Gamma_A/m_A = 2\%$  for A and  $m_H = 925 \text{ GeV}$ ,  $\Gamma_H/m_H = 3\%$  for H. The upper panel shows the sum of the background simulation (colored bars) and the observed data (black dots), while the lower panel shows the ratio of the data to the prediction with the postfit A and H signals, as well as their sum, overlaid.

3057 The same excess close to the  $t\bar{t}$  threshold already seen in Sec. 7.7.1 manifests as  
 3058 of a non-zero value of  $g_{A\bar{t}\bar{t}}$ , which Fig. 7.22 shows is preferred by more than five  
 3059 standard deviations, similar as for the interpretation in terms of  $\eta_t$ . In addition,  
 3060 there is also a preference for a non-zero value of  $g_{H\bar{t}\bar{t}}$ , though this is significant only  
 3061 at about 2 standard deviations and could thus be a simple statistical fluctuation.  
 3062 It should be noted that both of these values are local significances, i.e. they do not  
 3063 account for the look-elsewhere effect. The source of this preference is again evident  
 3064 from Fig. 7.21: it is due to a mild, broad excess in events compared to the prediction  
 3065 around  $m_{t\bar{t}} \approx 900 \text{ GeV}$ , which is more pronounced in the low  $c_{\text{han}}$  bins compared to  
 3066 the others as would be expected for a scalar particle H.

3067 It is important to stress that these results do not constitute any observation of a  
 3068 new BSM particle. Given the experimental resolution in  $m_{t\bar{t}}$ , as well as the signal  
 3069 mass points available, the  $t\bar{t}$  bound state  $\eta_t$  and a BSM pseudoscalar A cannot be  
 3070 conclusively distinguished.

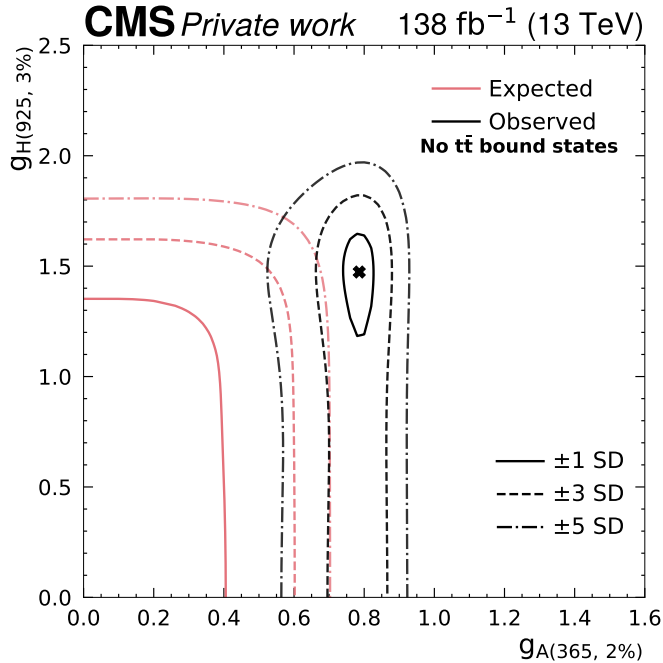


Figure 7.22: **Allowed coupling region in the A+H fit.** The two-dimensional allowed region for the coupling modifiers  $g_{A\bar{t}\bar{t}}$  and  $g_{H\bar{t}\bar{t}}$  in the A+H fit, for the best-fit A/H masses and widths of  $m_A = 365 \text{ GeV}$ ,  $\Gamma_A/m_A = 2\%$  for A and  $m_H = 925 \text{ GeV}$ ,  $\Gamma_H/m_H = 3\%$  for H, obtained through a scan of the profiled likelihood. The observed region is shown in black, while the SM expectation is shown in pink.

## 3071 7.8 Limits on A/H bosons

3072 Having discussed the excess seen at the  $t\bar{t}$  threshold and its possible interpretations,  
 3073 in this section exclusion limits on A/H bosons in the full considered mass range are  
 3074 presented. This is done for two different scenarios: In the first scenario, denoted  
 3075 “A/H only”, the SM  $t\bar{t}$  background is described by the FO pQCD prediction from  
 3076 POWHEG + PYTHIA reweighted to NLO EW and NNLO QCD, same as for the  $\eta_t$   
 3077 extraction in Sec. 7.7.1 and for the A+H fit in Sec. 7.7.4. The observed excess is thus  
 3078 expected to manifest in the limits in the form of a weaker observed than expected  
 3079 limit for low A/H masses.

3080 In the second scenario, denoted “A/H +  $\eta_t$ ”, the observed excess is assumed to  
 3081 originate solely from a  $t\bar{t}$  bound state, which is further assumed to be well described  
 3082 by the  $\eta_t$  model. Under this assumption, the  $\eta_t$  contribution is added to the  $t\bar{t}$   
 3083 background prediction, with a free-floating normalization as an additional nuisance  
 3084 parameter. A and/or H contributions are then considered as signals on top of this  
 3085 background. It should be stressed that, while Fig. 7.14 shows good agreement of the

3086  $\eta_t$  description with the data, the true cause of the excess cannot be fully determined  
 3087 with the available  $m_{t\bar{t}}$  resolution. Thus, all limits shown here should be treated with  
 3088 caution for low values of the A/H mass.

3089 In both scenarios, the limits are calculated with the  $CL_s$  prescription as introduced  
 3090 in Sec. 4.4. However, a complication is presented by the non-linearity of the A/H  
 3091 signal as a function of  $g_{A/Ht\bar{t}}$ , due to which the distribution of the test statistic is  
 3092 not necessarily  $\chi^2$ -distributed, and thus the  $p$ -values  $p_{s+b}$  and  $p_b$  cannot be easily  
 3093 computed. To avoid having to perform computationally expensive toy experiments,  
 3094 a *raster scan* method is used in the same way as in Ref. [17]. For a given A/H  
 3095 mass and width point, the coupling modifier  $g_{A/Ht\bar{t}}$  is scanned in the range 0–5.  
 3096 For each value of  $g_{A/Ht\bar{t}}$ , the total signal contribution is computed as the sum of  
 3097 the resonant signal, scaling with  $g_{A/Ht\bar{t}}^4$ , and the SM-signal interference, scaling with  
 3098  $g_{A/Ht\bar{t}}^2$ . An auxiliary linear signal strength  $\mu$  is then introduced, so that the total  
 3099 signal contribution becomes

$$s(\mu) = \mu \left( g_{A/Ht\bar{t}}^4 s_{\text{res}} + g_{A/Ht\bar{t}}^2 s_{\text{int}} \right) \quad (7.18)$$

3100 where  $s_{\text{res}}$  and  $s_{\text{int}}$  are the resonance and interference contributions, respectively,  
 3101 and  $g_{A/Ht\bar{t}}$  is held fixed.  $\mu = 1$  corresponds to the probed A/H signal, while  $\mu = 0$   
 3102 corresponds to the SM. Intermediate values of  $\mu$  are in principle unphysical since  
 3103 they do not correspond to any value of  $g_{A/Ht\bar{t}}$ .

3104 Since the A/H signal now scales linearly with  $\mu$ , the usual asymptotic approxima-  
 3105 tion can be used to obtain the  $CL_s$  value for  $\mu = 1$ . It has been shown as a part of  
 3106 Ref. [17] that the distribution of the test statistic obtained in this way approximates  
 3107 well the true test statistic for  $g_{A/Ht\bar{t}}$  as evaluated using toy experiments. This pro-  
 3108 cedure is repeated for all values of  $g_{A/Ht\bar{t}}$ , and a value of  $g_{A/Ht\bar{t}}$  is, as usual, excluded  
 3109 at 95% confidence level when the  $CL_s$  value drops below 0.05.

3110 The resulting observed and expected limits for all considered A and H masses and  
 3111 six representative width choices are shown in Figs. 7.23 and 7.24 for the “A/H only”  
 3112 scenario and in Figs. 7.25 and 7.26 for the “A/H +  $\eta_t$ ” scenario. In the “A/H only”  
 3113 scenario, the excess at the  $t\bar{t}$  threshold is visible at low A/H masses as expected. It is  
 3114 stronger for the pseudoscalar A than for the scalar H, consistent with the results  
 3115 in Sec. 7.7.2. In the “A/H +  $\eta_t$ ” scenario, the excess is fully absorbed by the  $\eta_t$   
 3116 contribution, and the observed and expected limits at low A/H masses agree. It is  
 3117 notable here that the expected limits change only little between the scenarios even  
 3118 though, in the “A/H +  $\eta_t$ ” scenario, the cross section of the  $\eta_t$  contribution is freely  
 3119 floating in the fit. This implies that, for those values of  $g_{A/Ht\bar{t}}$  corresponding to the  
 3120 expected limits, the simple peak of  $\eta_t$  can to a degree be distinguished from the  
 3121 peak-dip structure of A/H production by the fit. **TODO decide on whether I want**  
 3122 **to elaborate on this, would need a plot of the signal templates**

3123 Furthermore, the mild excess for H at high masses as seen in Fig. 7.22 is repro-  
 3124 duced in the limits on  $g_{Ht\bar{t}}$  in both scenarios in the approximate range of  $900 <$

<sup>3125</sup>  $m_H < 1000 \text{ GeV}$ .

## <sup>3126</sup> 7.9 Combination with the $\ell+\text{jets}$ channels

<sup>3127</sup> So far, all results in this section have covered only the dilepton decay channel of  $t\bar{t}$ ,  
<sup>3128</sup> which was analyzed as part of this thesis. In Ref. [9], the results on A/H bosons  
<sup>3129</sup> are combined with a separate analysis of the  $\ell+\text{jets}$  decay channel. The combina-  
<sup>3130</sup> tion (but not the  $\ell+\text{jets}$  analysis) was also performed as part of this thesis, and is  
<sup>3131</sup> presented in this chapter. The  $\ell+\text{jets}$  analysis strategy is roughly outlined in the  
<sup>3132</sup> following, for a more complete description, see Ref. [9].

### <sup>3133</sup> 7.9.1 Analysis strategy in the $\ell+\text{jets}$ channel

<sup>3134</sup> In the  $\ell+\text{jets}$  channel, events with exactly one lepton and at least three jets are  
<sup>3135</sup> selected, of which at least two need to be b tagged. In addition to the criteria  
<sup>3136</sup> outlined in Sec. 7.2.2, both the lepton and the jets are required to fulfill  $p_T > 30 \text{ GeV}$   
<sup>3137</sup> to account for the higher single-lepton trigger thresholds. Furthermore, the cut-  
<sup>3138</sup> based identification criteria for electrons, as described in Ref. [111], are applied  
<sup>3139</sup> instead of MVA-based criteria. Similar as in the dilepton channel, the events are  
<sup>3140</sup> categorized by the flavor of the lepton into the  $e+\text{jets}$  and  $\mu+\text{jets}$  channels.

<sup>3141</sup> The algorithm described in Ref. [228] is used to reconstruct the neutrino from the  
<sup>3142</sup> leptonic top decay. It enforces mass constraints on the W boson and leptonically  
<sup>3143</sup> decaying top quark and then minimizes the distance  $D_\nu = |p_T^\nu - p_T^{\text{miss}}|$  between the  
<sup>3144</sup> neutrino  $p_T$  and the missing transverse momentum. In events with four or more jets,  
<sup>3145</sup> the same distance  $D_\nu$  is then also used to assign the jets to the b and  $\bar{b}$  candidates  
<sup>3146</sup> as well as to the decay products of the hadronically decaying W boson. From this,  
<sup>3147</sup> the  $t\bar{t}$  system can then be reconstructed. In events with exactly three jets, where  
<sup>3148</sup> information has been lost due to either an out-of-acceptance jet or the merger of  
<sup>3149</sup> two jets into one, additional steps have to be taken. The procedure described in  
<sup>3150</sup> Ref. [229] is applied to these events, which involves applying an energy correction  
<sup>3151</sup> factor to the four-momentum of the hadronically decaying top quark, depending on  
<sup>3152</sup> its reconstructed mass. Since the resolution of this procedure is necessarily worse  
<sup>3153</sup> than for events where all jets are available, events with three jets and four or more  
<sup>3154</sup> jets are treated as separate categories in the fit.

<sup>3155</sup> A two-dimensional template is constructed from the reconstructed value of  $m_{t\bar{t}}$   
<sup>3156</sup> as well as  $|\cos \theta_\ell^*|$ , where  $\theta_\ell^*$  is the scattering angle of the leptonically decaying top  
<sup>3157</sup> quark with respect to the direction of flight of the  $t\bar{t}$  system in the laboratory frame.  
<sup>3158</sup> This variable is sensitive to the spin of a possible mediator in  $t\bar{t}$  production: For  
<sup>3159</sup> spin-0 mediators like A/H, the top quarks are emitted isotropically in the  $t\bar{t}$  rest  
<sup>3160</sup> frame, leading to a flat distribution of  $|\cos \theta_\ell^*|$ , while in the SM  $|\cos \theta_\ell^*|$  peaks at  
<sup>3161</sup> high values. However, it is not sensitive to the  $\mathcal{CP}$  structure of the mediator, in

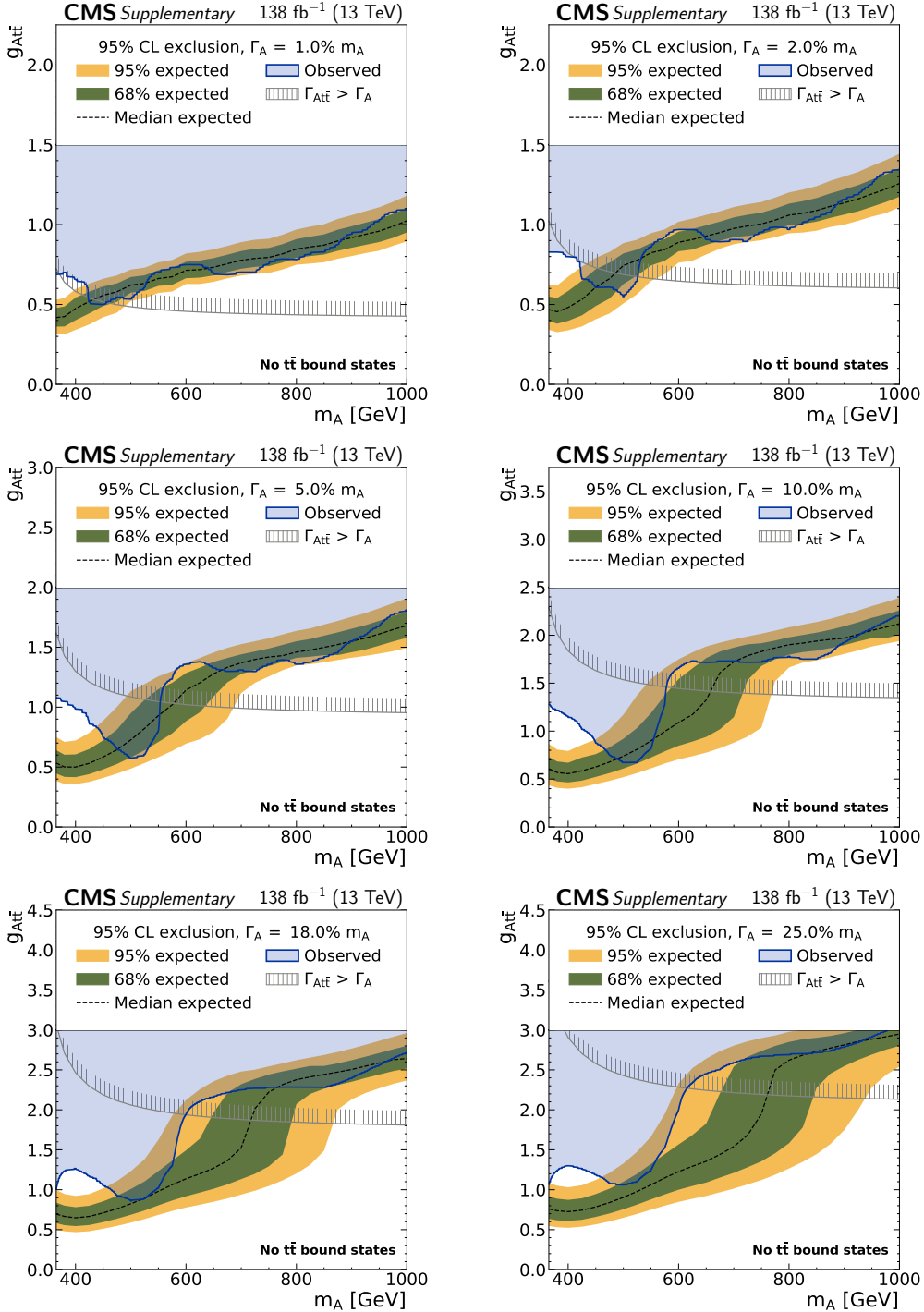


Figure 7.23: **Exclusion limits on  $g_{A\bar{t}\bar{t}}$  in the “A only” scenario** in the dilepton channels as a function of the mass of the A boson for relative widths of 1, 2, 5, 10, 18, and 25% (from upper left to lower right). The observed limits are indicated by the blue shaded area, and the inner green band and the outer yellow band indicate the regions containing 68 and 95%, respectively, of the distribution of limits expected under the background-only hypothesis. The unphysical region of phase space in which the partial width  $\Gamma_{A\rightarrow t\bar{t}}$  becomes larger than the total width of A is indicated by the hatched line.<sup>139</sup>

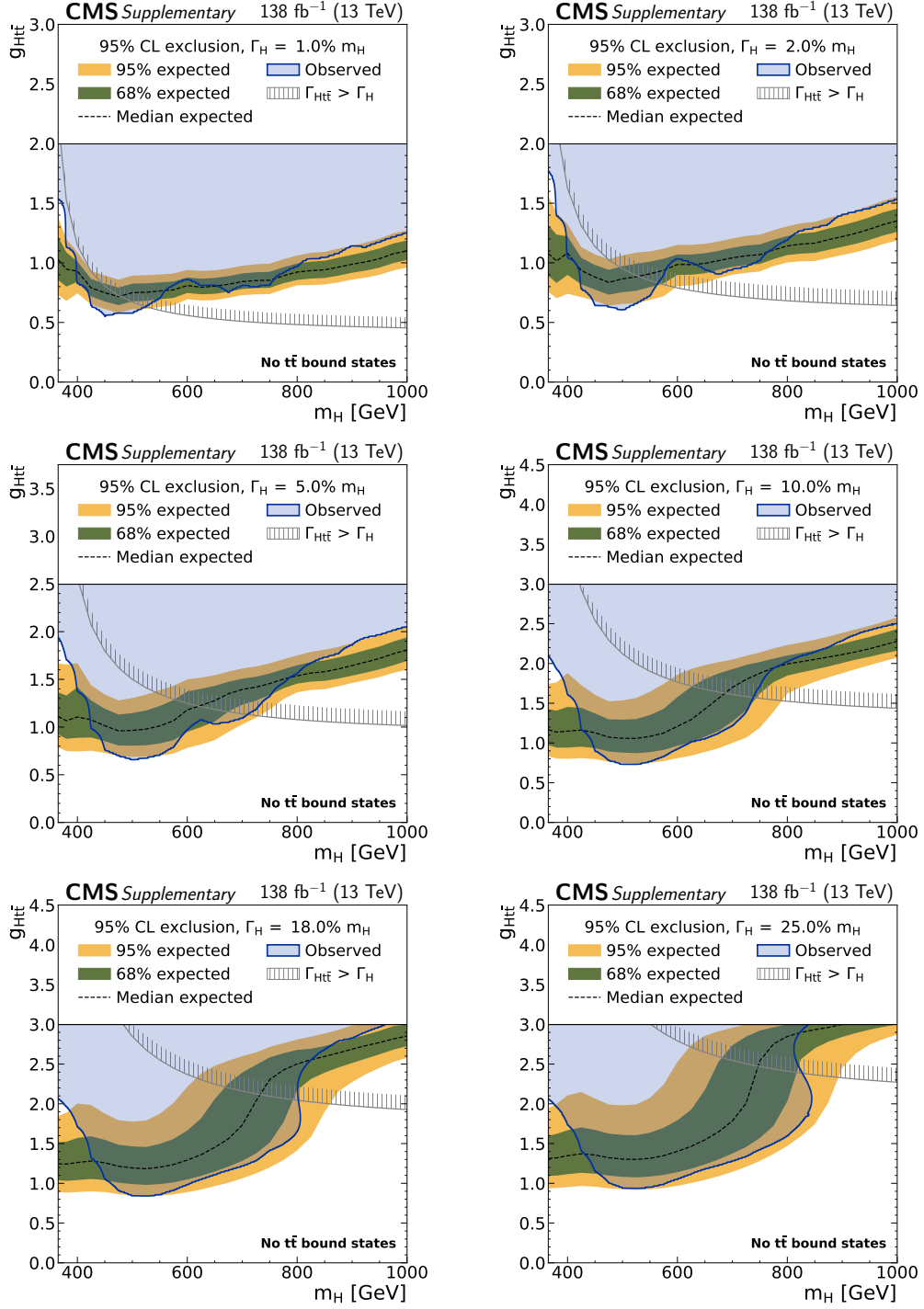


Figure 7.24: **Exclusion limits on  $g_{Htt}$  in the “H only” scenario** in the dilepton channels as a function of the mass of the H boson. Notations are equivalent to Fig. 7.23.

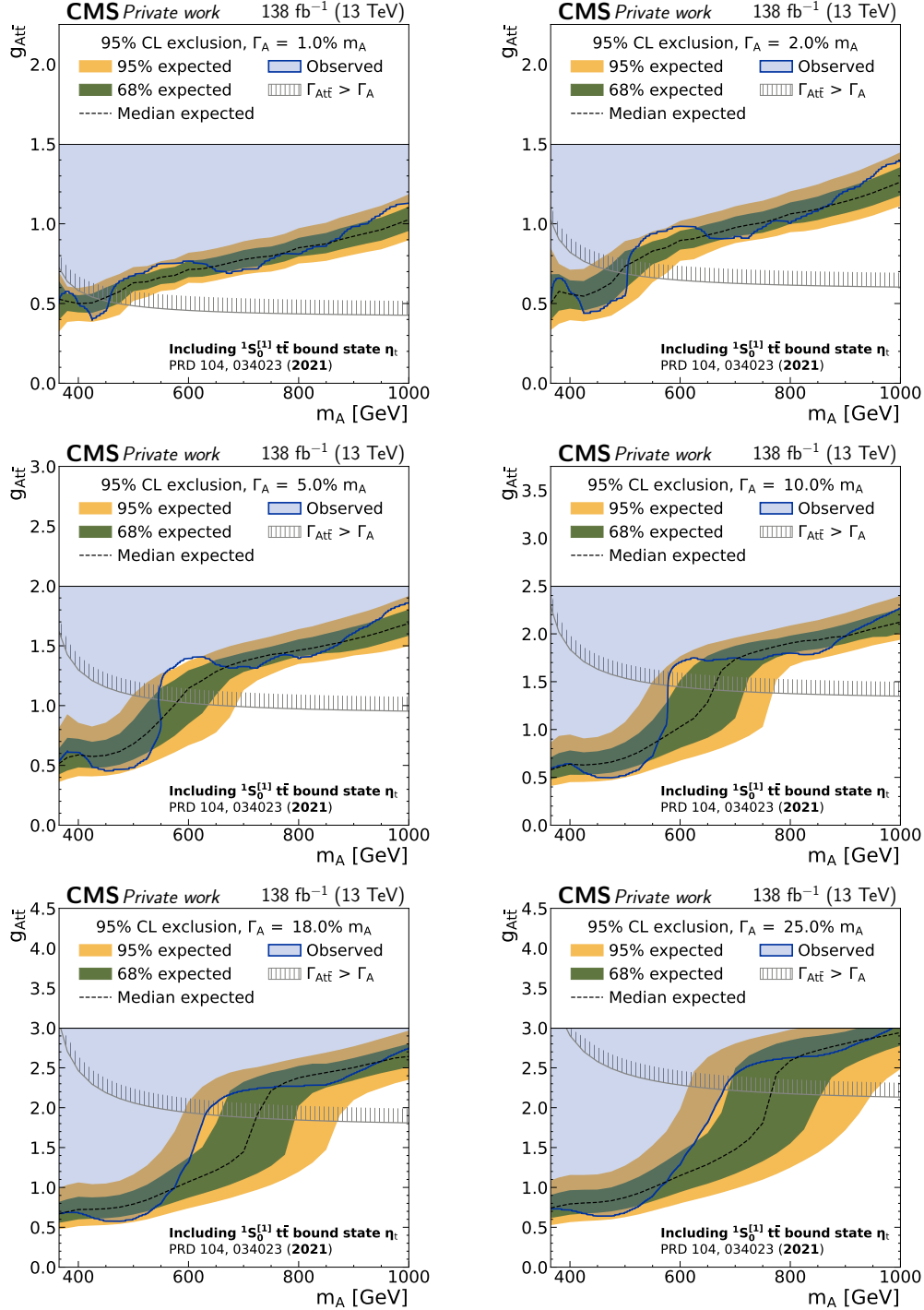


Figure 7.25: **Exclusion limits on  $g_{A\bar{t}\bar{t}}$  in the “A +  $\eta_t$ ” scenario** in the dilepton channels as a function of the mass of the A boson. Notations are equivalent to Fig. 7.23.

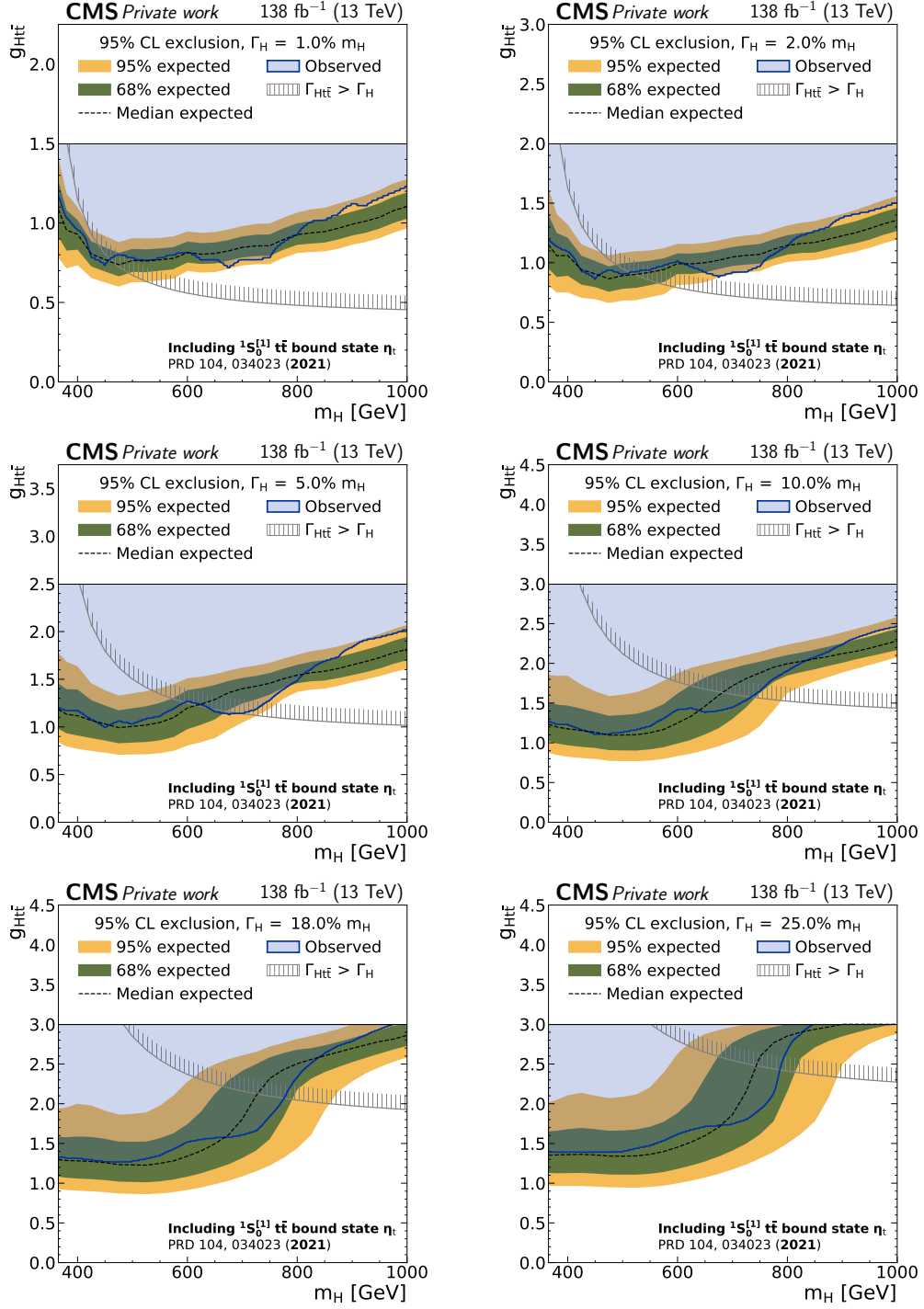


Figure 7.26: **Exclusion limits on  $g_{H\bar{t}\bar{t}}$  in the “H +  $\eta_t$ ” scenario** in the dilepton channels as a function of the mass of the H boson. Notations are equivalent to Fig. 7.23.

contrast to  $c_{\text{hel}}$  and  $c_{\text{han}}$ . Furthermore, the SM prediction changes as a function of  $m_{t\bar{t}}$ ; close to the  $t\bar{t}$  threshold, the difference to a flat spectrum is rather small, while for high  $m_{t\bar{t}}$  the difference is large due to the impact of the  $q\bar{q}$  initial state.

The  $t\bar{t}$  and  $tW$  background predictions as well as the A/H signals are estimated using the same MC simulation as in the dilepton channels. Additionally, there is a significant background contribution from QCD multijet production with a fake or non-prompt lepton as well as EW processes such as  $W+jets$  production. These are difficult to model using MC, and are instead estimated together by a data-driven approach (cf. Sec. 5.3.2). A sideband in which the b tagging requirement on the jets is inverted is used for this purpose; details can be found in Ref. [9].

The dilepton and  $\ell$ +jets channels are directly combined by performing a simultaneous likelihood fit to all categories. Systematic uncertainties related to modeling of the  $t\bar{t}$  and  $tW$  backgrounds are treated as fully correlated, while experimental uncertainties as well as uncertainties of the other minor backgrounds can be correlated or uncorrelated as appropriate. Again, both the “A/H only” and “A/H +  $\eta_t$ ” scenarios are considered. For the latter, the  $\ell$ +jets analysis uses a slightly different  $\eta_t$  model, in which the width of the bound state is set to  $\Gamma(\eta_t) = 7 \text{ GeV}$  and a cut on the invariant mass  $m_{WWb\bar{b}}$  is applied, as described in Sec. 2.2.3. For the sake of consistency, the same model is also used in the dilepton channels when performing the combination only. The resulting impact on the limits from the choice of  $\eta_t$  model is expected to be small.

### 7.9.2 A/H limits

The resulting observed and expected limits for the combination of both channels are found in Figs. 7.27 to 7.30 for both scenarios. It can be seen that the large excess for low A/H masses is still present in the channel combination in the “A/H only” scenario, and is again stronger for the pseudoscalar A. The mild excess for the scalar H at  $m_H \approx 925 \text{ GeV}$ , on the other hand, is not confirmed in the channel combination.

To assess the impact of the different channels, the expected limits for the dilepton and  $\ell$ +jets channels alone are also shown in red and orange, respectively. For most of the phase space, the  $\ell$ +jets channel leads to stronger limits than the dilepton channel, which is likely mostly due to the higher branching ratio and thus higher available statistics as well as the better  $m_{t\bar{t}}$  resolution in the  $\ell$ +jets channel especially at high  $m_{t\bar{t}}$ . The difference is large at high A and H masses, where the contribution from the dilepton channels is rather small, while the dilepton channel becomes much more important for low masses, i.e. close to the  $t\bar{t}$  threshold. This could be because of the lack of sensitivity of  $|\cos \theta_\ell^*|$  close to the  $t\bar{t}$  threshold, while  $c_{\text{hel}}$  and  $c_{\text{han}}$  do not suffer from such a problem. For H at low masses in particular, the dilepton channel in fact gives stronger limits than  $\ell$ +jets due to the sensitivity of  $c_{\text{han}}$  to scalar mediators.

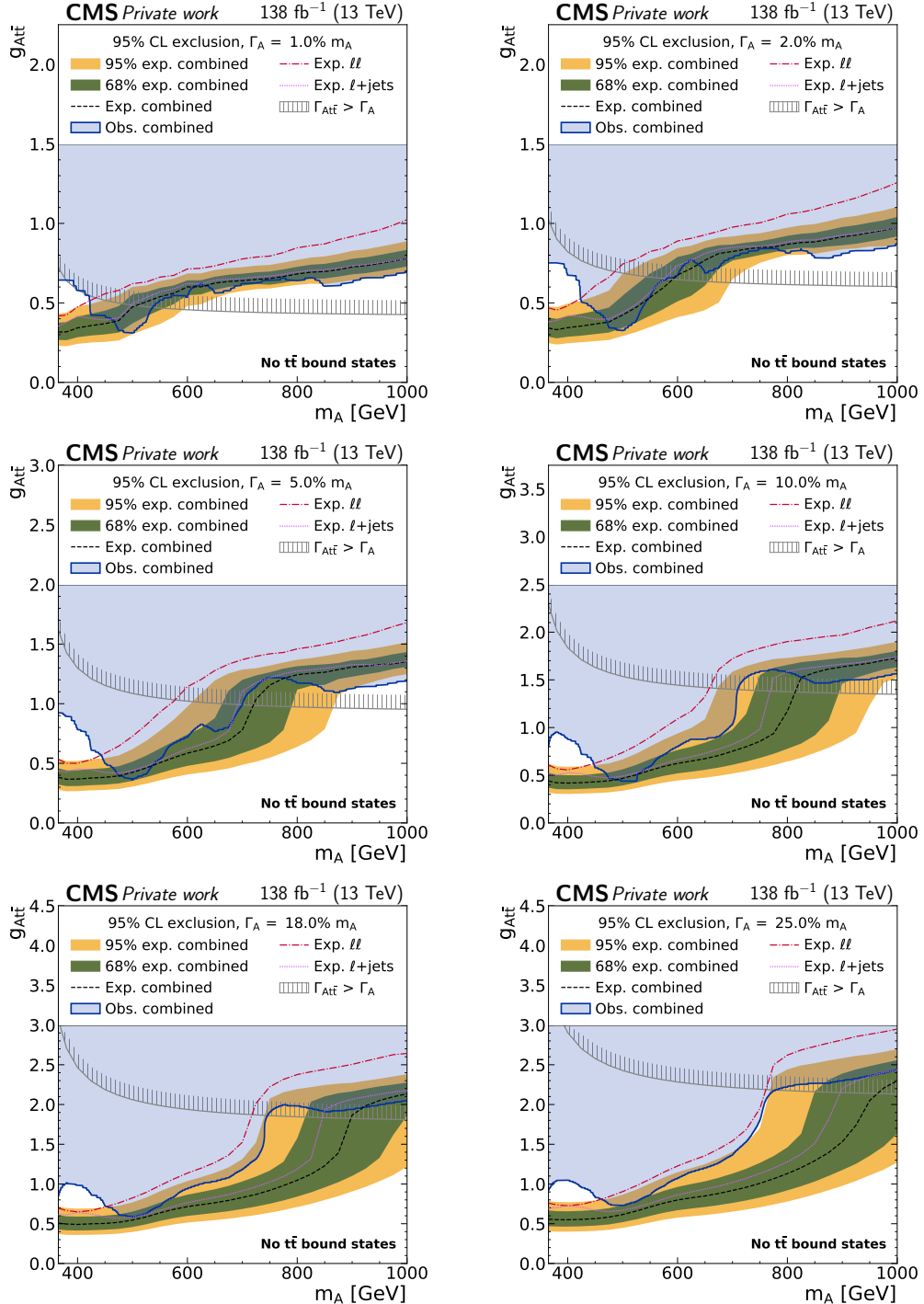


Figure 7.27: **Combined exclusion limits on  $g_{At̄}$  in the “A only” scenario** in the dilepton and  $\ell+\text{jets}$  channels as a function of the mass of the A boson. The expected limits in the dilepton and  $\ell+\text{jets}$  channels alone are shown as the red and purple lines for comparison. Otherwise, notations are equivalent to Fig. 7.23. *Figure adapted from Ref. [9].*

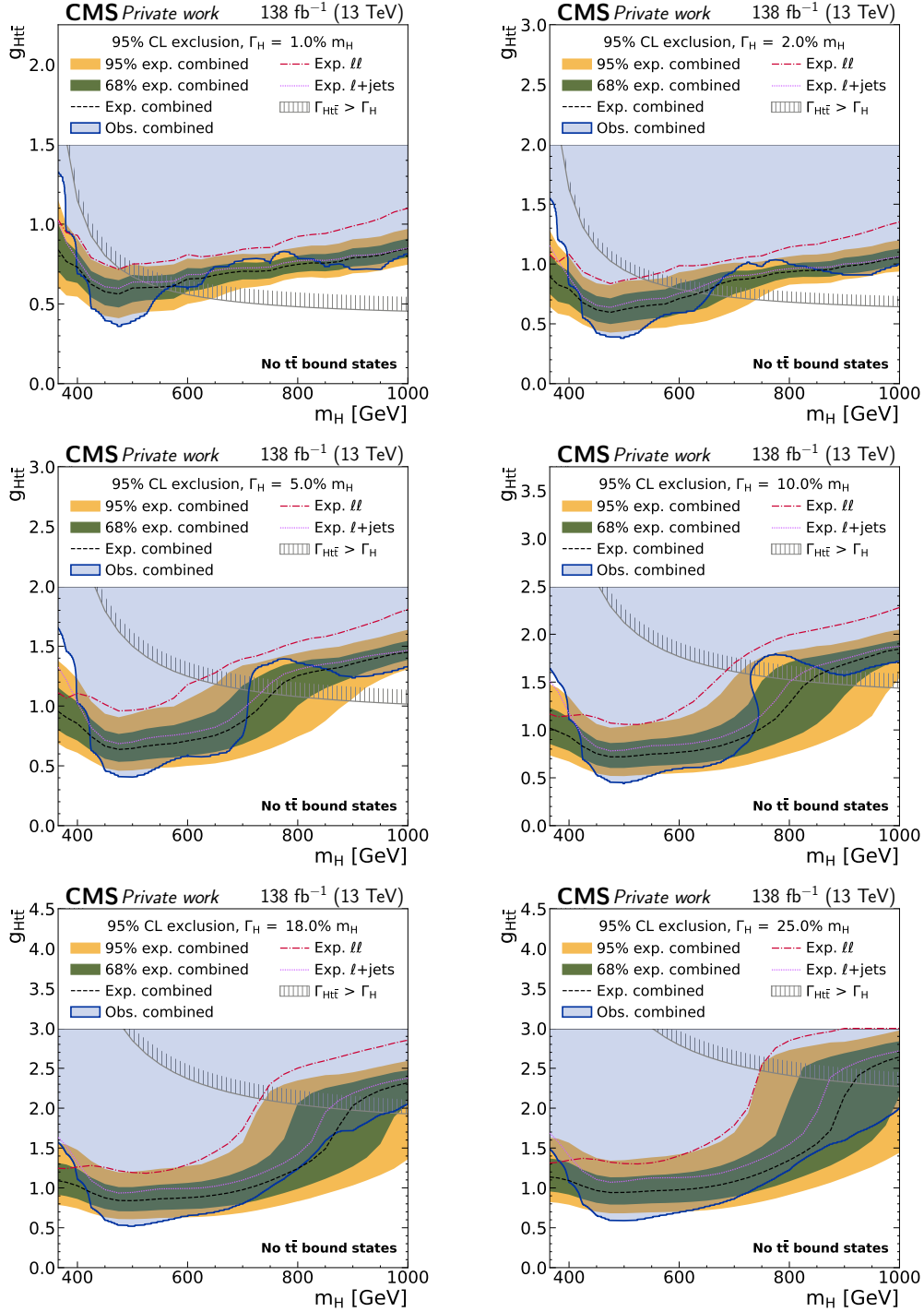


Figure 7.28: **Combined exclusion limits on  $g_{H\bar{t}\bar{t}}$  in the “H only” scenario** in the dilepton and  $\ell$ +jets channels as a function of the mass of the H boson. Notations are equivalent to Fig. 7.27. *Figure adapted from Ref. [9].*

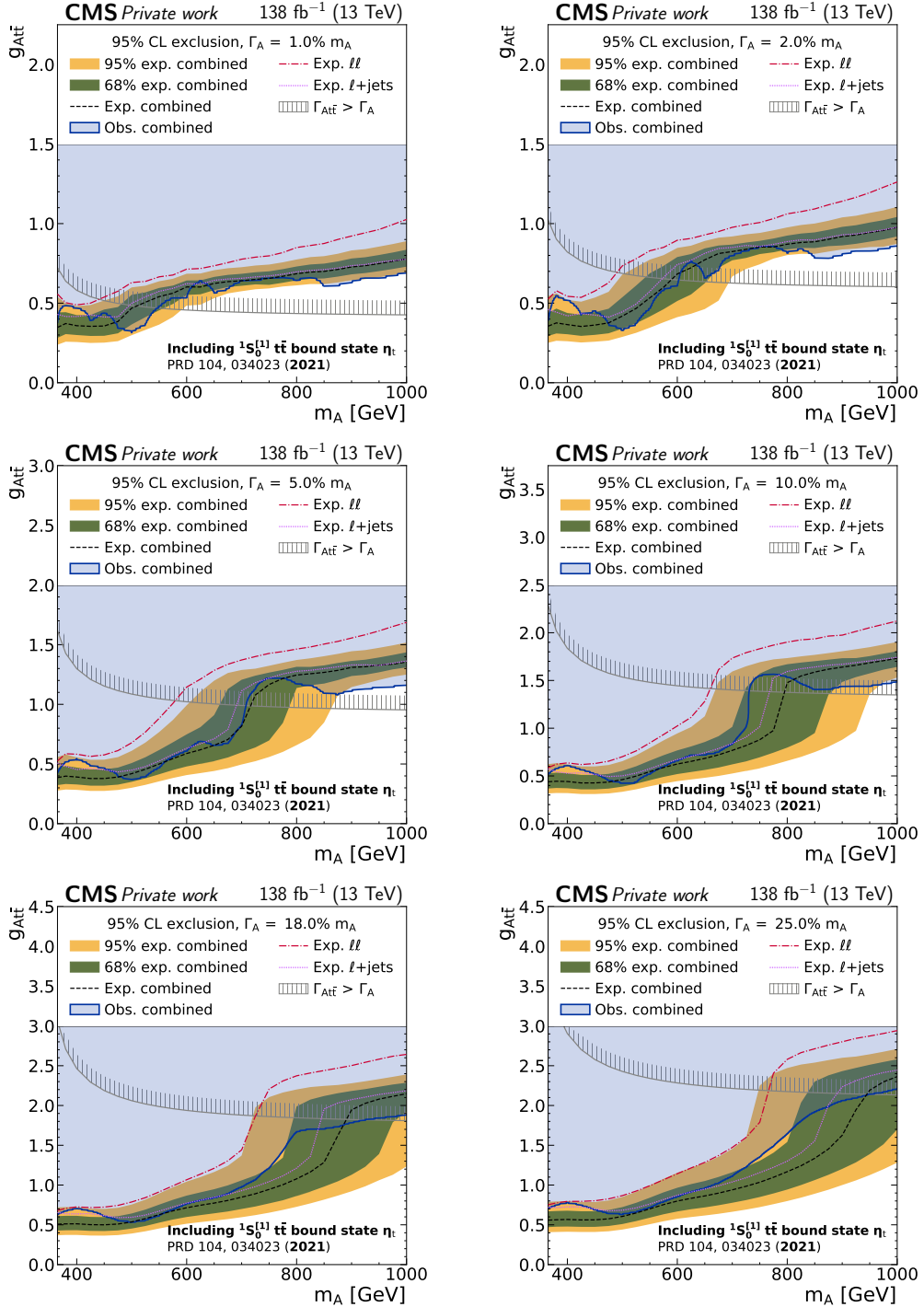


Figure 7.29: **Combined exclusion limits on  $g_{A\bar{t}}$  in the “A +  $\eta_t$ ” scenario** in the dilepton and  $\ell+$  jets channels as a function of the mass of the A boson. Notations are equivalent to Fig. 7.27. *Figure adapted from Ref. [9].*

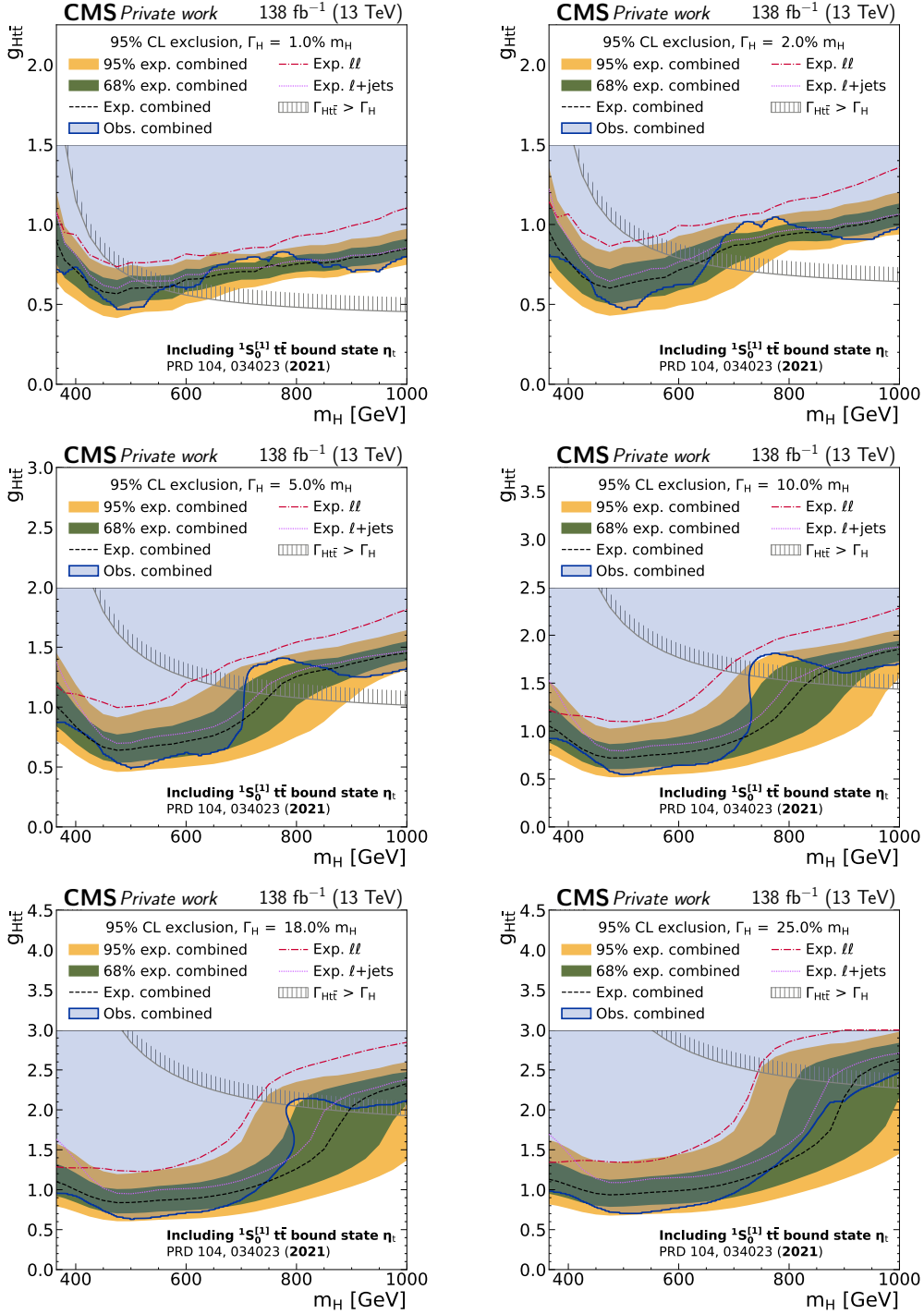


Figure 7.30: **Combined exclusion limits on  $g_{Ht\bar{t}}$  in the “H +  $\eta_t$ ” scenario** in the dilepton and  $\ell$ +jets channels as a function of the mass of the H boson. Notations are equivalent to Fig. 7.27. *Figure adapted from Ref. [9].*

### 3202 7.9.3 Simultaneous A+H exclusion contours

3203 In many possible BSM scenarios, multiple additional spin-0 states are expected at  
3204 the same time, such as A and H in e.g. the 2HDM (cf. Sec. 2.3.2). Often, the  
3205 masses of these scalars are close together since they originate from new physics at  
3206 the same energy scale, in which case their signatures would not easily factorize. It  
3207 is thus useful for future interpretations of the results to show exclusion contours not  
3208 only for either A or H, but for the simultaneous presence of both at the same time.

3209 To do so, simultaneous fits are performed with both A and H as freely floating  
3210 signals as in Sec. 7.7.4. Frequentist exclusion contours are set with the Feldman–  
3211 Cousins prescription [230, 231], in which the test statistic is numerically evaluated  
3212 using toy experiments at each point in the  $g_{A\bar{t}}\text{-}g_{H\bar{t}}$  plane. This procedure is fully  
3213 correct in the Frequentist sense and does not rely on approximations of the test  
3214 statistic, which are not guaranteed to hold for two non-linear signals, but is computa-  
3215 tionally expensive.

3216 Due to this, combined with the large four-dimensional phase space of possible  
3217 signals, only a few example mass and width points are shown in this work, and only  
3218 for the dilepton and  $\ell+\text{jets}$  combination in the “A/H +  $\eta_t$ ” scenario. They can be  
3219 found in Fig. 7.31 for the case of identical A and H masses as well as in Fig. 7.32 for  
3220 differing A and H masses. Alternatively, a coarse scan of the negative log-likelihood  
3221 of the full span is available online as part of the HepData record [232].

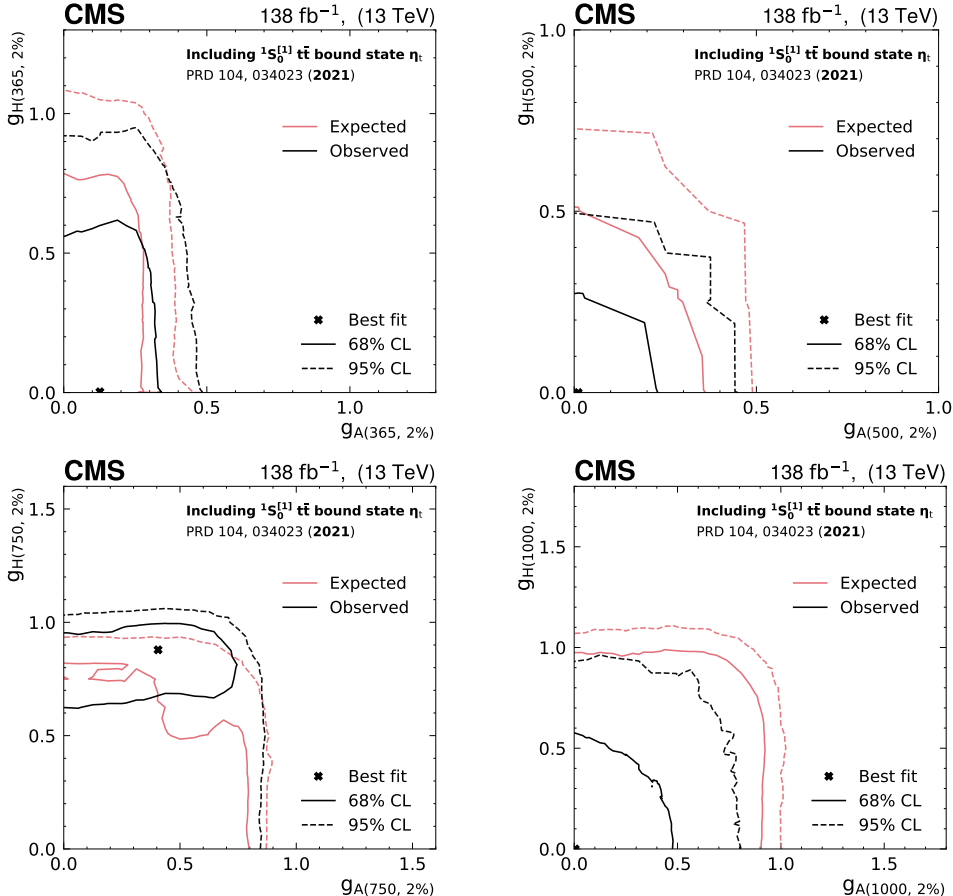


Figure 7.31: **Frequentist 2D exclusion contours for  $g_{A\bar{t}\bar{t}}$  and  $g_{H\bar{t}\bar{t}}$**  for four different signal hypotheses with identical A and H masses of 365 GeV (upper left), 500 GeV (upper right), 750 GeV (lower left) and 1000 GeV (lower right), all assuming a width of 2%. In all cases,  $\eta_t$  production is added to the background. *Figure taken from Ref. [9].*

## 3222 7.10 Comparison to other results

### 3223 7.10.1 ATLAS $t\bar{t}$ threshold measurement

3224 After this work was made public, the ATLAS Collaboration presented preliminary  
 3225 results for a similar measurement at the  $t\bar{t}$  threshold in Ref. [188], which confirmed  
 3226 the presence of a pseudoscalar excess over the  $t\bar{t}$  continuum prediction.

3227 The ATLAS result uses a very similar setup as presented in this work. It like-  
 3228 wise considers only the dilepton decay channel of  $t\bar{t}$ , uses the full Run 2 dataset  
 3229 (corresponding to  $140 \text{ fb}^{-1}$  for ATLAS), reconstructs the  $t\bar{t}$  system using a similar  
 3230 algorithm, and finally bins in  $m_{t\bar{t}}$ ,  $c_{\text{hel}}$  and  $c_{\text{han}}$  to extract the  $t\bar{t}$  bound state compo-

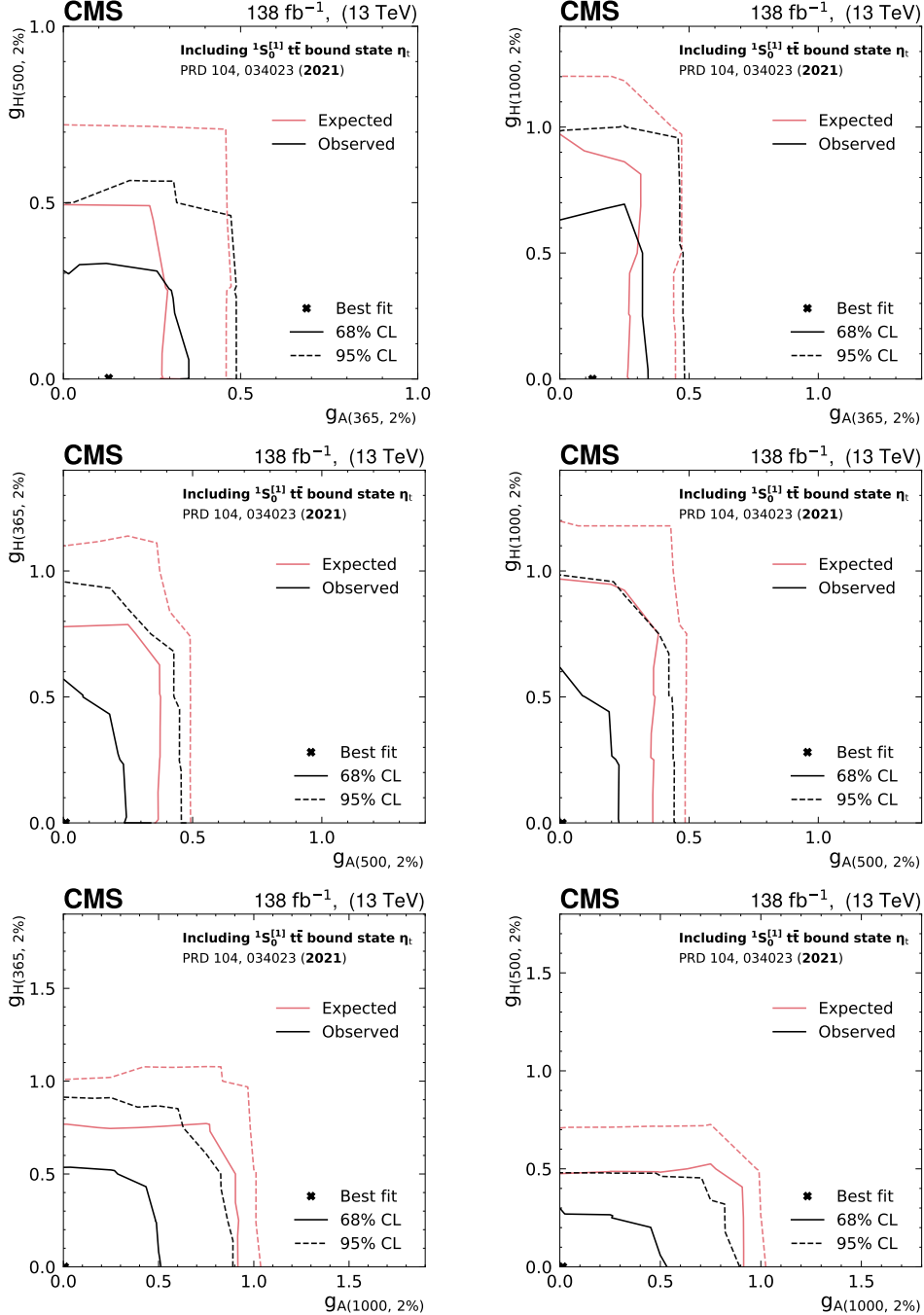


Figure 7.32: **Frequentist 2D exclusion contours for  $g_{At\bar{t}}$  and  $g_{Ht\bar{t}}$**  for six different signal hypotheses with differing A and H masses, corresponding to combinations of 365 GeV, 500 GeV and 1000 GeV, all assuming a width of 2%. In all cases,  $\eta_t$  production is added to the background. *Figure taken from Ref. [9].*

3231    uent using a simplified model. The binning in  $c_{\text{hel}}$  and  $c_{\text{han}}$  is identical to this work,  
 3232    while in  $m_{t\bar{t}}$  only four bins of 50 GeV width around the  $t\bar{t}$  threshold are considered.  
 3233    Events with high values of  $m_{t\bar{t}}$  are rejected. In the following, some further significant  
 3234    differences between the CMS and ATLAS results are briefly described.

3235    First, ATLAS considers two additional sets of control regions (CRs) which are  
 3236    directly included in the likelihood fit. One is defined by requiring  $m_{\ell\ell}$  to be within the  
 3237    vicinity of the Z boson mass, similar to the Z+jets scale factor estimation described  
 3238    in Secs. 5.3.2 and 7.2.4, and serves the same purpose of correcting the yield of the  
 3239    Z+jets simulation after the b tagging requirement. The other set of CRs targets  
 3240    fake or non-prompt leptons and is defined by requiring the two selected leptons to  
 3241    have the same charge. The dominant contribution here comes from  $t\bar{t} \rightarrow \ell + \text{jets}$   
 3242    events with an additional fake or non-prompt lepton. Such a CR is not included  
 3243    in the CMS result; it has however been internally checked using a similar selection  
 3244    that the data is well-described by the  $t\bar{t} \rightarrow \ell + \text{jets}$  MC simulation.

3245    Second, ATLAS employs a different systematics model, in particular for uncer-  
 3246    tainties related to the modeling of the  $t\bar{t}$  continuum. Notable differences are:

- 3247    • the ME scale uncertainties are estimated at NNLO by varying the scales in  
 3248      the reweighting to NNLO QCD and NLO EW (which is performed using the  
 3249      same tools as used here);
- 3250    • no uncertainty due to a variation of the top-SM Higgs Yukawa coupling is  
 3251      considered;
- 3252    • two-point uncertainties comparing the `hvq` + PYTHIA prediction to `hvq` +  
 3253      herwig as well as to `bb4l` + PYTHIA are included in the nominal result, similar  
 3254      as in Ref. [8] and in Sec. 7.7.3; these uncertainties are treated as partially (50%)  
 3255      decorrelated between the nine bins of  $c_{\text{hel}}$  and  $c_{\text{han}}$ ;
- 3256    • an additional ME-PS matching uncertainty is defined by varying the parameter  
 3257       $p_T^{\text{hard}}$  in PYTHIA [85];
- 3258    • an additional uncertainty due to the top recoil scheme in PYTHIA (cf. Sec. 6.5.3)  
 3259      is considered.

3260    In total, this results in significantly more degrees of freedom in the fit used by  
 3261    ATLAS than the one used by CMS.

3262    Third, the nominal model used by ATLAS to probe  $t\bar{t}$  bound state effects is based  
 3263    on Ref. [39], which includes a matrix-element level reweighting to an NRQCD cal-  
 3264    culation. As discussed in Sec. 2.2.3, this model could not be sufficiently scrutinized  
 3265    for inclusion in the results of this work, and particularly the modeling of spin corre-  
 3266    lations and the matching to the  $t\bar{t}$  continuum is under question. Using this model,  
 3267    ATLAS extracts a cross section of  $9.0 \pm 1.3 \text{ pb}$  [188].

3268 However, ATLAS also provides results using the same  $\eta_t$  model considered in  
3269 this work, using the same values for the  $\eta_t$  mass and width, which gives  $\sigma(\eta_t) =$   
3270  $13.4 \pm 1.9 \text{ pb}$  [188]. This figure is more appropriate to compare to the result of this  
3271 work,  $\sigma(\eta_t) = 8.7 \pm 1.1 \text{ pb}$ . The results are thus in tension with each other at the  
3272 level of ca. 2 standard deviations. Since the ATLAS results are preliminary and  
3273 very recent at the time of writing, the source of this tension is not yet known. It  
3274 will be the task of future studies and comparisons between the experiments to shed  
3275 further light on this topic.

### 3276 7.10.2 ATLAS A/H $\rightarrow t\bar{t}$ search

3277 Before the appearance of this result and Ref. [188], the ATLAS collaboration pre-  
3278 sented a similar search for heavy pseudoscalar or scalar bosons in  $t\bar{t}$  events using  
3279 the full LHC Run 2 data set in Ref. [187], and observed no excess at the  $t\bar{t}$  thresh-  
3280 old. To decide whether that result contradicts the one presented here as well as the  
3281 preliminary ATLAS result of Ref. [188], it is necessary to understand the differences  
3282 between the analyses.

3283 Ref. [187] combines the dilepton and  $\ell+\text{jets}$  decay channels of  $t\bar{t}$ , similar to the  
3284 combination presented in Sec. 7.9 for A and H, though the definitions of the chan-  
3285 nels are different: In the  $\ell+\text{jets}$  channel, ATLAS does not consider events with only  
3286 three jets as described in Sec. 7.9.1, but instead includes events with only one b  
3287 tag in addition to events with two or more b tags. Furthermore, ATLAS defines an  
3288 additional category with  $\ell+\text{jets}$  events in which the decay products of the hadroni-  
3289 cally decaying top quark are merged, though this is expected to contribute mostly  
3290 at high  $m_{t\bar{t}}$ .

3291 In the dilepton channels, Ref. [187] uses a fundamentally different strategy than  
3292 the one presented in this work. Instead of performing an explicit  $t\bar{t}$  reconstruction,  
3293 thus giving access to  $m_{t\bar{t}}$  and the spin correlation observables  $c_{\text{hel}}$  and  $c_{\text{han}}$ , Ref. [187]  
3294 simply uses the invariant mass  $m_{b\bar{b}\ell\ell}$  of the visible decay products as well as  $\Delta\phi_{\ell\ell}$ ,  
3295 the azimuthal distance between the two leptons in the laboratory frame. The former  
3296 can be considered a proxy for  $m_{t\bar{t}}$ , though with significant smearing due to the loss  
3297 of information from the two neutrinos, as also studied in Sec. 7.7.3. The latter has  
3298 indirect sensitivity to the  $t\bar{t}$  spin correlation, but this sensitivity is intermixed with  
3299 kinematic information due to the boosts of the leptons from their top quark parents.  
3300 As a result, it is known to be hard to model accurately and affected by theoretical  
3301 uncertainties [24, 233].

3302 Combining these properties, it is expected that the dilepton channels in Ref. [187]  
3303 give only subdominant sensitivity compared to the  $\ell+\text{jets}$  channels. In this work,  
3304 while the situation is similar for high  $m_{t\bar{t}}$ , the dilepton channels contribute signif-  
3305 icantly close to the  $t\bar{t}$  threshold. Furthermore, the direct use of spin correlation  
3306 information means that the effect of many systematic uncertainties which only af-  
3307 fect the kinematics is lessened greatly, as elaborated on in Sec. 7.7.3. It has been

checked internally that adopting the strategy employed in Ref. [187] for the dilepton channels in this work would lead to a greatly lessened sensitivity at the  $t\bar{t}$  threshold, and likely no claims of a significant excess.

A further cause of differences could be the different treatment of systematic uncertainties, similar as in Ref. [188]. Ref. [187] considers additional nuisance parameters for the modeling of the  $t\bar{t}$  continuum regarding the choice of parton shower (PYTHIA vs. HERWIG), the choice of calculation for the top quark decay (POWHEG vs. MAD-SPIN), and the choice of PDF in the calculation of the NNLO QCD and NLO EW corrections. The first of these has been studied here in Sec. 7.5.4, and found to not influence the results strongly in the dilepton channels due to the effect of  $c_{\text{hel}}$ . However, the important uncertainties due to the top quark Yukawa coupling and the EW correction scheme are not included in Ref. [187], since the EW corrections are calculated in a different manner. In an effort to be as conservative as possible, several significant uncertainties are moreover treated as decorrelated between different bins of the angular variables  $\cos \theta^*$  and  $\Delta\phi_{\ell\ell}$ , which could reduce the sensitivity gained from these variables.

Since no explicit signal model for a  $t\bar{t}$  bound state is considered in Ref. [187], the expected sensitivities to  $\eta_t$  cannot be directly compared. Instead, the closest considered signal is the generic pseudoscalar  $A$  at a mass of 400 GeV, higher than the minimum of 365 GeV considered here. Since a non-negligible excess is still present at that value in this work both in the dilepton channels alone (Fig. 7.23) and in the combination with  $\ell+\text{jets}$  (Fig. 7.27), while no such excess is visible in Fig. 15 of Ref. [187], the choice of signals is not the cause of the differences on its own. However, the shape difference between  $A$  at 400 GeV including the SM interference and  $\eta_t$  is not negligible. It is thinkable that, if the excess truly originates from a  $t\bar{t}$  bound state manifesting as a narrow peak at the  $t\bar{t}$  threshold, fitting the non-matching  $A$  signal to the data will worsen the issues due to modeling and systematic uncertainties as described in the previous paragraphs, though this is partly speculation.

Even with all this information, it is not fully clear whether the result of this work and the preliminary ATLAS result in Ref. [188] on the one hand and the ATLAS result in Ref. [187] on the other hand should be considered in conflict with each other or not. Together with the cross-checks performed in Sec. 7.7.3, it seems likely that the  $t\bar{t}$  kinematic reconstruction in the dilepton channels, in particular the access to spin correlation, is the most important difference.

### 7.10.3 Other $t\bar{t}$ measurements

While this work constitutes the first time that an excess consistent with a  $t\bar{t}$  bound state has been observed with a large significance, there have been hints for such an effect in other  $t\bar{t}$  measurements. First, several measurements of unfolded  $t\bar{t}$  differential cross sections have observed excesses in data compared to MC predictions of the  $t\bar{t}$  continuum at low invariant masses, such as  $m_{t\bar{t}}$  in dilepton events [234],

3348  $m_{\ell\ell}$  in  $e\mu$  events [235], and  $m_{t\bar{t}}$  in  $\ell+$ jets events [219]. The significances of these  
3349 excesses vary depending on the MC generator the data is compared to, and are also  
3350 strongly influenced by systematic uncertainties for the two  $m_{t\bar{t}}$  measurements.

3351 Secondly, the measurements of quantum entanglement in  $t\bar{t}$  pairs in the dilepton  
3352 channel presented in Refs. [26, 27] measure as a sensitive observable the value of  
3353  $D$ , i.e. the slope of  $c_{\text{hel}}$  (cf. Sec. 2.2.1), for low  $m_{t\bar{t}}$  events. This is very similar  
3354 in spirit to the observables  $m_{t\bar{t}}$  and  $c_{\text{hel}}$  used in the dilepton channel of this work,  
3355 though the measurement is only performed one-dimensionally in  $c_{\text{hel}}$  instead of the  
3356 3D  $m_{t\bar{t}} \times c_{\text{hel}} \times c_{\text{han}}$  template used here. In both Refs. [26, 27], a smaller (i.e. more  
3357 negative) value of  $D$  is observed in data compared to MC  $t\bar{t}$  continuum predictions,  
3358 though the significance is only at the level of one SD. This can be interpreted as  
3359 a hint for the presence of an additional pseudoscalar contribution from a  $t\bar{t}$  bound  
3360 state, consistent with the results of this work.

## 3361 7.11 Summary and Outlook

3362 In this chapter, a generic search for spin-0 states in  $t\bar{t}$  events with the full data of  
3363 LHC Run 2 was presented, targeting the dilepton decay channel of  $t\bar{t}$ . In addition  
3364 to the invariant mass  $m_{t\bar{t}}$ , it uses the spin correlation variables  $c_{\text{hel}}$  and  $c_{\text{han}}$  to probe  
3365 the spin and  $\mathcal{CP}$  structure of  $t\bar{t}$  and possible new particles.

3366 A statistically significant excess was observed in data for low  $m_{t\bar{t}}$  events, close  
3367 to the  $t\bar{t}$  production threshold, showing spin correlations consistent with a pseu-  
3368 doscalar state. This excess is interpreted as a pseudoscalar  $t\bar{t}$  quasi-bound state  $\eta_t$ ,  
3369 which is expected to be present in the SM according to NRQCD calculations. A  
3370 simplified model for the production of  $\eta_t$  is used to measure its cross section, yielding  
3371  $\sigma(\eta_t) = 8.7 \pm 1.1 \text{ pb}$ . Several cross-checks of this result, relaxing assumptions on the  
3372  $t\bar{t}$  kinematic reconstruction as well as considering alternate MC generator setups,  
3373 validate the observed excess. This result represents the first observation of  $\eta_t$ .

3374 Alternatively, the excess could be interpreted as an additional pseudoscalar boson  
3375 A, with mass close to the  $t\bar{t}$  threshold. While the explanation as a  $t\bar{t}$  bound state  
3376 might be favored *a priori* as it is part of the SM and does not invoke any new  
3377 physics, experimentally the two interpretations cannot be distinguished with the  
3378 current resolution. In addition to the interpretation of the excess, exclusion limits  
3379 are set on new pseudoscalar or scalar bosons A/H through their coupling strengths  
3380 to the top quark, allowing for either one or both of these bosons simultaneously.  
3381 They are presented for two scenarios, where the observed excess is either assumed  
3382 to be fully described by the bound state  $\eta_t$  or fully by the new boson A. These limits  
3383 are further combined with a separate analysis targeting the  $\ell+$ jets decay channel of  
3384  $t\bar{t}$ .

3385 It is clear that much remains to be studied about the excess observed in this  
3386 work. Firstly, the interpretation in terms of  $\eta_t$  presented here is performed only

in the dilepton channels. In the preliminary results of Ref. [189], the combination with the  $\ell$ +jets channels was also performed for the measurement of the  $\eta_t$  cross section; however, since the  $\ell$ +jets analysis used was not optimized for signals at the  $t\bar{t}$  threshold, little sensitivity could be gained compared to the dilepton channels alone. Instead, a separate  $\ell$ +jets analysis optimized for a  $t\bar{t}$  bound state should be performed in the future. In particular, spin correlation variables analogous to  $c_{\text{hel}}$  and  $c_{\text{han}}$  could be defined also in the  $\ell$ +jets channel, as has already been done in Ref. [25] through ML-based identification of the decay products of the hadronically decaying top quark.

By contrast, in the dilepton channel, the most pressing targets of improvement are the kinematic reconstruction and the  $t\bar{t}$  modeling uncertainties. For the former, it would again be useful to investigate ML-based reconstruction techniques, for which several proof-of-concept studies have already been performed [190, 236], in a realistic setup. For the latter, the differences between different generator setups, as briefly studied in Sec. 7.5.4, needs to be understood more deeply. It would be ideal to cover the difference between predictions by a set of well-motivated nuisance parameters with clear physical meaning, as has been recently used by CMS in the measurement of the  $W$  boson mass [76, 237]. Extending this approach to the  $t\bar{t}$  process however requires many theoretical advancements, and is likely to lie far in the future for now. In a similar fashion, it will be required to obtain a more precise prediction for the  $t\bar{t}$  bound state itself. A possible approach here, involving the reweighting of  $t\bar{t}$  events by the ratio of Green's functions, is presented in Ref. [39], though this remains to be validated.

To sidestep the issue of imperfect modeling of both  $\eta_t$  and the  $t\bar{t}$  continuum, one could attempt to observe the  $t\bar{t}$  bound state in other decay channels, the most promising being the decay  $\eta_t \rightarrow \gamma\gamma$  to two photons. This final state is experimentally extremely clean and does not require MC modeling of the  $\gamma\gamma$  background. Instead, a possible signal could be extracted using a parametric fit of a peak over a falling background, similar to the measurement of the SM Higgs boson in the  $h \rightarrow \gamma\gamma$  channel. The most important obstacle in such a project would be the small branching ratio of  $\eta_t$  to  $\gamma\gamma$ . Extrapolations of the partial width to  $\gamma\gamma$  from  $b\bar{b}$  and  $c\bar{c}$  bound states [238], combined with an expected total width of  $\Gamma(\eta_t) \approx 2m_t$ , predict a branching ratio of  $\approx 2 \times 10^{-5}$ , though this is a rough estimate that could be wrong by as much as an order of magnitude. If this prediction holds, it might be possible to probe this decay channel with the full statistics collected in Runs 2 and 3 of the LHC. Moreover, a measurement of the ratio of branching fractions to  $\gamma\gamma$  and  $t\bar{t}$  could help distinguish a bound state from possible BSM scenarios.

It is further necessary, of course, to repeat the analysis presented here with the data of LHC Run 3, ideally combining the results. While the  $\eta_t$  cross section, and similarly A/H limits at low masses, are dominated by systematic effects, especially the sensitivity at high A and H masses is limited by the statistics of the data. The increase in center-of-mass energy from 13 to 13.6 TeV will also help increase the

<sup>3429</sup> cross section of high-mass signals, together making it possible to extend the probed  
<sup>3430</sup> A/H mass range to higher values.

<sup>3431</sup> Furthermore, concerning the limits on A and H derived here, the next step is  
<sup>3432</sup> to include these generic exclusion limits into concrete bounds on BSM models of  
<sup>3433</sup> interest. A particular such model, the production of heavy Axion-Like Particles  
<sup>3434</sup> coupling to top quarks, is studied on a phenomenological basis in the following  
<sup>3435</sup> chapter.

3436 **8 Investigation of Axion-Like Particles**  
3437 **decaying to  $t\bar{t}$**

3438 **8.1 Introduction**

3439 Following the results of Chapter 7 including the interpretations as generic scalar or  
3440 pseudoscalar bosons and  $t\bar{t}$  bound states, this chapter is dedicated to Axion-Like  
3441 Particles decaying to  $t\bar{t}$ . As explained in Sec. 2.3.3, the coupling structure of ALPs  
3442 to top quarks is identical to those of the generic pseudoscalar A, such as e.g. in  
3443 the 2HDM, if the basis for the ALP is chosen appropriately (cf. Eq. (2.23)). The  
3444 difference comes from the gluon interaction term, which is absent for the model used  
3445 for A in Chapter 7, and which results in an additional diagram where the ALP is  
3446 produced through a contact interaction with the gluons.

3447 If the coefficient  $c_{\tilde{G}}$  of the ALP-gluon interaction term in Eq. (2.23) vanishes, the  
3448 forms of the Lagrangians for ALP and A become identical, and the limits for A  
3449 shown in Chapter 7 can be directly recasted. This is done in Sec. 8.2. If on the  
3450 other hand  $c_{\tilde{G}} \neq 0$ , the kinematic distributions of the ALP will differ from those of  
3451 A, and the experimental results are not easily translatable. This case is addressed in  
3452 the scope of this work through an phenomenological study on simulation only. The  
3453 technical setup of this study is described in Sec. 8.3, after which the distributions  
3454 of ALP and A are compared for different benchmark points in Sec. 8.4. Projected  
3455 exclusion limits for the  $c_{\tilde{G}} \neq 0$  case are presented in Sec. 8.5, and a short summary  
3456 is given in Sec. 8.6.

3457 The results of this chapter have been originally published in *JHEP* as Ref. [10].  
3458 Since the results of Chapter 7 (Refs. [8, 189]) were not yet public at the time, the  
3459 previous CMS result from Ref. [17] was used as a baseline. For this thesis, the  
3460 translation of limits in Sec. 8.2 has been updated to reflect the results of Chapter 7.

3461 All results presented in this chapter have been obtained as part of this thesis,  
3462 except for the comparison to other final states in Sec. 8.5, which was performed by  
3463 the coauthors of Ref. [10] as indicated.

3464 **8.2 Translation of experimental limits**

3465 In the basis of Eq. (2.23), the ALP Lagrangian is identical in form to the Lagrangian  
3466 of the generic pseudoscalar A given in Eq. (2.18) as long as the gluon interaction

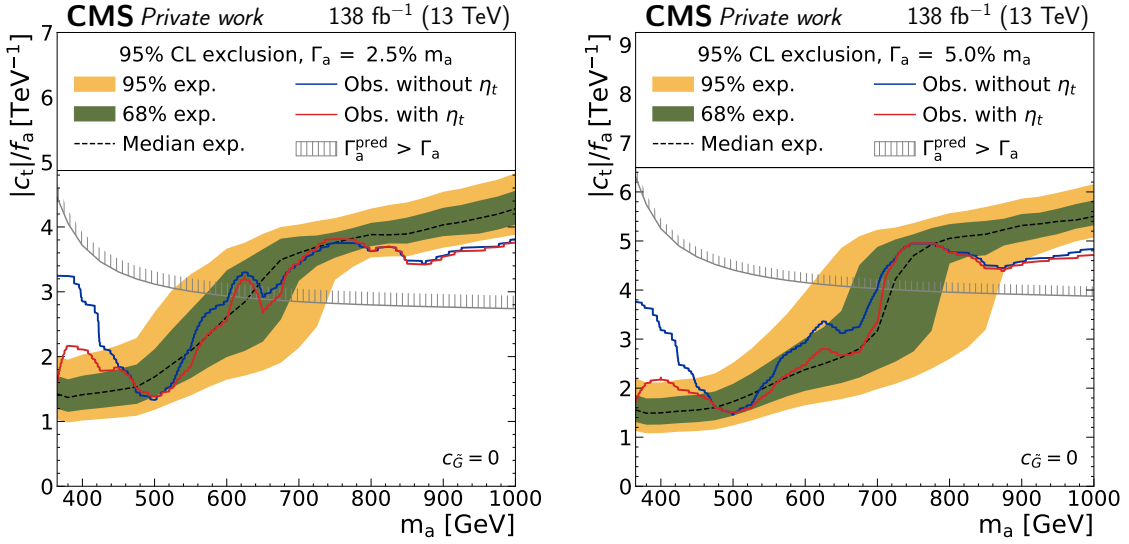


Figure 8.1: **ALP limits for  $c_{\tilde{G}} = 0$ .** Expected and observed limits on the ALP-top coupling  $c_t/f_a$  as a function of the ALP mass for the case  $c_{\tilde{G}} = 0$  for the combined dilepton and  $\ell+\text{jets}$  decay channels, translated from the results of Chapter 7. The expected limit (black line) is shown without contribution from  $t\bar{t}$  bound states in the background modeling, while the observed limit is shown both without  $t\bar{t}$  bound states (blue) and with  $\eta_t$  included in the background (red). *Figure adapted from Ref. [10].*

<sup>3467</sup> coefficient  $c_{\tilde{G}}$  vanishes. For this case, one finds by comparing the coefficients that  
<sup>3468</sup> the phenomenology will be identical if

$$\frac{c_t}{f_a} = \frac{g_{A t \bar{t}}}{v} \quad (8.1)$$

<sup>3469</sup> where  $v = 246$  GeV is the SM Higgs vacuum expectation value. Thus, the exper-  
<sup>3470</sup>imental results of Chapter 7, particularly the limits on  $g_{A t \bar{t}}$  from the combination of  
<sup>3471</sup>dilepton and  $\ell+\text{jets}$  decay channels as presented in Sec. 7.9.2, can be recasted into  
<sup>3472</sup>limits on the ALP coupling  $c_t/f_a$  for the case  $c_{\tilde{G}} = 0$ . This is shown in Fig. 8.1 for  
<sup>3473</sup>two different (fixed) ALP widths. The observed limits are shown with and without  
<sup>3474</sup>a  $t\bar{t}$  bound state contribution as modeled by  $\eta_t$  in the background modeling, corre-  
<sup>3475</sup>sponding to the two scenarios in Fig. 7.27 and Fig. 7.29, and the same excess as in  
<sup>3476</sup>Chapter 7 is seen for at low ALP masses when the  $\eta_t$  contribution is not included.

<sup>3477</sup> In a similar fashion, the best-fit point for A as presented in Eq. (7.17) can be  
<sup>3478</sup>translated to an ALP for the case of  $c_{\tilde{G}} = 0$ , giving

$$m_a = 365 \text{ GeV}, \quad \Gamma_a/m_a = 2\%, \quad \text{and} \quad \frac{c_t}{f_a} = 3.2 \pm 0.2 \text{ TeV}^{-1}.$$

This represents a third alternative interpretation of the excess besides a  $t\bar{t}$  bound state or a generic pseudoscalar  $A$ . The same caveats as for the  $A$  interpretation, as outlined in Sec. 7.7.4, apply; in particular, the mass of 365 GeV is the lowest mass point considered in the signal samples, and it is possible that lower masses closer to the  $t\bar{t}$  threshold would result in a better fit.

## 8.3 Phenomenological setup

The remainder of this chapter is dedicated to exploring an ALP decaying to  $t\bar{t}$  for the case  $c_{\tilde{G}} \neq 0$ , for which the results of Chapter 7 are not easily translatable since the distributions are expected to differ in shape. Due to time constraints, it was not possible as part of this work to investigate this case experimentally in the same fashion as done in Chapter 7. Instead, a phenomenological study is performed on MC simulation only, using a setup that approximates the workflow in Chapter 7.

To do so, MC samples for the signal are generated at LO in QCD with MG5\_AMC@NLO for two different ALP masses (400 GeV and 800 GeV). For the ALP, an UFO model taken from Ref. [239] is used and modified to include the top quark loop form factor including finite mass effects, according to the expressions given in Ref. [240]. Both possible production diagrams, as shown in Fig. 2.8, as well as their interference with the SM are considered. A similar ME reweighting technique as in Sec. 7.4 is used to obtain samples for different widths and  $c_{\tilde{G}}$  values. For the generic pseudoscalar  $A$  as well as the SM  $t\bar{t}$  background, the same generators as in Sec. 7.2.1 are used (MG5\_AMC@NLO and POWHEG v2 hvq, respectively). For all samples, the NNPDF 3.1 PDF set [73] is used, and PYTHIA 8.2 is used to simulate initial and final state radiation [84].

Only the dilepton decay channel of  $t\bar{t}$  is considered, and no detector simulation is performed. Instead, the truth-level top quarks and leptons after parton showering are used, and a Gaussian smearing is applied to  $m_{t\bar{t}}$  randomly on a per-event basis, the standard deviation of which is chosen so that the resolution of the resulting distribution matches that observed in full detector simulation. Since this study was performed before the results of Chapter 7 were public, its predecessor Ref. [17] is used to extract the resolution by fitting to the  $m_{t\bar{t}}$  distributions displayed therein. The result is  $\sigma(m_{t\bar{t}})/m_{t\bar{t}} = 15\%$ , which is somewhat lower than the widths found using the full detector simulation in Sec. 7.2.5 (c.f. Fig. 7.3). However, it should be cautioned that since the true  $m_{t\bar{t}}$  smearing in the full detector simulation is not perfectly Gaussian, the results are not one-to-one comparable.

The experimental acceptance and efficiency, defined as the fraction of  $t\bar{t} \rightarrow \ell\ell$  ( $\ell$  being electrons, muons or leptonically decaying taus) events to survive all trigger and selection requirements, is estimated to be 10.6% for both signal and  $t\bar{t}$  background, also based on Ref. [17]. This is lower compared to the updated analysis presented in Chapter 7, where values of 15–16% are achieved, varying slightly with the data-

3518 taking period. Thus, the projections in this chapter should be considered somewhat  
3519 conservative.

3520 Since the ALP always has a  $\mathcal{CP}$ -odd coupling to top quarks (cf. Eq. (2.23)), it  
3521 is expected to decay to a  $t\bar{t}$  system in the  ${}^1S_0$  state, identically to A. This is true  
3522 irrespective of the gluon coupling  $c_{\tilde{G}}$  since the latter only affects the production, not  
3523 the decay, and the ALP as a colorless, spinless particle has no internal degrees of  
3524 freedom. Thus,  $m_{t\bar{t}}$  and  $c_{\text{hel}}$  are good discriminating variables, again similar to A,  
3525 while  $c_{\text{han}}$  (optimal for  $\mathcal{CP}$ -even couplings) does not offer much additional discrim-  
3526 ination and is not considered here. For simplicity, instead of a multi-dimensional  
3527 binning in  $m_{t\bar{t}}$  and  $c_{\text{hel}}$  like in Chapter 7, a one-dimensional binning in  $m_{t\bar{t}}$  only is  
3528 used, and events are required to have  $c_{\text{hel}} > 0.6$  to enhance the ALP signal over the  
3529 background.

3530 A simplified version of the likelihood model from Chapter 7 is used, implemented  
3531 in `pyhf` [131], in order to estimate projected significances and limits. Only sources  
3532 of systematic uncertainty arising from theory are considered, namely:

- 3533 • Missing higher orders in the matrix element, estimated from varying renor-  
3534 malization and factorization scale by factors of 2,
- 3535 • The PDF uncertainty, estimated as the envelope of 100 pseudo-Hessian NNPDF 3.1  
3536 replicas [73],
- 3537 • The total  $t\bar{t}$  background production cross section, taken as a log-normal un-  
3538 certainty of 6% following Ref. [17],
- 3539 • The top quark mass in the  $t\bar{t}$  background, varied in the range  $m_t = 172.5 \pm$   
3540 1 GeV.

3541 It is clear that this simple treatment of systematic uncertainties can only give a  
3542 rough estimate of the full likelihood as used in Chapter 7, which is sensitive mostly to  
3543 the differences in shapes induced by the various systematic sources. In particular,  
3544 like in the experimental result, the variation in the top quark mass is important  
3545 especially for ALPs with masses close to the  $t\bar{t}$  threshold.

3546 To illustrate the dependence on the likelihood model, the significances in the fol-  
3547 lowing results will be quoted for three different setups including different systematic  
3548 uncertainties, namely all of the above, all of the above except for the top quark  
3549 mass, and statistical uncertainties only. By comparing to the expected significance  
3550 given in Ref. [17] for the best-fit point of the pseudoscalar A, it is found that the  
3551 full setup overestimates the uncertainty, while the setup without the top quark mass  
3552 slightly underestimates it.

$c_t/f_a [\text{TeV}^{-1}]$	$c_{\tilde{G}}/f_a [\text{TeV}^{-1}]$	$A$	$(\sigma^{\text{tot}} - \sigma^{\text{SM}}) [\text{pb}]$
3.0	+0.015	0.95	+6.7
3.0	-0.015	0.43	-2.7
1.0	+0.025	0.75	-1.7
1.0	-0.025	0.87	+2.0

Table 8.1: **Benchmark points for comparing ALP and A.** In addition to the ALP couplings  $c_t/f_a$  and  $c_{\tilde{G}}/f_a$  for the benchmark points, also the difference in integrated cross section to the SM is shown, as well as a value of  $g_{A\bar{t}\bar{t}}$  corresponding to a generic pseudoscalar A with the same integrated cross section.

## 3553 8.4 Comparison of ALP and A

3554 To investigate the differences and possible discrimination between ALP and A, four  
 3555 different ALP benchmark points with  $c_{\tilde{G}} \neq 0$  are defined for a mass of 400 GeV and  
 3556 a width of 2.5%. Each of the benchmarks is compared to a generic pseudoscalar A  
 3557 with its coupling  $g_{A\bar{t}\bar{t}}$  chosen such that the total integrated cross section of ALP and  
 3558 A are identical, i.e. that they cannot be distinguished by cross section information  
 3559 alone. The chosen couplings and resulting cross sections can be found in Tab. 8.1.

3560 The expected  $m_{t\bar{t}}$  distributions, including the smearing and acceptance described  
 3561 in Sec. 8.3, for the four benchmark points are shown in Fig. 8.2, together with the  
 3562 expected statistical uncertainty for both Run 2 and the HL-LHC.

3563 It can be seen that the shapes of the distributions differ qualitatively for the differ-  
 3564 ent benchmarks: For example, the case  $c_t/f_a = 3.0 \text{ TeV}^{-1}$  and  $c_{\tilde{G}}/f_a = 0.015 \text{ TeV}^{-1}$   
 3565 (top left) shows a clear peak-dip structure similar to the A case, and as a result will  
 3566 likely not be distinguishable from it. In contrast, e.g. the case  $c_t/f_a = 1.0 \text{ TeV}^{-1}$   
 3567 and  $c_{\tilde{G}}/f_a = -0.025 \text{ TeV}^{-1}$  (bottom right) shows a dip-peak structure instead, which  
 3568 cannot be reproduced by the A. This is possible because of the relative sign of the  
 3569 two couplings in this case, i.e.  $c_t c_{\tilde{G}} < 0$ , which flips the sign of the interference  
 3570 between the gluon interaction diagram in Fig. 2.8 and the SM.

3571 By comparing the distributions to the expected statistical uncertainty, one can  
 3572 already estimate roughly whether discrimination of the signals with respect to the  
 3573 SM or with respect to each other is possible. To quantify this further, the expected  
 3574 significance to reject the SM-only hypothesis under the benchmark scenarios are  
 3575 reported in Tab. 8.2. They are computed with the likelihood model as defined in  
 3576 Sec. 8.3, and quoted both for the three different described uncertainty setups as  
 3577 well as for three different eras of the LHC, corresponding to different (expected)  
 3578 integrated luminosities: full Run 2 ( $138 \text{ fb}^{-1}$ ), Run 2+3 ( $300 \text{ fb}^{-1}$ ), and the HL-  
 3579 LHC ( $3 \text{ ab}^{-1}$ ). For the latter case, all systematic uncertainties are halved to account

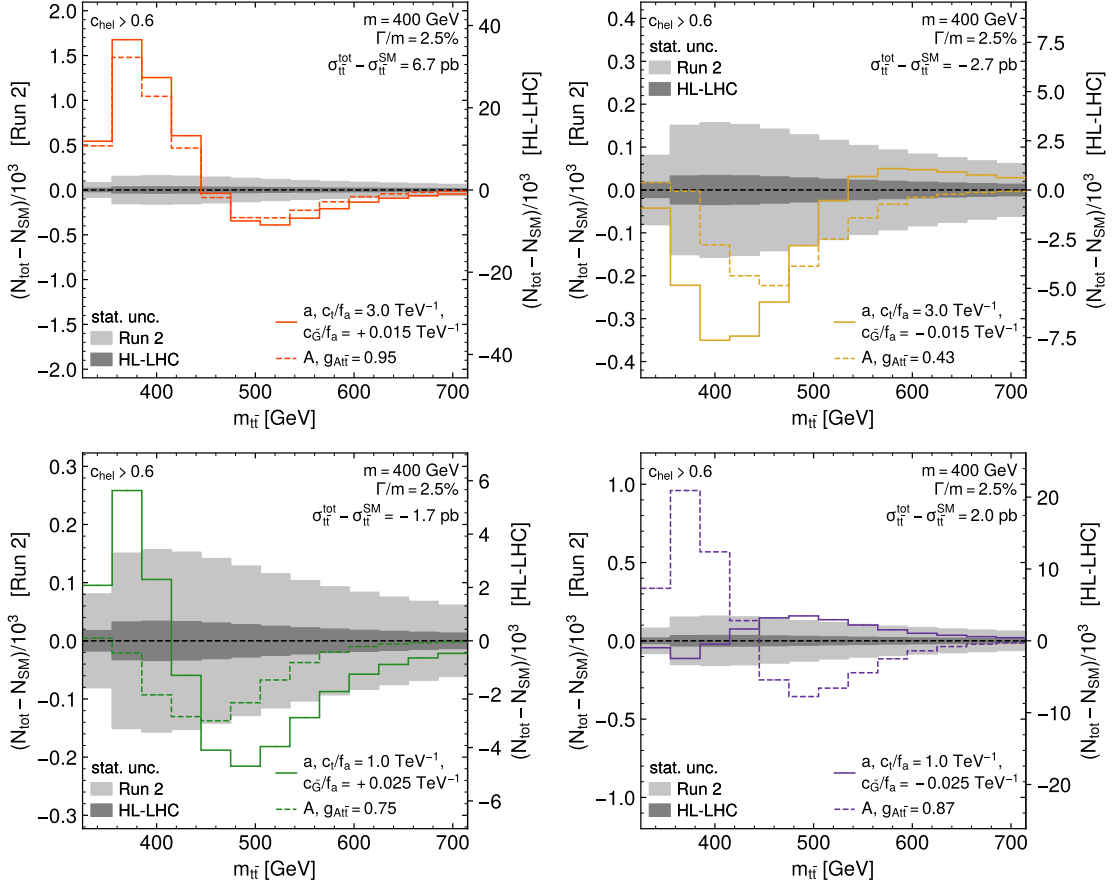


Figure 8.2: **Expected  $m_{t\bar{t}}$  distributions for  $pp \rightarrow a/A \rightarrow t\bar{t}$ .** Shown are both ALP and A at a mass of 400 GeV for four benchmark points, with the SM subtracted. The couplings for A and a are adjusted such that the inclusive cross section is identical. The gray bands show the expected statistical uncertainty for Run 2 and HL-LHC. *Figure taken from Ref. [10].*

for the expected increase in data reconstruction quality and reduction in theoretical uncertainty.

Tab. 8.2 shows that all considered benchmark scenarios can be expected to be distinguished from the SM with  $> 5\sigma$  significance if the top quark mass uncertainty is not considered in the model, that is, if experimentally it can be significantly reduced from the estimate used in this study.

If one such signal would be discovered in the future, it would be important to ascertain the particle it originates from. The  $m_{t\bar{t}}$  distribution could then be used to distinguish between an ALP, exhibiting both couplings to top quarks and gluons, and the more restrictive case of A, in which only a top quark coupling is allowed. To quantify this, Tab. 8.3 now shows, for the four benchmark points, the expected

		<sup>a</sup>	Significance ( $a$ vs. SM)		
			all syst.	no $m_t$	stats only
3.0	$+0.015$	Run 2	3.9	$> 10$	$> 10$
		Run 2+3	5.2	$> 10$	$> 10$
		HL-LHC	$> 10$	$> 10$	$> 10$
3.0	$-0.015$	Run 2	2.1	2.2	4.4
		Run 2+3	3.0	3.0	6.5
		HL-LHC	8.7	8.8	$> 10$
1.0	$+0.025$	Run 2	1.1	2.6	4.0
		Run 2+3	1.4	3.2	5.9
		HL-LHC	3.9	8.2	$> 10$
1.0	$-0.025$	Run 2	0.7	1.7	2.8
		Run 2+3	0.9	2.2	4.1
		HL-LHC	2.3	5.5	$> 10$

Table 8.2: **Significances for detecting an ALP** with a mass of 400 GeV and a width of 2.5% for the benchmark scenarios considered in Fig. 8.2. Three different treatments of the uncertainties as defined in Sec. 8.3 are shown. For the HL-LHC projection, all systematic uncertainties are scaled by a factor of 0.5.

significances for rejecting the A hypothesis assuming that the corresponding ALP model is realized in nature. Again, the three different uncertainty models and three LHC eras are shown in the same fashion. It can be seen that for all benchmarks, the HL-LHC data would make it possible to distinguish the two scenarios with  $> 5\sigma$  significance in the case of an observation.

## 8.5 Projected limits for ALPs

In case that no (additional) signal is seen in either Run 3 or at the HL-LHC, one would quantify the exclusion of ALP models based on limits in the plane of  $c_t/f_a$  and  $c_{\tilde{G}}/f_a$ . Projections for such expected 95% exclusion limits are presented in Fig. 8.3 for the three different considered luminosities as well as for ALP masses of 400 and 800 GeV, again computed with the same likelihood model. All systematic uncertainties save for the top quark mass are considered here, same as in the “no  $m_t$ ” column in Tabs. 8.2 and 8.3.

The figures show that strong limits can be set for values of  $|c_{\tilde{G}}|/f_a \gtrsim 0.05 \text{ TeV}^{-1}$  where the gluon-ALP interaction dominates and leads to signals with large cross sections, while the limits are weaker close to  $c_{\tilde{G}} = 0$ . Notably, the smallest signals are obtained for slightly negative values of  $c_{\tilde{G}}/f_a$  due to destructive interference between the two production diagrams, leading to a slight tilt of the curve in the

$c_t/f_a$ [TeV $^{-1}$ ]	$a$	$c_{\tilde{G}}/f_a$ [TeV $^{-1}$ ]	$A$ $g_{A t\bar{t}}$	Luminosity	Significance ( $a$ vs. $A$ )		
					all syst.	no $m_t$	stats only
3.0	+0.015	0.95	Run 2 Run 2+3 HL-LHC	1.3	1.9	3.3	
				1.8	2.3	4.9	
				5.3	5.7	> 10	
3.0	−0.015	0.43	Run 2 Run 2+3 HL-LHC	1.2	1.9	3.3	
				1.7	2.4	4.9	
				5.0	6.0	> 10	
1.0	+0.025	0.75	Run 2 Run 2+3 HL-LHC	1.5	2.3	2.7	
				2.0	3.1	3.9	
				5.8	8.8	> 10	
1.0	−0.025	0.87	Run 2 Run 2+3 HL-LHC	3.7	9.0	> 10	
				4.6	> 10	> 10	
				> 10	> 10	> 10	

Table 8.3: **Significances for the discrimination of an ALP and A** for the benchmark scenarios considered in Fig. 8.2. The uncertainties are treated as in Tab. 8.2.

left panel of Fig. 8.3. Of the four considered benchmark points for a 400 GeV ALP, all can be safely expected to be excluded with HL-LHC data, while those with  $c_t/f_a = 3 \text{ TeV}^{-1}$  might already be excluded by the combination of Run 2 and 3.

As part of the work of the coauthors in Ref. [10], the projected limits for Run 2 were compared with limits derived from existing analyses in other search channels, using the tool `HiggsTools` [241]. These are reproduced briefly in the following in order to provide a point of reference; details can be found in Ref. [10]. The following search channels were found to be of relevance:

- $pp \rightarrow a \rightarrow \gamma\gamma$ , from a generic narrow-resonance search in ATLAS [242],
- $pp \rightarrow a \rightarrow Zh$ , from a search for pseudoscalars decaying into a Z boson and a SM Higgs boson in ATLAS [243],
- $pp \rightarrow t\bar{t}a \rightarrow t\bar{t}t\bar{t}$ , from the CMS measurement of the four-top production cross section [244],
- interference effects between the ALP effective Lagrangian and SM Effective Field Theory (SMEFT), which would induce non-zero Wilson coefficients of SMEFT operators in electroweak precision observables such as e.g. the W boson mass, leading to indirect limits [245].

The comparison of all these limits to the projected limits from  $pp \rightarrow a \rightarrow t\bar{t}$  derived in this work is shown in Fig. 8.4 in the  $c_t$ - $c_{\tilde{G}}$  plane for a 400 GeV ALP.

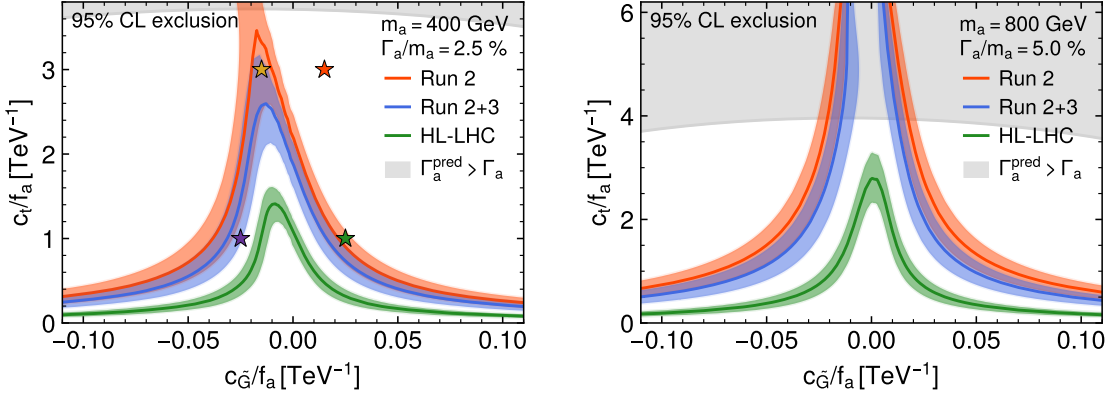


Figure 8.3: **Projected ALP limits.** Projected 95% exclusion limits in the plane of  $c_{\tilde{G}}/f_a$  and  $c_t/f_a$  for a mass of 400 GeV and a width of 2.5% (left) as well as 800 GeV and 5.0% (right). The limits are shown for three different integrated luminosities, corresponding to Run 2, Run 2+3, and the HL-LHC, where for the latter the systematic uncertainties are halved. *Figure taken from Ref. [10].*

3628 For almost all points,  $\text{pp} \rightarrow a \rightarrow t\bar{t}$  leads to stronger limits than all other direct  
 3629 search channels. Furthermore, for  $|c_{\tilde{G}}|/f_a \gtrsim 0.03 \text{ TeV}^{-1}$  the projected limits are also  
 3630 stronger than the indirect ones from ALP-SMEFT interference, while this is not the  
 3631 case for smaller  $|c_{\tilde{G}}|/f_a$ . It should however be noted here that the indirect limits are  
 3632 subject to more assumptions, in particular, that the ALP is the only new physics  
 3633 contribution at the ALP scale ( $\approx f_a$ ). For a more detailed discussion, see again  
 3634 Ref. [10].

## 3635 8.6 Summary and Outlook

3636 In this chapter, the  $t\bar{t}$  final state is found to be an excellent channel for searching  
 3637 for heavy ALPs coupling to top quarks. Depending on the value of the explicit  
 3638 gluon-ALP coupling  $c_{\tilde{G}}$ , two scenarios are considered. For  $c_{\tilde{G}} = 0$ , the results of  
 3639 the experimental search for a generic pseudoscalar presented in Chapter 7 of this  
 3640 work, including the excess observed there, are directly translated into limits on the  
 3641 ALP-top coupling  $c_t/f_a$ .

3642 For  $c_{\tilde{G}} \neq 0$ , on the other hand, a phenomenological study targeting the dilepton  
 3643 decay channel of  $t\bar{t}$  is performed on simulation only, comparing ALPs to a generic  
 3644 pseudoscalar A which does not couple directly to gluons. It is found that ALP  
 3645 and A can lead to drastically different  $m_{t\bar{t}}$  distributions depending on the coupling  
 3646 values, and could possibly be distinguished at the HL-LHC if a signal is observed.  
 3647 Furthermore, projected expected limits in the plane of the ALP couplings  $c_t/f_a$  and

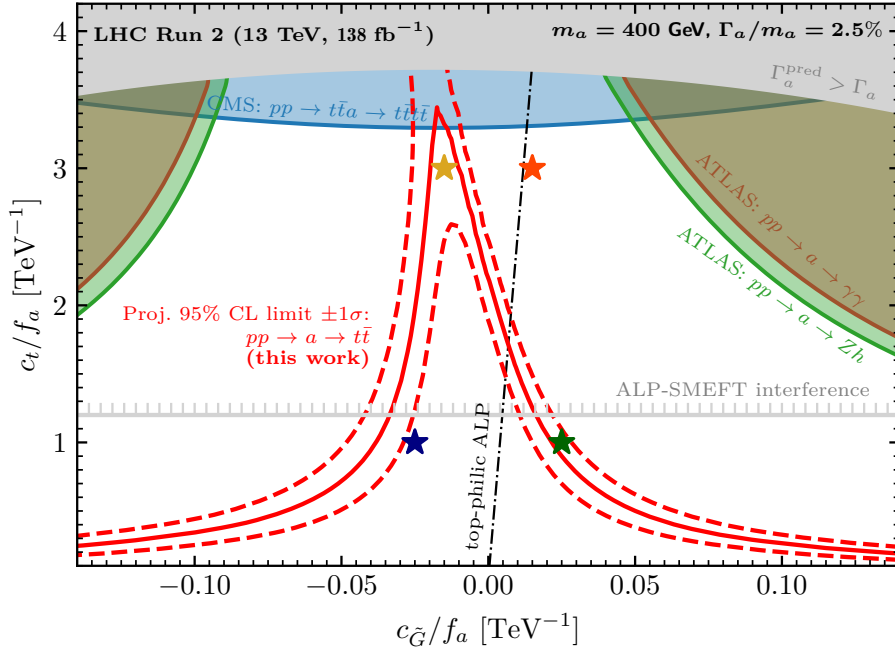


Figure 8.4: **Comparison of limits from different search channels.** 95% exclusion limits in the plane of  $c_{\tilde{G}}/f_a$  and  $c_t/f_a$  for a mass of 400 GeV and a width of 2.5% (left) from different search channels. The projected limits from this work are overlaid in red. *Figure taken from Ref. [10].*

3648  $c_{\tilde{G}}/f_a$  are set for different integrated luminosities. They are more sensitive than  
3649 other possible direct search channels in almost the whole parameter space.

3650 The obvious continuation of this work would be to include the ALP signals for  
3651 the  $c_{\tilde{G}} \neq 0$  case into an experimental search like the one performed in Chapter 7.  
3652 For the purpose of this thesis, this was not possible within the time constraints, and  
3653 needs to be postponed to the future. Alternatively, one could investigate how the  
3654 parameter space considered in this work - in particular, the very large ALP mass  
3655 and comparatively strong top coupling - match to possible UV completions of the  
3656 ALP effective Lagrangian and, if such models exist, whether they can still solve the  
3657 strong  $\mathcal{CP}$  problem.

## 3658 9 Summary and Conclusions

3659 In this work, several aspects of top quark pair ( $t\bar{t}$ ) production with the CMS detector  
3660 at the Large Hadron Collider (LHC) were studied. First, a measurement of the  
3661 inclusive  $t\bar{t}$  production cross section at a center-of-mass energy of  $\sqrt{s} = 13.6$  TeV was  
3662 performed, using  $1.21 \text{ fb}^{-1}$  of early LHC Run 3 data. By combining the dilepton and  
3663  $\ell+\text{jets}$  decay channels of  $t\bar{t}$  for the first time and categorizing the events by their  
3664 number of b-tagged jets, the analysis is capable of constraining lepton and b tagging  
3665 efficiencies directly *in situ*.

3666 The result is  $\sigma_{t\bar{t}} = 882 \pm 23 \text{ (stat+syst)} \pm 20 \text{ (lumi)} \text{ pb}$ , compatible with the SM  
3667 prediction within one standard deviation. The measurement became public only  
3668 two months after data taking, constituting the first physics result of LHC Run 3,  
3669 and despite the small considered luminosity is of comparable precision with previous  
3670  $\sigma_{t\bar{t}}$  measurements. At the time, it served as an important validation of the quality  
3671 of CMS Run 3 data.

3672 Second, off-shell  $t\bar{t}$  production as well as interference between  $t\bar{t}$  and tW produc-  
3673 tion was studied in simulation using the Monte Carlo (MC) generator **bb41**, which  
3674 generates the full  $\text{pp} \rightarrow b\bar{b}\ell\ell\nu\nu$  amplitude at next-to-leading order (NLO) in quan-  
3675 tum chromodynamics (QCD). In this work, **bb41** matched to the parton shower  
3676 in PYTHIA is implemented and validated in the CMS software stack for the first  
3677 time and compared to several other  $t\bar{t}$  MC generators. Good agreement between  
3678 **bb41** and unfolded ATLAS data is found for the variable  $m_{b\ell}^{\min\max}$ , which is sensitive  
3679 to the  $t\bar{t}/\text{tW}$  interference, and significant shifts in the reconstructed top mass line  
3680 shape compared to other generators are observed. Additionally, a brief investigation  
3681 of the matching procedure between **bb41** and PYTHIA is presented. These studies  
3682 represent the starting point for future precision  $t\bar{t}$  analyses in CMS using **bb41**, such  
3683 as measurements of the top mass and width.

3684 Finally, a search for spin-0 states decaying to  $t\bar{t}$  in the dilepton channel has  
3685 been presented. The search uses the full CMS Run 2 data set, corresponding to  
3686  $138 \text{ fb}^{-1}$  and  $\sqrt{s} = 13$  TeV, and employs the invariant  $t\bar{t}$  mass ( $m_{t\bar{t}}$ ) as well as two  
3687  $t\bar{t}$  spin correlation observables to gain sensitivity to the  $\mathcal{CP}$  structure of possible  
3688 new states. An excess compared to the  $t\bar{t}$  continuum prediction is observed for  
3689 low  $m_{t\bar{t}}$  events, consistent with spin correlations as expected from a pseudoscalar  
3690 state. This excess is interpreted as a pseudoscalar  $t\bar{t}$  bound state  $\eta_t$ , as predicted  
3691 by several calculations in non-relativistic QCD (NRQCD). The production cross  
3692 section of  $\eta_t$  is measured using a simplified  $\eta_t$  model, resulting in  $\sigma(\eta_t) = 8.7 \pm$   
3693  $1.1 \text{ pb}$ , which is of the same order of magnitude as NRQCD-based estimates. The

## 9 Summary and Conclusions

---

3694 uncertainty is dominated by its systematic component, in particular the challenging  
3695 modeling of the  $t\bar{t}$  continuum. Several detailed cross-checks, such as bypassing  
3696 the experimental  $t\bar{t}$  reconstruction as well as using different MC generators, are  
3697 discussed, and all confirm the presence of the excess. The significance of the result  
3698 exceeds five standard deviations.

3699 Alternatively, the same search is interpreted in terms of new, generic pseudoscalar  
3700 (A) or scalar (H) particles coupling to top quarks, as expected e.g. in Two-Higgs  
3701 Doublet models (2HDMs). The interference between the new particles and the SM  
3702 is taken into account. Besides an interpretation of the same excess at low  $m_{t\bar{t}}$ ,  
3703 exclusion limits on the couplings to the top quark are presented in two scenarios,  
3704 assuming the excess to be either fully described by A and H or fully by a  $t\bar{t}$  bound  
3705 state. These limits are combined with a similar search in the  $\ell+$ jets decay channels  
3706 of  $t\bar{t}$ , and exclusion regions are also provided for the simultaneous presence of A and  
3707 H.

3708 For a third interpretation, Axion-Like Particles (ALPs) decaying to  $t\bar{t}$  are con-  
3709 sidered. It is found that in the case of vanishing tree-level couplings between ALP  
3710 and gluons  $c_{\tilde{G}}$ , the results for the generic pseudoscalar A are directly translatable,  
3711 and experimental limits on the coupling between ALP and top quark are presented.  
3712 The more generic case of  $c_{\tilde{G}} \neq 0$  is studied using simulated events, and projected  
3713 significances and exclusion limits on such ALPs decaying to  $t\bar{t}$  are derived for var-  
3714 ious phases of the LHC. It is found that at the high-luminosity LHC, ALPs and  
3715 other pseudoscalars as e.g. in the 2HDM could be distinguishable based on their  
3716  $m_{t\bar{t}}$  distribution. The resulting projected limits are expected to improve on limits  
3717 from other final states in large areas of phase space.

3718 Branching out from the different aspects of this work, many directions of further  
3719 study could be pursued. The most pressing one is certainly a further investigation  
3720 of the excess at the  $t\bar{t}$  production threshold observed here. Since the ATLAS ex-  
3721 periment has confirmed the excess in a preliminary result, it would now be of great  
3722 interest to attempt to determine the origin of the excess - in particular, whether it  
3723 is purely the result of a SM bound state or whether it originates in BSM physics  
3724 - though this will likely be challenging. Searches at the same invariant mass in  
3725 other decay channels, in particular  $\gamma\gamma$ , as well as measurements of other kinematic  
3726 distributions for low  $m_{t\bar{t}}$  events could represent first steps towards this goal. It is  
3727 also in general important to improve the experimental  $t\bar{t}$  reconstruction techniques  
3728 e.g. with modern machine learning approaches, which would also greatly contribute  
3729 to precision measurements of top quark properties. From the theoretical side, more  
3730 precise calculations of the  $t\bar{t}$  threshold region are required, for which this work will  
3731 hopefully serve as a motivation.

3732 It is not every day that such an excess is observed in high energy physics. One can  
3733 only hope that, regardless of its origin, its study will produce many further results  
3734 of great interest.

3735 

## A Bibliography

- 3736 [1] ATLAS Collaboration, “Observation of a new particle in the search for the  
3737 standard model Higgs boson with the ATLAS detector at the LHC”, *Phys.*  
3738 *Lett. B*, vol. 716, p. 1, 2012. DOI: 10.1016/j.physletb.2012.08.020. arXiv:  
3739 1207.7214 [hep-ex].
- 3740 [2] CMS Collaboration, “Observation of a new boson at a mass of 125 GeV with  
3741 the CMS experiment at the LHC”, *Phys. Lett. B*, vol. 716, p. 30, 2012. DOI:  
3742 10.1016/j.physletb.2012.08.021. arXiv: 1207.7235 [hep-ex].
- 3743 [3] CMS Collaboration, “Observation of a new boson with mass near 125 GeV  
3744 in pp collisions at  $\sqrt{s} = 7$  and 8 TeV”, *JHEP*, vol. 06, p. 081, 2013. DOI:  
3745 10.1007/JHEP06(2013)081. arXiv: 1303.4571 [hep-ex].
- 3746 [4] CMS Collaboration, “The CMS Experiment at the CERN LHC”, *JINST*,  
3747 vol. 3, S08004, 2008. DOI: 10.1088/1748-0221/3/08/S08004.
- 3748 [5] CMS Collaboration, “First measurement of the top quark pair production  
3749 cross section in proton-proton collisions at  $\sqrt{s} = 13.6$  TeV”, *JHEP*, vol. 08,  
3750 p. 204, 2023. DOI: 10.1007/JHEP08(2023)204. arXiv: 2303.10680 [hep-ex].
- 3751 [6] CMS Collaboration, “Simulation of on- and off-shell  $t\bar{t}$  production with the  
3752 Monte Carlo generator b\_bbar\_4l at CMS”, CERN, Geneva, Tech. Rep.,  
3753 2023. [Online]. Available: <https://cds.cern.ch/record/2884265>.
- 3754 [7] T. Ježo, J. M. Lindert, P. Nason, C. Oleari, and S. Pozzorini, “An NLO+PS  
3755 generator for  $t\bar{t}$  and  $Wt$  production and decay including non-resonant and  
3756 interference effects”, *Eur. Phys. J. C*, vol. 76, p. 691, 2016. DOI: 10.1140/  
3757 epjc/s10052-016-4538-2. arXiv: 1607.04538 [hep-ph].
- 3758 [8] CMS Collaboration, “Observation of a pseudoscalar excess at the top quark  
3759 pair production threshold”, 2025, submitted to *Rep. Prog. Phys.* arXiv: 2503.  
3760 22382 [hep-ex].
- 3761 [9] CMS Collaboration, “Search for heavy pseudoscalar and scalar bosons decaying  
3762 to a top quark pair in proton-proton collisions at  $\sqrt{s} = 13$  TeV”, 2025,  
3763 submitted to *Rep. Prog. Phys.* arXiv: 2507.05119 [hep-ex].
- 3764 [10] A. Anuar et al., “ALP-ine quests at the LHC: hunting axion-like particles  
3765 via peaks and dips in  $t\bar{t}$  production”, *JHEP*, vol. 24, p. 197, 2024. DOI: 10.  
3766 1007/JHEP12(2024)197. arXiv: 2404.19014 [hep-ph].
- 3767 [11] R. L. Workman et al., “Review of Particle Physics”, *PTEP*, vol. 2022, p. 083C01,  
3768 2022. DOI: 10.1093/ptep/ptac097.

- 3769 [12] P. W. Higgs, “Broken symmetries, massless particles and gauge fields”, *Phys.*  
3770 *Lett.*, vol. 12, pp. 132–133, 1964. DOI: [10.1016/0031-9163\(64\)91136-9](https://doi.org/10.1016/0031-9163(64)91136-9).
- 3771 [13] F. Englert and R. Brout, “Broken Symmetry and the Mass of Gauge Vector  
3772 Mesons”, *Phys. Rev. Lett.*, vol. 13, J. C. Taylor, Ed., pp. 321–323, 1964. DOI:  
3773 [10.1103/PhysRevLett.13.321](https://doi.org/10.1103/PhysRevLett.13.321).
- 3774 [14] CDF Collaboration, “Observation of top quark production in  $\bar{p}p$  collisions”,  
3775 *Phys. Rev. Lett.*, vol. 74, pp. 2626–2631, 1995. DOI: [10.1103/PhysRevLett.74.2626](https://doi.org/10.1103/PhysRevLett.74.2626). arXiv: [hep-ex/9503002](https://arxiv.org/abs/hep-ex/9503002).
- 3777 [15] D0 Collaboration, “Observation of the top quark”, *Phys. Rev. Lett.*, vol. 74,  
3778 pp. 2632–2637, 1995. DOI: [10.1103/PhysRevLett.74.2632](https://doi.org/10.1103/PhysRevLett.74.2632). arXiv: [hep-ex/9503003](https://arxiv.org/abs/hep-ex/9503003).
- 3780 [16] Y. Kats and D. Uzan, “Prospects for measuring quark polarization and spin  
3781 correlations in  $b\bar{b}$  and  $c\bar{c}$  samples at the LHC”, *JHEP*, vol. 03, p. 063, 2024.  
3782 DOI: [10.1007/JHEP03\(2024\)063](https://doi.org/10.1007/JHEP03(2024)063). arXiv: [2311.08226 \[hep-ph\]](https://arxiv.org/abs/2311.08226).
- 3783 [17] CMS Collaboration, “Search for heavy Higgs bosons decaying to a top quark  
3784 pair in proton-proton collisions at  $\sqrt{s} = 13$  TeV”, *JHEP*, vol. 04, p. 171, 2020,  
3785 [Erratum: *JHEP* 03, 187 (2022)]. DOI: [10.1007/JHEP04\(2020\)171](https://doi.org/10.1007/JHEP04(2020)171). arXiv:  
3786 [1908.01115 \[hep-ex\]](https://arxiv.org/abs/1908.01115).
- 3787 [18] W. Bernreuther, A. Brandenburg, Z. G. Si, and P. Uwer, “Top quark pair  
3788 production and decay at hadron colliders”, *Nucl. Phys. B*, vol. 690, pp. 81–  
3789 137, 2004. DOI: [10.1016/j.nuclphysb.2004.04.019](https://doi.org/10.1016/j.nuclphysb.2004.04.019). arXiv: [hep-ph/0403035](https://arxiv.org/abs/hep-ph/0403035).
- 3791 [19] F. Maltoni, C. Severi, S. Tentori, and E. Vryonidou, “Quantum detection of  
3792 new physics in top-quark pair production at the LHC”, *JHEP*, vol. 03, p. 099,  
3793 2024. DOI: [10.1007/JHEP03\(2024\)099](https://doi.org/10.1007/JHEP03(2024)099). arXiv: [2401.08751 \[hep-ph\]](https://arxiv.org/abs/2401.08751).
- 3794 [20] K. Cheng, T. Han, and M. Low, “Optimizing entanglement and Bell inequality  
3795 violation in top antitop events”, *Phys. Rev. D*, vol. 111, no. 3, p. 033004,  
3796 2025. DOI: [10.1103/PhysRevD.111.033004](https://doi.org/10.1103/PhysRevD.111.033004). arXiv: [2407.01672 \[hep-ph\]](https://arxiv.org/abs/2407.01672).
- 3797 [21] A. Czarnecki, M. Jezabek, and J. H. Kuhn, “Lepton Spectra From Decays  
3798 of Polarized Top Quarks”, *Nucl. Phys. B*, vol. 351, pp. 70–80, 1991. DOI:  
3799 [10.1016/0550-3213\(91\)90082-9](https://doi.org/10.1016/0550-3213(91)90082-9).
- 3800 [22] W. Bernreuther, A. Brandenburg, Z. G. Si, and P. Uwer, “Spin properties of  
3801 top quark pairs produced at hadron colliders”, *Acta Phys. Polon. B*, vol. 34,  
3802 K. Fialkowski, M. Jezabek, and M. Rozanska, Eds., pp. 4477–4490, 2003.  
3803 arXiv: [hep-ph/0304244](https://arxiv.org/abs/hep-ph/0304244).

- 3804 [23] CMS Collaboration, “Measurements of t t-bar spin correlations and top quark  
3805 polarization using dilepton final states in pp collisions at sqrt(s) = 8 TeV”,  
3806 *Phys. Rev. D*, vol. 93, no. 5, p. 052007, 2016. DOI: 10.1103/PhysRevD.93.  
3807 052007. arXiv: 1601.01107 [hep-ex].
- 3808 [24] CMS Collaboration, “Measurement of the top quark polarization and t̄t spin  
3809 correlations using dilepton final states in proton-proton collisions at  $\sqrt{s} =$   
3810 13 TeV”, *Phys. Rev. D*, vol. 100, no. 7, p. 072002, 2019. DOI: 10.1103/  
3811 PhysRevD.100.072002. arXiv: 1907.03729 [hep-ex].
- 3812 [25] CMS Collaboration, “Measurements of polarization and spin correlation and  
3813 observation of entanglement in top quark pairs using lepton+jets events from  
3814 proton-proton collisions at  $\sqrt{s} = 13$  TeV”, *Phys. Rev. D*, vol. 110, no. 11,  
3815 p. 112016, 2024. DOI: 10.1103/PhysRevD.110.112016. arXiv: 2409.11067  
3816 [hep-ex].
- 3817 [26] CMS Collaboration, “Observation of quantum entanglement in top quark  
3818 pair production in proton–proton collisions at  $\sqrt{s} = 13$  TeV”, *Rept. Prog.*  
3819 *Phys.*, vol. 87, no. 11, p. 117801, 2024. DOI: 10.1088/1361-6633/ad7e4d.  
3820 arXiv: 2406.03976 [hep-ex].
- 3821 [27] ATLAS Collaboration, “Observation of quantum entanglement with top quarks  
3822 at the ATLAS detector”, *Nature*, vol. 633, no. 8030, pp. 542–547, 2024. DOI:  
3823 10.1038/s41586-024-07824-z. arXiv: 2311.07288 [hep-ex].
- 3824 [28] A. A. Anuar, “Top Quark Spin and Polarization Properties in Searches for  
3825 New Phenomena with the CMS Detector at the LHC”, PhD thesis, DESY,  
3826 Hamburg, 2019.
- 3827 [29] W. Bernreuther, P. Galler, Z.-G. Si, and P. Uwer, “Production of heavy Higgs  
3828 bosons and decay into top quarks at the LHC. II: Top-quark polarization and  
3829 spin correlation effects”, *Phys. Rev. D*, vol. 95, no. 9, p. 095012, 2017. DOI:  
3830 10.1103/PhysRevD.95.095012. arXiv: 1702.06063 [hep-ph].
- 3831 [30] W. Bernreuther, D. Heisler, and Z.-G. Si, “A set of top quark spin correlation  
3832 and polarization observables for the LHC: Standard Model predictions and  
3833 new physics contributions”, *JHEP*, vol. 12, p. 026, 2015. DOI: 10.1007/  
3834 JHEP12(2015)026. arXiv: 1508.05271 [hep-ph].
- 3835 [31] V. S. Fadin, V. A. Khoze, and T. Sjöstrand, “On the threshold behaviour  
3836 of heavy top production”, *Z. Phys. C*, vol. 48, p. 613, 1990. DOI: 10.1007/  
3837 BF01614696.
- 3838 [32] Y. Kiyo, J. H. Kuhn, S. Moch, M. Steinhauser, and P. Uwer, “Top-quark  
3839 pair production near threshold at LHC”, *Eur. Phys. J. C*, vol. 60, pp. 375–  
3840 386, 2009. DOI: 10.1140/epjc/s10052-009-0892-7. arXiv: 0812.0919  
3841 [hep-ph].

- [33] Y. Sumino and H. Yokoya, “Bound-state effects on kinematical distributions of top quarks at hadron colliders”, *JHEP*, vol. 09, p. 034, 2010, [Erratum: JHEP 06, 037 (2016)]. DOI: 10.1007/JHEP09(2010)034. arXiv: 1007.0075 [hep-ph].
- [34] W.-L. Ju, G. Wang, X. Wang, X. Xu, Y. Xu, and L. L. Yang, “Top quark pair production near threshold: single/double distributions and mass determination”, *JHEP*, vol. 06, p. 158, 2020. DOI: 10.1007/JHEP06(2020)158. arXiv: 2004.03088 [hep-ph].
- [35] M. V. Garzelli, G. Limatola, S. Moch, M. Steinhauser, and O. Zenaiev, “Updated predictions for toponium production at the LHC”, Dec. 2024. arXiv: 2412.16685 [hep-ph].
- [36] F. Maltoni, C. Severi, S. Tentori, and E. Vryonidou, “Quantum tops at circular lepton colliders”, *JHEP*, vol. 09, p. 001, 2024. DOI: 10.1007/JHEP09(2024)001. arXiv: 2404.08049 [hep-ph].
- [37] B. Fuks, K. Hagiwara, K. Ma, and Y.-J. Zheng, “Signatures of toponium formation in LHC run 2 data”, *Phys. Rev. D*, vol. 104, no. 3, p. 034023, 2021. DOI: 10.1103/PhysRevD.104.034023. arXiv: 2102.11281 [hep-ph].
- [38] J. A. Aguilar-Saavedra, “Toponium hunter’s guide”, *Phys. Rev. D*, vol. 110, no. 5, p. 054032, 2024. DOI: 10.1103/PhysRevD.110.054032. arXiv: 2407.20330 [hep-ph].
- [39] B. Fuks, K. Hagiwara, K. Ma, and Y.-J. Zheng, “Simulating toponium formation signals at the LHC”, *Eur. Phys. J. C*, vol. 85, no. 2, p. 157, 2025. DOI: 10.1140/epjc/s10052-025-13853-3. arXiv: 2411.18962 [hep-ph].
- [40] T. Barnes, S. Godfrey, and E. S. Swanson, “Higher charmonia”, *Phys. Rev. D*, vol. 72, p. 054026, 2005. DOI: 10.1103/PhysRevD.72.054026. arXiv: hep-ph/0505002.
- [41] G. Bertone, D. Hooper, and J. Silk, “Particle dark matter: Evidence, candidates and constraints”, *Phys. Rept.*, vol. 405, pp. 279–390, 2005. DOI: 10.1016/j.physrep.2004.08.031. arXiv: hep-ph/0404175.
- [42] T. A. Porter, R. P. Johnson, and P. W. Graham, “Dark Matter Searches with Astroparticle Data”, *Ann. Rev. Astron. Astrophys.*, vol. 49, pp. 155–194, 2011. DOI: 10.1146/annurev-astro-081710-102528. arXiv: 1104.2836 [astro-ph.HE].
- [43] A. Arbey and F. Mahmoudi, “Dark matter and the early Universe: a review”, *Prog. Part. Nucl. Phys.*, vol. 119, p. 103865, 2021. DOI: 10.1016/j.ppnp.2021.103865. arXiv: 2104.11488 [hep-ph].
- [44] A. de Gouv  a, “Neutrino Mass Models”, *Ann. Rev. Nucl. Part. Sci.*, vol. 66, pp. 197–217, 2016. DOI: 10.1146/annurev-nucl-102115-044600.

- 3880 [45] A. Dev, “Neutrino Oscillations and Mass Models”, Oct. 2023. arXiv: 2310.  
3881 17685 [hep-ph].
- 3882 [46] P. Nelson, “Naturalness in Theoretical Physics”, *American Scientist*, vol. 73,  
3883 no. 1, pp. 60–67, 1985.
- 3884 [47] S. Koren, “New Approaches to the Hierarchy Problem and their Signatures  
3885 from Microscopic to Cosmic Scales”, Ph.D. dissertation, UC Santa Barbara,  
3886 2020. arXiv: 2009.11870 [hep-ph].
- 3887 [48] N. Craig, “Naturalness: past, present, and future”, *Eur. Phys. J. C*, vol. 83,  
3888 no. 9, p. 825, 2023. DOI: 10.1140/epjc/s10052-023-11928-7. arXiv:  
3889 2205.05708 [hep-ph].
- 3890 [49] R. D. Peccei and H. R. Quinn, “CP Conservation in the Presence of In-  
3891 stantons”, *Phys. Rev. Lett.*, vol. 38, pp. 1440–1443, 1977. DOI: 10.1103/  
3892 PhysRevLett.38.1440.
- 3893 [50] R. D. Peccei and H. R. Quinn, “Constraints Imposed by CP Conservation in  
3894 the Presence of Instantons”, *Phys. Rev. D*, vol. 16, pp. 1791–1797, 1977. DOI:  
3895 10.1103/PhysRevD.16.1791.
- 3896 [51] CMS Collaboration, “Search for dark matter produced in association with  
3897 a single top quark or a top quark pair in proton-proton collisions at  $\sqrt{s} =$   
3898 13 TeV”, CERN, Geneva, Tech. Rep., 2024. [Online]. Available: <https://cds.cern.ch/record/2895470>.
- 3900 [52] T. D. Lee, “A Theory of Spontaneous T Violation”, *Phys. Rev. D*, vol. 8, G.  
3901 Feinberg, Ed., pp. 1226–1239, 1973. DOI: 10.1103/PhysRevD.8.1226.
- 3902 [53] G. C. Branco, P. M. Ferreira, L. Lavoura, M. N. Rebelo, M. Sher, and  
3903 J. P. Silva, “Theory and phenomenology of two-Higgs-doublet models”, *Phys.  
3904 Rept.*, vol. 516, pp. 1–102, 2012. DOI: 10.1016/j.physrep.2012.02.002.  
3905 arXiv: 1106.0034 [hep-ph].
- 3906 [54] H. E. Haber and G. L. Kane, “The Search for Supersymmetry: Probing  
3907 Physics Beyond the Standard Model”, *Phys. Rept.*, vol. 117, pp. 75–263,  
3908 1985. DOI: 10.1016/0370-1573(85)90051-1.
- 3909 [55] J. E. Kim, “Light Pseudoscalars, Particle Physics and Cosmology”, *Phys.  
3910 Rept.*, vol. 150, pp. 1–177, 1987. DOI: 10.1016/0370-1573(87)90017-2.
- 3911 [56] S. Weinberg, “A New Light Boson?”, *Phys. Rev. Lett.*, vol. 40, pp. 223–226,  
3912 1978. DOI: 10.1103/PhysRevLett.40.223.
- 3913 [57] F. Wilczek, “Problem of Strong  $P$  and  $T$  Invariance in the Presence of  
3914 Instantons”, *Phys. Rev. Lett.*, vol. 40, pp. 279–282, 1978. DOI: 10.1103/  
3915 PhysRevLett.40.279.

- [58] L. Di Luzio, M. Giannotti, E. Nardi, and L. Visinelli, “The landscape of QCD axion models”, *Phys. Rept.*, vol. 870, pp. 1–117, 2020. DOI: 10.1016/j.physrep.2020.06.002. arXiv: 2003.01100 [hep-ph].
- [59] J. M. Pendlebury et al., “Revised experimental upper limit on the electric dipole moment of the neutron”, *Phys. Rev. D*, vol. 92, no. 9, p. 092003, 2015. DOI: 10.1103/PhysRevD.92.092003. arXiv: 1509.04411 [hep-ex].
- [60] C. Abel et al., “Measurement of the Permanent Electric Dipole Moment of the Neutron”, *Phys. Rev. Lett.*, vol. 124, no. 8, p. 081803, 2020. DOI: 10.1103/PhysRevLett.124.081803. arXiv: 2001.11966 [hep-ex].
- [61] J. E. Kim, “Weak Interaction Singlet and Strong CP Invariance”, *Phys. Rev. Lett.*, vol. 43, p. 103, 1979. DOI: 10.1103/PhysRevLett.43.103.
- [62] M. A. Shifman, A. I. Vainshtein, and V. I. Zakharov, “Can Confinement Ensure Natural CP Invariance of Strong Interactions?”, *Nucl. Phys. B*, vol. 166, pp. 493–506, 1980. DOI: 10.1016/0550-3213(80)90209-6.
- [63] M. Dine, W. Fischler, and M. Srednicki, “A Simple Solution to the Strong CP Problem with a Harmless Axion”, *Phys. Lett. B*, vol. 104, pp. 199–202, 1981. DOI: 10.1016/0370-2693(81)90590-6.
- [64] A. R. Zhitnitsky, “On Possible Suppression of the Axion Hadron Interactions”, *Sov. J. Nucl. Phys.*, vol. 31, p. 260, 1980.
- [65] H. Georgi, D. B. Kaplan, and L. Randall, “Manifesting the Invisible Axion at Low-energies”, *Phys. Lett. B*, vol. 169, pp. 73–78, 1986. DOI: 10.1016/0370-2693(86)90688-X.
- [66] V. A. Rubakov, “Grand unification and heavy axion”, *JETP Lett.*, vol. 65, pp. 621–624, 1997. DOI: 10.1134/1.567390. arXiv: hep-ph/9703409.
- [67] B. Holdom and M. E. Peskin, “Raising the Axion Mass”, *Nucl. Phys. B*, vol. 208, pp. 397–412, 1982. DOI: 10.1016/0550-3213(82)90228-0.
- [68] S. Dimopoulos, A. Hook, J. Huang, and G. Marques-Tavares, “A collider observable QCD axion”, *JHEP*, vol. 11, p. 052, 2016. DOI: 10.1007/JHEP11(2016)052. arXiv: 1606.03097 [hep-ph].
- [69] T. Gherghetta, N. Nagata, and M. Shifman, “A Visible QCD Axion from an Enlarged Color Group”, *Phys. Rev. D*, vol. 93, no. 11, p. 115010, 2016. DOI: 10.1103/PhysRevD.93.115010. arXiv: 1604.01127 [hep-ph].
- [70] M. E. Peskin and D. V. Schroeder, *An Introduction to quantum field theory*. Reading, USA: Addison-Wesley, 1995, ISBN: 978-0-201-50397-5, 978-0-429-50355-9, 978-0-429-49417-8. DOI: 10.1201/9780429503559.
- [71] G. Altarelli and G. Parisi, “Asymptotic Freedom in Parton Language”, *Nucl. Phys. B*, vol. 126, pp. 298–318, 1977. DOI: 10.1016/0550-3213(77)90384-4.

- 3953 [72] P. Skands, “Introduction to QCD”, in *Searching for New Physics at Small*  
 3954 *and Large Scales*, 2013, pp. 341–420. DOI: [10.1142/9789814525220\\_0008](https://doi.org/10.1142/9789814525220_0008).  
 3955 arXiv: [1207.2389](https://arxiv.org/abs/1207.2389) [hep-ph].
- 3956 [73] R. D. Ball et al., “Parton distributions from high-precision collider data”,  
 3957 *Eur. Phys. J. C*, vol. 77, p. 663, 2017. DOI: [10.1140/epjc/s10052-017-5199-5](https://doi.org/10.1140/epjc/s10052-017-5199-5). arXiv: [1706.00428](https://arxiv.org/abs/1706.00428) [hep-ph].
- 3959 [74] F. Maltoni and T. Stelzer, “MadEvent: Automatic event generation with  
 3960 MadGraph”, *JHEP*, vol. 02, p. 027, 2003. DOI: [10.1088/1126-6708/2003/02/027](https://doi.org/10.1088/1126-6708/2003/02/027). arXiv: [hep-ph/0208156](https://arxiv.org/abs/hep-ph/0208156).
- 3962 [75] M. D. Schwartz, *Quantum Field Theory and the Standard Model*. Cambridge  
 3963 University Press, Mar. 2014, ISBN: 978-1-107-03473-0, 978-1-107-03473-0.
- 3964 [76] F. J. Tackmann, “Beyond Scale Variations: Perturbative Theory Uncertain-  
 3965 ties from Nuisance Parameters”, Nov. 2024. arXiv: [2411.18606](https://arxiv.org/abs/2411.18606) [hep-ph].
- 3966 [77] P. Nason and B. Webber, “Next-to-Leading-Order Event Generators”, *Ann.*  
 3967 *Rev. Nucl. Part. Sci.*, vol. 62, pp. 187–213, 2012. DOI: [10.1146/annurev-nucl-102711-094928](https://doi.org/10.1146/annurev-nucl-102711-094928). arXiv: [1202.1251](https://arxiv.org/abs/1202.1251) [hep-ph].
- 3969 [78] J. Alwall et al., “The automated computation of tree-level and next-to-  
 3970 leading order differential cross sections, and their matching to parton shower  
 3971 simulations”, *JHEP*, vol. 07, p. 079, 2014. DOI: [10.1007/JHEP07\(2014\)079](https://doi.org/10.1007/JHEP07(2014)079).  
 3972 arXiv: [1405.0301](https://arxiv.org/abs/1405.0301) [hep-ph].
- 3973 [79] C. Degrande, C. Duhr, B. Fuks, D. Grellscheid, O. Mattelaer, and T. Re-  
 3974 iter, “UFO - The Universal FeynRules Output”, *Comput. Phys. Commun.*,  
 3975 vol. 183, pp. 1201–1214, 2012. DOI: [10.1016/j.cpc.2012.01.022](https://doi.org/10.1016/j.cpc.2012.01.022). arXiv:  
 3976 [1108.2040](https://arxiv.org/abs/1108.2040) [hep-ph].
- 3977 [80] P. Nason, “A new method for combining NLO QCD with shower Monte Carlo  
 3978 algorithms”, *JHEP*, vol. 11, p. 040, 2004. DOI: [10.1088/1126-6708/2004/11/040](https://doi.org/10.1088/1126-6708/2004/11/040). arXiv: [hep-ph/0409146](https://arxiv.org/abs/hep-ph/0409146).
- 3980 [81] S. Frixione, P. Nason, and C. Oleari, “Matching NLO QCD computations  
 3981 with parton shower simulations: The POWHEG method”, *JHEP*, vol. 11,  
 3982 p. 070, 2007. DOI: [10.1088/1126-6708/2007/11/070](https://doi.org/10.1088/1126-6708/2007/11/070). arXiv: [0709.2092](https://arxiv.org/abs/0709.2092)  
 3983 [hep-ph].
- 3984 [82] S. Alioli, P. Nason, C. Oleari, and E. Re, “A general framework for imple-  
 3985 menting NLO calculations in shower Monte Carlo programs: The POWHEG  
 3986 BOX”, *JHEP*, vol. 06, p. 043, 2010. DOI: [10.1007/JHEP06\(2010\)043](https://doi.org/10.1007/JHEP06(2010)043). arXiv:  
 3987 [1002.2581](https://arxiv.org/abs/1002.2581) [hep-ph].
- 3988 [83] S. Frixione, G. Ridolfi, and P. Nason, “A positive-weight next-to-leading-  
 3989 order Monte Carlo for heavy flavour hadroproduction”, *JHEP*, vol. 09, p. 126,  
 3990 2007. DOI: [10.1088/1126-6708/2007/09/126](https://doi.org/10.1088/1126-6708/2007/09/126). arXiv: [0707.3088](https://arxiv.org/abs/0707.3088) [hep-ph].

- [3991] [84] T. Sjöstrand et al., “An introduction to PYTHIA8.2”, *Comput. Phys. Commun.*, vol. 191, p. 159, 2015. DOI: 10.1016/j.cpc.2015.01.024. arXiv: 1410.3012 [hep-ph].
- [3994] [85] C. Bierlich et al., “A comprehensive guide to the physics and usage of PYTHIA 8.3”, *SciPost Phys. Codeb.*, vol. 2022, p. 8, 2022. DOI: 10.21468/SciPostPhysCodeb.8. arXiv: 2203.11601 [hep-ph].
- [3997] [86] S. Frixione and B. R. Webber, “Matching NLO QCD computations and parton shower simulations”, *JHEP*, vol. 06, p. 029, 2002. DOI: 10.1088/1126-6708/2002/06/029. arXiv: hep-ph/0204244.
- [4000] [87] M. L. Mangano, M. Moretti, F. Piccinini, and M. Treccani, “Matching matrix elements and shower evolution for top-quark production in hadronic collisions”, *JHEP*, vol. 01, p. 013, 2007. DOI: 10.1088/1126-6708/2007/01/013. arXiv: hep-ph/0611129.
- [4004] [88] R. Frederix and S. Frixione, “Merging meets matching in MC@NLO”, *JHEP*, vol. 12, p. 061, 2012. DOI: 10.1007/JHEP12(2012)061. arXiv: 1209.6215 [hep-ph].
- [4007] [89] J. Bellm et al., “HERWIG7.0/HERWIG++3.0 release note”, *Eur. Phys. J. C*, vol. 76, p. 196, 2016. DOI: 10.1140/epjc/s10052-016-4018-8. arXiv: 1512.01178 [hep-ph].
- [4010] [90] M. Bähr et al., “HERWIG++ physics and manual”, *Eur. Phys. J. C*, vol. 58, p. 639, 2008. DOI: 10.1140/epjc/s10052-008-0798-9. arXiv: 0803.0883 [hep-ph].
- [4013] [91] P. Skands, S. Carrazza, and J. Rojo, “Tuning PYTHIA 8.1: the Monash 2013 Tune”, *Eur. Phys. J. C*, vol. 74, no. 8, p. 3024, 2014. DOI: 10.1140/epjc/s10052-014-3024-y. arXiv: 1404.5630 [hep-ph].
- [4016] [92] CMS Collaboration, “Extraction and validation of a new set of CMS Pythia 8 tunes from underlying-event measurements”, *Eur. Phys. J. C*, vol. 80, p. 4, 2020. DOI: 10.1140/epjc/s10052-019-7499-4. arXiv: 1903.12179 [hep-ex].
- [4020] [93] B. Andersson, G. Gustafson, G. Ingelman, and T. Sjostrand, “Parton Fragmentation and String Dynamics”, *Phys. Rept.*, vol. 97, pp. 31–145, 1983. DOI: 10.1016/0370-1573(83)90080-7.
- [4023] [94] T. Sjostrand, “Jet Fragmentation of Nearby Partons”, *Nucl. Phys. B*, vol. 248, pp. 469–502, 1984. DOI: 10.1016/0550-3213(84)90607-2.
- [4025] [95] S. Argyropoulos and T. Sjöstrand, “Effects of color reconnection on  $t\bar{t}$  final states at the LHC”, *JHEP*, vol. 11, p. 043, 2014. DOI: 10.1007/JHEP11(2014)043. arXiv: 1407.6653 [hep-ph].

- 4028 [96] J. R. Christiansen and P. Z. Skands, “String Formation Beyond Leading  
4029 Colour”, *JHEP*, vol. 08, p. 003, 2015. DOI: 10.1007/JHEP08(2015)003.  
4030 arXiv: 1505.01681 [hep-ph].
- 4031 [97] CMS Collaboration, “Pileup mitigation at CMS in 13 TeV data”, *JINST*,  
4032 vol. 15, no. 09, P09018, 2020. DOI: 10.1088/1748-0221/15/09/P09018.  
4033 arXiv: 2003.00503 [hep-ex].
- 4034 [98] CMS Collaboration, “Precision luminosity measurement in proton-proton  
4035 collisions at  $\sqrt{s} = 13$  TeV in 2015 and 2016 at CMS”, *Eur. Phys. J. C*,  
4036 vol. 81, no. 9, p. 800, 2021. DOI: 10.1140/epjc/s10052-021-09538-2.  
4037 arXiv: 2104.01927 [hep-ex].
- 4038 [99] S. Agostinelli et al., “GEANT4 — a simulation toolkit”, *Nucl. Instrum. Meth.*  
4039 *A*, vol. 506, p. 250, 2003. DOI: 10.1016/S0168-9002(03)01368-8.
- 4040 [100] “LHC Design Report Vol.1: The LHC Main Ring”, O. S. Bruning et al., Eds.,  
4041 Jun. 2004. DOI: 10.5170/CERN-2004-003-V-1.
- 4042 [101] ATLAS Collaboration, “The ATLAS Experiment at the CERN Large Hadron  
4043 Collider”, *JINST*, vol. 3, S08003, 2008. DOI: 10.1088/1748-0221/3/08/  
4044 S08003.
- 4045 [102] LHCb Collaboration, “The LHCb Detector at the LHC”, *JINST*, vol. 3,  
4046 S08005, 2008. DOI: 10.1088/1748-0221/3/08/S08005.
- 4047 [103] ALICE Collaboration, “The ALICE experiment at the CERN LHC”, *JINST*,  
4048 vol. 3, S08002, 2008. DOI: 10.1088/1748-0221/3/08/S08002.
- 4049 [104] I. Zurbano Fernandez et al., “High-Luminosity Large Hadron Collider (HL-  
4050 LHC): Technical design report”, vol. 10/2020, I. Béjar Alonso, O. Brüning,  
4051 P. Fessia, L. Rossi, L. Tavian, and M. Zerlauth, Eds., Dec. 2020. DOI: 10.  
4052 23731/CYRM-2020-0010.
- 4053 [105] CMS Collaboration, “Technical Proposal for the Phase-II Upgrade of the  
4054 CMS Detector”, Geneva, Tech. Rep., 2015. DOI: 10.17181/CERN.VU8I.D59J.  
4055 [Online]. Available: <https://cds.cern.ch/record/2020886>.
- 4056 [106] CMS Collaboration, “Development of the CMS detector for the CERN LHC  
4057 Run 3”, *JINST*, vol. 19, P05064, 2024. DOI: 10.1088/1748-0221/19/05/  
4058 P05064. arXiv: 2309.05466 [physics.ins-det].
- 4059 [107] CMS Collaboration, *CMS Detector Slice*, 2016. [Online]. Available: <https://cds.cern.ch/record/2120661>.
- 4060 [108] CMS Collaboration, “Description and performance of track and primary-  
4061 vertex reconstruction with the CMS tracker”, *JINST*, vol. 9, P10009, 2014.  
4062 DOI: 10.1088/1748-0221/9/10/P10009. arXiv: 1405.6569 [physics.ins-  
4063 det].

- 4065 [109] W. Adam et al., “The CMS Phase-1 Pixel Detector Upgrade”, *JINST*, vol. 16,  
4066 no. 02, P02027, 2021. DOI: 10.1088/1748-0221/16/02/P02027. arXiv:  
4067 2012.14304 [[physics.ins-det](#)].
- 4068 [110] “The CMS electromagnetic calorimeter project: Technical Design Report”,  
4069 Tech. Rep., 1997.
- 4070 [111] CMS Collaboration, “Electron and photon reconstruction and identification  
4071 with the CMS experiment at the CERN LHC”, *JINST*, vol. 16, no. 05,  
4072 P05014, 2021. DOI: 10.1088/1748-0221/16/05/P05014. arXiv: 2012.06888  
4073 [[hep-ex](#)].
- 4074 [112] “The CMS hadron calorimeter project: Technical Design Report”, Tech. Rep.,  
4075 1997.
- 4076 [113] “CMS Technical Design Report for the Phase 1 Upgrade of the Hadron  
4077 Calorimeter”, Tech. Rep., Sep. 2012. DOI: 10.2172/1151651.
- 4078 [114] “The CMS muon project: Technical Design Report”, Tech. Rep., 1997.
- 4079 [115] N. Pozzobon, “The CMS Muon System performance during the LHC Run-2”,  
4080 CERN, Geneva, Tech. Rep., 2019. DOI: 10.1088/1748-0221/14/11/C11031.  
4081 [Online]. Available: <https://cds.cern.ch/record/2701333>.
- 4082 [116] V. Khachatryan et al., “The CMS trigger system”, *JINST*, vol. 12, no. 01,  
4083 P01020, 2017. DOI: 10.1088/1748-0221/12/01/P01020. arXiv: 1609.02366  
4084 [[physics.ins-det](#)].
- 4085 [117] CMS Collaboration, “Performance of the CMS Level-1 trigger in proton-  
4086 proton collisions at  $\sqrt{s} = 13$  TeV”, *JINST*, vol. 15, no. 10, P10017, 2020.  
4087 DOI: 10.1088/1748-0221/15/10/P10017. arXiv: 2006.10165 [[hep-ex](#)].
- 4088 [118] W. Adam et al., “The CMS high level trigger”, *Eur. Phys. J. C*, vol. 46,  
4089 pp. 605–667, 2006. DOI: 10.1140/epjc/s2006-02495-8. arXiv: [hep-ex/0512077](#).
- 4090 [119] S. Varghese, “CMS High Level Trigger Performance for Run 3”, *PoS*, vol. EPS-  
4091 HEP2023, p. 517, 2023. DOI: 10.22323/1.449.0517.
- 4093 [120] CMS Collaboration, “Particle-flow reconstruction and global event descrip-  
4094 tion with the CMS detector”, *JINST*, vol. 12, P10003, 2017. DOI: 10.1088/  
4095 1748-0221/12/10/P10003. arXiv: 1706.04965 [[physics.ins-det](#)].
- 4096 [121] D. Bertolini, P. Harris, M. Low, and N. Tran, “Pileup Per Particle Identifica-  
4097 tion”, *JHEP*, vol. 10, p. 059, 2014. DOI: 10.1007/JHEP10(2014)059. arXiv:  
4098 1407.6013 [[hep-ph](#)].
- 4099 [122] M. Cacciari, G. P. Salam, and G. Soyez, “The anti- $k_t$  jet clustering algo-  
4100 rithm”, *JHEP*, vol. 04, p. 063, 2008. DOI: 10.1088/1126-6708/2008/04/063.  
4101 arXiv: 0802.1189 [[hep-ph](#)].

- [123] E. Bols, J. Kieseler, M. Verzetti, M. Stoye, and A. Stakia, “Jet Flavour Classification Using DeepJet”, *JINST*, vol. 15, no. 12, P12012, 2020. DOI: 10.1088/1748-0221/15/12/P12012. arXiv: 2008.10519 [hep-ex].
- [124] CMS Collaboration, “Performance of missing transverse momentum reconstruction in proton-proton collisions at  $\sqrt{s} = 13$  TeV using the CMS detector”, *JINST*, vol. 14, no. 07, P07004, 2019. DOI: 10.1088/1748-0221/14/07/P07004. arXiv: 1903.06078 [hep-ex].
- [125] G. Cowan, K. Cranmer, E. Gross, and O. Vitells, “Asymptotic formulae for likelihood-based tests of new physics”, *Eur. Phys. J. C*, vol. 71, p. 1554, 2011, [Erratum: Eur.Phys.J.C 73, 2501 (2013)]. DOI: 10.1140/epjc/s10052-011-1554-0. arXiv: 1007.1727 [physics.data-an].
- [126] S. S. Wilks, “The large-sample distribution of the likelihood ratio for testing composite hypotheses”, *Annals Math. Statist.*, vol. 9, no. 1, pp. 60–62, 1938. DOI: 10.1214/aoms/1177732360.
- [127] A. Wald, “Tests of statistical hypotheses concerning several parameters when the number of observations is large”, *Trans. Am. Math. Soc.*, vol. 54, no. 3, pp. 462–482, 1942. DOI: 10.1090/S0002-9947-1943-0012401-3.
- [128] T. Junk, “Confidence level computation for combining searches with small statistics”, *Nucl. Instrum. Meth. A*, vol. 434, p. 435, 1999. DOI: 10.1016/S0168-9002(99)00498-2. arXiv: hep-ex/9902006.
- [129] A. L. Read, “Presentation of search results: The CL<sub>s</sub> technique”, *J. Phys. G*, vol. 28, p. 2693, 2002. DOI: 10.1088/0954-3899/28/10/313.
- [130] CMS Collaboration, “The CMS Statistical Analysis and Combination Tool: Combine”, *Comput. Softw. Big Sci.*, vol. 8, no. 1, p. 19, 2024. DOI: 10.1007/s41781-024-00121-4. arXiv: 2404.06614 [physics.data-an].
- [131] L. Heinrich, M. Feickert, G. Stark, and K. Cranmer, “Pyhf: Pure-Python implementation of HistFactory statistical models”, *Journal of Open Source Software*, vol. 6, no. 58, p. 2823, 2021. DOI: 10.21105/joss.02823. [Online]. Available: <https://doi.org/10.21105/joss.02823>.
- [132] CMS Collaboration, “First measurement of the top quark pair production cross section in proton-proton collisions at  $\sqrt{s} = 13.6$  TeV”, CMS Physics Analysis Summary CMS-PAS-TOP-22-012, 2022. [Online]. Available: <https://cds.cern.ch/record/2834110>.
- [133] ATLAS Collaboration, “Measurement of the  $t\bar{t}$  cross section and its ratio to the Z production cross section using pp collisions at  $\sqrt{s} = 13.6$  TeV with the ATLAS detector”, *Phys. Lett. B*, vol. 848, p. 138376, 2024. DOI: 10.1016/j.physletb.2023.138376. arXiv: 2308.09529 [hep-ex].

- [134] M. Czakon and A. Mitov, “TOP++: A program for the calculation of the top-pair cross-section at hadron colliders”, *Comput. Phys. Commun.*, vol. 185, p. 2930, 2014. DOI: [10.1016/j.cpc.2014.06.021](https://doi.org/10.1016/j.cpc.2014.06.021). arXiv: [1112.5675](https://arxiv.org/abs/1112.5675) [hep-ph].
- [135] J. Campbell, T. Neumann, and Z. Sullivan, “Single-top-quark production in the  $t$ -channel at NNLO”, *JHEP*, vol. 02, p. 040, 2021. DOI: [10.1007/JHEP02\(2021\)040](https://doi.org/10.1007/JHEP02(2021)040). arXiv: [2012.01574](https://arxiv.org/abs/2012.01574) [hep-ph].
- [136] S. Camarda et al., “DYTURBO: Fast predictions for Drell–Yan processes”, *Eur. Phys. J. C*, vol. 80, p. 251, 2020. DOI: [10.1140/epjc/s10052-020-7757-5](https://doi.org/10.1140/epjc/s10052-020-7757-5). arXiv: [1910.07049](https://arxiv.org/abs/1910.07049) [hep-ph].
- [137] M. Grazzini, S. Kallweit, and M. Wiesemann, “Fully differential NNLO computations with MATRIX”, *Eur. Phys. J. C*, vol. 78, p. 537, 2018. DOI: [10.1140/epjc/s10052-018-5771-7](https://doi.org/10.1140/epjc/s10052-018-5771-7). arXiv: [1711.06631](https://arxiv.org/abs/1711.06631) [hep-ph].
- [138] N. Kidonakis and N. Yamanaka, “Higher-order corrections for tW production at high-energy hadron colliders”, *JHEP*, vol. 05, p. 278, 2021. DOI: [10.1007/JHEP05\(2021\)278](https://doi.org/10.1007/JHEP05(2021)278). arXiv: [2102.11300](https://arxiv.org/abs/2102.11300) [hep-ph].
- [139] CMS Collaboration, “Performance of the CMS muon detector and muon reconstruction with proton-proton collisions at  $\sqrt{s} = 13$  TeV”, *JINST*, vol. 13, no. 06, P06015, 2018. DOI: [10.1088/1748-0221/13/06/P06015](https://doi.org/10.1088/1748-0221/13/06/P06015). arXiv: [1804.04528](https://arxiv.org/abs/1804.04528) [physics.ins-det].
- [140] CMS Collaboration, “Identification of heavy-flavour jets with the CMS detector in pp collisions at 13 TeV”, *JINST*, vol. 13, no. 05, P05011, 2018. DOI: [10.1088/1748-0221/13/05/P05011](https://doi.org/10.1088/1748-0221/13/05/P05011). arXiv: [1712.07158](https://arxiv.org/abs/1712.07158) [physics.ins-det].
- [141] CMS Collaboration, “Jet energy scale and resolution in the CMS experiment in pp collisions at 8 TeV”, *JINST*, vol. 12, P02014, 2017. DOI: [10.1088/1748-0221/12/02/P02014](https://doi.org/10.1088/1748-0221/12/02/P02014). arXiv: [1607.03663](https://arxiv.org/abs/1607.03663) [hep-ex].
- [142] CMS Collaboration, “Determination of Jet Energy Calibration and Transverse Momentum Resolution in CMS”, *JINST*, vol. 6, P11002, 2011. DOI: [10.1088/1748-0221/6/11/P11002](https://doi.org/10.1088/1748-0221/6/11/P11002). arXiv: [1107.4277](https://arxiv.org/abs/1107.4277) [physics.ins-det].
- [143] CDF Collaboration, “Measurement of  $\sigma \cdot B(W \rightarrow e\nu)$  and  $\sigma \cdot B(Z^0 \rightarrow e^+e^-)$  in  $p\bar{p}$  Collisions at  $\sqrt{s} = 1.8$  TeV”, *Phys. Rev. Lett.*, vol. 76, pp. 3070–3075, 1996. DOI: [10.1103/PhysRevLett.76.3070](https://doi.org/10.1103/PhysRevLett.76.3070). arXiv: [hep-ex/9509010](https://arxiv.org/abs/hep-ex/9509010).
- [144] CDF Collaboration, “Measurement of the  $W$  boson mass with the Collider Detector at Fermilab”, *Phys. Rev. D*, vol. 64, p. 052001, 2001. DOI: [10.1103/PhysRevD.64.052001](https://doi.org/10.1103/PhysRevD.64.052001). arXiv: [hep-ex/0007044](https://arxiv.org/abs/hep-ex/0007044).

- 4175 [145] CMS Collaboration, “Search for dark matter particles produced in association  
 4176 with a top quark pair at  $\sqrt{s} = 13$  TeV”, *Phys. Rev. Lett.*, vol. 122, no. 1,  
 4177 p. 011803, 2019. DOI: 10.1103/PhysRevLett.122.011803. arXiv: 1807.  
 4178 06522 [hep-ex].
- 4179 [146] CMS Collaboration, “Luminosity monitoring with z counting in early 2022  
 4180 data”, CMS Detector Performance Note CMS-DP-2023-003, 2023. [Online].  
 4181 Available: <https://cds.cern.ch/record/2851655>.
- 4182 [147] CMS Collaboration, “Luminosity measurement in proton-proton collisions at  
 4183 13.6 TeV in 2022 at CMS”, CERN, Geneva, CMS Physics Analysis Summary,  
 4184 2024. [Online]. Available: <http://cds.cern.ch/record/2890833>.
- 4185 [148] M. Cacciari, S. Frixione, M. L. Mangano, P. Nason, and G. Ridolfi, “The  $t\bar{t}$   
 4186 cross-section at 1.8 and 1.96 TeV: A study of the systematics due to parton  
 4187 densities and scale dependence”, *JHEP*, vol. 04, p. 068, 2004. DOI: 10.1088/  
 4188 1126-6708/2004/04/068. arXiv: hep-ph/0303085.
- 4189 [149] J. Butterworth et al., “PDF4LHC recommendations for LHC Run II”, *J.  
 4190 Phys. G*, vol. 43, p. 023001, 2016. DOI: 10.1088/0954-3899/43/2/023001.  
 4191 arXiv: 1510.03865 [hep-ph].
- 4192 [150] CMS Collaboration, “Investigations of the impact of the parton shower tuning  
 4193 in PYTHIA 8 in the modelling of  $t\bar{t}$  at  $\sqrt{s} = 8$  and 13 TeV”, CMS Physics  
 4194 Analysis Summary CMS-PAS-TOP-16-021, 2016. [Online]. Available: <https://cds.cern.ch/record/2235192>.
- 4196 [151] CMS Collaboration, “Measurements of  $t\bar{t}$  differential cross sections in proton-  
 4197 proton collisions at  $\sqrt{s} = 13$  TeV using events containing two leptons”, *JHEP*,  
 4198 vol. 02, p. 149, 2019. DOI: 10.1007/JHEP02(2019)149. arXiv: 1811.06625  
 4199 [hep-ex].
- 4200 [152] CMS Collaboration, “Measurement of normalized differential  $t\bar{t}$  cross sections  
 4201 in the dilepton channel from  $pp$  collisions at  $\sqrt{s} = 13$  TeV”, *JHEP*, vol. 04,  
 4202 p. 060, 2018. DOI: 10.1007/JHEP04(2018)060. arXiv: 1708.07638 [hep-ex].
- 4203 [153] CMS Collaboration, “Measurement of differential cross sections for top quark  
 4204 pair production using the lepton+jets final state in proton-proton collisions  
 4205 at 13 TeV”, *Phys. Rev. D*, vol. 95, no. 9, p. 092001, 2017. DOI: 10.1103/  
 4206 PhysRevD.95.092001. arXiv: 1610.04191 [hep-ex].
- 4207 [154] M. Czakon, D. Heymes, A. Mitov, D. Pagani, I. Tsinikos, and M. Zaro, “Top-  
 4208 pair production at the LHC through NNLO QCD and NLO EW”, *JHEP*,  
 4209 vol. 10, p. 186, 2017. DOI: 10.1007/JHEP10(2017)186. arXiv: 1705.04105  
 4210 [hep-ph].
- 4211 [155] R. Barlow and C. Beeston, “Fitting using finite Monte Carlo samples”, *Comput.  
 4212 Phys. Commun.*, vol. 77, p. 219, 1993. DOI: 10.1016/0010-4655(93)  
 4213 90005-W.

- [4214] [156] CMS Collaboration, “Measurement of the  $t\bar{t}$  production cross section, the  
 [4215] top quark mass, and the strong coupling constant using dilepton events in  
 [4216] pp collisions at  $\sqrt{s} = 13$  TeV”, *Eur. Phys. J. C*, vol. 79, p. 368, 2019. DOI:  
 [4217] [10.1140/epjc/s10052-019-6863-8](https://doi.org/10.1140/epjc/s10052-019-6863-8). arXiv: 1812.10505 [hep-ex].
- [4218] [157] ATLAS Collaboration, “Measurement of the  $t\bar{t}$  production cross-section in the  
 [4219] lepton+jets channel at  $\sqrt{s} = 13$  TeV with the ATLAS experiment”, *Phys.*  
 [4220] *Lett. B*, vol. 810, p. 135797, 2020. DOI: [10.1016/j.physletb.2020.135797](https://doi.org/10.1016/j.physletb.2020.135797).  
 [4221] arXiv: 2006.13076 [hep-ex].
- [4222] [158] CMS Collaboration, “Measurement of the  $t\bar{t}$  production cross section in the  
 [4223] all-jet final state in pp collisions at  $\sqrt{s} = 7$  TeV”, *JHEP*, vol. 05, p. 065,  
 [4224] 2013. DOI: [10.1007/JHEP05\(2013\)065](https://doi.org/10.1007/JHEP05(2013)065). arXiv: 1302.0508 [hep-ex].
- [4225] [159] CMS Collaboration, “Measurement of the  $t\bar{t}$  production cross section in the  
 [4226] all-jets final state in pp collisions at  $\sqrt{s} = 8$  TeV”, *Eur. Phys. J. C*, vol. 76,  
 [4227] p. 128, 2016. DOI: [10.1140/epjc/s10052-016-3956-5](https://doi.org/10.1140/epjc/s10052-016-3956-5). arXiv: 1509.06076  
 [4228] [hep-ex].
- [4229] [160] CMS Collaboration, “Measurements of the  $t\bar{t}$  production cross section in  
 [4230] lepton+jets final states in pp collisions at 8 TeV and ratio of 8 to 7 TeV cross  
 [4231] sections”, *Eur. Phys. J. C*, vol. 77, p. 15, 2017. DOI: [10.1140/epjc/s10052-016-4504-z](https://doi.org/10.1140/epjc/s10052-016-4504-z). arXiv: 1602.09024 [hep-ex].
- [4233] [161] CMS Collaboration, “Measurement of the  $t\bar{t}$  production cross section in the  
 [4234]  $e\mu$  channel in proton-proton collisions at  $\sqrt{s} = 7$  and 8 TeV”, *JHEP*, vol. 08,  
 [4235] p. 029, 2016. DOI: [10.1007/JHEP08\(2016\)029](https://doi.org/10.1007/JHEP08(2016)029). arXiv: 1603.02303 [hep-ex].
- [4236] [162] CMS Collaboration, “Measurement of the top quark pair production cross  
 [4237] section in dilepton final states containing one  $\tau$  lepton in pp collisions at  
 [4238]  $\sqrt{s} = 13$  TeV”, *JHEP*, vol. 02, p. 191, 2020. DOI: [10.1007/JHEP02\(2020\)191](https://doi.org/10.1007/JHEP02(2020)191).  
 [4239] arXiv: 1911.13204 [hep-ex].
- [4240] [163] CMS Collaboration, “Measurement of differential  $t\bar{t}$  production cross sections  
 [4241] in the full kinematic range using lepton+jets events from proton-proton col-  
 [4242] lisions at  $\sqrt{s} = 13$  TeV”, *Phys. Rev. D*, vol. 104, p. 092013, 2021. DOI:  
 [4243] [10.1103/PhysRevD.104.092013](https://doi.org/10.1103/PhysRevD.104.092013). arXiv: 2108.02803 [hep-ex].
- [4244] [164] CMS Collaboration, “Measurement of the inclusive  $t\bar{t}$  production cross sec-  
 [4245] tion in proton-proton collisions at  $\sqrt{s} = 5.02$  TeV”, *JHEP*, vol. 04, p. 144,  
 [4246] 2022. DOI: [10.1007/JHEP04\(2022\)144](https://doi.org/10.1007/JHEP04(2022)144). arXiv: 2112.09114 [hep-ex].
- [4247] [165] M. Czakon, P. Fiedler, and A. Mitov, “Total top-quark pair-production cross  
 [4248] section at hadron colliders through  $\mathcal{O}(\alpha_S^4)$ ”, *Phys. Rev. Lett.*, vol. 110,  
 [4249] p. 252004, 2013. DOI: [10.1103/PhysRevLett.110.252004](https://doi.org/10.1103/PhysRevLett.110.252004). arXiv: 1303.6254 [hep-ph].
- [4251] [166] R. Tarrach, “The Pole Mass in Perturbative QCD”, *Nucl. Phys. B*, vol. 183,  
 [4252] pp. 384–396, 1981. DOI: [10.1016/0550-3213\(81\)90140-1](https://doi.org/10.1016/0550-3213(81)90140-1).

- [167] M. C. Smith and S. S. Willenbrock, “Top quark pole mass”, *Phys. Rev. Lett.*, vol. 79, pp. 3825–3828, 1997. DOI: 10.1103/PhysRevLett.79.3825. arXiv: hep-ph/9612329.
- [168] A. H. Hoang, “What is the Top Quark Mass?”, *Ann. Rev. Nucl. Part. Sci.*, vol. 70, pp. 225–255, 2020. DOI: 10.1146/annurev-nucl-101918-023530. arXiv: 2004.12915 [hep-ph].
- [169] ATLAS Collaboration, “Probing the quantum interference between singly and doubly resonant top-quark production in  $pp$  collisions at  $\sqrt{s} = 13\text{TeV}$  with the ATLAS detector”, *Phys. Rev. Lett.*, vol. 121, p. 152002, 2018. DOI: 10.1103/PhysRevLett.121.152002. arXiv: 1806.04667 [hep-ex].
- [170] T. Ježo, J. M. Lindert, and S. Pozzorini, “Resonance-aware NLOPS matching for off-shell  $t\bar{t} + tW$  production with semileptonic decays”, *JHEP*, vol. 10, p. 008, 2023. DOI: 10.1007/JHEP10(2023)008. arXiv: 2307.15653 [hep-ph].
- [171] T. Ježo and P. Nason, “On the treatment of resonances in next-to-leading order calculations matched to a parton shower”, *JHEP*, vol. 12, p. 065, 2015. DOI: 10.1007/JHEP12(2015)065. arXiv: 1509.09071 [hep-ph].
- [172] <https://powhegbox.mib.infn.it>.
- [173] S. Frixione, E. Laenen, P. Motylinski, and B. R. Webber, “Angular correlations of lepton pairs from vector boson and top quark decays in Monte Carlo simulations”, *JHEP*, vol. 04, p. 081, 2007. DOI: 10.1088/1126-6708/2007/04/081. arXiv: hep-ph/0702198.
- [174] E. Re, “Single-top  $Wt$ -channel production matched with parton showers using the powheg method”, *Eur. Phys. J. C*, vol. 71, p. 1547, 2011. DOI: 10.1140/epjc/s10052-011-1547-z. arXiv: 1009.2450 [hep-ph].
- [175] S. Frixione, E. Laenen, P. Motylinski, B. R. Webber, and C. D. White, “Single-top hadroproduction in association with a  $W$  boson”, *JHEP*, vol. 07, p. 029, 2008. DOI: 10.1088/1126-6708/2008/07/029. arXiv: 0805.3067 [hep-ph].
- [176] T. M. P. Tait, “The  $tW^-$  mode of single top production”, *Phys. Rev. D*, vol. 61, p. 034001, 1999. DOI: 10.1103/PhysRevD.61.034001. arXiv: hep-ph/9909352.
- [177] J. M. Campbell, R. K. Ellis, P. Nason, and E. Re, “Top-pair production and decay at NLO matched with parton showers”, *JHEP*, vol. 04, p. 114, 2015. DOI: 10.1007/JHEP04(2015)114. arXiv: 1412.1828 [hep-ph].
- [178] S. Ferrario Ravasio, T. Ježo, P. Nason, and C. Oleari, “A theoretical study of top-mass measurements at the LHC using NLO+PS generators of increasing accuracy”, *Eur. Phys. J. C*, vol. 78, p. 458, 2018. DOI: 10.1140/epjc/s10052-018-5909-7. arXiv: 1906.09166 [hep-ph].

- 4291 [179] C. Bierlich et al., “Robust independent validation of experiment and the-  
4292 ory: Rivet version 3”, *SciPost Phys.*, vol. 8, p. 026, 2020. DOI: 10.21468/  
4293 [SciPostPhys.8.2.026](#). arXiv: 1912.05451 [hep-ph].
- 4294 [180] M. Cacciari and G. P. Salam, “Pileup subtraction using jet areas”, *Phys. Lett.  
4295 B*, vol. 659, pp. 119–126, 2008. DOI: 10.1016/j.physletb.2007.09.077.  
4296 arXiv: 0707.1378 [hep-ph].
- 4297 [181] M. Cacciari, G. P. Salam, and G. Soyez, “The Catchment Area of Jets”,  
4298 *JHEP*, vol. 04, p. 005, 2008. DOI: 10.1088/1126-6708/2008/04/005. arXiv:  
4299 0802.1188 [hep-ph].
- 4300 [182] ATLAS Collaboration, “Studies of  $t\bar{t}/tW$  interference effects in  $b\bar{b}\ell^+\ell^-\nu\bar{\nu}$ ’  
4301 final states with POWHEG and MG5\_AMC@NLO setups”, ATLAS PUB  
4302 Note ATL-PHYS-PUB-2021-042, 2021. [Online]. Available: <https://cds.cern.ch/record/2792254>.
- 4303
- 4304 [183] D. Boer et al., “Gluons and the quark sea at high energies: Distributions,  
4305 polarization, tomography”, Aug. 2011. arXiv: 1108.1713 [nucl-th].
- 4306 [184] H. Brooks and P. Skands, “Coherent showers in decays of colored resonances”,  
4307 *Phys. Rev. D*, vol. 100, no. 7, p. 076006, 2019. DOI: 10.1103/PhysRevD.100.  
4308 076006. arXiv: 1907.08980 [hep-ph].
- 4309 [185] ATLAS Collaboration, “Measurement of the top-quark mass using a leptonic  
4310 invariant mass in  $pp$  collisions at  $\sqrt{s} = 13$  TeV with the ATLAS detector”,  
4311 *JHEP*, vol. 06, p. 019, 2023. DOI: 10.1007/JHEP06(2023)019. arXiv: 2209.  
4312 00583 [hep-ex].
- 4313 [186] ATLAS Collaboration, “Search for Heavy Higgs Bosons  $A/H$  Decaying to  
4314 a Top Quark Pair in  $pp$  Collisions at  $\sqrt{s} = 8$  TeV with the ATLAS De-  
4315 tector”, *Phys. Rev. Lett.*, vol. 119, no. 19, p. 191803, 2017. DOI: 10.1103/  
4316 [PhysRevLett.119.191803](#). arXiv: 1707.06025 [hep-ex].
- 4317 [187] ATLAS Collaboration, “Search for heavy neutral Higgs bosons decaying into  
4318 a top quark pair in  $140 \text{ fb}^{-1}$  of proton-proton collision data at  $\sqrt{s} = 13$   
4319 TeV with the ATLAS detector”, *JHEP*, vol. 08, p. 013, 2024. DOI: 10.1007/  
4320 [JHEP08\(2024\)013](#). arXiv: 2404.18986 [hep-ex].
- 4321 [188] ATLAS Collaboration, “Observation of a cross-section enhancement near the  
4322  $t\bar{t}$  production threshold in  $\sqrt{s} = 13$  TeV  $pp$  collisions with the ATLAS de-  
4323 tector”, ATLAS Conference Note ATLAS-CONF-2025-008, 2025. [Online].  
4324 Available: <https://cds.cern.ch/record/2937636>.
- 4325 [189] CMS Collaboration, “Search for heavy pseudoscalar and scalar bosons de-  
4326 caying to top quark pairs in proton-proton collisions at  $\sqrt{s} = 13$  TeV”, CMS  
4327 Physics Analysis Summary CMS-PAS-HIG-22-013, 2024. [Online]. Available:  
4328 <https://cds.cern.ch/record/2911775>.

- [4329] [190] J. Rübenach, “Search for Heavy Higgs Bosons in Conjunction with Neural-Network-Driven Reconstruction and Upgrade of the Fast Beam Condition Monitor at the CMS Experiment”, PhD thesis, DESY, Hamburg, May 2023.
- [4332] [191] CMS Collaboration, “Simulation of the silicon strip tracker pre-amplifier in early 2016 data”, CMS Detector Performance Note CMS-DP-2020-045, 2020. [Online]. Available: <https://cds.cern.ch/record/2740688>.
- [4335] [192] P. F. Monni, P. Nason, E. Re, M. Wiesemann, and G. Zanderighi, “MiNNLO<sub>PS</sub>: a new method to match NNLO QCD to parton showers”, *JHEP*, vol. 05, p. 143, 2020, [Erratum: JHEP 02, 031 (2022)]. DOI: 10.1007/JHEP05(2020)143. arXiv: 1908.06987 [hep-ph].
- [4339] [193] P. F. Monni, E. Re, and M. Wiesemann, “MiNNLO<sub>PS</sub>: optimizing  $2 \rightarrow 1$  hadronic processes”, *Eur. Phys. J. C*, vol. 80, no. 11, p. 1075, 2020. DOI: 10.1140/epjc/s10052-020-08658-5. arXiv: 2006.04133 [hep-ph].
- [4342] [194] M. Aliev, H. Lacker, U. Langenfeld, S. Moch, P. Uwer, and M. Wiedermann, “HATHOR: Hadronic top and heavy quarks cross section calculator”, *Comput. Phys. Commun.*, vol. 182, p. 1034, 2011. DOI: 10.1016/j.cpc.2010.12.040. arXiv: 1007.1327 [hep-ph].
- [4346] [195] P. Kant et al., “HatHor for single top-quark production: Updated predictions and uncertainty estimates for single top-quark production in hadronic collisions”, *Comput. Phys. Commun.*, vol. 191, pp. 74–89, 2015. DOI: 10.1016/j.cpc.2015.02.001. arXiv: 1406.4403 [hep-ph].
- [4350] [196] K. Melnikov and F. Petriello, “Electroweak gauge boson production at hadron colliders through  $\mathcal{O}(\alpha_S^2)$ ”, *Phys. Rev. D*, vol. 74, p. 114017, 2006. DOI: 10.1103/PhysRevD.74.114017. arXiv: hep-ph/0609070.
- [4353] [197] Y. Li and F. Petriello, “Combining QCD and electroweak corrections to dilepton production in FEWZ”, *Phys. Rev. D*, vol. 86, p. 094034, 2012. DOI: 10.1103/PhysRevD.86.094034. arXiv: 1208.5967 [hep-ph].
- [4356] [198] T. Gehrmann et al., “ $W^+W^-$  Production at Hadron Colliders in Next to Next to Leading Order QCD”, *Phys. Rev. Lett.*, vol. 113, no. 21, p. 212001, 2014. DOI: 10.1103/PhysRevLett.113.212001. arXiv: 1408.5243 [hep-ph].
- [4359] [199] J. M. Campbell and R. K. Ellis, “MCFM for the Tevatron and the LHC”, *Nucl. Phys. B Proc. Suppl.*, vol. 205-206, J. Blümlein, S.-O. Moch, and T. Riemann, Eds., pp. 10–15, 2010. DOI: 10.1016/j.nuclphysbps.2010.08.011. arXiv: 1007.3492 [hep-ph].
- [4363] [200] CMS Collaboration, “Measurement of the differential cross section for top quark pair production in pp collisions at  $\sqrt{s} = 8$  TeV”, *Eur. Phys. J. C*, vol. 75, no. 11, p. 542, 2015. DOI: 10.1140/epjc/s10052-015-3709-x. arXiv: 1505.04480 [hep-ex].

- [201] L. Sonnenschein, “Analytical solution of ttbar dilepton equations”, *Phys. Rev. D*, vol. 73, p. 054015, 2006, [Erratum: Phys.Rev.D 78, 079902 (2008)]. DOI: 10.1103/PhysRevD.78.079902. arXiv: hep-ph/0603011.
- [202] I. Korol, “Measurement of double differential  $t\bar{t}$  production cross sections with the CMS detector”, CERN-THESIS-2016-060, DESY-THESIS-2016-011, Ph.D. dissertation, Universität Hamburg, 2016. DOI: 10.3204/DESY-THESIS-2016-011.
- [203] J. H. Kühn, A. Scharf, and P. Uwer, “Electroweak corrections to top-quark pair production in quark-antiquark annihilation”, *Eur. Phys. J. C*, vol. 45, p. 139, 2006. DOI: 10.1140/epjc/s2005-02423-6. arXiv: hep-ph/0508092.
- [204] J. H. Kühn, A. Scharf, and P. Uwer, “Electroweak effects in top-quark pair production at hadron colliders”, *Eur. Phys. J. C*, vol. 51, p. 37, 2007. DOI: 10.1140/epjc/s10052-007-0275-x. arXiv: hep-ph/0610335.
- [205] J. H. Kühn, A. Scharf, and P. Uwer, “Weak interactions in top-quark pair production at hadron colliders: An update”, *Phys. Rev. D*, vol. 91, p. 014020, 2015. DOI: 10.1103/PhysRevD.91.014020. arXiv: 1305.5773 [hep-ph].
- [206] CMS Collaboration, “Combined measurements of Higgs boson couplings in proton-proton collisions at  $\sqrt{s} = 13$  TeV”, *Eur. Phys. J. C*, vol. 79, no. 5, p. 421, 2019. DOI: 10.1140/epjc/s10052-019-6909-y. arXiv: 1809.10733 [hep-ex].
- [207] CMS Collaboration, “CMS pythia 8 colour reconnection tunes based on underlying-event data”, *Eur. Phys. J. C*, vol. 83, no. 7, p. 587, 2023. DOI: 10.1140/epjc/s10052-023-11630-8. arXiv: 2205.02905 [hep-ex].
- [208] ATLAS Collaboration, “Measurement of the inclusive cross-sections of single top-quark and top-antiquark  $t$ -channel production in pp collisions at  $\sqrt{s} = 13$  TeV with the ATLAS detector”, *JHEP*, vol. 04, p. 086, 2017. DOI: 10.1007/JHEP04(2017)086. arXiv: 1609.03920 [hep-ex].
- [209] CMS Collaboration, “Measurement of the single top quark and antiquark production cross sections in the  $t$  channel and their ratio in proton-proton collisions at  $\sqrt{s} = 13$  TeV”, *Phys. Lett. B*, vol. 800, p. 135042, 2020. DOI: 10.1016/j.physletb.2019.135042. arXiv: 1812.10514 [hep-ex].
- [210] CMS Collaboration, “Measurement of the production cross section for single top quarks in association with W bosons in proton-proton collisions at  $\sqrt{s} = 13$  TeV”, *JHEP*, vol. 10, p. 117, 2018. DOI: 10.1007/JHEP10(2018)117. arXiv: 1805.07399 [hep-ex].
- [211] CMS Collaboration, “Measurement of the cross section for top quark pair production in association with a W or Z boson in proton-proton collisions at  $\sqrt{s} = 13$  TeV”, *JHEP*, vol. 08, p. 011, 2018. DOI: 10.1007/JHEP08(2018)011. arXiv: 1711.02547 [hep-ex].

- 4406 [212] ATLAS Collaboration, “Measurement of the  $t\bar{t}Z$  and  $t\bar{t}W$  cross sections in  
 4407 proton-proton collisions at  $\sqrt{s} = 13$  TeV with the ATLAS detector”, *Phys.  
 4408 Rev. D*, vol. 99, p. 072009, 2019. DOI: 10.1103/PhysRevD.99.072009. arXiv:  
 4409 1901.03584 [hep-ex].
- 4410 [213] ATLAS Collaboration, “Measurements of top-quark pair to Z-boson cross-  
 4411 section ratios at  $\sqrt{s} = 13, 8, 7$  TeV with the ATLAS detector”, *JHEP*, vol. 02,  
 4412 p. 117, 2017. DOI: 10.1007/JHEP02(2017)117. arXiv: 1612.03636 [hep-ex].
- 4413 [214] CMS Collaboration, “CMS luminosity measurement for the 2017 data-taking  
 4414 period at  $\sqrt{s} = 13$  TeV”, CMS Physics Analysis Summary CMS-PAS-LUM-  
 4415 17-004, 2018. [Online]. Available: <https://cds.cern.ch/record/2621960>.
- 4416 [215] CMS Collaboration, “CMS luminosity measurement for the 2018 data-taking  
 4417 period at  $\sqrt{s} = 13$  TeV”, CMS Physics Analysis Summary CMS-PAS-LUM-  
 4418 18-002, 2019. [Online]. Available: <https://cds.cern.ch/record/2676164>.
- 4419 [216] CMS Collaboration, “Measurement of the inelastic proton-proton cross sec-  
 4420 tion at  $\sqrt{s} = 13$  TeV”, *JHEP*, vol. 07, p. 161, 2018. DOI: 10.1007/JHEP07(2018)  
 4421 161. arXiv: 1802.02613 [hep-ex].
- 4422 [217] W. S. Cleveland, “Robust locally weighted regression and smoothing scat-  
 4423 terplots”, *Journal of the American Statistical Association*, vol. 74, no. 368,  
 4424 pp. 829–836, 1979. DOI: 10.1080/01621459.1979.10481038.
- 4425 [218] W. S. Cleveland and S. J. Devlin, “Locally weighted regression: An approach  
 4426 to regression analysis by local fitting”, *Journal of the American Statistical  
 4427 Association*, vol. 83, no. 403, pp. 596–610, 1988. DOI: 10.1080/01621459.  
 4428 1988.10478639.
- 4429 [219] CMS Collaboration, “Measurement of differential cross sections for the pro-  
 4430 duction of top quark pairs and of additional jets in lepton+jets events from  
 4431 pp collisions at  $\sqrt{s} = 13$  TeV”, *Phys. Rev. D*, vol. 97, no. 11, p. 112003, 2018.  
 4432 DOI: 10.1103/PhysRevD.97.112003. arXiv: 1803.08856 [hep-ex].
- 4433 [220] CMS Collaboration, “Development and validation of HERWIG 7 tunes from  
 4434 CMS underlying-event measurements”, *Eur. Phys. J. C*, vol. 81, no. 4, p. 312,  
 4435 2021. DOI: 10.1140/epjc/s10052-021-08949-5. arXiv: 2011.03422 [hep-  
 4436 ex].
- 4437 [221] B. R. Webber, “A QCD Model for Jet Fragmentation Including Soft Gluon  
 4438 Interference”, *Nucl. Phys. B*, vol. 238, pp. 492–528, 1984. DOI: 10.1016/  
 4439 0550-3213(84)90333-X.
- 4440 [222] F. J. Llanes-Estrada, “Ensuring that toponium is glued, not nailed”, Nov.  
 4441 2024. arXiv: 2411.19180 [hep-ph].

- 4442 [223] D. d'Enterria and K. Kang, “Exclusive photon-fusion production of even-  
4443 spin resonances and exotic QED atoms in high-energy hadron collisions”,  
4444 Mar. 2025. arXiv: 2503.10952 [hep-ph].
- 4445 [224] CMS Collaboration, “Measurement of the top quark mass using a profile  
4446 likelihood approach with the lepton + jets final states in proton–proton col-  
4447 lisions at  $\sqrt{s} = 13$  TeV”, *Eur. Phys. J. C*, vol. 83, no. 10, p. 963, 2023. DOI:  
4448 10.1140/epjc/s10052-023-12050-4. arXiv: 2302.01967 [hep-ex].
- 4449 [225] ATLAS and CMS Collaborations, “Combination of Measurements of the Top  
4450 Quark Mass from Data Collected by the ATLAS and CMS Experiments at  
4451  $\sqrt{s} = 7$  and 8 TeV”, *Phys. Rev. Lett.*, vol. 132, no. 26, p. 261902, 2024. DOI:  
4452 10.1103/PhysRevLett.132.261902. arXiv: 2402.08713 [hep-ex].
- 4453 [226] A. Djouadi, J. Ellis, A. Popov, and J. Quevillon, “Interference effects in  $t\bar{t}$   
4454 production at the LHC as a window on new physics”, *JHEP*, vol. 03, p. 119,  
4455 2019. DOI: 10.1007/JHEP03(2019)119. arXiv: 1901.03417 [hep-ph].
- 4456 [227] A. Djouadi, J. Ellis, and J. Quevillon, “Discriminating between Pseudoscalar  
4457 Higgs and Toponium States at the LHC and Beyond”, Dec. 2024. arXiv:  
4458 2412.15138 [hep-ph].
- 4459 [228] B. A. Betchart, R. Demina, and A. Harel, “Analytic solutions for neutrino  
4460 momenta in decay of top quarks”, *Nucl. Instrum. Meth. A*, vol. 736, p. 169,  
4461 2014. DOI: 10.1016/j.nima.2013.10.039. arXiv: 1305.1878 [hep-ph].
- 4462 [229] R. Demina, A. Harel, and D. Orbaker, “Reconstructing  $t\bar{t}$  events with one  
4463 lost jet”, *Nucl. Instrum. Meth. A*, vol. 788, p. 128, 2015. DOI: 10.1016/j.  
4464 nima.2015.03.069. arXiv: 1310.3263 [hep-ex].
- 4465 [230] G. J. Feldman and R. D. Cousins, “Unified approach to the classical statistical  
4466 analysis of small signals”, *Phys. Rev. D*, vol. 57, p. 3873, 1998. DOI: 10.1103/  
4467 PhysRevD.57.3873. arXiv: physics/9711021.
- 4468 [231] R. D. Cousins and V. L. Highland, “Incorporating systematic uncertainties  
4469 into an upper limit”, *Nucl. Instrum. Meth. A*, vol. 320, pp. 331–335, 1992.  
4470 DOI: 10.1016/0168-9002(92)90794-5.
- 4471 [232] HEPData record for analysis “Search for heavy pseudoscalar and scalar bosons  
4472 decaying to a top quark pair in proton-proton collisions at  $\sqrt{s} = 13$  TeV”  
4473 (CMS-HIG-22-013), 2025. DOI: 10.17182/hepdata.159298.
- 4474 [233] ATLAS Collaboration, “Measurement of the  $t\bar{t}$  production cross-section and  
4475 lepton differential distributions in  $e\mu$  dilepton events from  $pp$  collisions at  
4476  $\sqrt{s} = 13$  TeV with the ATLAS detector”, *Eur. Phys. J. C*, vol. 80, no. 6,  
4477 p. 528, 2020. DOI: 10.1140/epjc/s10052-020-7907-9. arXiv: 1910.08819  
4478 [hep-ex].

- 4479 [234] CMS Collaboration, “Differential cross section measurements for the produc-  
4480 tion of top quark pairs and of additional jets using dilepton events from pp  
4481 collisions at  $\sqrt{s} = 13$  TeV”, *JHEP*, vol. 02, p. 064, 2025. DOI: 10.1007/  
4482 JHEP02(2025)064. arXiv: 2402.08486 [hep-ex].
- 4483 [235] ATLAS Collaboration, “Inclusive and differential cross-sections for dilepton  $t\bar{t}$   
4484 production measured in  $\sqrt{s} = 13$  TeV pp collisions with the ATLAS detector”,  
4485 *JHEP*, vol. 07, p. 141, 2023. DOI: 10.1007/JHEP07(2023)141. arXiv: 2303.  
4486 15340 [hep-ex].
- 4487 [236] J. A. Raine, M. Leigh, K. Zoch, and T. Golling, “Fast and improved neu-  
4488 trino reconstruction in multineutrino final states with conditional normalizing  
4489 flows”, *Phys. Rev. D*, vol. 109, no. 1, p. 012005, 2024. DOI: 10.1103/  
4490 PhysRevD.109.012005. arXiv: 2307.02405 [hep-ph].
- 4491 [237] CMS Collaboration, “High-precision measurement of the W boson mass with  
4492 the CMS experiment at the LHC”, Dec. 2024. arXiv: 2412.13872 [hep-ex].
- 4493 [238] S.-J. Jiang, B.-Q. Li, G.-Z. Xu, and K.-Y. Liu, “Study on Toponium: Spec-  
4494 trum and Associated Processes”, Dec. 2024. arXiv: 2412.18527 [hep-ph].
- 4495 [239] I. Brivio et al., “ALPs Effective Field Theory and Collider Signatures”, *Eur.*  
4496 *Phys. J. C*, vol. 77, no. 8, p. 572, 2017. DOI: 10.1140/epjc/s10052-017-  
4497 5111-3. arXiv: 1701.05379 [hep-ph].
- 4498 [240] J. Bonilla, I. Brivio, M. B. Gavela, and V. Sanz, “One-loop corrections to ALP  
4499 couplings”, *JHEP*, vol. 11, p. 168, 2021. DOI: 10.1007/JHEP11(2021)168.  
4500 arXiv: 2107.11392 [hep-ph].
- 4501 [241] H. Bahl et al., “HiggsTools: BSM scalar phenomenology with new versions of  
4502 HiggsBounds and HiggsSignals”, *Comput. Phys. Commun.*, vol. 291, p. 108803,  
4503 2023. DOI: 10.1016/j.cpc.2023.108803. arXiv: 2210.09332 [hep-ph].
- 4504 [242] ATLAS Collaboration, “Search for resonances decaying into photon pairs in  
4505  $139 \text{ fb}^{-1}$  of  $pp$  collisions at  $\sqrt{s}=13$  TeV with the ATLAS detector”, *Phys.*  
4506 *Lett. B*, vol. 822, p. 136651, 2021. DOI: 10.1016/j.physletb.2021.136651.  
4507 arXiv: 2102.13405 [hep-ex].
- 4508 [243] ATLAS Collaboration, “Search for heavy resonances decaying into a  $Z$  or  $W$   
4509 boson and a Higgs boson in final states with leptons and  $b$ -jets in  $139 \text{ fb}^{-1}$   
4510 of  $pp$  collisions at  $\sqrt{s} = 13$  TeV with the ATLAS detector”, *JHEP*, vol. 06,  
4511 p. 016, 2023. DOI: 10.1007/JHEP06(2023)016. arXiv: 2207.00230 [hep-ex].
- 4512 [244] CMS Collaboration, “Observation of four top quark production in proton-  
4513 proton collisions at  $\sqrt{s} = 13$  TeV”, *Phys. Lett. B*, vol. 847, p. 138290, 2023.  
4514 DOI: 10.1016/j.physletb.2023.138290. arXiv: 2305.13439 [hep-ex].

## A Bibliography

---

- <sup>4515</sup> [245] A. Biekötter, J. Fuentes-Martín, A. M. Galda, and M. Neubert, “A global  
<sup>4516</sup> analysis of axion-like particle interactions using SMEFT fits”, *JHEP*, vol. 09,  
<sup>4517</sup> p. 120, 2023. DOI: 10.1007/JHEP09(2023)120. arXiv: 2307.10372 [hep-ph].

*This was a triumph.  
I'm making a note here: HUGE SUCCESS.  
It's hard to overstate my satisfaction.*

— GLaDOS

## 4518 B Acknowledgements

4519 I wish to thank, first and foremost, my excellent PhD supervisors: Christian Schwa-  
4520 nnenberger and Alexander Grohsjean. You gave me feedback when I needed it, left  
4521 me space when I did not, and always had my back in our common (mis-)adventures  
4522 in the wide and wonderful and sometimes wondrous world that is Experimental  
4523 Particle Physics. You also gave me great (and honest) advice and support for my  
4524 further career, for which I am extremely thankful. Working with you has been a  
4525 pleasure.

4526 I am also deeply grateful to the many colleagues, postdocs and other PhD stu-  
4527 dents, who taught me the intricacies of CMS and provided technical and moral  
4528 support: Afiq Anuar, for unleashing  $A/H \rightarrow t\bar{t}$  in the first place, and for always  
4529 distracting me with interesting physics; Evan Ranken, who for some reason agreed  
4530 to help perform a measurement in only two months; Jonas Rübenach and Dominic  
4531 Stafford, for collectively sparing me from ROOT with their framework; again Jonas,  
4532 for setting up the  $A/H$  analysis and giving me an excess to interpret; and again  
4533 Dominic, for tolerating me as an officemate. Thanks to all of you.

4534 Furthermore, I would like to thank my additional collaborators and supervisors  
4535 on the different projects I worked on: Maria Aldaya and Andreas Meyer for the  $t\bar{t}$   
4536 cross section in Run 3; Simone Amoroso for **bb4l**; as well as Georg Weiglein, Sven  
4537 Heinemeyer, and the Biekötter Cousins for ALPs  $\rightarrow t\bar{t}$ .

4538 Finally, I wish to give a huge thanks to the DESY CMS group for being a great  
4539 place to work.

## 4540 C Appendices

### 4541 C.1 Sample normalizations in the matrix element 4542 reweighting

4543 In this section, a derivation of the optimal way to combine multiple independent  
4544 origin samples for the purpose of matrix element reweighting, as described in Sec. 7.4  
4545 is given. In particular, Eq. (7.15) is proven for the case that the cross section  
4546 corresponding to the target hypothesis is known from an external calculation.

4547 The notation used is the same as in Sec. 7.4. Let  $\hat{w}_{i,j}$  be the weight of event  $i$  in  
4548 origin sample  $j$  after reweighting, i.e. the product of ME weight and generator weight  
4549 of the origin sample, and  $v_j$  the per-sample normalization that is to be determined.  
4550 The per-event weight after normalization is  $v_j \hat{w}_{i,j}$ .

4551 First, consider the case that the total cross section  $\sigma$  is known for the target  
4552 hypothesis, meaning that the ME reweighting needs to only predict the shapes  
4553 of the distributions. In Sec. 7.4, this is achieved by explicitly calculating  $\sigma$  with  
4554 MG5\_AMC@NLO for each target A/H hypothesis. The goal is now to minimize  
4555 the total variance of the sample, given by

$$V = \sum_{i,j} v_j^2 \hat{w}_{i,j}^2, \quad (\text{C.1})$$

4556 under the constraint that the total yield is

$$N = \sum_{i,j} v_j \hat{w}_{i,j} \equiv \sigma L, \quad (\text{C.2})$$

4557 where  $L$  is the integrated luminosity. This is done with the method of Lagrange  
4558 multipliers, giving the Lagrange function

$$\mathcal{L}(v_j, \lambda) = \sum_{i,j} v_j^2 \hat{w}_{i,j}^2 + \lambda \left( \sum_{i,j} v_j \hat{w}_{i,j} - \sigma L \right) \quad (\text{C.3})$$

4559 which needs to be minimized simultaneously over  $v_j$  and  $\lambda$ . Differentiating by  $v_j$   
4560 gives

$$\frac{\partial \mathcal{L}}{\partial v_j} = 2v_j \sum_i \hat{w}_{i,j}^2 + \lambda \sum_i \hat{w}_{i,j} \equiv 0 \quad \Rightarrow \quad v_j = -\frac{\lambda}{2} \frac{\sum_i \hat{w}_{i,j}}{\sum_i \hat{w}_{i,j}^2}. \quad (\text{C.4})$$

4561 By substituting this into Eq. (C.2) to find  $\lambda$ , one obtains

$$v_j = \sigma L \left( \sum_k \frac{\sum_i \hat{w}_{i,k}}{\sum_i \hat{w}_{i,k}^2} \right)^{-1} \frac{\sum_i \hat{w}_{i,j}}{\sum_i \hat{w}_{i,j}^2} \quad (\text{C.5})$$

4562 which has the form of Eq. (7.15).

4563 Alternatively, one might consider the case that the cross section  $\sigma$  is not known  
4564 and should be predicted by the reweighting. In this case, one should require that  
4565 the normalizations  $v_j$  do not change the total yield in the limit of large statistics,  
4566 implying  $\sum_j v_j = 1$ . This leads to the Lagrange function

$$\mathcal{L}(v_j, \lambda) = \sum_{i,j} v_j^2 \hat{w}_{i,j}^2 + \lambda \left( \sum_j v_j - 1 \right) \quad (\text{C.6})$$

4567 from which one finds through an analogous calculation

$$v_j = \left( \sum_k \frac{1}{\sum_i \hat{w}_{i,k}^2} \right)^{-1} \frac{1}{\sum_i \hat{w}_{i,j}^2}. \quad (\text{C.7})$$